Deciphering the brainstem, hippocampal and whole-brain dynamics by neuronal-ensemble event signatures

Dissertation

zur Erlangung des Grades eines
Doktors der Naturwissenschaften

der Mathematisch-Naturwissenschaftlichen Fakultät
und
der Medizinischen Fakultät
der Eberhard-Karls-Universität Tübingen

vorgelegt
von

Juan Felipe Ramirez-Villegas, Dipl.-Ing.
aus Santiago de Cali, Kolumbien

December - 2017

Tag der mündlichen Prüfung: ....

Dekan der Math.-Nat. Fakultät: Prof. Dr. W. Rosenstiel
Dekan der Medizinischen Fakultät: Prof. Dr. I. B. Autenrieth

1. Berichterstatter: Prof. Dr. Nikos K. Logothetis
2. Berichterstatter: Prof. Dr. Andreas Bartels

Prüfungskommission: Prof. Dr. Nikos K. Logothetis
Prof. Dr. Andreas Bartels
Prof. Dr. Gustavo Deco
Prof. Dr. Uwe Ilg

Erklärung / Declaration:

Ich erkläre, dass ich die zur Promotion eingereichte Arbeit mit dem Titel:

"Deciphering the brainstem, hippocampus and whole-brain dynamics by neuronal-ensemble event signatures"

selbständig verfasst, nur die angegebenen Quellen und Hilfsmittel benutzt und wörtlich oder inhaltlich übernommene Stellen als solche gekennzeichnet habe. Ich versichere an Eides statt, dass diese Angaben wahr sind und dass ich nichts verschwiegen habe. Mir ist bekannt, dass die falsche Abgabe einer Versicherung an Eides statt mit Freiheitsstrafe bis zu drei Jahren oder mit Geldstrafe bestraft wird.

I hereby declare that I have produced the work entitled ***"Deciphering the brainstem, hippocampus and whole-brain dynamics by neuronal-ensemble event signatures"***, submitted for the award of a doctorate, on my own (without external help), have used only the sources and aids indicated and have marked passages included from other works, whether verbatim or in content, as such. I swear upon oath that these statements are true and that I have not concealed anything. I am aware that making a false declaration under oath is punishable by a term of imprisonment of up to three years or by a fine.

Tübingen, den ....
Datum / Date Unterschrift / Signature

A mis padres

Contents

List of Figures

Abbreviations

ACC	Anterior cingulate cortex
AMPA	α-amino-3-hydroxy-5-methyl-4-isoxazolepropionic acid
Arc	activity-regulated cytoskeletal protein
BDNF	Brain-derived nerve grow factor
CA1	Cornu ammonis field 1
CA2	Cornu ammonis field 2
CA3	Cornu ammonis field 3
CaMKII	calmodulin-dependent protein kinase II
cAMP	cyclic adenosine monophosphate
CCK	Cholecystokinin
C-PBL	Caudolateral parabrachial area
CREB	cAMP response element binding protein
DG	Dentate gyrus
EC	Entorhinal cortex
EEG	Electroencephalogram
E-I balance	Excitation-inhibition balance
ENK	Enkephalin
EPSC (EPSP)	Excitatory post-synaptic current (Excitatory post-synaptic potential)
GABA	Gamma-Aminobutyric acid
IPSC (IPSP)	Inhibitory post-synaptic current (Inhibitory post-synaptic potential)
LC	Locus coeruleus
LEC	Lateral entothinal cortex
LFP	Local field potential
LGB	Lateral geniculate body
LGN	Lateral geniculate nucleus
LIA	Large-amplitude irregular activity
LTP	Long-term potentiation
MAPK	mitogen-activated protein kinase
MEC	Medial entothinal cortex
mEFP	Mean extracellular field potential
ML	Molecular layer
MM	Medial mammillary nucleus
MS-DB	Medial septum - Diagonal band of Broca
MUA	Multi-unit activity

NE	Norepinephrine
NMDA	N-methyl-D-aspartate
PBL (PBn)	Parabrachial area (Parabrachial nucleus)
PCC	Posterior cingulate cortex
PFC	Prefrontal cortex
PGO wave	Pontogeniculooccipital wave
PH	Posterior hypothalamic nucleus
PKA	Protein kinase-A
PPT	Pedunculopontine tegmental nucleus
PV	Parvalbumin
REM	Rapid-eye movement
R-PBL	Rostral parabrachial area
RPO	Reticularis pontis oralis
SL	Stratum lucidum
SL-M	Stratum lacunosum-moleculare
SO	Stratum oriens
SP	Stratum pyramidale
SR	Stratum radiatum
SUA	Single-unit activity
SubCD	Subcoeruleus nucleus
SuM	Supramammillary nucleus
SWR	Sharp wave-ripple
SWS	Slow-wave sleep
TA	Temporoammonic
VTA	Ventral tegmental area
VTE	Vicarious trial and error

Keywords

Sleep, Memory, Electrophysiology, Local field potential, Hippocampus, Sharp wave-ripples, Pontogeniculooccipital waves, Brainstem, Pons, Neuromodulation, functional MRI.

Acknowledgements

The completion of this dissertation has been a great challenge at multiple levels, and it has taken longer than I expected it would take. The quest of understanding brain computations has brought me through a journey of unprecedented questioning, observing and reasoning, heavily intermingled with contingent-world vicissitudes and perils that were also greatly enjoyed. Conversely, this work has withstood the vicissitudes inherent to myself, and my quasi-mercurial character. As for being in the road (which is not an easy thing), there are several people that I'm truly indebted to, for supporting me and making this experience the best, and most successful one:

I'm extremely grateful with Michel Besserve, a very bright scientist with whom I pursued most of (if not all) my research in this Laboratory. More importantly than that, I acknowledge his role as a friend. I'm grateful for many constructive discussions, and for the disposition and availability showed during the development of my project (despite of my sometimes 'abusive' use of his time). It has been really stimulating and a good mechanism to generate ideas all the way through. In a similar vein, I'm grateful with Nikos K. Logothetis, whose intelligence and inspiration are themselves an inspiration. It's been somewhat unexpected but undoubtedly a true honor that he has contributed much to mentor me. Besides, Nikos' tight involvement in the last part of this project has been of paramount importance for its final outcome.

I thank Yusuke Murayama, Oxana Eschenko and Henry Evrard for helpful discussions. This project has benefited big time from their hard work. Furthermore, I'm grateful to Joachim Werner and Michael Schnabel for their never-ending IT support, anytime, anywhere. To Conchy Moya for her help and friendly assistance whenever I needed it. To Markus Schneller, for his great disposition to help me whenever I did not have access to published research work, and also for being kind and letting me work in the library for long hours.

I would like to thank very much the involvement of Uwe Ilg, Andreas Bartels, and Gus Deco as committee members of this thesis. Their thoughtful feedback and questions have enhanced my scientific output. Despite the last-minute notice, Uwe agreed to be part of my thesis committee as a fourth member, for which I'll always be grateful. I'm greatly indebted with Andreas, who helped a great deal with my postdoctoral fellowship application. Likewise, special thanks go to Gus Deco, for the countless informal meetings at conferences and through Skype, and the very nice and charming interaction we have

had along these years.

David F. Ramírez-Moreno, together with Odelia Schwartz, supported my first (and likely most important) steps in this career path. I sincerely thank them for their unique support during difficult times alongside Araceli Ramirez, Daniel Zaldívar and Jozien Goense. Your prompt and intelligent personal advice served to save me in several opportunities.

I'd like to extend my gratitude to my friends Araceli Ramírez, Mario Baez, Marlon Pérez, Daniel Zaldívar and, of course, Diego Sánchez, for withstanding my quirky behaviour, for the endless hours of acid humour, food and beer, and for showing more personal support than I ever provided myself. In particular, Araceli provided much (medical and emotional) help during difficult times. Furthermore, Andre Marreiros has been a great, sensitive friend (thanks for the many 'logistic' favours). I'm thankful to Filip Sobczak for his friendship, and for helping me carrying stuff up and down Tübingen's hills. My classical, all-time friends Henry A. Tabares, Fernando Correa, Mauricio Montes, Arlex ('Arley') Salcedo, my cousin Victor Mahecha, and my brother Daniel Ramírez have supported me since my first years in academia. Riya Paul and Konstantin Willeke were the best and nicest students anybody can possibly have. I thank members of the Besserve-group Yiling Yang, Kaidi Shao and Shervin Safavi, with whom I had group discussions. Finally, Carlos Hernán Silva and Carlos Fernando Mafla (a.k.a. 'Manto') have provided the internet memes necessary for the completion of this work.

I have an increasing debt to my fiancée, Maria Constantinou, for her invaluable support during the last period of this doctorate. For withstanding me during several days (possibly months) of high stress, and for her role in preventing me from having a spontaneous burnout, a spontaneous jump-off from the terrace etc. Amongst others, also for spending a significant amount of her time proof-reading this work, making me forget about neuronal processing as of the beginning of many weekends, the delicious Cypriot recipes, and our many unforgettable moments in Manchester (including our hard goodbyes at the airport).

Last but not least, this work is dedicated to my parents: Luz Mary (Luzma) Villegas and Rafael Ramírez. This thesis would have been impossible without their endless reservoir of support. Their fearless courage in life not only continues to impress me, but has been the most powerful engine to pursue and stand stoically by my goals. Likewise, more often than not, I have relied on the invaluable help and support of my brother, Julian Ramírez-Villegas, one of the brightest scientists I have ever come across in life. His enduring influence, intelligence and work passion have been present in many steps of my career, and continue to this day.

Juan F. Ramirez Villegas, 2017.

Summary

Memories are a fundamental part of our lives. We use stored information in order to make decisions and perform activities that require high-order mental processing. Such ability relies on network mechanisms, involving prominently the hippocampal and parahippocampal systems, and their interaction with the rest of the brain. The neural computations underlying memory storage and retrieval are thought to involve highly transient microcircuit activities that correlate with changes in the excitability of neural circuits. These changes selectively modulate the signaling between groups of cells across distinct brain circuits, ultimately supporting the emergence of more globally coordinated activities.

Intracortically-recorded brain signals display a rich variety of such transient activities: brief, recurring episodes of *deflection* or oscillatory activities that reflect cooperative neural circuit mechanisms. These network patterns of activity, also called *neural events*, span multiple spatio-temporal scales, and are believed to be basic computing elements during cognitive processes such as learning and off-line memory consolidation. However, both the large-scale and microscopic-scale cooperative mechanisms associated with these episodes remain poorly understood. This knowledge gap arises partly due to methodological limitations of existing experimental approaches, specifically in measuring simultaneous micro- and macroscopic aspects of neuronal activity in the brain. Therefore, this dissertation sought to study the relationship between ongoing spontaneous neural events in the hippocampus, brainstem and thalamic structures at micro-, meso- and macroscopic scales by combining data from intracortical recordings, multi-compartmental network models, and functional magnetic resonance imaging (fMRI).

In the first paper of this dissertation, we investigated the dynamics of neural events in the hippocampus. We isolated various types of events corresponding to hippocampal sharp wave-ripples (SWR) –episodes of release of synchronous neuronal activity in CA1, thought to be critical for memory consolidation– and investigated their neuronal correlates. Specifically, we investigated whether variations in the local field potential (LFP) signature reflected differences in the coordination of global neural activity translated into changes of brain-wide blood-oxygenation-level-dependent (BOLD) fMRI activity. SWR LFP activity –classified into several subtypes– was indeed associated with distinct neocortical and subcortical BOLD fMRI activation patterns. Our results suggest that SWR episodes are highly heterogeneous and may instantiate cortico- and subcortico-hippocampal interactions of differentiated nature. The interactions at play during each SWR subtype may occur in support of distinct off-line and waking-related mnemonic processes.

In the second paper, we investigated the neurophysiological mechanisms underlying SWR episodes. In this study, we sought to address the role played by CA3 rhythmic input, as well as the role of CA1 local pyramidal cells and interneurons in SWR emergence. Using a multi-compartmental model of the CA3-CA1 network, we found that SWR emerge locally from the driving of CA1 pyramidal cells by local interneurons' recurrent somatic inhibition, whereas somatic excitation controls the amount of pyramidal cells involved in single ripples. Local interactions within CA1 and incoming input from CA3 are largely frequency-specific, where CA3 coordinates its interactions with CA3 assemblies by gamma, but not ripple oscillations. Our model reproduces a wide range of characteristics present in *in vivo* cellular and LFP activites associated with SWR, offers key insights to precisely establish the hippocampus-dependent mechanisms underlying memory trace reactivation and consolidation, and suggests new experimental directions.

In the third paper, we investigated the dynamics of pontogeniculooccipital (PGO) waves across several brain regions, and specifically their relationship with hippocampal activity. The link between pontine-thalamic and hippocampal activities has been reported in the literature, yet, the neurophysiological nature of this selective coupling is not well-understood. We recorded the activity of the pontine region, lateral geniculate nucleus (LGN) and hippocampus simultaneously, and found that PGO waves –brief potentials propagating from pons to LGN and to neocortex– come in two different types. Marked by antagonistic neuronal population responses, PGO wave types co-occurred with hippocampal events in a differentiated manner. Type I PGO waves (also referred to as slow-wave sleep-PGO waves) co-occurred with SWR complexes; whereas type II PGO waves (also referred to as rapid-eye movement (REM) sleep-PGO waves) co-occurred with highly transient bouts of theta-like activity in the hippocampus. These results provide the first evidence for brain state-dependent, transient and long-range interactions likely related to hippocampal-neocortical, and ponto-geniculo-neocortical functional networks, possibly associated with distinct memory-related functions.

Altogether, the results of this dissertation support the view that neural events are triggers or modulators for specific mnemonic processes extending across several global brain states (namely, slow-wave sleep and REM sleep). These events herald interactions across networks of several brain domains. Throughout this work I present experimental and theoretical evidence that distinct subtypes of events –segregated on the basis of their physiological properties– are likely associated with distinct brain-wide dynamics. Thus, the local microcircuit activities and the global activity of the brain are tightly intertwined during neuronal processing across diverse behavioural states. Finally, our results hold wide implications for existing mechanistic models of hippocampal SWR and PGO waves, for future large-scale computational models, together with directions for new *in vivo* experiments in behaving animals.

Chapter 1

Synopsis

1.1 General motivation of the project

Containing ∼86 billion nerve cells (Azevedo et al., 2009), the brain is one of the most complicated systems we know of in the universe. Nerve cells are massively interconnected, establishing numerous interactions that occur many times per second. It is, therefore, difficult to imagine how with a machinery of such complexity, the human brain is functional at all. The brain is capable of supporting and regulating all aspects of physiological activity in the body. In order to account for this large diversity of processes, brain activity displays a high degree of self-organised coordination, occurring across several large-scale neural networks. The dynamical states that underlie the interactions in such a complex system cannot be described in terms of the individual activities of its billions of cells. Indeed, brains –as many physical systems– undergo transitions between macroscopic states. Thus, a better understanding may be achieved by monitoring the network-level activity of multiple processing centres in a concurrent manner.

The organisation of brain activity suggests that processes such as learning and memory result from the concerted activity of many regions, spanning several states. For instance, it is well-known that upon changes in neuromodulatory activity the brain can display different types of activities associated with behavioural states of waking, and the distinct stages of sleep (Hobson, 2009; Pace-Schott and Hobson, 2002). These activities translate into distinct dynamical regimes of individual anatomically-coupled networks. Neural patterns of activity within these subsystems often signal periods of both enduring and transient changes of neuronal excitability that affect the activity of other sub-structures in a precise manner (Logothetis, 2015).

A remarkable emerging characteristic of brain networks is oscillatory activity, often referred to as *brain rhythms*. These rhythmic activities are highly dependent on the global state of the brain, and are thought to be crucial for cognitive processing (Pace-Schott and

Hobson, 2002). During periods of quiescence and slow-wave sleep (SWS), slow oscillations –prevalent across the neocortex– organise several oscillatory activities occurring in other subsystems of the brain (Sirota and Buzsaki, 2005). Such activities come in the form of transient episodes which we call *neural events*. Neural events include K-complexes, thalamo-cortical spindles, and population events in the hippocampal CA1 subfield known as sharp wave-ripples (SWR). K-complexes correspond to large, slow deflections in the electrical activity associated with bursting cortical neurons. They are temporally coupled with spindles, and both are correlated with the occurrence of both slow changes in neural firing and SWR episodes in the hippocampal formation (Siapas and Wilson, 1998; Ji and Wilson, 2007; Peyrache et al., 2011). Thus, it is clear that the physiology underlying cognitive processes largely falls within complex-system paradigms. Yet, to date, it remains incompletely understood.

In my dissertation, I pursued this quest by studying the physiological activity of the brain associated with learning and memory. In particular, recordings of the electrical potential of CA1, and across pontine-thalamic-neocortical systems during sleep have provided evidence for a constellation of neural events critical for memory consolidation (Buzsaki, 2015; Datta, 2006). Our fascination for these spontaneous events is catalysed by their striking correlation with activity patterns across the whole brain (Logothetis et al., 2012; Logothetis, 2015) whose properties have become our question generators. Thus, we studied the activity of the hippocampal CA1, the pontine region and the thalamus during periods associated with off-line memory consolidation. Specifically, through principled analyses of concurrent multi-site intracortical recordings, whole-brain fMRI and a series of minimal multi-compartmental models, we investigated the micro-circuits and brain-wide structures whose activities are modulated during different types of memory-associated neural events.

1.2 Memory in the brain

Storing information and then using it to guide behaviour is a remarkable ability of the brain. Decades of investigation have established that the hippocampus plays a central role in these processes. The link between the hippocampus and memory processes was first suggested by the seminal work of Scoville and Milner (1957). In their investigation, a patient known as H.M. was unable to create new episodic memories after bilateral medial temporal lobe resection, including the resection of both hippocampi. After this study, accumulating experimental evidence identified the hippocampus as a critical structure for declarative memory.

A series of later studies attributed a role for spatial memory to the hippocampus of rodents. O'Keefe and Dostrovsky (1971) observed that a subset of hippocampal neurons selectively increased their firing rates as the animals occupied specific locations in an environment. The existence of these cells, known as place cells, and the observed spatial memory deficits upon lesion of the hippocampus have led to the proposal that hippocampal activity provides a cognitive map of the animal's spatial environment (O'Keefe and Nadel, 1978). Subsequent research revealed that cells in the hippocampal formation can encode other aspects of space such as boundaries (Lever et al., 2009), direction of the animal's head (Taube et al., 1990a,b), and speed (Kropff et al., 2015). In addition, grid cells found in the medial entorhinal cortex (MEC) suggest the existence of a spatial code in the form of 'triangular coordinates'. This code is thought to be the basis of spatial location represention in absence of sensory input, and updated by the animal's movements (Fyhn et al., 2004; Hafting et al., 2005). Nevertheless, the hippocampus does not only code for spatial properties. Recent experimental evidence demonstrates that cells in the hippocampal formation are involved in a repertoire of other representations including contextual information, object recognition and time (Eichenbaum et al., 1987; Eichenbaum, 2014; Hok et al., 2007; Moita et al., 2003; Manns and Eichenbaum, 2009).

Whereas the hippocampus is fundamental in encoding declarative memories, the hippocampus alone cannot store stable, long-lasting representations. Indeed, a great body of evidence suggests that information is stored in the neocortex in the long-term. It is currently assumed that the role of the hippocampus in enabling the neocortex to acquire new knowledge can be explained using a two-stage process. Learning trials are first encoded in the hippocampus during ongoing behaviour. In a second stage, the hippocampus allows the brain to experience 'virtual' training trials, manifested as the spontaneous retrieval of episodic memory while the brain is in an off-line state, e.g. during periods of calmness or sleep. This reactivation process of labile memories in hippocampus and neocortex is thought to potentiate cortico-cortical connections, hence providing the basis for the formation of new assemblies. This theoretical account is in line with the seminal studies of Wilson and McNaughton (1994), and Skaggs and McNaughton (1996), where reactivation of cell pairs was observed during sleep after a spatial experience.

After these studies, increasing experimental evidence demonstrated that after 1 to 2 hours of a behavioural experience, during periods of calmness or SWS hippocampal CA1 cells fired brief sequences of action potentials that were also expressed during waking (Lee and Wilson, 2002). These sequences have several important properties. First, they are often concurrently replayed in both hippocampus and neocortex (Lee and Wilson, 2002; Ji and Wilson, 2007). Second, in both hippocampus and neocortex, firing sequences correspond to series of temporally-compressed versions of place-cell firing sequences played during wakefulness (Euston et al., 2007). Third, replay occurs in neocortex during periods where delta oscillations/K-complexes field activities are observed (Peyrache et al., 2009; Johnson et al., 2010). Finally, hippocampal replay occurs simultaneously with a special pattern of field activity known as SWR complexes, also occurring within the CA1 subfield (Buzsaki et al., 1992; Lee and Wilson, 2002), which are discussed in depth later in this work. Notably, neocortical reactivation tends to follow that in the hippocampus (including the occurrence of SWR), suggesting that the hippocampus is driving the neocortex during the reactivation process (Wierzynski et al., 2009). As consolidation progresses, memories that initially depend on the hippocampus become distributed in neocortical circuits, possibly displaying categorical structure, i.e. a form of 'hierarchical clustering' of neuronal representations over time (McClelland et al., 1995).

Whereas these theoretical and experimental advances have been fundamental to our understanding of memory, how the brain networks interact in order to store and retrieve complex information remains unknown. The original discovery of SWR episodes and their intrinsic properties was a critical step towards this understanding (Buzsaki et al., 1992; Buzsaki, 1986, 2015). Indeed, the reactivation process occurring during hippocampal SWR is thought to be a convenient mechanism for memory consolidation from a theoretical perspective. For example, SWR are the most synchronous events in the mammalian brain, associated with a robust enhancement of excitability in the hippocampal formation, and behaviourally-relevant spiking content (Mizunuma et al., 2014; Csicsvari et al., 1999; Lee and Wilson, 2002). These, together with their electrical and intrinsic properties, are thought to be ideal to induce plasticity in target structures. Furthermore, although it was initially observed during SWS and quiescence periods, SWR reactivation also occurs during active behaviour (Foster and Wilson, 2006; Dupret et al., 2010; Singer et al., 2013), indicating that reactivation during several brain states could support consolidation. The generation of SWR complexes in various behavioural contexts and brain states likely involves brain-wide network mechanisms, and as a consequence, SWR-related brain dynamics may vary, reflecting different types of interactions with cortical and subcortical systems. Furthermore, a detailed study of SWR and its underlying elementary network activities is fundamental to understand its physiological mechanisms, and may provide new insights into the mechanisms of fast oscillatory episodes observed during epilepsy (Karlocai et al., 2014).

In this thesis work, we combined data from a novel multi-modal experimental approach known as neural-event-triggered functional magnetic resonance imaging (NET-fMRI) with biophysically-inspired computational models in order to investigate the SWR phenomenon to a full extent, comprising several spatio-temporal scales. Although most of this investigation is dedicated to SWR episodes, partly motivated by our first results, we also investigated the relationship between brainstem and thalamic neuronal activities –more specifically, that of pontine nuclei and LGN, respectively– and hippocampal neuronal activities during SWR and non-SWR epochs. In particular, we studied a second type of episode thought to represent the main drive of glutamatergic discharges during sleep-dependent memory formation known as pontogeniculooccipital (PGO) waves (Datta, 1997, 2006).

The rest of the introduction is organised as follows: First, I present an overview of the anatomy of the hippocampal formation, followed by a brief summary of the physiological electrical activity of the hippocampus, with emphasis on primates. Finally, I summarise the main subcortical circuits that modulate hippocampal activity, and provide an overview of PGO waves and their putative role in memory formation.

1.3 Anatomical organisation of the hippocampal formation

To understand the relationship between the hippocampal circuits' dynamics and the emergence of macroscopic brain activity, it is fundamental to have a basic understanding of the connectivity within the hippocampus, and its anatomical links with the rest of the brain. Therefore, in this section, I focus on the fundamental aspects of the anatomical organisation within the hippocampal formation that relate to processing of mnemonic information.

1.3.1 Structures and connectivity within the hippocampal formation

The hippocampal formation is an elongated, bilateral structure located in the medial temporal lobe and highly preserved across mammalian species. The hippocampus runs along a posterior-anterior axis in primates (dorsal/septal to ventral/temporal in rodents). Its anatomy and physiology are well-preserved with phylogenetic development (Andersen et al., 2006). This fact has served to unify views on the structure and role of the hippocampus in primates and humans, with extensive experimental demonstrations in other animal species such as rodents.

The regions of the hippocampal formation include the dentate gyrus (DG), subiculum, presubiculum, parasubiculum, entorhinal cortex (EC) and the subfields of the hippocampus proper (referred to as cornu ammonis, CA fields) (Andersen et al., 2006). In the following subsections I give an overview of the anatomy of these structures in the rodent, as most of the existent evidence has been derived from experimental preparations in such animal species. For extensive reviews on the anatomical details of the hippocampal formation, the reader is referred to Andersen et al. (2006), van Strien et al. (2009), and Witter and Amaral (2004).

The rodent hippocampal formation is a C-shaped structure situated in the caudal part of the brain. The shape of the hippocampal formation is commonly appreciated from its dorso-ventral (also referred to as septo-temporal) axis. Several of its anatomical properties vary across its proximo-distal and transverse axes (see Figure 1.1) (Witter et al., 2000). Each hippocampal subfield is organised in a series of layers formed by oriented pyramidal cells (Amaral and Witter, 1989). The first layer (from top to bottom in Figure 1.1B) is a basal dendritic layer in the CA called stratum oriens (SO), followed by the pyramidal cell layer (or stratum pyramidale, SP) composed by principal cells and interneurons, and two other (apical) dendritic layers known as stratum radiatum (SR) and stratum lacunosum-moleculare (SL-M). In the DG, the first layer is known as hilus composed by interneurons and so-called mossy fibers, followed by a granule cell layer and a molecular layer that separates the DG from the hippocampal fissure.

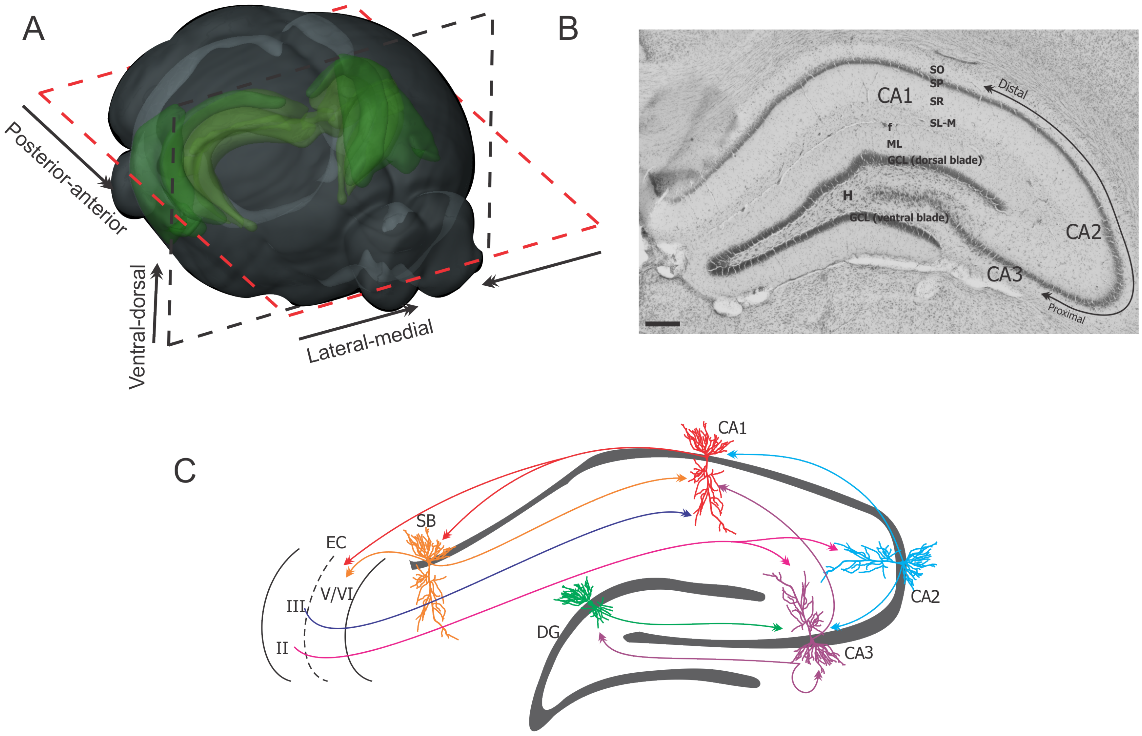

Figure 1.1: (A) Location of the hippocampal formation (bilateral, curved structure in green) in the rodent brain. The illustration displays the hippocampus, subiculum and EC (lateral part of the brain). (B) Nissl-stained coronal section (as indicated in A by the black dotted plane) illustrating the transverse axis of the hippocampus. Abbreviations are as follows: CA, cornu ammonis; SO, stratum oriens; SP, stratum pyramidale; SR, stratum radiatum; SL-M, stratum lacunosum-moleculare; f, hippocampal fissure; ML, molecular layer; GCL, granule cell layer; H, hilus. Scale bar 200 μm. (C) Horizontal section of the rodent brain (as indicated in A by the red dotted plane) indicating the location of subiculum and EC. The horizontal slice is useful to depict the connectivity of the hippocampal formation and the tri-synaptic loop. Arrows indicate synaptic links between cell populations of each subfield. EC projects to DG/CA3 and CA1 subfields of the hippocampus through the perforant and temporoamonic pathways, respectively, targetting the distal dendritic layer of CA subfields (at SL-M). DG projects to CA3 through the mossy fibers. CA3 and CA1 are coupled by means of so-called Schaffer collaterals. Finally, the projections between CA1 and subiculum are reciprocal (see also Witter et al. (2000)), and both subiculum and CA1 project back to EC. Panel A is adapted from the Allen Mouse Brain Atlas (Brain Explorer 2, Allen Institute for Brain Science), available online at http://mouse.brain-map.org. Panel C is adapted from Sosa et al. (2016).

The hippocampus is strongly and reciprocally connected to an adjacent system referred to as the parahippocampal region (van Strien et al., 2009). The parahippocampal region comprises the presubiculum, parasubiculum and EC, together with the perirhinal and postrhinal cortices. The parahippocampal region is organised in a layered structure, where each layer receives and sends projections of differentiated nature. For example, the EC –subdivided into medial (MEC) and lateral (LEC)– receives sensory input that travels into the hippocampus via the perforant pathway. This pathway consists of projections from EC layer II to the apical dendrites of DG granule cells (in the molecular layer), and the SL-M of CA2 and CA3. EC layer III targets subicular neurons and the SL-M of CA1. This projection –known as temporoammonic (TA) pathway– is organised in the proximo-distal axis analogous to that of layer II, with the LEC projecting to the proximal and distal portion of the subiculum and CA1, respectively, and the MEC projecting to the distal and proximal portion of the subiculum and CA1, respectively (Ito and Schuman, 2012; Gigg, 2006).

Probably the most well-known aspect of the hippocampal anatomical connectivity is the so-called tri-synaptic circuit. This circuit connects in a feedforward manner the EC to the DG, DG to CA3, CA3 to CA1, and CA1 back to EC (Ramon y Cajal, 1893; Andersen et al., 2006). The intra-subfield connectivity of hippocampal structures has been object of extensive research, given the complexity of its local recurrent connections and long-range afferents.

1.3.2 Dentate gyrus (DG)

The DG comprises three layers. The molecular layer contains interneurons, and is excitatory-cell free. The granule cell layer –forming the V- or U-shape of DG– is a densely packed layer of somata, which borders with the hilus. The main cell types of the DG are the granule cell and the pyramidal basket cell. Other types of interneurons are also present in the granule cell layer and the hilus.

The primary excitatory input to the granule cells originates from EC layer II, although they also receive feedback input from mossy cells (located in the hilus) (Buckmaster et al., 1996). Mossy fibers form either recurrent or feedforward connections, with virtually no presence in the molecular layer. Mossy fibers target both CA3 pyramidal cells and interneurons. DG neurons do not project to any region other than CA3 within the hippocampus or outside the hippocampus, including the parahippocampal region. Finally, the DG receives projections from subcortical areas such as the septal nuclei, hypothalamus and brainstem neuromodulatory inputs (Bland and Oddie, 1998; Vertes, 1982; Vertes et al., 2004).

1.3.3 Hippocampus proper

The rodent hippocampus, also known as hippocampus proper, is divided into three cornu ammonis (CA) fields (CA1, CA2 and CA3), each comprising four or five layers. In primates –including humans– the hippocampus proper is divided into four CA fields, where the CA4 corresponds to the region between the DG and the most proximal end of CA3. The layer organisation of the CA fields is very similar, with one somatic layer (SP), one basal dendritic field (SO) and two apical dendritic layers (SR and SL-M). Notably, CA3 has an additional dendritic layer –absent in both CA1 and CA2– referred to as stratum lucidum (SL), corresponding to the region where the DG granule cells contact CA3 synaptically through the mossy fibers.

The subfields CA3, CA2 and CA1 have different recurrent local connectivity, giving rise to a repertoire of population activities. These activities can be modulated upon the state of subcortical and neocortical systems as discussed in Sections 1.4 to 1.6 of this work.

1.3.3.1 CA3 and CA1 networks

The DG granule cells receive primary input from EC via the perforant pathway. These cells then project to CA3 through the mossy fibers. In contrast to the usual tri-synaptic model, there are several back-projections from CA3 to the hilus and the inner molecular layer of DG across the whole septo-temporal axis (van Strien et al., 2009). The only documented extrahippocampal projection to CA3 is that of the septal nucleus (Bland and Oddie, 1998).

The recurrent nature of the CA3 network is historically well-acknowledged (Lorente de No, 1934), where recurrent circuits were initially linked to feedback chains of connected neurons. CA3 pyramidal cell axons have extensive ramifications in stratum oriens and radiatum of CA3 establishing synaptic contacts with other CA3 partners. The recurrent (often called associational) connections of CA3 are sometimes locally concentrated. For example, along its proximo-distal axis (1.1B), cells located proximally in CA3 synapse with other proximal cells. However, projections from middle and distal CA3 project extensively throughout the transverse axis of CA3 (Andersen et al., 2006). Experimental evidence from paired recordings in CA3 pyramidal cells suggests that one pyramidal cell contacts 30-60% other pyramidal cells (Li et al., 1994; Debanne et al., 1995; Pavlidis and Madison, 1999) with postsynaptic potentials of approximately 1 mV (Miles and Wong, 1986) (see also Ramirez-Villegas et al. (2017b)).

All portions of CA3 contact CA1, being the major input of the latter structure. Synaptic terminal distribution strongly depends on the spatial location of the CA3 neurons sending projections. The CA3-CA1 connectivity follows both transverse and oblique orientations through CA1. Note that in Figure 1.1C I have drawn the Schaffer pathway as it is conventional from research papers (from CA3 pointing to SR), however, both SR and SO of CA1 are targets of CA3 projections (Andersen et al., 2006).

As the reader will see in the computational models of the CA3-CA1 network (Paper 2 of this dissertation), in sharp contrast to CA3 anatomical connectivity, the CA1 network does not possess associational connections (for a quantitative estimate see Bezaire and Soltesz (2013)). The reason for this is that most CA1 axonal projections travel throughout the extent of the alveus (bordering the deep part of CA1) or SO to the subiculum. It is possible that CA1 collaterals target interneurons in the basal dendritic fields (such as SL-M interneurons), although CA1 principal neurons also target other CA1 interneurons such as peri-somatic basket cells (Takacs et al., 2012; Amaral et al., 1991). This rather 'odd' connectivity pattern is the neural basis of population neuronal activities that I investigated in the second paper of this dissertation. Finally, CA1 pyramidal cells and interneurons are synaptic targets of EC (layer III) through the TA pathway (Kloosterman et al., 2004; Ito and Schuman, 2012). The TA pathway contributes to shape the activity of CA1 (Spruston, 2008) depending on the behavioural state of the animal (Sirota et al., 2003; Hahn et al., 2012), yet its neurophysiological characteristics are not well-understood.

CA1 sends projections to subiculum and EC. The projection of CA1 to subiculum is topographically organised (Amaral et al., 1991; Gigg, 2006). Proximal CA1 pyramidal cells target distal subiculum, whereas distal CA1 cells project to proximal subiculum (the portion closest to CA1). The projection of CA1 to EC terminates in the deep layers of EC. The proximal part of CA1 projects to MEC, whereas distal CA1 projects to LEC. Finally, CA1 also sends projections to perirhinal and postrhinal cortices (Witter et al., 2000).

1.3.3.2 CA2

Historically, much of the investigation has focused on CA3, CA1 and DG networks, while CA2 has received scarce attention. However, recent evidence suggests that CA2 plays an important role in spatial memory formation and consolidation (Oliva et al., 2016; Kay et al., 2016). CA2 receives projections from EC layer II via perforant pathway and CA3, and is the only subfield in the hippocampus that receives input from the supramammilary nucleus (SuM, located in the hypothalamus) (Vertes and McKenna, 2000; Magloczky et al., 1994). Like CA3, CA2 neurons have strong associational connections, and send afferents to CA1 primarily located in SO, but also in SR. CA2 sends axons that back-propagate to CA3 (Tamamaki et al., 1988; Ishizuka et al., 1990), yet the role of this backpropagation is unclear.

1.3.4 Subiculum

The subiculum is the major output structure of the hippocampus, projecting to EC and perirhinal cortices, retrosplenial area, prefrontal (PFC) and anterior cingulate (ACC) cortices, and several subcortical structures including the hypothalamus, septal nuclei, amygdala, nucleus reuniens of the thalamus and nucleus accumbens (O'Mara et al., 2001; O'Mara, 2005). The CA1 subfield sends its primary projection to the subiculum. The existence of a subicular oligosynaptic anatomical backprojection to CA1 is supported by early and recent evidence (Kohler, 1985; Sun et al., 2014). The simultaneously excitatory and inhibitory subicular projection targets all layers of CA1, where connections return back to their CA1 cell of origin (Sun et al., 2014).

The inputs and outputs of the subiculum differ along the septo-temporal axis, and along the proximo-distal axis. The dorsal subiculum mostly targets cortical regions, and receives afferents from anterior thalamus, medial septum (MS), perirhinal, PFC, visual cortex and intrahippocampal input from CA1; whereas the ventral subiculum receives inputs mostly from subcortical structures such as vestibular nuclei and hypothalamic nuclei, sending return projections to these areas (O'Mara et al., 2001; Gigg, 2006).

1.3.5 Entorhinal cortex (EC)

The EC is a major interface in the flow of information in the hippocampal formation, as it is the entry point of sensory information and the point of relay of information from the hippocampus to the neocortex. The EC is a structure comprising six layers: four cellular ones (II, III, V, VI) and two plexiform ones (I, IV). The EC forms strong associational connections, originating from both superficial and deep layers. While layers II and III (superficial layers) project mainly to superficial layers, deep layers project to both superficial and deep layers (Andersen et al., 2006). Interestingly, this connectivity pattern completes a loop where the information that arrives to the EC can be relayed back to the hippocampus. On the basis of anatomical connectivity, the EC is also regionally divided into medial (MEC) and lateral (LEC) portions. The MEC has been long ascribed to spatial information processing, while LEC is thought to convey information about objects, cues and odors (Deshmukh and Knierim, 2011, 2013).

Cells across the EC have been shown to be functionally distinct, thus adding another dimension of complexity to these circuits. This functional distinction is thought to be the basis of spatial-navigation neural coding. For instance, grid cells are the most common subtype (Hafting et al., 2005), found in MEC layers II and III (Zhang et al., 2013), and have been also found in the human EC (Jacobs et al., 2013). Border cells which exhibit fields selective to the spatial limits of an environment, and head-direction cells, which are selective for the orientation of the head of the animal, comprise another two major groups of MEC cells (Solstad et al., 2008; Giocomo et al., 2014). As many neurons in the brain, MEC cells also show mixed selectivity in encoding these aspects of spatial navigation (Sosa et al., 2016).

The EC receives numerous projections from several areas of the brain, which could allow for this elaborated spatial processing. These inputs can be divided into two main groups: inputs to EC superficial layers (I-III), and inputs to EC deep layers (IV-VI). The inputs to superficial layers are the source of information to the DG, CA and subiculum. These inputs are thought to be fundamental for memory processing and form the basis of cortico-hippocampal communication across several behavioural states (Sirota et al., 2003; Isomura et al., 2006; Hahn et al., 2012; Schomburg et al., 2014). The major cortical inputs to superficial EC originate from olfactory and piriform cortices, together with polysensory areas perirhinal and postrhinal. Inputs to deep layers arise from the ACC, insular cortex, and retrosplenial area, whose activities can be relied back from deep to superficial EC layers and hence, to the hippocampus. The anatomical organisation of the EC may be partly the basis of the functional dissociation between ventral and dorsal parts of the hippocampus (Moser et al., 1995; Henke, 1990), as only the caudal and lateral parts of the EC –which project to septal hippocampus– are targetted extensively by cortex. Other EC afferents include insular, temporal, parietal and occipital areas (Andersen et al., 2006). The major proportion of EC efferents contribute to high-order associational and polysensory cortices.

The anatomical substrates of the hippocampal formation, its highly recurrent intra-field connectivity and the nature of its afferents are the basis for a wide range of characteristic electrical activities, which I studied extensively in this dissertation and shall introduce in the next section.

1.4 Electrical signatures of hippocampal activity. Part I

Recording the neuronal activity of the hippocampus allows us to understand how information processing about the outside world takes place in the brain circuits, and how this highly dynamical process is translated into memories. The principles outlined in this section, however, apply to any brain circuit under study.

Brain activity can be recorded as electroencephalogram (EEG) using surface electrodes placed on the scalp, as electrocorticogram using electrodes directly in contact with the cortical surface, or using electrodes that penetrate the cortical surface, reaching the extracellular milieu, often referred to as intracortical EEG. Electrophysiological preparations on unrestrained animals typically use electrodes placed into brain structures of interest in order to investigate their function on the basis of an integrated and spatially localised signal known as mean extracellular field potential (mEFP). The mEFP is a measure of the electrical activity generated by the various neural processes surrounding the recording electrode tip (Quian Quiroga and Panzeri, 2013; Buzsaki et al., 2012; Logothetis and Wandell, 2004).

The electrode –depending on its construction properties– can isolate the activity of single neurons, i.e. the extracellular signature of their action potentials, also known as single-unit activity (SUA). These action potentials are markers of the interaction between one cell and its partner cells, and therefore can be used to study the relationship between the neural activity of a given cell or a small group of cells, and the behaviour of the animal during a specific task. Alternatively, an electrode can be used to record the summed action potentials from hundreds of neurons within one or more subpopulations. This summed activity is known as multi-unit activity (MUA). Both SUA and MUA reflect similar processes, however, MUA recordings are less sensitive to electrode placement than SUA, and MUA represents a larger spatial integration of neuronal activities from which the activity of single cells is difficult to isolate. Typically, both SUA and MUA –as they correspond to very fast time-scale processes– can be isolated by high-pass filtering the mEFP signal using standard digital filtering techniques.

What neural processes do the lower frequencies of the mEFP represent? The low-frequency activity (up to ca. 330 Hz) of the mEFP signal –known as the local field potential (LFP)– represents slow fluctuations of the extracellular voltage. The origin of the LFP is not straightforward, and represents the weighted sum of neural processes present in the transmembrane currents exerted by individual neurons (Buzsaki et al., 2012). These microscopic-scale events include synaptic activity (Whittingstall and Logothetis, 2013; Logothetis and Wandell, 2004), action potentials (Ray and Maunsell, 2011; Schomburg et al., 2012; Reimann et al., 2013), calcium spikes (Schiller et al., 2000), intrinsic currents (Llinas, 1988), spike afterpotentials (Reimann et al., 2013; Gustafsson, 1984; Harada and Takahashi, 1983), gap junctions (Draguhn et al., 1998; Traub and Bibbig, 2000), neuron-glia interactions (Kang et al., 1998), and ephaptic coupling (Anastassiou et al., 2011).

The LFP also shows some dependence on the neuronal geometry. For instance, pyramidal cells have long apical dendrites and –in the CA of the hippocampus, for example– lie oriented perpendicular to the surface of the stratum pyramidale. This so-called ‘open field’ configuration generates dipoles along the neural axis due to the spatially separated active portion of the membrane from its corresponding return currents. These dipoles contribute strongly to the LFP. Conversely, this is not the case for radially-symmetric neurons, which due to geometric cancellation on radially-even arborisations, have a weaker contribution to the extracellular potential than pyramidal cells (Schomburg et al., 2012). However, in a strict sense, a ‘closed field’ would only occur when all dendrites are activated at the same time, which is not the case in reality (Buzsaki et al., 2012). Furthermore, some radially-symmetric neurons –such as some hippocampal interneuron subtypes– have the capacity to pace network oscillatory episodes due to their fast kinetic properties (Schlingloff et al., 2014; Stark et al., 2014). These activities are likely broadband with predominant high-frequencies, and may contribute to the shape of the LFP spectrum. Thus, the LFP should be understood in the specific context of underlying network dynamics.

There is a direct link between transmembrane currents and the dipolar structure of the LFP (for details the reader is referred to the seminal contributions of Nicholson and Llinas (1971), Nicholson (1973), and Nicholson and Freeman (1975)). Briefly, the extracellular milieu is assumed continuous, homogeneous, ohmic (that is, there is no charge accumulation; rather, there are currents that appear and disappear in the medium), and isotropic (the same in all directions). The last assumption allows us to express the conductivity as a scalar quantity σ. The transmembrane currents are distributed along the axis of the cell (parallel to the dendritic tree), that is, along lines at the cylindrical axes of the neurons (Nicholson and Llinas, 1971). The field potential is observed at some point of the extracellular medium. In reality, the observation point is the point in space occupied by the measuring electrode. Therefore, the potential at that point can be computed as a volume integral of the transmembrane current that is inversely proportional to the distance between the current generator and the observation point (that is, the location of the electrode). One may infer that due to the planar symmetry of the neuronal population in an oriented array of neurons, current changes mainly occur along the axis of the neuron, vanishing in other directions (Nicholson and Llinas, 1971).

From the previous physical notions, we can already conclude that the LFP is a highly integrated measure, reflecting the input to a given cell population, together with its local active processes and includes the activity of several cellular subtypes. It follows that the LFP is a key signal to understand neuronal network mechanisms that result from cognitive processes (e.g. learning and memory, attention, perception) and pathology (e.g. epilepsy, Alzheimer's disease). The use of LFP, however, has limitations. Namely, since it reflects many neuronal processes at the population level happening at a given time point, the LFP is inherently ambiguous (Einevoll et al., 2013). Consequently, it requires principled methodological approaches to understand its content, and to turn this understanding into conclusions about neuronal processing. I argue that –to some extent– it is possible to decompose the LFP into several biophysically-relevant *elementary components*. In particular, the second paper of this dissertation shows that some frequency-dependent LFP components can be ascribed to dynamical aspects of network-level processing (e.g. coordinated post-synaptic potentials and spiking currents). In turn, these components may correlate with activities specific to distinct cell groups, thus reflecting the dynamical context in which certain neuronal processing occurs (Ramirez-Villegas et al., 2017b).

1.4.1 Content of the hippocampal LFP

The LFP of the hippocampus reflects the intrinsic dynamics of highly recurrent subcircuits (see section 1.3). This property provides the hippocampus with the ability to exert a number of distinct rhythmic activities, varying across hippocampal subfields and with the behavioural state of the animal. More importantly, *rhythms* in the hippocampal LFP are associated with population-level processing of mnemonic information as it will be discussed in the present subsection of this dissertation.

1.4.2 Place cells and theta rhythm

As mentioned earlier, a notable characteristic of the cells in the rodent hippocampus is their ability to fire at specific spatial locations. Due to this spatial specificity these (excitatory) cells are referred to as place cells (O'Keefe and Dostrovsky, 1971). The spatially-tuned receptive field of a place cell is called *place field*, and represents the region in which the cell fires at its maximum, while remaining silent (or almost silent) at other locations. Place cells fire at specific phase of the hippocampal LFP rhythm known as theta (O'Keefe and Recce, 1993). The elementary notions about this rhythm that I describe here apply to rodents. Later on, I generalise them to other animal species, and particularly primates.

Theta is a low frequency –quasi sinusoidal– oscillation in the frequency range 3-12 Hz with a center frequency of approximately 8 Hz, that dominates the hippocampal field activity during the locomotor state (Vanderwolf, 1969; O'Keefe and Recce, 1993; Wilson and McNaughton, 1994), and also during periods of paradoxical (rapid-eye movement, REM) sleep (Jouvet, 1969). Theta has been long associated with coordination of information processing within the hippocampus. In particular, with coordinating the activity of place cells that ultimately encode locations in space (Buzsaki, 2002). For reasons explained later in this chapter, the physiological significance of theta remains elusive. However, it is possible that a theta-like low-frequency rhythm (whether transient or sustained) bears a similar role across several mammalian species (Sosa et al., 2016).

The theta rhythm is thought to be controlled by a chain of linked subcortical structures. Amongst these, the medial septum/diagonal band of Broca (MS-DB) is thought to play a critical role. Lesion studies suggest that inactivation of MS-DB abolish theta oscillations in all cortical targets (Petsche et al., 1962; Bland et al., 1994). MS-DB sends inhibitory connections onto DG/CA3/CA1 basket cells, whose rhythmic input results in transient bouts of disinhibition of pyramidal cells. Similarly, cholinergic input into the hippocampus depolarizes both pyramidal neurons and basket cells promoting their rhythmic discharge (Bland and Oddie, 1998; Buzsaki, 2002). Thus, the theta phases represent ongoing changes of excitation and inhibition (Csicsvari et al., 1999). Other structures contributing to the theta rhythm are the SuM nucleus (Kocsis and Vertes, 1994; Kirk and McNaughton, 1993), EC (Kamondi et al., 1998), posterior hypothalamus and the pontine region (Oddie et al., 1994; Kirk and McNaughton, 1993; Bland et al., 1994; Vertes et al., 1993).

Although the foundations of theta remain somewhat unclear, one may safely conclude that theta relies on the rhythmic discharge of both inhibitory and excitatory hippocampal cells, and depends upon local network interactions that can be greatly influenced by the activity of a chain of subcortical nuclei and the EC. Finally, the interplay between spiking activity, theta and gamma rhythms may establish the basis of episodic memory encoding in the brain (Lisman and Idiart, 1995; Lisman, 2005; Schomburg et al., 2014; Fernandez-Ruiz et al., 2017).

1.4.3 Gamma oscillations

Gamma activities –LFP oscillations in the frequency band 25-100 Hz in rodents– are expressed by hippocampal circuits during the awake state (locomotion), periods of quiescence, SWS and REM sleep (Sullivan et al., 2011, 2014; Schomburg et al., 2014). The exact definition of gamma activity in terms of an explicit frequency range is obscure in the rodent literature. Ranging from a lower bound of 20 Hz, and reaching an upper bound of 140 Hz, gamma activity seems to contribute to information transfer and to bind neuronal ensembles (Csicsvari et al., 2003; Schomburg et al., 2014). Hippocampal gamma activity also comes in different flavors. A low range –known as slow gamma– corresponding to 25-55 Hz (or 20-50 Hz) (Colgin et al., 2009; Sosa et al., 2016), and a high range –or fast gamma– comprising the frequencies 60-100 Hz (or 50-90 Hz, or 50-140 Hz) (see Colgin et al. (2009), and Sullivan et al. (2011)).

Evidence suggests that within the hippocampal formation gamma activity is generated due to the activity of interneurons (Csicsvari et al., 2003; Colgin, 2016; Buzsaki and Wang, 2012) and input from EC (Schomburg et al., 2014). The emergence of gamma correlates with that of theta, as it is also prominent during awake, locomotor and REM-sleep states. Furthermore, gamma phase and amplitude are coupled to theta (Colgin et al., 2009; Bragin et al., 1995).

Whether slow and fast gamma are two network-related activities generated by distinct mechanisms was an open question until very recently. Recent evidence suggests that different gamma rhythms are differentially expressed by distinct layers of CA1 (Colgin et al., 2009; Schomburg et al., 2014). Slow gamma activity –obeying the CA3-related Schaffer collateral input– is expressed in SR, whereas fast gamma –arising from the EC layer III or TA pathway– dominates in SL-M. These activities were consistently observed during locomotion and REM sleep, suggesting common mechanisms of information routing during hippocampal theta-related states (Colgin et al., 2009; Schomburg et al., 2014). Furthermore, subpopulations of CA1 interneurons are differentially activated by CA3- and EC-related gamma activities (Lasztoczi and Klausberger, 2014).

1.4.4 Sharp wave-ripples (SWR)

In contrast to the regular theta activity during locomotion and paradoxical sleep, the hippocampus also exerts periods of asynchronous activity, also referred to as large-amplitude irregular activity (LIA). Unlike theta, LIA displays a pattern of activity covering the entire LFP spectrum (<330 Hz), rather than a narrow-band, regular rhythm. The hippocampus displays LIA during periods of awake immobility and SWS, when synchronous activity occurs only transiently. These transient activities include gamma oscillations (Sullivan et al., 2011), spindles (Sullivan et al., 2014), and SWR complexes (Buzsaki, 1986; Buzsaki et al., 1992). SWR episodes have been the focus of enormous attention (the reader is referred to Buzsaki (2015) for an extensive review), due to their involvement in declarative memory processes (Girardeau et al., 2009; Nakashiba et al., 2009; van de Ven et al., 2016).

As pointed out earlier in this work, SWR episodes are likely the most synchronous activities in the brain (Chrobak and Buzsaki, 1994, 1996). When theta-related inhibition from MS-DB is released in the hippocampus, due to the recurrent nature of the CA3 circuitry, groups of cells produce irregular, but recurring episodes of highly synchronous activity. These bursts of activity –associated with gamma-like LFP activity (Sullivan et al., 2011)– produce a large population-level depolarization in the apical dendritic fields of CA1. The synchronous, yet massive recruitment of CA1 pyramidal cells and interneurons –with an estimate of 50000 to 100000 participating neurons– produces a short-lived (50-150 ms) high frequency oscillation (ca. 150-250 Hz in rodents) known as ripple (Buzsaki et al., 1992; Csicsvari et al., 1999). SWR episodes are ubiquitous across several mammalian species, and have been recorded in mice, rats (Buzsaki et al., 1992; Csicsvari et al., 1999; Sullivan et al., 2011), bats (Ulanovsky and Moss, 2007), rabbits (Nokia et al., 2010), cats (Kanamori, 1985), monkeys (Skaggs et al., 2007; Logothetis et al., 2012; Leonard et al., 2015), and humans (Axmacher et al., 2008). This fact has lead to the hypothesis that the physiological role of these episodes is phylogenetically conserved (Buzsaki, 2015).

In section 1.2, I have discussed that episodic memory is initially encoded in the hippocampus. Furthermore, the structures of the hippocampus may give the brain the ability to spontaneously retrieve memories. A phenomenon known as replay is thought to underlie this process. During replay hippocampal cells that were active during previous awake experience reactivate to form brief snippets of experience-related activity (Wilson and McNaughton, 1994; Skaggs et al., 1996; Lee and Wilson, 2002). These brief snippets of activity –in line with theoretical and experimental evidence– must be fast so as to be suitable to induce plasticity in neuronal populations of target structures (Euston et al., 2007). The first demonstration that a spatial-sequence replay occurs simultaneously with field SWR episodes was established by the study of Lee and Wilson (2002). In their experiment, rats ran back and forth linear tracks for a reward at each end. During theta, place cells were selectively activated as the animals traversed the tracks. However, during off-line periods (i.e. periods of quiescence and SWS) the place cells that fired during the task were selectively active during SWR episodes, following the same sequence of place-field activations of the awake experience. This replay, representing an immediate spatial experience of a rodent, occurs both in the forward and reverse orders in a brain state-dependent fashion (Diba and Buzsaki, 2007).

The physiological significance of SWR has been demonstrated by several studies, where selective suppression of SWR episodes was a sufficient condition to impair the animal's performance during spatial memory tasks (Girardeau et al., 2009; Nakashiba et al., 2009; Jadhav et al., 2012; van de Ven et al., 2016; Ego-Stengel and Wilson, 2010; Gerrard et al., 2008). However, despite the increasing number of studies investigating the role of SWR and replay, whether memory consolidation and retrieval are a direct consequence of the SWR phenomenon remains debated (see Carr et al. (2011), Dupret et al. (2010), van de Ven et al. (2016), Leonard et al. (2015); Leonard and Hoffman (2016)). SWR epochs form about 10% of the hippocampal LIA during immobility (Buzsaki, 2015), thus, it is likely that the remaining proportion of activity contributes to encoding and retrieval of information as well (see Kay et al. (2016)), and that the SWR phenomenon is one part of (probably the chain of) memory consolidation and retrieval mechanisms.

Recent studies link the occurrence of awake SWR with consolidation of new information. For instance, van de Ven et al. (2016) found that off-line reactivation is only required when establishing ensemble patterns representing a novel environment, but not a familiar one. Furthermore, the reinstatement of the new spatial memory was impaired by suppressing SWR, but also depended on its initial encoding stage. In another study, Papale et al. (2016) observed that the occurrence rate of awake SWR diminished after epochs of vicarious trial and error (VTE), whereas increases of awake SWR rate at reward sites were associated with decrease in VTE subsequently, at choice points. Furthermore, decreases of VTE with prevalence of SWR ocurred as animals learned to exploit the learning rule. Altogether, these studies suggest that SWR that occur during waking –associated with periods of quiescence or rest at rewarded locations– are important for awake learning processes, whereas already stabilised memories may not require this mechanism in order to be further strengthened. In addition, the interplay between theta sequences, VTE and SWR may contribute to states of deliberation and consolidation processes that could link an experience to its outcome (Foster and Wilson, 2006; Gupta et al., 2010).

1.4.5 Neuronal mechanisms of SWR

The underlying neuronal mechanisms of SWR have been the topic of many investigations (also extensively reviewed in Buzsaki (2015)). However, since the discovery of these transient episodes (O'Keefe, 1976; Buzsaki, 1986; Buzsaki et al., 1992), these mechanisms are not well understood. The candidate mechanisms of SWR generation appointed so far by experimental and theoretical investigations include remote and intrahippocampal network interactions (Buzsaki et al., 1992; Csicsvari et al., 1999; Sirota et al., 2003; Vandecasteele et al., 2014), pyramidal neuron-interneuron synaptic interactions (Schlingloff et al., 2014; Stark et al., 2014), axo-axonal electrical coupling (gap junctions) (Dermietzel and Spray, 1993; Traub and Bibbig, 2000), and ephaptic effects (Ozen et al., 2010; Anastassiou et al., 2011; Buzsaki, 2015).

There are a series of global circuit mechanisms that permit the emergence of SWR complexes. These mechanisms include the control of inhibition and glutamate release within the hippocampus. One of the most extensively studied hippocampal inputs in relation to this process is that of the MS-DB due to its ability to exert strong influence on hippocampal neuronal activity (Petsche et al., 1962; Bland et al., 1994; Oddie et al., 1994). Experimental evidence indicates that cholinergic input to the hippocampus from MS-DB interferes with SWR emergence. In line with early electrical stimulation and pharmacological studies (Gray and Ball, 1970; Bland and Bland, 1986; Lawson and Bland, 1993; Oddie et al., 1994), *in vivo* optogenetic stimulation of MS cholinergic neurons increases theta oscillations. In addition, this theta enhancement occurs at the expense of a significant decrease in SWR occurrence even when excitation to septal cholinergic cells is not sufficiently strong to generate theta (Vandecasteele et al., 2014). Thus, in the absence of the suppressing effects of distinct neuromodulatory systems –due to the recurrent nature of the hippocampal circuitry– SWR episodes are 'released' in the hippocampus proper. I discuss the topic of neuromodulatory control of hippocampal circuits more in depth in a separate subsection of this work (see Subsection 1.6).

SWR-related bursts usually emerge from the CA3a subfield (adjacent to CA2 in the hippocampus transverse axis), and this synchronous discharge causes depolarization of CA1 apical dendrites due to CA3c (at the proximal end of CA3, closest to the hilus) output (Csicsvari et al., 2000). Although this represented the most accepted mechanism of SWR until very recently, two studies have provided evidence for the role of CA2 in SWR initiation. Oliva et al. (2016) recorded network and single-cell activity of all structures in the hippocampus proper (namely, all CA subfields) *in vivo*, and observed that SWR-related synchronous activation of CA2 ensembles preceded that of all other CA subfields during both SWS and waking states. Interestingly, CA2 neurons depolarised the basal dendrites of CA1 cells that produced an inverse-polarity sharp wave (i.e. a positive field deflection) in apical dendritic fields of CA1, indicating that different patterns of SWR field activities may be co-expressed in CA1 due to the CA2-triggering network. These findings are in line with those of the first paper of this dissertation, wherein SWR complexes were classified into distinct putative groups. Notably, I found that one of the groups correspond to a sharp wave with inverse polarity, whose time-frequency characteristics differ from the 'classical' sharp waves reported in other studies.

In addition, a subpopulation of CA2 neurons fires selectively before SWR episodes (Oliva et al., 2016; Kay et al., 2016). These cells were found in the deep layers of CA2, suggesting subcircuit anatomical and functional differences (Oliva et al., 2016). Finally, this group of neurons were suggested to encode location during periods of immobility (Kay et al., 2016). These observations suggest a role for CA2 during mnemonic processing, and initiation of SWR episodes.

Experimental observations in trangenic mice suggest that ripples persist after blockade of CA3 (Nakashiba et al., 2009). However, time-frequency features of CA3-blockade SWR were largely modified, resulting in a weaker form of oscillation with a lower high frequency peak (∼110 Hz). Ripple persistence in this scenario leads to the hypothesis that input may arrive from EC via the TA pathway to the SL-M of CA1, where otherwise the effectiveness of EC in generating CA1-bursts is limited by CA3 due to the activation of oriens lacunosum-moleculare (OLM) interneurons during physiological SWR activity (Buzsaki, 2015).

Another contributor to hippocampal SWR activity may be the subiculum. An *in vitro* study –combining electrophysiology and calcium imaging– reported that a subset of subicular neurons was activated approximately 100 ms before the occurrence of hippocampal SWR (Norimoto et al., 2013). Surgical resection of the CA1-subiculum projection further revealed that, while subiculum activities following SWR were abolished, those preceding SWR were still observed. Altogether, these *in vitro* data suggest that CA1 circuits may be also controlled by a subicular-CA1 backprojection, specifically during SWR. However, since CA1 SWR episodes' rate was not significantly affected upon inactivation of the CA1-subiculum projection, this input may not be critical for SWR to emerge in the hippocampal network.

The local (CA1) generators of SWR episodes seem to be more controversial than their remote contributors. The associational CA3 network's bursting activity is brought to CA1 apical dendrites, wherein a large depolarization can be recorded. What happens in stratum pyramidale, however, offers more room for debate. The frequency of ripple oscillations in pyramidal cells is not voltage dependent, suggesting network rather than intrinsic ionic mechanisms (Ylinen et al., 1995). Several lines of evidence suggest that the interplay between pyramidal cells and inhibitory cells produces the high-frequency oscillation in CA1. This excitation-inhibition interaction (E-I model) was suggested by the first experimental studies and several modeling studies on SWR (Buzsaki et al., 1992; Ylinen et al., 1995;

Brunel and Wang, 2003; Memmesheimer, 2010). Others, with less popular lines of thought, argue that ripples may come about by excitation of electrically-coupled pyramidal cells (axo-axonal gap junctions), while interneurons are relatively passive elements in the rhythmic discharges (Draguhn et al., 1998; Traub and Bibbig, 2000; Schmitz et al., 2001; Traub et al., 2012).

Recent experimental evidence offers new insights into the mechanisms of ripple oscillations in CA1 and CA3 networks. Stark et al. (2014) studied SWR-related CA1 activities *in vivo*, whereas Schlingloff et al. (2014) investigated SWR in CA3 *in vitro*. Although recordings were done in different hippocampal subfields and experimental conditions, these studies agreed in many findings. First, both studies concluded that a minimal amount of excitation is a necessary prerequisite for SWR episodes to emerge. Specifically, Stark and collaborators observed that SWR-like episodes emerged after applying localised optogenetic depolarizations to pyramidal cells and interneurons. Second, the role of excitation is critical, as SWR are aborted upon silencing of pyramidal cells. Third, silencing the activity of perisomatic interneurons terminates ripples. Notably, this effect was observed by Schlingloff and collaborators after applying gabazine *in vitro*, while also observed by Stark and collaborators by optogenetically silencing parvalbumin (PV)-expressing interneurons. Thus, ripple oscillations may depend upon a transient regime of synchrony of interacting pyramidal cells and interneurons. It is hypothesised that SWR underlie both mutual synaptic inhibition, together with E-I loops. This scenario supports the results obtained in both studies on the basis of pyramidal cell-related discharges, time-locked and paced by fast coordinated inhibition, which in turn is ripple-coherent due to the inhibitory-inhibitory cell connections (Schlingloff et al., 2014). Furthermore, inhibitory-inhibitory synapses may partly establish the conditions for SWR to emerge upon a transient imbalance of excitatory activity (Stark et al., 2014; Mizunuma et al., 2014).

Despite the experimental evidence provided by previous studies, it is difficult to establish a dichotomy between E-I and E-I-I models (for a discussion see Buzsaki (2015)), and to what extent they are implemented in CA1/CA3 networks (see also the work of Chiovini et al. (2014), who propose that interneurons have highly resonant firing properties, and ripples may result from fast dendritic calcium events). Moreover, it is difficult to assess to what degree silencing interneurons is effective in abolishing SWR, or to what extent progressively enhanced interneuronal activity would either reduce or enhance ripples and their physiological time-frequency characteristics.

These questions are investigated in the second paper of this dissertation (Ramirez-Villegas et al., 2017b). By a series of modeling studies combined with *in vivo* intracortical data, we identify frequency-dependent components of SWR. These components rely on network interactions associated with the incoming CA3 activity onto CA1, and specific firing and synaptic events of pyramidal cells and perisomatic-targeting interneurons within CA1. Our model points to specific neural mechanisms underlying the neurophysiology of peri-SWR activity, thus establishing a relationship between its LFP and the context of its underlying network-level activities. The state-of-art controversies on this topic are discussed in the next subsection of this work.

1.4.5.1 Content of SWR-related LFP

The content of SWR-related LFP –that is asking: what do LFP sharp waves and ripples represent in terms of underlying neural activity?– remains highly controversial. In general, fast oscillations in CA1 have stereotypical time-frequency features. These oscillations consist of brief (∼200 ms) power increases in several frequency bands. Usually, the 'classical' SWR is ascribed to two frequency bands: the sharp wave (<20 Hz) and the ripple (∼150-250 Hz, in rodents; ∼80-180 Hz in non-human primates). The *in vivo* distribution of frequencies in CA3, however, varies reflecting a gamma-like ('epsilon') episode (Sullivan et al., 2011; Oliva et al., 2016). The fact that CA1 and CA3 produce somewhat distinct (and largely incoherent) fast oscillatory patterns during SWR episodes has led hippocampologists to theorise possible mechanisms of CA1 sharp waves and ripples. Briefly, the converging excitatory drive of CA3 over CA1 may be stronger than what CA3 itself can produce due to collateral-related activity, which could in turn explain the differences in oscillation frequency.

However, if CA1 ripples are generated *de novo* after CA3 ripples, the question would be: how optimal is this strategy for information transfer and coordination between these hippocampal subfields? In fact, SWR are field episodes, and as such, their power spectral distribution in the LFP frequencies is largely broad, rather than well-localised. During most SWR episodes both CA3 and CA1 display a transient, somewhat prominent slow gamma rhythm (Carr et al., 2012). The observation that this slow gamma rhythm has an impact in CA1 processing is almost as controversial as its existence, as some authors have related it to 'spectral leakage'. However, beyond beliefs, compelling experimental evidence suggests that SWR-related slow gamma (∼ 30-50 Hz) synchronises CA3 and CA1 and supports memory replay, as CA3-CA1 gamma coherence is predictive of replay quality (Carr et al., 2012). In addition, gamma may also serve as a clocking mechanism in the coordination of memory-related activity across the hippocampal network (see also Gillespie et al. (2016), and Pfeiffer and Foster (2015)).

On the basis of the previous evidence one could expect two main frequency components conflating in the CA1 SR LFP: a sharp wave deflection and gamma oscillations. Furthermore, as SWR episodes are release phenomena, it is expected that their associated MUA is elevated. Ascribed to the high coordination of activity in an exceptionally short time window, the temporal summation of spiking activity is a significant component in SWR episodes. These summed events (Schomburg et al., 2012) represent 'mini-population spikes' (Buzsaki, 1986), and are thought to be responsible for the ‘spiky’ appearance of ripple oscillations.

Furthermore, LFP have been classically associated with synaptic currents in the extracellular space (Ajmone-Marsan, 1965; Buchwald et al., 1965), to date still used in modelling studies as a LFP proxy (Taxidis et al., 2012; Mazzoni et al., 2015). Analogously, post-synaptic currents (PSC) are thought to be a major contributor to the LFP ripple, given the capacity of summed synaptic events to account for lower LFP frequencies as compared to spikes (Schomburg et al., 2012). Moreover, synchronised gamma-aminobutyric acid-A (GABA-A) receptor-mediated currents (therefore inhibitory post-synaptic currents, IPSC) during ripples may establish a major contribution to the ripple, as ripples are induced even after blockade of glutamatergic receptors in CA3 (Schlingloff et al., 2014). However, this finding is seemingly at odds with *in vivo* and *in vitro* evidence showing that inhibitory activity alone cannot produce ripple activity (Stark et al., 2014; Ellender et al., 2010). Both *in vivo* and *in vitro* results can be explained on the basis of a network effect involving the action of CA1 pyramidal cells. For instance, due to the incoming activity from CA3, pyramidal cells in CA1 also generate coordinated excitatory post-synaptic currents (EPSC), and CA1 pyramidal cell EPSC contribute to the discharge of inhibitory interneurons.

Although the contribution of these EPSC to the ripple LFP signature is unclear on the basis of the existent experimental evidence, they may well be a component of ripple oscillations. In fact, we investigated this question in the second paper of this dissertation, and we show that not only IPSC due to interneuron activity, but also EPSC onto interneurons by local pyramidal cells underlie ripple activity. Our results in a way challenge common beliefs, as interneuronal activity produces a pacing rhythm to the pyramidal cell’s membrane potentials and constrains the number of SWR-participating cells in CA1. This control of participation is at the same time further enforced by the action of EPSC onto interneurons (Ramirez-Villegas et al., 2017b).

1.4.5.2 Inhibitory activity during SWR

SWR activity is controlled by the rapid activity of interneurons. Interneurons in the CA1 subfield are extremely diverse (for extensive reviews the reader is referred to Freund and Buzsaki (1996), Klausberger and Somogyi (2008), and Somogyi et al. (2014)), albeit they represent ∼11% of the total CA1 cell population (Andersen et al., 2006). As discussed in the previous subsection, interneurons present a major contribution in shaping the circuit dynamics during SWR. These contributions partly establish the recruitment pyramidal cells, and the temporal structure of pyramidal cell firing (Buzsaki, 2015).

The firing of interneurons during SWR is largely dependent on the interneuron subtype. Amongst hippocampal interneurons, the peri-somatic basket cell has been the most studied subtype. Similar to peri-somatic basket cells, bistratified cells increase their discharge probability sharply during SWR. In contrast, PV-expressing axo-axonic cells and OL-M cells are largely suppressed during SWR, yet with augmented discharge probability at the beginning and the end of and SWR event. The suppression of the interneuron subtypes may provide pyramidal cells with increased excitability necessary for SWR to emerge and impact target structures (Mizunuma et al., 2014; Ellender et al., 2010), while their activation may be related to the control of the circuit and SWR emergence over large time scales (Ellender et al., 2010).

In a recent work, Varga et al. (2014) investigated the impact of distinct subpopulations of CA1 interneurons in the dynamics of low- and high-frequency oscillations. Their study suggested that basket, axo-axonic and bistratified cells could be clustered into multiple functional sub-classes on the basis of their activity, which segregated along specific features of dendritic structure and somatic location. Notably, ‘fast ripples’ (ripple episodes of higher frequency peak) were generated upon the selective activation of a specific functional subtype of bistratified cell, as opposed to basket cells which participated virtually during every SWR. In addition, a subclass of axo-axonic cells (with somatic location in CA1 SO) showed prominent activity during SWR. The distinct interneuron types established a rich repertoire of LFP-spike relationships during ripples, highlighting their consistent rhythmicity (Csicsvari et al., 1999). Overall, this evidence suggests that SWR may be highly heterogeneous. This heterogeneity may be a result of differential modulation of subcircuits of interneurons via local or extra-hippocampal inputs (see also the first paper of this thesis, Ramirez-Villegas et al. (2015), where we discovered that SWR episodes come in multiple, possibly functionally distinct subtypes).

In addition, there are other subtypes of interneurons thought to contribute to SWR bursts, but not much is known about them. Basket cells expressing cholecystokinin (CCK) are also perisomatic. However, unlike PV-expressing basket cells, CCK cells fire at low discharge rates during SWR, yet they may contribute to pyramidal cell auto-desinhibition (Buzsaki, 2015). So-called ivy cells also present slow discharge rate that appears unaffected during SWR. Finally, a small group of cells expressing endogenous opioid encephalin (ENK) do not fire during SWR but exhibit rebound during post-ripple suppression, possibly contributing to the post-SWR hyperpolarisation (English et al., 2014; Hulse et al., 2016).

Finally, interneurons with long-range axons are thought to control extra-hippocampal input during periods of LIA by suppressing interneuron targets in the MS, hippocampus, subiculum and retrohippocampal areas (Klausberger and Somogyi, 2008).

1.5 Electrical signatures of hippocampal activity. Part II: Beyond rodents

So far we have reviewed the patterns of electrical activity expressed in the hippocampus of rodents. Although much less is know about non-human and human primates, several studies have shown that the general correlates of hippocampal activity in these species follows similar patterns as that of the rodents. For instance, SWR are observed in both monkeys and humans (Axmacher et al., 2008; Le Van Quyen et al., 2008; Staresina et al., 2015; Logothetis et al., 2012), presenting similar cell discharge patterns, but slightly different LFP time-frequency characteristics such as the high-frequency power spectral density peak (Logothetis et al., 2012). On the basis of these qualitative similarities, several investigators have hypothesised that patters of hippocampal activity in primates imply underlying mechanisms similar to those found in rodents.

1.5.1 Neural correlates of exploratory behaviour: theta rhythm revisited

When I introduced the term *theta* in this thesis, it was done in the context of rodent navigation (locomotor state). However, theta oscillations have been ascribed to a number of other behavioural states in other animals species. Early studies in cats (Bennet et al., 1973; Bennet, 1970) indicated that the activity of the hippocampus during waking was dominated by LIA (desynchronisation), except when the animals displayed 'orienting' responses, including periods dominated by visual or olfactory search, and other so-called investigative behaviours. Task-related theta activities were related to attention to cues required for task exploitation. Thus, depending on the animal species, theta can be a highly transient event-like low-frequency oscillation (Bennet et al., 1973), or a sustained oscillatory regime. In fact, there is no consensus on both the behavioural correlates, and the significance of theta across animal species (Buzsaki, 2002),

The hippocampal circuits of the primate and the dominant rodent model have similar connectivity between substructures as well as between neuronal types (Andersen et al., 2006). However, several differences persist between primates and rodents. A notable example of these differences is that primates do not necessarily require ambulatory behaviour to explore their environment. Indeed, human and non-human primates are visual animals *par excellence*. This fact probably leads to multiple functional differences expressed in the macroscopic dynamics of the brain, from the activity of subcortical structures that lead to hippocampal synchronisation to primary and associative cortical structures. For example, like in the cat, theta-related field activities are observed during visual exploratory behaviours in monkeys. Jutras et al. (2013) investigated the neuronal activity of the hippocampus of macaques during visual exploration. As monkeys freely observed novel images, a theta-band (3-12 Hz) pattern of activity was present in the hippocampal field recordings. Notably, these theta oscillations were not sustained, but rather transient event-like activities, and were predictive of stimulus coding. These results indicate that the activity of the hippocampus, in addition to visual sensory and associative areas may act in concert to support nmemonic processing in macaques.

Theta oscillations have been observed in the field activity of the macaque hippocampus during anaesthesia (Stewart and Fox, 1991), and more recently during awake behaviour (Leonard et al., 2015). Transient bouts of theta oscillations have been also observed in humans during virtual spatial nagivation tasks (Ekstrom et al., 2005; Vass et al., 2016; Aghajan et al., 2016).

1.5.2 SWR and hippocampal-cortical communication

In section 1.4.4, I discussed the behavioural significance of SWR activity at a system level, in light of current hypotheses of consolidation and recall of spatial memories in rodents (Carr et al., 2011). Several investigators have tried to address whether similar processes govern memory consolidation in non-human primates. The occurrence of SWR complexes in the hippocampus of primates suggests that these events may have similar roles in such animal species.

Intracortical recordings in behaving macaques have been performed during visual exploration in a recent study in order to advance our current understanding of the activities of hippocampal circuits during the occurrence of SWR, together with their associated behavioural correlates (Leonard et al., 2015). This study shows that SWR occur across distinct behavioural epochs, namely visual exploration (during which the animals are required to find and select a target object in a visual scene), quiescence (periods with no sensory stimulation, including SWS) and quiet wakefulness (inactive periods during wakefulness). In line with rodent investigations, these episodes are observed during epochs during which the theta rhythm is absent. Furthermore, SWR were shown to occur when the animal performs visual search.

Exploration-SWR in macaques have similar visual and power-spectral density characteristics as compared to SWR observed during quiescence and immobility. These episodes selectively occur at points where memory recall may be required, as suggested by the demonstration that SWR occur more often when the animals look at familiar scenes as compared to novel scenes (Leonard and Hoffman, 2016). Overall, these data suggest that SWR may be instrumental for solving visual-memory tasks in primates, possibly indicating periods of memory recall, or consolidation processes that could link a visual experience to reward (Papale et al., 2016).

Post-experience reactivation of neuronal ensemble activities in hippocampus and neocortex has been hypothesised to underlie systems memory consolidation (Wilson and McNaughton, 1994; Kudrimoti et al., 1999; Skaggs et al., 1996). Yet, it is unknown how consolidation-related information is transferred to neocortical ensembles. If the functional organisation of memory emerges from the concerted activity of several brain areas occurring at multiple spatio-temporal scales, its operational principles may be better understood on the basis of the relationship between global and local dynamical aspects of its operations. For instance, for a recently acquired memory, neocortical reactivation tends to follow hippocampal reactivation (Wierzynski et al., 2009). Yet, this relationship may change for SWR involved in memory retrieval (e.g. modulating a coordinated top-down process prompted by high-order neocortical areas). These aspects could only be mapped on the basis of global neocortical activities.

The study of Logothetis et al. (2012) offers a glimpse into the complexity of the brain-wide correlates of SWR in primates. Through a novel experimental methodology combining concurrent multi-site hippocampal recordings and whole-brain fMRI, Logothetis and collaborators investigated the regions of the macaque brain whose activity is modulated during the occurrence of hippocampal neural events. Remarkably, during SWR –unlike gamma or high-gamma episodes– a large portion of the neocortex, including visual and associative areas, is activated, while subcortical structures including most diencephalic, midbrain and brainstem reagions are consistently deactivated (Logothetis et al., 2012). In addition, the metabolic responses of neocortical and subcortical structures displayed a variety of time lags, suggesting *anti-causal* relationships with hippocampal SWR-related activities. That is, the remarkably concerted and consistent set of brain activations during SWR is correlated with, but not necessarily an effect of SWR. Furthermore, the interpretation of peri-event BOLD signals is not straightforward, yet it is likely correlated with general decreases or increases in MUA of the local circuits, which again deserve careful consideration. For instance, overall decreases in MUA may give rise to interactions that are highly selective at the microcircuit level, rather than corresponding to an overall neuronal 'shut-down' (Logothetis et al., 2012; Logothetis, 2015).

1.6 Brainstem origin of the hippocampal electrical potential

To understand how subcortical networks modulate hippocampal activity, and how these interactions may contribute to learning and memory, it is important to grasp some basic details on the synaptic connectivity, patterns of activity, and how upon manipulation of some subcortical nuclei, the activity of the hippocampus changes from a synchronised state to a desynchronised one, and vice-versa. For extensive reviews on these matters, the reader is referred to Bland and Oddie (1998); Vertes (1982); Vertes et al. (2004).

The activity of the hippocampus depends largely on the activity of extra-hippocampal regions, whose synaptic inputs often synchronise hippocampal activity. A major component of these projections –mostly, part of the ascending cholinergic system in the brain– is a polysynaptic pathway originating in the pontine region, and terminating in the MS-DB. As emphasised earlier, the MS-DB distributes inputs to the hippocampal formation inducing rhythmic theta oscillations on its targets under certain conditions.

Hippocampal *synchronisation* or theta has been observed during locomotion, paradoxical sleep, and anaesthesia. The origin of the ascending brainstem-hippocampus pathway is thought to be located in a subcortical structure known as nucleus reticularis pontis oralis (RPO). Experimental evidence suggests that electrical stimulation of the RPO is effective in generating theta oscillations in the hippocampus (Green and Arduini, 1954; Macadar et al., 1974; Vertes, 1981). The contribution of RPO to the ascending hippocampal-synchronisation pathway has been confirmed by pharmacological studies using the cholinergic agonist carbachol (Bland et al., 1994). As a consequence of the enhanced activity of septal theta-on cells upon RPO carbachol microinfusions, disruption of hippocampal LIA is observed simultaneously with an increase of theta field activity. Notably, stimulation to the pedunculopontine tegmental nucleus (PPT) via carbachol can also elicit hippocampal theta activity (Vertes et al., 1993).

In a similar vein, posterior hypothalamic (PH) cells in the caudal diencephalic area display augmented discharge with stimulation of the RPO. Notably, the discharge patterns of PH cells seem to be largely irregular during hippocampal LIA (Kirk et al., 1996). During stimulation-induced theta, however, PH cells discharge in a regular, tonic manner, unlike that of SuM and medial mammillary nucleus (MM). Finally, unlike MM, SuM and PH cells display theta-related activity even after septal procaine infusion, indicating that the last structures are part of an ascending pons-hippocampus synchronising system, and may receive limited septal backprojections (Kirk et al., 1996).

1.6.1 The supramammillary (SuM) nucleus

The SuM nucleus is a central piece in the synchronisation of hippocampal activity as demonstrated by pharmacological and electrical stimulation studies. Microinfusion of procaine into the SuM nucleus reversibly abolishes both spontaneous and RPO electrical stimulation-induced theta (Oddie et al., 1994). Procaine microinfusion into the SuM nucleus also results in reduction of the hippocampal field potential amplitude during LIA (Oddie et al., 1994).

The SuM nucleus can also exert a direct effect upon its hippocampal targets, namely CA2/CA3a and DG (Vertes, 1992). For instance, Ohara et al. (2013) studied first-order inputs to DG, and showed that its major afferents originate in the SuM, MS-DB nuclei, and EC. Ohara et al. (2013) also showed that medial SuM nucleus mainly projected to ventral DG, and the lateral SuM nucleus to the dorsal part of DG. The SuM-DG projection is both excitatory (glutamatergic) and inhibitory (GABAergic). Finally, SuM nucleus efferents are thought to be almost exclusively to hippocampal principal cells (Magloczky et al., 1994).

Overall, this evidence suggests that the SuM nucleus receives projections from brainstem, upon which theta-related rhythmicity is generated. SuM, in turn strongly targets the MS-DB, driving septal pacemaking cells (theta-on cells) which drive hippocampal theta (Pan and McNaughton, 2004). Furthermore, the direct and second-level SuM-hippocampal projections may have differentiated roles in encoding of information as well as off-line memory reactivation and consolidation.

1.6.2 Hippocampus under neuromodulation

Other than projections arising from the brainstem cholinergic system, the hippocampus has direct and relatively dense noradrenergic, serotonergic and dopaminergic innervation (Andersen et al., 2006). In general, neuromodulators mediate changes to network excitation-inhibition balance, whose effects control the activity of neural circuits to encode and transfer information (Zaldivar et al., 2014; Zaldivar, 2016), and are involved in processes such as memory reactivation, consolidation, as well as awake retrieval (Atherton et al., 2015).

Neuromodulation is known to have both tonic and fast (phasic) effects on both hippocampus and cortex. For example, neurons in the *locus coeruleus* (LC) exhibit both phasic and tonic modes of activity, where phasic activation has been associated with task-related decision processes, with typical latencies of 15 to 70 ms, followed by a 300 to 700 ms period of suppression of discharge activity (Aston-Jones and Cohen, 2005). It follows that levels of extrasynaptic norepinephrine (NE) are linearly related to LC discharges (Berridge and Waterhouse, 2003; Huang et al., 2007).

A recent study on the effects of neuromodulation on hippocampal circuits, reports that upon phasic LC stimulation during ripples, both ripple and cortical spindles were transiently suppressed (for $\sim$1 to 2 s). Suppression of ripples via ripple-triggered LC stimulation consistently lead to learning deficits (Novitskaya et al., 2016). This evidence suggests that hippocampal circuits can be controlled by rapid LC responses. In an *in vitro* study, Ul Haq et al. (2012) investigated the noradrenergic system influence on hippocampal circuits and network events. Through the application of NE, both spontaneous and high-frequency stimulation-induced SWR episodes were reversibly abolished. Suppressed SWR activity was paired to the activation of $\alpha 1$ adrenoreceptors. However, SWR rates and amplitude increased with stimulation of $\beta 1$ adrenoreceptors via isoproterenol. These effects caused reduction on the amplitude of IPSP in cells that were silent during SWR. In addition, the slow after-hyperpolarisation of pyramidal cells during SWR (English et al., 2014) was reduced, which may be also associated with increased depolarisation and input resistance of CA3. Altogether, these data suggests that LC may have differentiated effects on hippocampal circuits across different brain states, associated with enhanced or reduced SWR activity, and possibly serving during information coding and memory-related functions (see also Eschenko and Sara (2008)).

The raphe nucleus is also important for regulating hippocampal activity, and likely also mnemonic processing in this area. In a recent work, Varga et al. (2009) showed that selective stimulation of raphe contacts in interneuronal dendritic fields evoked EPSP of large amplitude and latencies in the order of ∼3 ms. Then, via electrical stimulation of serotonergic median raphe-hippocampus-projecting neurons, the authors found that a subset of raphe cells responded with latencies of less than 10 ms, while another subset responded with latencies in the order of tens of milliseconds, subsequently activating hippocampal interneurons.

Thus, it is likely that raphe nucleus acts selectively on hippocampal interneurons to regulate hippocampal network activity (e.g. by silencing SWR-related ‘release’ circuits) with a subsequent impact on memory reactivation and consolidation (Wang et al., 2015; Ul Haq et al., 2016). Finally, although highly speculative, the raphe nucleus may also regulate hippocampal activity with net effects that enhance SWR activity, rather than just silencing (Ellender et al., 2010). It is possible that fast ripple activity –during which some interneuronal groups participate selectively (Varga et al., 2014)– is mediated by the extrahippocampal influence of the raphe nucleus (see also the first two papers of this thesis Ramirez-Villegas et al. (2015); Ramirez-Villegas et al. (2017b)).

The hippocampus receives projections from dopaminergic neurons in the ventral tegmental area (VTA), substantia nigra, and LC (Gasbarri et al., 1994). VTA neurons exert elevated firing in relation to reward or reward-predicting stimuli, and during exposure to previously unexplored enclosures (McNamara et al., 2014). Hippocampal neuronal ensembles are more SWR-reactivated after exploration of a new environment (Cheng and Frank, 2008; McNamara et al., 2014), and after rewarded tasks (Singer and Frank, 2009). This evidence is likely linked to the idea of a selective neuromodulatory influence in hippocampal circuits not only may relate specific decisions with their potential outcome (Papale et al., 2016), but also also bear several information-coding implications (Gupta et al., 2010). Concordantly, inhibition of VTA using pharmacological manipulations impairs CA1 place-cell stability (Martig and Mizumori, 2011). Overall, this evidence suggests that VTA dopamine release enhances hippocampal activity, and thus facilitate synaptic plasticity, which may be instrumental to stabilise hippocampal memory representations.

The specific effects of neuromodulatory activity on hippocampal SWR occurring during awake experience are unknown. SWR may be instrumental for stabilization of memory traces of locations of the visual/traversing field with particular behavioural relevance, due to their associated reward or stimulus properties, in line with previous studies in rodents during spatial exploration (McNamara et al., 2014; Gomperts et al., 2015). Whereas this hypothesis may appear conflicting with the common assumption that consolidation is performed during off-line states (but see van de Ven et al. (2016)), the possibility remains that 'short-lived off-line states' are elicited by rapid actions of neuromodulatory centres (see also Ramirez-Villegas et al. (2015)). For instance, a proportion of VTA neurons increases firing during SWR episodes during quiet wakefulness, and these increases diminish during SWS, suggesting that VTA neuromodulation over hippocampal circuits may have contributions to memory functions in a state-dependent manner (Gomperts et al., 2015).

1.7 Rapid-eye-movement (REM) sleep

Beyond its phenomenological description, the emergence of distinct neural events during REM sleep has motivated a growing body of research to establish their role in cognitive processes (Datta, 1997, 2006; Pace-Schott and Hobson, 2002). Are REM sleep-associated neuronal processes necessary for the formation of new memories, reactivation and retrieval? Selective inactivation of the brainstem-hippocampus synchronising pathway during REM sleep provides insight into these questions (Boyce et al., 2016; Mavanji and Datta, 2003; Mavanji et al., 2004). Thus, we find important reasons to study the physiological activity of the brain during REM sleep and to examine its putative computations.

REM sleep has been considered a *paradoxical* brain state (hence my deliberate usage of the term in this work, after Michel Jouvet). Despite being a state of high behavioural threshold to arousing external stimuli, forebrain neural activity resembles that of waking states (Jouvet, 1965). Indeed, initial studies suggested that this brain state is highly active due to its correlation with EEG fast neocortical activity, subcortical activation, and dreaming (Datta and MacLean, 2007).

REM sleep is characterised by low-amplitude, fast cortical activity, also referred to as *EEG activation* (Jouvet and Michel, 1959; Jouvet et al., 1959b,a). There are a series of characteristics that make paradoxical sleep a very striking phenomenon. For example, paradoxical sleep is dominated by muscle atonia with occasional muscle twitches. The retained high tone of ocular muscles is tightly related to the generation of clusters of REM in the electrooculogram. Apart from these physiological signs, there are two signs of brain electorphysiological activity that correlate with the occurrence of paradoxical sleep: first –as pointed out previously in this dissertation– the theta rhythm is ubiquitous in the hippocampal fields (Jouvet and Michel, 1959; Jouvet et al., 1959b,a) and that of related extrahippocampal structures (Buzsaki, 2002; Bland and Oddie, 1998). Second, spiky field potential waves can be recorded from the pontine region of rodents, cats, human and non-human primates. These potentials are observed simultaneously in the LGN, and the occipital cortex, and are therefore termed pontogeniculooccipital (PGO) waves (Jouvet and Michel, 1959; Jouvet et al., 1959b; Datta, 1997), reviewed in the next section of this work.

The mechanisms that determine the shift between predominantly external inputs during waking, to predominantly internal inputs during sleep remain unknown. However, the states of waking, non-REM sleep, and paradoxical sleep rely on the activity of brainstem structures (Hobson, 2009). Generally speaking, the brainstem dictates the activity of forebrain structures by modulating the extent of their activities at a given state. In this sense, both cholinergic and aminergic (catecholaminergic, serotonergic, and histaminergic) tones are high during waking and reduced during non-REM sleep. During REM sleep, however, cholinergic tone is high, co-occurring with aminergic demodulation (Pace-Schott and Hobson, 2002; Hobson, 2009).

The cellular mechanisms underlying paradoxical sleep are believed to involve a reciprocal interaction between aminergic and cholinergic neurons (Leonard and Llinas, 1994; Sakai and Koyama, 1996). Since the pontine aminergic system is highly active during waking, part of the cholinergic PPT may be inhibited by this action. During paradoxical sleep excitatory cholinergic-non-cholinergic interactions may enhance the firing of PPT cells. At the same time, inhibition of LC and raphe is attained by GABAergic mechanisms, contributing to the release of a proportion of PPT cells from aminergic suppression (Gervasoni et al., 2000; Nitz and Siegel, 1997).

Experimental evidence suggests that the PPT is causally involved in generating both wakefulness and REM sleep (Datta and Siwek, 1997). In line with this suggestion, approximately 60% of the PPT cells are active during both wakefulness and paradoxical sleep, whereas the remaining group are REM-on cells or wake-on cells. Notably, most PPT cells are active right before waking, and remain active until few seconds before the end of wakefulness (Datta and Siwek, 1997).

The temporal organisation of wake, non-REM and REM sleep episodes is highly complex, and remarkably different across animal species. These brainstem-orchestrated cycles of activity can impact the excitability of cells across all structures of the brain. Concordantly, recent experimental evidence suggests that non-REM episodes are associated with progressively increasing firing rates of pyramidal cell and interneuron populations in the hippocampus. This progressive increase is interrupted by the appearance of REM sleep, where firing rates are largely decelerated (Grosmark et al., 2012; Montgomery et al., 2008). On the basis of this large-scale *sawtooth* pattern, preceding REM-related theta activity power correlates with a subsequent increase in population synchrony during non-REM. Notably, SWR-related synchrony is increased from the early to the late stage of non-REM sleep (Grosmark et al., 2012).

Another important observation is that acetylcholine release in thalamus is highest during waking and REM, and minimum during SWS (Williams et al., 1994). Conversely, coordinated thalamo-cortical spindles are prominent during SWS, in contrast with the activated state (Steriade et al., 1985, 1987). Hippocampal REM-theta –although with a similar field signature– is fundamentally different to sleep spindles (Sullivan et al., 2014). In addition, theta during REM is also different to theta during waking experience. REM-theta is characterised by higher theta- and gamma-synchrony between DG and CA3, and lower gamma-synchrony between CA3 and CA1 subfields, as compared to waking-theta in rodents (Montgomery et al., 2008). Overall, this evidence suggests that brain activity during paradoxical sleep is markedly different to that of SWS, and notably, to that during waking despite the similar cholinergic activation.

1.8 Pontogeniculooccipital (PGO) waves

PGO waves have stood as one of the most striking phenomenological aspects of REM sleep. PGO waves have been related to multiple putative functions such as sensorimotor integration, development of the visual system, and learning and memory (Datta, 1997).

PGO waves are phasic potentials co-occurring in the pontine region (*ponto*), the lateral geniculate body (LGB) (*geniculo*), and the occipital cortex (*occipital*). PGO waves are biphasic potentials, with a centre frequency of approximately 10 Hz ($\sim$100 ms duration) and amplitude of 200-300 μV Datta (1997). To date, they have been observed in other regions of the neocortex and thalamus (Brooks, 1968; Hobson, 1964), oculomotor nuclei (Brooks and Bizzi, 1963), and the cerebellum (Jouvet, 1965). So far, all studies acknowledge the pontine region as the ultimate generator of PGO waves (for review see Datta (1997)).

PGO waves are widespread phenomena. Namely, they co-occur across many regions of the brain. This fact suggests that their occurrence can influence the activity of many brain subsystems, and therefore PGO waves may be involved in cognitive processing. Classically, PGO waves have been studied mostly in cats (Jouvet and Michel, 1959; Jouvet et al., 1959b,a). However, they consistently appear in recordings from non-human (Cohen and Feldman, 1968; Feldman and Cohen, 1968; Vuillon-Cacciuttolo et al., 1978), and human primates (McCarley et al., 1983; Fernandez-Mendoza et al., 2009; Lim et al., 2007). Later studies identified PGO-like waves in rats (Reiner and Morrison, 1980; Marks et al., 1980a; Farber et al., 1980), which were also observed in subsequent rodent studies both in the pons (Datta, 2000; Karashima et al., 2004), and cerebellum (Marks et al., 1980a,b).

PGO waves exhibit a striking variability which seems largely sleep-stage dependent. Several classical studies suggested that PGO waves come as singlets (singlet PGO waves), or as clusters containing bouts of several waves in very close temporal proximity (Datta et al., 1992; Morrison and Pompeiano, 1966). Singlet PGO waves occur during SWS, whereas clustered ones usually occur during REM sleep. Several observations have led to the speculation that these two types of activities are different in their physiological nature. First, singlets are seemingly independent of eye movements, whereas clustered PGO waves are associated with eye movement bursts (REM) (Morrison and Pompeiano, 1966). Second, inactivation of vestibular nuclei (sending monosynaptic input to PGO-wave triggering neurons) abolishes bursts of REM and type II PGO wave activity, while facilitating type I PGO wave activity with consequent reduction of desynchronized sleep periods (Morrison and Pompeiano, 1966). Third, pharmacological manipulations upon PGO-generating circuits via carbachol enhance the activity of cholinergic and PGO burst cells. This evidence indicates that REM and associated clustered PGO activity may be specifically mediated by endogenous release of acetylcholine (Datta et al., 1992). Similar effects have been encountered in experimental preparations by other authors (Quatrochi and Hobson, 1999; Denlinger et al., 1988).

PGO waves are related to episodes of similar electrical signature in the basolateral amygdala, anterior and posterior cingulate gyrus, dorsal hippocampus, anterior ventral thalamic nucleus, and sensory motor cortex in the cat brain (Calvo and Fernandez-Guardiola, 1984; Hobson, 1965). The nature of these potentials is unknown, but may be associated with the emergence of diverse neuronal events. For instance, paradoxical sleep PGO waves are associated with, and are known to exert synchronising effects over theta oscillations in the hippocampus of cats (Karashima et al., 2005), and the hippocampus and amygdala of rodents (Karashima et al., 2001, 2002, 2004, 2010). Specifically, the appearance of PGO waves correlates with increases in the amplitude and frequency of theta (Karashima et al., 2004).

Establishing an equivalence between the sustained theta activity of rats and a correlate in the primate is a challenging task, as the presence of theta in hippocampal recordings of the macaque remains debated (see Section 1.5.1 of this thesis). However, I hope to convince the reader after the third paper of this thesis, that a low-frequency event type (also reported in Logothetis et al. (2012) under the name of hp-sigma) presents similar correlates to rodent theta activity. These theta-like episodes co-occur with paradoxical-sleep PGO waves in a synchronous manner, following similar time courses. Thus, it is possible that the events observed by Calvo and Fernandez-Guardiola (1984) in cats are indeed bouts of theta oscillations as they similarly occur in awake monkeys (Leonard et al., 2015; Jutras et al., 2013), and monkeys under sleep-like conditions (Logothetis et al., 2012; Ramirez-Villegas et al., 2017a).

Furthermore, there is no evidence relating SWS PGO waves to the dynamics of forebrain structures such as the hippocampus. As pointed out earlier, the activity of the hippocampus during SWS and REM is markedly different, and therefore the mediating (or modulating) role of PGO waves in this sleep stage over hippocampus may be different to that of REM-related PGO waves. These activities may serve distinct putative memory-associated functions. These questions were addressed in the third paper of this thesis (Ramirez-Villegas et al., 2017a). We show that PGO waves co-occur with hippocampal SWR complexes, as well as theta-like events in the hippocampus of macaques. These events –although with similar LFP frequency profiles– are associated with markedly opposite neuronal population responses across pontine, thalamic and hippocampal regions. Notably, these responses may correlate with signatures in the global activity of the brain as suggested by earlier work (Logothetis et al., 2012).

In line with the foregoing, both SWS and REM may be highly favorable states for memory integration and consolidation of memories (Datta, 2006; Boyce et al., 2016). Similar to SWR complexes during SWS, the density of PGO-like episodes during post-training REM in the rodent correlates positively with consolidation, and recall of the learning task (Datta, 2000). The period of transition between SWS and REM is also reported to augment significantly, together with PGO wave density and time spent in REM during after-learning sleep (Datta, 2000).

PGO waves have been also reported to boost retention of learned information. Mavanji and Datta (2003) studied the activity of the pontine region of the rat in relation to an avoidance task. After learning, a subgroup of animals were administered with a pontine carbachol injection. Upon this manipulation, REM sleep-related PGO-like episodes increased significantly above that in control animals, together with a significant improvement in task performance (Mavanji and Datta, 2003). Similarly, REM sleep deprivation is correlated with learning deficits in similar learning paradigms, and these deficits can be prevented by selective activation of the PGO-wave brainstem generator (Datta et al., 2004). In addition, learning deficits can also be induced when PGO potentials –but not REM sleep itself– are pharmacologically suppressed (Mavanji et al., 2004). Overall, these studies suggest that REM sleep, and specifically PGO waves may have a boosting role in consolidation and integration of memories.

1.8.1 Pontine triggering, transfering, and SWS-selective neurons

PGO wave generation relies on the activity of two different subgroups known as *triggering* and *transferring* neurons. These groups of neurons are located within the parabrachial area

(PBL). Anatomically, the PBL contains the PPT, the laterodorsal tegmentum, cuneiform nuclei, and other adjacent nuclei (Datta, 1997).

The PGO-wave triggering elements are located in the caudolateral PBL (C-PBL). This conjecture comes from the fact that most of C-PBL neurons firings precede the onset of PGO waves (Datta and Hobson, 1994), and that these neurons' firing precede that of PBL cells in the rostral part of the nucleus (R-PBL) (Nelson et al., 1983; Steriade et al., 1990b). In addition to an increase in REM PGO waves upon carbachol injections in C-PBL (Datta et al., 1992), lesions to C-PBL eliminate PGO waves in the LGB (Shouse and Siegel, 1992; Datta and Hobson, 1995).

There is also a group of PBL neurons that is selectively active during SWS. Using immunohistochemical techniques, Torterolo et al. (2011) observed a group of cells located in the C-PBL region selectively active during SWS. This cell cluster was neither cholinergic, nor (catechol-) aminergic. Rather, the group of cells was ca. 50% GABAergic. In this study, the number of SWS-immunoreactive PBL cells in their study was positively correlated with the time spent in SWS by the animals. Whether these activities are associated in particular with PGO waves is unknown. Yet, although highly speculative, this group of cells –strikingly located in the PGO-triggering zone– may act in concert with other brain areas during SWS-associated neural events.

Neurons of the R-PBL –likely both cholinergic (Datta et al., 1992), and catecholaminergic (Vincent et al., 1986)– are thought to transfer PGO-related activity to the thalamus (Nelson et al., 1983; Steriade et al., 1990b). During PGO-associated potentials R-PBL responds with short latency to the discharge of C-PBL neurons (Datta, 1995). The subsequent chain of depolarisations is thought to occur through long-range connections to the thalamus and several forebrain structures (Steriade et al., 1990b,a; Datta and Hobson, 1994; Datta et al., 1989; Ahlsen, 1984; Isaacson et al., 1986; Hallanger et al., 1987).

In summary, PGO activity is controlled by the interaction of several brainstem structures, likely generated by C-PBL triggering elements, and modulated by aminergic, cholinergic and GABAergic mechanisms, in addition to inputs from vestibular nuclei (Morrison and Pompeiano, 1966; Datta and Hobson, 1994).

1.8.2 PGO waves and thalamo-cortical spindles

In this subsection I shall briefly introduce thalamo-cortical spindles. As it is customary, spindles and related thalamic rhythmic activities can be explained in the context of PGO waves, and the activation of brainstem cholinergic elements.

The activity of the thalamus –as likely other forebrain areas– is controlled by brainstem inputs. PGO waves in thalamus and neocortical EEG activation occur with the suppression of spindle-generating mechanisms (Hu et al., 1989a,b) which are at play exclusively during SWS. Thalamic neurons receive direct cholinergic excitation from mesopontine cholinergic nuclei. Elicited by stimulation of cholinergic receptors, thalamo-cortical cells undergo a process of disinhibition consequent to the hyperpolarisation of reticular thalamic neurons (Hu et al., 1989a,b; McCormick and Prince, 1986). As reticular thalamic neurons have been ascribed a pace-making role during spindle activity, tonic inactivation of these cells abolishes spindles. Together with hyperpolarisation of reticular neurons, mesopontine cholinergic neurons also activate thalamocortical neurons, which consequently depolarise widespread cortical targets (Steriade et al., 1990a). Thus, activated neocortical activity is fast and has low amplitude at the population level. A similar set of mechanisms may be in action during arousal, during which the cholinergic tone is also high, and may act in synergy with activities of other brainstem neuromodulators such as the LC (McCormick and Prince, 1988).

As opposed to REM, SWS is a brain state of low cholinergic tone. During this state, neocortical slow oscillations (<1 Hz) correlate with recurrent, coordinated and abrupt transitions of neuronal activity from a hyperpolarised state (often referred to as *down state*, to a depolarised state (often referred to as *up state*) (Steriade et al., 1993a). Rhythmic shifts of activity between down and up states have also been observed in striatal (Stern et al., 1997), hippocampal (Ji and Wilson, 2007), and thalamic neurons (Steriade et al., 1993b,a; Timofeev and Steriade, 1996). In classical studies, the down-to-up state transition was often observed to occur in the form a 'sharp potential', referred to as K-complex. K-complexes contribute to both slow oscillations, and delta rhythms.

Spindles –highly oscillatory low-frequency (∼7-14 Hz) events ∼1-2 s in duration– are commonly observed after the occurrence of K-complexes. The first suggestion regarding the occurrence of thalamical spindle activity was described by Morison and Bassett (1945), where spindles were recorded in the intralaminar thalamic region of brainstem-transected, decorticated cats.

The mechanistic details of spindles were described by a series of studies from Steriade and collaborators (Steriade et al., 1985, 1987), where abolition of spindle-related rhythmic activity was observed after disconnecting the thalamic reticular nucleus of cats. Importantly, the disconnected reticular nucleus preserved its rhythmicity and cell firing properties after disconnection from cortical and thalamic inputs, whereas thalamo-cortical neurons displayed single event-like activities. Thus, the time-frequency properties of sleep spindles are therefore set by the cellular properties of reticular neurons, and the interplay between excitation and inhibition of glutamatergic thalamo-cortical cells and GABAergic reticular cells. In addition, the thalamo-cortical loop is important to generate global and possibly neocortex-wide synchrony (McCormick and Bal, 1997).

1.9 Summary and aims of the project

The hippocampus is widely and critically involved in learning and memory. Lesions to the hippocampal formation lead to deficits in the formation of new declarative memories (Scoville and Milner, 1957). However, the persistence of older (early stabilised) memories after hippocampus lesions has lead to the hypothesis of a two-stage memory model of memory consolidation: memory traces are encoded during waking, and subsequently transferred to the neocortex for long-term storage. In addition, these processes rely on the coordinated activity of several anatomically- and functionally-coupled subnetworks within and beyond the hippocampal formation.

The physiological mechanisms by which the brain regulates itself to store memory representations remain debated. Nonetheless, the correlative evidence discussed in this thesis suggests that it partly relies upon emergence of global states, upon the control of several key structures such as thalamic nuclei and brainstem neuromodulatory systems. Neuromodulatory systems establish the global conditions for reactivation, consolidation and recall to occur, upon dynamical changes in brain state. Beyond the emergence of neocortical up and down states, the brain exhibits a complex system-like organisation, marked by slow changes. Neural patterns of activity during these slow transitions herald changes in neuronal excitability that affect the collective activity of subsystems, allowing them to express a variety of patterns of activation. In addition, a given state may exert influences upon the expression of other states.

A notable example of this dynamics –as discussed along this chapter– is the interplay between REM and non-REM sleep. REM- and non-REM-related activities seem largely antagonistic from the viewpoint of the brainstem (Pace-Schott and Hobson, 2002). This antagonism is also apparent in the activity of forebrain structures. Yet, REM and non-REM states seem to interact. For instance, REM sleep seems to be largely involved in determining the excitability of hippocampal cells during subsequent non-REM periods (Grosmark et al., 2012). Thus, it is likely that not only non-REM sleep-related activities (Buzsaki et al., 1992; Buzsaki, 1986) are major determinants of mnemonic processing, but also REM-associated activities (Jouvet and Michel, 1959; Jouvet et al., 1959b,a; Boyce et al., 2016) are instrumental for similar cognitive demands.

In this dissertation we investigated transient signatures of electrical activity present in the extracellular field potential of the brain (neural events) that underlie cognitive processes such as consolidation and retrieval of mnemonic information. For such a purpose, this project encompasses the following specific aims, associated with the attached manuscripts:

a. To characterize the meso- and macroscopic dynamics of hippocampal SWR episodes, and how selective activation of circuits across the brain may exert effects on the electrical signature of SWR, with a potential subsequent impact in mnemonic processing.

b. To understand the microscopic dynamics of hippocampal SWR episodes. Specifically, how the underlying structure and physiology of hippocampal networks support the repertoire of activities that endow the hippocampus with its putative computation abilities during SWR.

c. To address how excitation-inhibition balance –a marker of the dynamical state of the network– is altered during the initiation and development of SWR episodes. In addition, to establish the mesoscopic correlates of these changes present in synaptic and non-synaptic activities so as to better understand the information provided by the hippocampal LFP.

d. To understand the meso- and macroscopic dynamics of PGO waves, phasic activities of pontine origin and landmarks of REM sleep. Specifically, to investigate the relationship of PGO waves to neuronal ensemble activities in the hippocampus, and how these long-range multi-structure interactions may impact off-line mnemonic processing.

1.10 Introduction to manuscripts

1.10.1 Paper I: Diversity of sharp wave-ripple LFP signatures reveals differentiated brain-wide dynamical events

Introduction: During epochs of both wakefulness and off-line states, hippocampus and cortex replay behaviourally-relevant sequences of action potentials. These sequences –often referred to as reactivations– reflect the animals' previous and potential spatial experiences. Transient episodes of highly synchronous activity known as SWR complexes co-occur with sequence-reactivation within the hippocampus. Although this suggests that SWR mediate memory processes, the underlying multi-scale dynamics relating to these episodes remains poorly understood. In this work, we sought to investigate how the LFP signature of SWR events varies during hippocampal ongoing activity, and whether the full extent of these electrical variations reflects differences in the coordination of neuronal activity at multiple spatio-temporal scales.

Materials and Methods: We addressed this question by studying the signature of SWR complexes at multiple scales. Specifically, using concurrent multi-site LFP recordings and functional MRI (fMRI) in anaesthetised macaque monkeys (*Macaca Mulatta*) together with clustering techniques, we studied the SWR phenomenon on the basis of variations of its LFP signature. This decomposition allowed us to identify several SWR subtypes, which were then characterised in terms of their time-frequency and spike-LFP coupling features. Subsequently, using fMRI and statistical procedures –inspired by the work of Logothetis et al. (2012)– we investigated the whole extent of brain areas that are modulated at times of SWR-subtype occurrence.

Results: The clustering SWR yielded four event subtypes. Notably, these subtypes were robustly identified across experimental sessions and animals. SWR subtypes differed on the basis of the temporal sharp wave-to-ripple coupling, and their low-frequency sharp wave pattern. 'Classical' SWR subtypes –those observed in classical studies– were different with respect to their 'non-classical' counterparts in their neuronal correlates. These differences also included time-frequency and spike-LFP synchronisation characteristics. SWR-triggered fMRI revealed that 'classical' SWR are characterised by enhanced neocortical activation and subcortical suppression (after Logothetis et al. (2012)). Furthermore, subcortical down-regulations were almost absent at times of non-classical SWR subtypes whose ripples occurred close to the trough of their associated sharp waves. Importantly, 'non-classical' SWR were also associated with low levels of suppression of aminergic neuromodulatory structures, namely LC and dorsal raphe areas.

Conclusions: Our results indicate that *in vivo* SWR complexes are significantly diverse. These –possibly functionally-distinct– SWR subtypes may arise upon complex long-range subcortical network inputs to the hippocampal formation. Finally, these episodes may endow the hippocampus with a variety of computing and modulatory abilities associated with specific memory-related functions both during sleep and wakefulness.

1.10.2 Paper II: Dissection of frequency-dependent spiking and synaptic contributions to in vivo hippocampal sharp wave-ripples

Introduction: SWR –a prominent feature associated with systems memory consolidation– are neural events resulting from the interaction between neuronal populations across distinct substructures of the hippocampus. Yet, the role of afferent CA3 inputs and recurrent CA1 activities in precisely coordinating these events is not well-understood. This knowledge gap arises partly due to the inherent difficulties in inferring neural network-level dynamics from population measures such as the LFP. In this work, we tested the hypothesis that SWR complexes result from frequency-specific contributions of the population-level extracellular currents exerted by the CA3 network and local groups of neurons in CA1. These currents establish well-differentiated network mechanisms associated with the emergence of sharp waves, and the generation of CA1 ripples.

Materials and Methods: To test this hypothesis, we developed a minimal network model of multi-compartmental neurons accounting for CA3 and CA1 populations. Using the line-source approximation (Schomburg et al., 2012), we estimated the LFP activity of CA3 and CA1 neuronal populations. That is, the weighted contribution of the transmembrane currents of each simulated cell to a measurement point given by the location of a 'virtual' electrode. Subsequently, we sought to assess the contributions of pyramidal neuron and interneuron populations to SWR episodes. This assessment was done on the basis of population-level synaptic and non-synaptic activities. By analysing the spatial distribution and the timing of these activities relative to the occurrence of single SWR episodes, we determined whether and how CA3 provides the necessary input onto CA1 populations in order for SWR to be initiated. Furthermore, we assessed the role of CA1-associated dendritic and somatic peri-synaptic activities in coordinating the ripple phenomenon. Finally, by selectively blocking synaptic connections inherent to the CA1 network, we investigated the extent of synaptic interactions that are critical for the emergence of SWR complexes.

Results: We found that sharp waves ($<$20 Hz) and slow-gamma activities (30-55 Hz) components originate due to CA3 activity impinging onto CA1 stratum radiatum. Specifically, CA3 input provides the necessary transient modification of E-I balance initiating the phenomenon, and coordinates its interactions with CA1 assemblies by gamma, but not the ripple oscillations. Crucially, LFP ripples emerge due to the driving of inhibitory post-synaptic currents (Gan et al., 2017), whereas excitatory post-synaptic currents of CA1 pyramidal neurons onto interneurons control the amount of pyramidal cells participating in single ripples. In line with previous experimental work, we found that recurrent inhibitory connections, whether I-E or I-I, but not recurrent excitation onto interneurons, are critical for the emergence of ripple oscillations.

Conclusions: Overall, these results suggest that several elementary components underlie the ensemble dynamics of physiological SWR activity. These dynamical components are embedded into the complex electrical signature of SWR, but are differentially contributed by remote CA3 input and endogenous activity within CA1. Furthermore, our investigation indicates a previously unknown correlate of concerted excitatory PSC during SWR, which has been typically ascribed only to coordinated inhibitory PSC. It is thus likely that interneuronal-network synaptic influences –with notable ripple-pacing properties– act in concert with pyramidal cell synaptic influences to select the assemblies that participate during SWR complexes. Finally, together with an unprecedented reproduction of *in vivo* experimental findings, this work suggests a relationship between neuronal activity over meso- and microscopic scales that provides a way for studying

E-I balance during hippocampal spontaneous activity relying purely on LFP signals.

1.10.3 Paper III: Pontogeniculooccipital (PGO) waves reflect transient competition between brain stem and hippocampus

Introduction: Pontogeniculooccipital (PGO) waves are potentials observed simultaneously in the pontine, genicular and neocortical LFP of several mammalian species during periods of paradoxical sleep. Correlative evidence suggests that these brief oscillatory episodes are central to learning and memory processes (Mavanji and Datta, 2003; Datta et al., 2004). However, how these phasic widespread events participate in brain-wide network activities remains unknown. In this work, we investigated the large-scale interactions between PGO waves, and the activities of the major brain hub for memory: the hippocampus. We hypothesised that PGO waves –in association with the concerted activity of several subcortical structures– may partly coordinate activity within the hippocampus, and hence support off-line information processing.

Materials and Methods: We tested this hypothesis using multi-site extracellular recordings from the pons, LGN and hippocampus of anaesthetized macaque monkeys (*Macaca Mulatta*, *Macaca Fascicularis*). PGO waves were identified as low-frequency neural events that co-occurred simultaneously in pontine and LGN LFP. Through a first series of experiments, we identified distinct subtypes of PGO activities on the basis of their oscillatory nature and underlying MUA. Furthermore, we characterised the extracted PGO wave types across several frequency sub-bands on the basis of band-limited power (BLP) signals spanning the whole mEFP of the pons and LGN recordings (< 2000 Hz). We then compared the PGO-wave-triggered responses using standard statistical procedures. Finally, through a second series of experiments, we detected episodes of synchronous activity co-occurring in pons, LGN and hippocampus, thus corresponding to PGO waves. Using analogous analysis techniques, we characterised the extent of hippocampal LFP neuronal events that co-occurred with PGO waves.

Results: We identified two PGO wave types: type I, associated with a significant MUA decrease around the event occurrence, and type II associated with a significant MUA increase around the event occurrence. Typically, type I PGO waves exhibited a single biphasic oscillatory pattern, whereas type II PGO waves displayed multiple successive field oscillations. Type II PGO waves –likely REM PGO waves– related to the spontaneous interruption of thalamic spindles, as reported in classical studies (Hu et al., 1989a,b). Interestingly, the two types of PGO waves co-occurred with hippocampal neural events. We found that type II PGO waves were coupled to the spontaneous emergence of hippocampal theta-like oscillations (hp-sigma events, after Logothetis et al. (2012)), whereas –more strikingly– type I PGO waves were associated with SWR complexes. These effects were observed across all animals and experimental sessions in a consistent manner.

Conclusions: This work establishes an important line of evidence for the field as we show, for the first time, PGO wave signatures associated with specific off-line and state-dependent interactions between brainstem, thalamic and hippocampal circuits. In addition, our data offers insight on a hypothetical competition (or antagonism) over short time scales between hippocampal-neocortical and ponto-geniculo-neocortical networks. This competition is likely driven by distinct, possibly antagonistic brain states and may establish the basis of two global mechanisms whose correspondence may account for off-line memory consolidation.

Chapter 2

List of papers and statements of contribution

(Darstellung des Eigenanteils bei Gemeinschaftsarbeiten nach §9 para. 2)

2.1 Paper I

Title: Diversity of sharp-wave-ripple LFP signatures reveals differentiated brain-wide dynamical events

Authors: Juan F. Ramirez-Villegas, Nikos K. Logothetis, Michel Besserve

Status of paper: Published in Proceedings of the National Academy of Sciences of the United States of America (see Ramirez-Villegas, 2015). Available online at www.pnas.org/cgi/doi/10.1073/pnas.1518257112 since 4 November 2015.

Declaration of author contributions: All data analyses were conducted by JFRV. All experimental data were provided by NKL (from Logothetis et al. (2012)). MB designed and supervised the research. JFRV performed the research. JFRV, NKL, and MB contributed new reagents/analytic tools. JFRV produced the figures of the manuscript. The draft of the manuscript was written by JFRV. MB provided critical feedback on the draft and, together with NKL, helped to produce the final version of the text. JFRV and MB revised the manuscript according to the critique of anonymous expert reviewers.

2.2 Paper II

Title: Dissecting the frequency-dependent network mechanisms of *in vivo* hippocampal sharp wave-ripples

Authors: Juan F. Ramirez-Villegas, Konstantin Willeke, Nikos K. Logothetis, Michel Besserve

Status of paper: Manuscript in revision for Neuron.

Declaration of author contributions: All data analyses were conducted by JFRV. All experimental data were provided by NKL (from Logothetis et al. (2012)). JFRV and MB designed the research. MB supervised the research. JFRV performed the research. Multi-compartmental computational models were designed by JFRV. Model connectivity and synaptic parameters were fitted by KW to account for realistic anatomical and physiological constraints. JFRV, KW, NKL, and MB contributed new reagents/analytic tools. JFRV produced the figures of the manuscript. JFRV and MB wrote the paper. All authors provided critical feedback on the draft.

2.3 Paper III

Title: Pontogeniculooccipital (PGO) waves reflect transient competition between brain stem and hippocampus

Authors: Juan F. Ramirez-Villegas, Yusuke Murayama, Henry C. Evrard, Michel Besserve, Nikos K. Logothetis

Status of paper: Manuscript in preparation for Science.

Declaration of author contributions: All data analyses were conducted by JFRV, under the supervision of NKL and MB. All experimental data were recorded by YM. NKL designed the research. NKL and MB supervised the research. JFRV and YM performed the research. All authors contributed new reagents/analytic tools. HCE contributed all the anatomical details required to define ROIs and enable registration of functional images to anatomical scans, and to define the location of multi-site electrophysiological recordings. JFRV produced the figures of the manuscript. The draft of the manuscript was written by JFRV, with critical feedback from NKL and MB. All authors provided comments on the manuscript.

Chapter 3

General Discussion

Memory processes rely on a precise coordination of the activities of several brain circuits. These interactions span several spatio-temporal scales and seem to be governed by a high degree of self-organisation throughout multiple stereotypical so-called 'global' or 'macroscopic' brain sates. This dissertation aimed at better understanding the relationship between the micro-, meso- and macroscopic dynamics underlying neuronal events in the hippocampus, brainstem, and thalamus. In particular, I investigated how these events –encountered locally in the electrical microcircuit activity of these structures– may relate to: first, the emergence of macroscopic activity throughout all structures of the brain; and second, the processing of mnemonic information during off-line states.

The specific aims of this dissertation (listed in Section 1.9) were addressed as follows: the first paper of this dissertation (Ramirez-Villegas et al., 2015) addresses the first aim; the second paper (Ramirez-Villegas et al., 2017b) addresses the second and third aims; finally, the third paper (Ramirez-Villegas et al., 2017a) provides evidence toward the last aim. In the following, our main contributions are discussed on the basis of the existing literature, with emphasis on how each manuscript filled specific knowledge gaps in the field. Furthermore, a number of hypotheses, potential interpretations and directions for future computational and experimental work that were not included in the manuscripts shall be mentioned, alongside their relationship to state-of-art findings in the field.

3.1 Diversity of SWR complexes and brain-wide dynamics

SWR complexes are paradigmatic episodes of synchronous activity within the hippocampus, thought to mediate and/or modulate brain-wide processes associated with reactivation, transfer and consolidation of memories both in rodents (Girardeau et al., 2009; Nakashiba et al., 2009; van de Ven et al., 2016; Ego-Stengel and Wilson, 2010) and primates (Leonard and Hoffman, 2016; Axmacher et al., 2008; Staresina et al., 2015). However, the large-scale mechanisms associated with these episodes and their relationship to the observed SWR electrical signature has remained largely unknown. In the first study of this dissertation, we investigated the system-level properties of hippocampal SWR episodes at multiple spatio-temporal scales. This knowledge gap arose from experimental limitations, as the only way to gain insight into the global activity of the brain is to record its activities at different sites simultaneously. This high-spatial resolution is limited with standard electrophysiology techniques. In order to address this issue, we used multi-modal recordings, namely concurrent intracortical electrophysiology with functional MRI (as first reported in Logothetis et al. (2012)).

In the first paper of this dissertation, we identified distinct subtypes of *in vivo* SWR activities. To our knowledge, this is the first time that distinct SWR subtypes are reported. These event types give rise to several differences that span the local microcircuitry of the hippocampus, and likely reflect differentiated brain-wide events. On the basis of the existing literature, these stereotypical variations in SWR signatures had not been yet reported. Notably, we found a similar result when analysing rodent recordings during naturalistic sleep preparations (not shown in this dissertation; the data was courtesy of Dr. Oxana Eschenko, $N = 2$ rats). Thus, it is likely that the computational roles and correlates associated with SWR subtypes –like that of SWR in general (Buzsaki, 2015)– are conserved with phylogenetic development.

Our results agree with a number of *in vivo* and *in vitro* studies (Oliva et al., 2016; Kay et al., 2016; Hofer et al., 2014). Hofer et al. (2014) found that CA3 SWR may come in two main types: first, with prominent LFP negativity in SR, associated with the usual current source in SP (Ylinen et al., 1995); and second, with LFP positivity in SR, as a result of a current sink in SP (possibly stratum lucidum) and a current source in SO. Concordantly, these episodes present differentiated time-frequency properties as we found in our study. However, the correspondence between SWR from *in vitro* preparations and that of *in vivo* ones is often difficult to establish (Buzsaki, 2015). In a similar vein, the observations reported by Hofer et al. (2014) correspond to the electrical activity of CA3, rather than CA1, as we report. Furthermore, slice preparations have several other limitations. For instance, neuromodulatory activity generated by brainstem structures may influence the activity of hippocampal circuits in a state-dependent manner, and such potential influences are absent in slice preparations. The same would apply for any long-range interaction between hippocampus and the rest of the brain. Moreover, preparation-specific conditions may affect dramatically the physiological properties of the observed SWR complexes (Wu et al., 2005; Maier et al., 2003; Schlingloff et al., 2014). Among others, these factors may account for the observed differences between CA3 SWR-related LFP *in vitro* (Reichinnek et al., 2010; Hajos et al., 2013) and in the intact brain (Oliva et al., 2016; Sullivan et al., 2011).

The observed SWR-related LFP variability suggests that the extracellular currents in

CA1 are distributed differently across the cells' somato-dendritic segments. One possible explanation –as discussed in the paper– are the differences in recruitment of neuronal subgroups, specifically non-homogeneously-distributed groups of interneurons in stratum pyramidale (Mizuseki et al., 2011; Lee et al., 2014). Indeed, the CA3/CA2/CA1 pyramidal cell layer (SP) of the primate hippocampus presents well-differentiated laminar structure as compared to that of the rodent (Andersen et al., 2006). In the rodent, PV+ basket cells evoke greater inhibition in the deep layer of the CA1 stratum pyramidale, and in turn, receive more excitatory input from CA1 superficial pyramidal cells. PV+ basket cells preferentially innervate amygdala-projecting pyramidal cells, and are targeted preferentially by PFC-projecting pyramidal cells (Lee et al., 2014). This highly organised circuit heterogeneity could contribute to the emergence of many computation modes and differentiated SWR events, organised into several inhibitory subcircuits.

In addition, the CA2 network could contribute to this variability by triggering specific SWR subtypes. Recent experimental evidence suggests that CA2 is involved in SWR initiation (Oliva et al., 2016; Kay et al., 2016). For instance, Oliva et al. (2016) report that synchronous activity of CA2 cells precedes that of CA3 and CA1 during SWR-related discharges. SWR were observed following a CA2-CA3-CA1 activation chain, and also as a consequence of CA2-induced CA1 SO depolarization. In the latter case, a current sink –corresponding to a negative LFP deflection– was observed in the SO (basal dendrites) and SP (somatic layer) of CA1, together with a current source –corresponding to a positive LFP deflection– in SR (apical dendrites). The electrical profile of this event subtype is similar to that encountered by us (SWR subtype 1 in Ramirez-Villegas et al. (2015)), and it opens the question as to whether this SWR subtype is generated by the intrinsic activity of CA2 or as a byproduct of the activation of subcortical-hippocampal projections (Vertes, 1992; Magloczky et al., 1994). Furthermore, it is important to note that CA2 seems more involved in driving the hippocampal network during waking than during SWS (Oliva et al., 2016), suggesting that this CA2-induced SWR via CA2-CA1 interaction might play an influential role in mnemonic processing during waking (see also Hitti and Siegelbaum (2014)).

Furthermore, in a recent study, two distinct types of SWR episodes were found to be related to reactivations of trajectory- and immobility-associated hippocampal representations. These two SWR subtypes –differing in their time-frequency LFP properties– were found to differentially modulate neocortical populations (Yu et al., 2017). Finally, this waking-related processing is likely coordinated by brainstem neuromodulatory structures, as waking is associated with high histaminergic, noradrenergic, serotonergic and cholinergic tones. The activity of these structures likely establishes the transient network conditions for hippocampal SWR-related processing to occur (Freund et al., 1990; Yavich et al., 2005; Varga et al., 2009; Gomperts et al., 2015; McNamara et al., 2014).

3.1.1 Hippocampal-neocortical interaction during SWR

Our results suggest that, at times of SWR subtype occurrence, patterns of brain-wide activation change. These changes, heralded by the extent of BOLD up-regulation and down-regulation, suggest that SWR subtypes may be functionally distinct. Furthermore, SWR subtypes may themselves be associated with differentiated brain-wide dynamical events. Brain-wide activations are likely very selective in order to support processing of distinct mnemonic representations (Hoffman and McNaughton, 2002; Ciocchi et al., 2015), and may also reflect modulations of the 'strength' of hippocampal-cortical communication. In line with this hypothesis, the 'snippets' of activity typically replayed by hippocampus (exerted previously during theta activity) are temporally coordinated with those occurring in the neocortex (Euston et al., 2007). Indeed, for a recently-acquired memory, neocortical reactivation follows that of hippocampus, suggesting hippocampus drives the off-line reactivation process (Euston et al., 2007; Wierzynski et al., 2009). Recent experimental evidence supports this view, as hippocampal SWR episodes sometimes co-occur with cortical neural events with similar dynamics (Khodagholy et al., 2017). These episodes were found to occur in neocortical associative areas (PFC, PPC and midline cortices), but not in primary sensory areas. Ripple-associated hippocampal-cortical interactions were enhanced during sleep following learning, suggesting that ripples in both hippocampus and neocortex support off-line memory consolidation (Khodagholy et al. (2017), similarly, see Wilber et al. (2017)).

The hippocampal-cortical temporal relationship may be 'plastic', as neocortical reactivation can pass from lagging hippocampal reactivation, to leading it in well-trained animals (see Place et al. (2016)). This shift in 'causal-direction' is consistent with memory trace retrieval. Thus, although speculative, it is likely –as hinted by our data– that non-classical SWR subtypes may be: first, more likely to be encountered during periods of waking; and second, some SWR signatures may be associated with retrieval of memories, rather than off-line consolidation *per se*. This possibility is in agreement with recent experimental data, where SWR complexes were clustered into distinct classes on the basis of their associated MUA (Karimi et al., 2017). Interestingly, in this study, distinct patterns of cortical activation were associated with the occurrence of different SWR classes. Cortical activation tended to either lead, lag or be coincident with the peak of SWR activity. These results suggest that the differentiated relationship between hippocampal and cortical activities might reflect the degree of consolidation of distinct putative memory traces (Karimi et al., 2017). While this possibility was not systematically explored in our study (Ramirez-Villegas et al., 2015), there are many ways in which this scenario becomes plausible, resulting in great computational benefits to memory operations in the hippocampus and neocortex.

According to the two-stage memory model, memory constructs are stored temporally in the hippocampus, subsequently becoming independent of it. The hippocampal-neocortical interaction may provide the system with the ability to express ‘virtual’ learning trials, that is, the spontaneous reactivation of acquired memories. During this process, hippocampal ensembles may provide linking patterns to weakly stored patterns (‘weakly interacting’ modules) in neocortex (see Schwindel et al. (2016)). Thus, the possibility remains that reactivation is partly instantiated by the neocortex (Cowansage et al., 2014; Lesburgueres et al., 2011), possibly shifting to a leading role as consolidation progresses (see also Teyler and DiScenna (1986); Teyler and Rudy (2007)). In this scenario, hippocampal activity can be controlled through interactions with neocortex, which in turn can be subsequently controlled back by hippocampus in line with retrieval and/or consolidation operations.

In line with the foregoing, in a recent work, Rothschild et al. (2016) recorded neuronal activity from the auditory cortex and hippocampus during a sound-guided task, together with periods of sleep. Sleep-related activation in auditory cortex neurons was found to precede and predict –to a certain extent– the hippocampal single-cell activity at times of SWR. Conversely, hippocampal firing patterns during SWR predicted subsequent auditory cortex single-cell activity. The authors demonstrated that auditory-cue delivery during sleep biased the activity of auditory cortex, and this activity predicted subsequent hippocampal single-cell activity. In addition, during post-learning epochs, higher SWR rates were recorded following a ‘target’ sound, as compared with other task-unrelated sounds, indicating that the ‘target’ sound became behaviourally relevant, and its presentation was associated with increased incidence of SWR.

The previous findings are seemingly at odds with evidence reporting learning deficits in rodents upon medial septum inactivation. In this study, neither the structure of replay, nor SWR themselves were affected by this manipulation. This suggests that, rather than experience-related consolidation, SWR-replay reflects formed hippocampal ensembles (Wang et al., 2016). Nonetheless, SWR enhancement is expected upon medial septum silencing, as theta-like inhibition and pacemaking to the hippocampus is eliminated by this manipulation, releasing the network and promoting LIA. It follows that SWR episodes occur during periods of LIA, necessary for the CA3 network to generate transient synchronous bursting (Ylinen et al., 1995; Vandecasteele et al., 2014). Furthermore, the fact that SWR-replay was observed without apparent impact on task performance suggests that indeed the SWR mechanism may be unrelated to retrieval, which is somewhat contrary to the hypothesis estabished by Rothschild et al. (2016). However, inactivation of the medial septum also implies that spatial coding mechanisms are affected, which may explain both performance deficits and SWR-replay ineffectiveness. Thus, SWR may act more as a ‘modulator’ rather than a ‘mediator’ of activity (Leonard and Hoffman, 2016). Another possibility is that SWR-replay is necessary for memories in the process of being formed, rather than early-consolidated or stabilised ones (Kovacs et al., 2016; van de Ven et al., 2016).

Finally, both the computational and behavioural roles of SWR subtypes remain to be addressed in future research, and large-network effects (probing neuromodulation, neocortical activation and feedback to hippocampus, and control of the brainstem-hippocampus synchronisation pathway) remain to be demonstrated using more direct methods. The possibility remains that the collection of SWR events endow hippocampal microcircuits (and related neocortical and subcortical ones) with distinct modes of selective processing and routing of information across multiple scales (Ramirez-Villegas et al., 2015).

3.2 Frequency-dependent synaptic and spiking components elaborate the LFP signature of *in vivo* hippocampal SWR complexes

In the second paper of this dissertation, we identified several network mechanisms associated with hippocampal SWR complexes by a series of modelling experiments together with *in vivo* recordings from the macaque hippocampus. These mechanisms contribute to transient oscillatory regimes spanning the whole LFP spectrum, and reflect local CA1 strata- and CA3 subfield-specific activities. Our main conclusions and observations are in line with recent evidence regarding SWR dynamics, where the model was found to account for an unparalleled number of observations from *in vivo* studies (Buzsaki et al., 1992; Csicsvari et al., 2000; Stark et al., 2014; English et al., 2014; Hulse et al., 2016; Carr et al., 2012; Sullivan et al., 2011; Gan et al., 2017) (see Ramirez-Villegas et al. (2017b)).

In summary, our results provide major insights into SWR in three main directions. First, the neural phenomena underlying SWR episodes has been extensively studied (reviewed in Buzsaki (2015)), yet, there seems to be no agreement in regard to its underlying neuronal mechanisms. Our results suggest that low-frequency sharp waves and gamma, in addition to high-frequency ripple and supra-ripple components, constitute the basic frequency-specific LFP dynamic assets underlying physiological SWR activity. These network-related activities account for the coordinated activities of the upstream CA3 assemblies, and local interactions between pyramidal neurons and interneurons in CA1, respectively (Carr et al., 2012; Gillespie et al., 2016; Buzsaki et al., 1992; Csicsvari et al., 1999; Gan et al., 2017).

Second, in line with the foregoing, our findings reveal the basis for analysing the relationship between neuronal activity at meso- and microscopic scales, instrumental to better understand the underpinnings of hippocampal LFP, at the time of occurrence of any neural event. Such an approach relies on filtering the LFP signals into several frequency bands of interest, and will be useful to study network properties such as E/I balance on the basis of LFP, without resorting to single unit activity, or activities that could only be recorded in intracellular preparations (English et al., 2014; Gan et al., 2017; Mizunuma et al., 2014; Hulse et al., 2016; Maier et al., 2011).

Third, we generate a number of predictions regarding the synaptic interactions necessary for the emergence of physiological SWR activity. In particular, we predict that recurrent synaptic inhibition via perisomatic interactions onto both CA1 interneurons and CA1 pyramidal neurons (in agreement with Stark et al. (2014)), but not synaptic excitation of CA1 pyramidal neurons onto CA1 interneurons, is critical for SWR emergence. However, we postulate that synaptic excitation may be instrumental for the inhibitory control of the circuit, and therefore, may have a strong role in selecting specific assemblies that participate in single ripples. This finding holds wide implications for the neuronal mechanisms that establish the spike sequences associated with SWR. For instance, synaptic excitation may partly determine the off-line replay of behaviourally-relevant spatial exploration trajectories in rodents (Lee and Wilson, 2002), which is thought to be critical for spatial memory consolidation (Girardeau et al., 2009; van de Ven et al., 2016), and might be at play during retrieval of memories associated with visual scenes as suggested by experiments with primates (Leonard and Hoffman, 2016).

In a recent study, using simultaneous intracellular and extracellular recordings from the CA1 subfield of rodents, Gan et al. (2017) addressed the question whether temporally modulated excitation or inhibition underlies SWR complexes. Their observations agree with the general notion that SWR are a high conductance state (English et al., 2014). Yet, inhibition dominates over excitation by several-fold in peak conductance ratio, that is, the inhibition conductance gain is more elevated than that of excitation during SWR occurrence. While discharges of both pyramidal cell and interneuron populations are locked to the ripple oscillation (Buzsaki et al., 1992; Ylinen et al., 1995), only the coordinated IPSC –but not EPSC– were phase-locked to individual ripple cycles (Gan et al., 2017). Finally, using optogenetic techniques, Gan et al. (2017) discovered that a major contribution to the SWR phenomenon is provided by PV+ cells, on the basis of changes in the events' properties such as duration and number of ripple cycles per SWR, in addition to perturbed IPSC and IPSC-to-ripple locking properties. The results of this study are in agreement with our modelling results (Ramirez-Villegas et al., 2017b). However, these results also counter mechanistic models of SWR established in a number of experimental and theoretical investigations (Nakashiba et al., 2009; Maier et al., 2011; Draguhn et al., 1998; Memmesheimer, 2010; Hulse et al., 2016).

The discrepancies with existing mechanistic models of SWR episodes are summarised in the following remarks. First, phasic inhibition, but not excitation, is positively correlated with SWR amplitude (Gan et al., 2017). It is worth mentioning that the EPSC recorded in the study of Gan et al. (2017) are the EPSC generated due to incoming CA3 bursting into CA1 assemblies (hence, dEPSC, following the notation we use in Ramirez-Villegas et al. (2017b)). In the same study, it remains ambiguous whether the authors selected the wide-band SWR amplitude or the ripple (as stated in numerous sections of their paper, in relation to their Figure 2). However, one can say that SW amplitude and peri-ripple LFP power are correlated (see recent findings reported by Ramirez-Villegas et al. (2015); Patel et al. (2013)), and thus, IPSC may be more correlated to these two than EPSC. However, the lack of correlation between EPSC and SWR remains striking, because the sum of EPSC due to synaptic inputs impinging onto CA1 apical dendrites (SR) is represented by the sharp wave at the LFP level (see Mizunuma et al. (2014)).

Second, the work of Stark et al. (2014) indicates that both excitation and inhibition play critical roles in the generation of SWR complexes. Indeed, abolishing the inhibitory activity is related with the emergence of non-physiological high-frequency epileptiform discharges (Stark et al., 2014; Karlocai et al., 2014), whereas SWR cannot be induced on the basis of inhibition enhancement (Stark et al. (2014), but see Schlingloff et al. (2014); Ellender et al. (2010)). Our results are in agreement with these possibilities, as selective suppression of synaptic inhibition was largely associated with epileptiform-like events (I-E synapse suppression), and ripple abolishment (I-I synapses suppression). In particular, selective suppression of I-to-E cell synapses within CA1 prompts the entire pyramidal cell population to spike in a very synchronous manner (which is somewhat equivalent to optogenetic silencing of interneurons as performed in Stark et al. (2014)). It follows that ripples cannot be induced by driving only interneurons to spike (Stark et al., 2014), even when interneurons themselves are released from synaptic inhibition (Ramirez-Villegas et al., 2017b). These observations remain conflicting with mechanistic models in which ripples are coordinated via E-E synapses in CA1 (Hulse et al., 2016; Maier et al., 2011; Memmesheimer, 2010; Jahnke et al., 2015). The lack of excitatory collaterals in the CA1 subfield anatomy seems also at odds with the previous models (see Bezaire and Soltesz (2013) for the transverse axis, but see Yang et al. (2014) for the septo-temporal axis). Furthermore, as we do not consider the influence of axo-axonal electrical coupling between pyramidal cells, these are not critical for the emergence of SWR in our model (Draguhn et al., 1998; Traub and Bibbig, 2000) (see also an experimental consideration about these models in Buzsaki (2015)).

Third, another line of evidence is provided by the work of Maier et al. (2011), where the authors found ripple-locked PSC. However, contrary to Gan et al. (2017) and our results, on the basis of their intrinsic properties and intracellular GABAergic transmission blockade, these currents were determined to be excitatory. At the same time, however, our model predicts that EPSC (relied by CA3 input) are predictive of low-frequency spectral power (up to the slow gamma frequencies), whereas IPSC selectively capture both ripple and supra-ripple spectral power (Ramirez-Villegas et al., 2017b). As mentioned in the introduction of this dissertation, the equivalence between *in vivo* and *in vitro* SWR is difficult to establish (Buzsaki, 2015). In a similar vein, if ripples are coordinated via EPSC, there are three possible ways to explain the results of Maier et al. (2011): first, on the basis of the existence of E-E synapses within CA1 in the transverse axis; second, on the basis of ripple coordination relied by CA3 inputs; and third, on the basis of E-to-I excitatory interactions within CA1. The first possibility is at odds with existent anatomical evidence indicating that E-E synapses in the transverse axis of CA1 are scarce (Andersen et al., 2006; Bezaire and Soltesz, 2013). Furthermore, all the existing *in vivo* experimental evidence suggests that ripples are generated *de novo* within CA1, rather than being relayed by CA3 assemblies (Sullivan et al., 2011; Carr et al., 2012; Gillespie et al., 2016). Finally, our results argue against the third possibility, as we predict that E-I synapses are not critical for the emergence of SWR complexes (Racz et al., 2009). Furthermore, since interneurons are more scarce than pyramidal neurons (in our model following a 1:10 ratio, after Andersen et al. (2006)), the overall contribution of somatic EPSC to the ripple may be rather limited as compared to that of somatic IPSC as suggested by our results (Ramirez-Villegas et al., 2017b). Nonetheless, SWR episodes may be modulated by E-E synaptic connections along the septo-temporal axis of the hippocampus (which might be in line with the findings of Patel et al. (2013)). The contribution of CA1 collaterals across this long axis (Yang et al., 2014) to the SWR phenomenon has not been elucidated yet, and therefore, needs to be addressed in future experimental and theoretical work.

In addition to the aforementioned, further experimental work and extended computational models are needed to address the contribution of other interneuron types to the SWR phenomenon (Klausberger et al., 2003), and whether some specific contributions to the SWR-LFP signature originate from interneuron subtypes other than the PV+ basket cells considered in our model (see Varga et al. (2014, 2012)). Concordantly, our computational model predicts that dendritic inhibition may underlie the observed post-SWR hyperpolarisation observed in extracellular recordings (Varga et al., 2014; English et al., 2014; Ramirez-Villegas et al., 2015; Leonard et al., 2015). Yet, this component seems to be correlated with higher ripple frequency (Ramirez-Villegas et al., 2015) in SWR where higher dendritic inhibition drive has been suggested to occur (Varga et al., 2014). In line with these observations, when including dendritic inhibition in our model, we observed that the magnitude of dendritic IPSC was markedly correlated with the LFP post-ripple hyperpolarisation (Ramirez-Villegas et al., 2017b). The specific mechanisms of these inhibitory synapses within the CA1 network and their influence to SWR episodes should be extensively addressed in future investigations.

3.3 Systems and synaptic memory consolidation: when hippocampus, thalamus and brainstem unite?

In the third paper of this dissertation, we investigated large-scale interactions occurring between pontine neural circuits, the thalamus (LGN) and hippocampus at times when physiological PGO wave activity occurs. Through clustering techniques, we identified two distinct types of PGO waves on the basis of their associated MUA profiles and their electrical LFP signatures. These two LFP patterns are in close correspondence with that of classical findings (Datta et al., 1992; Morrison and Pompeiano, 1966; Quatrochi and Hobson, 1999; Denlinger et al., 1988), where SWS-related PGO waves are known to come mostly in isolation (as 'singlets'), whereas REM-related ones are predominantly 'clustered', displaying bouts of several waves. The neurophysiological mechanisms underlying this phenomenon remain vastly unknown. Yet, we have advanced in establishing their possible computational roles. Our results indicate that the two types of PGO waves have differentiated impacts over downstream forebrain targets. These relationships, together with their associated opposite neuronal population responses are a strong suggestion of distinct brainstem-thalamic and brain-wide neuronal mechanisms that may be instrumental for off-line memory processing.

PGO waves are widespread phenomena in the mammalian brain (Datta, 1997). The differentiated physiological nature of singlet and clustered PGO waves was first suggested by early studies (Datta et al., 1992; Morrison and Pompeiano, 1966). According to these studies, PGO-wave singlets are independent of eye movements, whereas clustered PGO waves are associated with eye movement bursts (REM) (Morrison and Pompeiano, 1966). In the work of Morrison and Pompeiano (1966) (confirmed by the experiments of Perenin et al. (1972)) inactivation of vestibular nuclei abolished bursts of REM and type II PGO wave activity, while facilitating type I PGO wave activity with consequent reduction of paradoxical sleep periods (Morrison and Pompeiano, 1966). Pharmacological manipulations of PGO-generating circuits by carbachol enhanced the activity of cholinergic and PGO burst cells. This evidence indicates that REM sleep and associated (typically) clustered PGO activity occur in a state of endogenous release of acetylcholine (Datta et al., 1992). The fact that carbachol injections enhanced signs of REM sleep at the 'expense' of the time spent in SWS (Datta et al., 1992), has led to the hypothesis that these sleep states may be 'antagonistic' or even 'competing'. In line with this hypothesis, we discovered that SWS-related PGO waves are related to transient, significant decreases in neuronal population activity in the ponto-thalamic network, whereas REM-related ones are associated with the opposite effect (Ramirez-Villegas et al., 2017a). Thus, 'clustered' (type II) PGO waves may be related with activation of *bona fide* cholinergic mechanisms, active during naturalistic paradoxical sleep. In contrast, 'singlet' (type I) PGO waves may be associated with brainstem activities characteristic of SWS, where other population-level mechanisms may be at play (Torterolo et al., 2011).

It is worth noting that the terms 'singlet' and 'clustered' PGO waves are used here after the adopted convention of classical studies. As a matter of fact, a minority of REM-sleep PGO waves are singlets as well (Steriade et al., 1990b; Datta et al., 1992). However, although qualitatively similar to SWS PGO waves, these REM-sleep PGO singlets are associated with increase of pontine neuronal population activities (Steriade et al., 1990b). Moreover, most isolated or pairs of PGO waves during paradoxical sleep are highly variable in amplitude, whereas SWS PGO waves seem to fit better a profile of large-amplitude biphasic waves (Bowker, 1985). These differences –together with the difficulties related to establishing ground-truth sleep states in our data– have prompted us to rather use the MUA as a marker for PGO-wave identity, rather than the 'oscillatoriness' of the peri-event LFP signals (Ramirez-Villegas et al., 2017a). Thus, as supported by our data, one may safely conclude that SWS-PGO waves usually come as events displaying a single biphasic pattern, whereas REM-PGO waves in their majority occur as clusters of variable number of consecutive waves (Datta et al., 1992; Callaway et al., 1987).

In Ramirez-Villegas et al. (2017a), we studied PGO waves and their relationship with potentials occurring in forebrain areas such as the hippocampus. As discussed throughout this dissertation, the hippocampus has been markedly related to offline memory consolidation. Furthermore, it is believed that memory processes are partly modulated by the occurrence of hippocampal SWR during SWS. One question that has received (by far) scarcer attention in the literature is whether REM-related activities are necessary for such off-line consolidation processes. In the literature, the term *systems consolidation* is associated with broadcasting of information stored temporally in hippocampus to assemblies where it will be stored in the long-term (in the neocortex) (Battaglia et al., 2011; Carr et al., 2011; van de Ven et al., 2016; Girardeau et al., 2009; Nakashiba et al., 2009). On the basis of our findings, this might be just part of the story. One of the key findings of the third paper of this dissertation is that SWS-PGO waves co-occur with hippocampal SWR complexes, whereas REM-PGO waves co-occur with bouts of hippocampal theta-like oscillations. Potentials corresponding to PGO waves seem to be widespread across several brain domains including the basolateral amygdala, cingulate gyrus, sensory motor cortex (Calvo and Fernandez-Guardiola, 1984), and ventral and dorsal hippocampus (Calvo and Fernandez-Guardiola, 1984; Hobson, 1965). The computational role of these potentials is also critically related to memory consolidation (Mavanji and Datta, 2003; Mavanji et al., 2004; Datta et al., 2004). Crucially, it is likely that REM-related enhancement of theta oscillations is also involved in off-line memory processes, which may include strengthening of representations after SWS-related re-distribution or *systems consolidation*.

In line with these hypotheses, in a recent study, Boyce et al. (2016), using optogenetic techniques, selectively silenced medial septum GABAergic neurons during paradoxical sleep in rodents reducing significantly the power of hippocampal theta oscillations. Strikingly, optogenetic silencing of MS GABAergic neurons during REM periods was sufficient to erase subsequent novel-object place recognition and impaired fear contextual memory formation. These results indicate that REM sleep-related phenomena, specifically the MS GABAergic input to hippocampus is critical for memory consolidation. Notably, the results of Boyce et al. (2016) are in line with evidence reviewed earlier in this dissertation on the behavioural role of PGO-like episodes in rodents (Mavanji and Datta, 2003; Mavanji et al., 2004). In a similar vein, Siwek et al. (2014) recorded from neurons in the rodent subcoeruleus nucleus (SubCD) during both sleep and wake after fear conditioning training. As mentioned previously in this dissertation, the SubCD is known to be the generator of P-waves in rodents (Datta, 2006). Damage to the SubCD was sufficient to impair consolidation of fear conditioning memory, suggesting that the SubCD may be an important memory-promoting locus (Siwek et al., 2014).

Although highly speculative, it is possible that starting in the brainstem there is a chain of events that promotes off-line synaptic memory consolidation. P-waves generated within the brainstem may propagate through the ascending brainstem-hippocampal pathway influencing the activity of several nuclei, finally reaching the MS-DB and the hippocampal formation. Experimental evidence indicates that frequency and amplitude of hippocampal theta are correlated with the emergence of PGO-like potentials in the brainstem of rodents (Karashima et al., 2002, 2001, 2004). If selective elimination of P-waves or, alternatively, interruption of this propagation mechanism causes the observed learning deficits, PGO-related theta enhancement may be necessary for memory formation. The observed behavioural effect –although corresponding to distinct types of manipulations– would be likely analogous in both situations (Siwek et al., 2014; Boyce et al., 2016). This notion further agrees with experimental evidence showing that activation of the brainstem P-wave generator prevents REM deprivation-related learning impairments in rodents (Datta et al., 2004). In particular, rats trained in an avoidance task received either saline or carbachol microinjections in the SubCD. Learning deficits were prominent in animals that received saline and were selectively REM-sleep deprived; but neither rats that received SubCD carbachol nor rats that were allowed to sleep naturally presented learning impairments (Datta et al., 2004).

Our results also suggest that PGO-hippocampal theta coordination occurs in the form of ‘neural events’ in primates. That is, in the form of highly transient increases of hippocampal low-frequency LFP power (Ramirez-Villegas et al., 2017a). Previous studies in human and non-human primates do confirm that hippocampal theta has analogous electrical properties to that found in our anaesthetised model (Jutras et al., 2013; Leonard et al., 2015; Aghajan et al., 2016; Vass et al., 2016). On top of these characteristic observations, we showed that hippocampal theta-like episodes in macaques may co-occur with PGO waves (Ramirez-Villegas et al., 2017a), as also observed in classical studies during episodes of paradoxical sleep (Datta, 1997; Callaway et al., 1987). Furthermore, our results suggest a tight relationship between these hippocampal theta episodes and SWR, as they were found significantly correlated in the time scale of a few seconds. This effect was also captured by our NET-BLP analysis, where hippocampal theta events were associated with a power increase of high-frequency oscillations, which was then countered by a sharp power drop at the time of the event occurrence. These transitions may signal the transition between SWS-like and REM-like states in our experimental data (Ramirez-Villegas et al., 2017a).

These observations suggest that PGO and hippocampal events are tightly intertwined, and may be signatures of possibly competing, yet complementary mechanisms of off-line memory-related processing. This view is supported by experimental evidence relating episodes of REM sleep with shaping the excitability of hippocampal ensembles in subsequent periods of SWS (Grosmark et al., 2012). Grosmark et al. (2012) found a progressive increase in discharge rates of neuronal populations throughout the development of SWS. This increase in discharge rates were accompanied by increases in SWR-related discharge toward the end of a given SWS episode. This SWR-related synchrony may be related to the emergence of brainstem type I PGO waves, occurring in synchrony with SWR complexes as we found in our work (Ramirez-Villegas et al., 2017a). Concordantly, PGO-SWR coupling occurred for 'classical' SWR, rather than other SWR subtypes studied previously (Ramirez-Villegas et al., 2015). Furthermore, upon state transition, the increase in excitation of neuronal populations is countered by a cell discharge rate deceleration, heralding the initiation of REM sleep (Grosmark et al., 2012). This activity drop (deceleration) at the onset of paradoxical sleep is similar to the transition to theta activity in primates found in our study, where analogously, firing rates were observed to decelerate at the time of event occurrence. Strikingly, if hippocampal theta power is correlated with subsequent SWS neuronal synchrony, it is possible that type II PGO-related mechanisms –associated with this enhancement– subsequently determine hippocampal SWS-associated activity. Thus, it is possible that the brainstem not only coordinates SWS and REM changes, but also determines the population excitability of a given state on the basis of the previous state.

Overall, our results suggest that a repertoire of neuronal events may coordinate and modulate distinct neural networks in a sleep stage-dependent manner. This coordination may serve several purposes including off-line memory consolidation. Mechanistically speaking these processes may be largely distributed in time, and prompted by characteristic interactions between brainstem and forebrain structures. Finally, our data, and the discussions presented in this subsection of the dissertation bridge the results of SWS-related research (specifically, on SWR complexes and their putative role in memory formation), with those of REM-related investigations (specifically, on PGO waves and brainstem activity-dependent memory formation). The presented event typologies in this work will permit the characterisation of neuronal events in natural sleep preparations in human and non-human primates in order to establish the functional role of each event subtype. Thus, our approach suggests distinct venues for new experiments, and as to generate new system-level mechanistic insights on pathological brain activity (for example, see Kerber et al. (2014); Wang et al. (2013); Karlocai et al. (2014); Saito et al. (2014)).

3.3.1 Systems and synaptic memory consolidation: from molecules to systems-level neural events

In this subsection of the General Discussion, I discuss the connection between molecular and systems-level mechanisms of memory consolidation. Whereas this link can be established on the basis of the current literature in Molecular and Systems Neuroscience, it is not always straightforward to determine how –from the experimental data presented in this work– I point to the specific microscopic sub-events that may be associated with distinct types of neural events, together with the functions they achieve.

In line with the early suggestion of Ramon y Cajal (Ramon y Cajal, 1984), synaptic connections between neurons can be modified by learning, and anatomical modifications likely subserve memory storage. Early experimental evidence suggests that the Aplysia sensory neurons exposed to habituation retract some of their pre-synaptic terminals, whereas neurons exposed to sensitisation display increased number of pre-synaptic terminals. Subsequently, motor neurons can remodel to accommodate the extra sensory input (Bailey and Chen, 1988). The underpinnings of this elementary form of memory depend on the activation of mechanisms that lead to the release of serotonin onto the sensory neuron, which in turn increases the concentration of cyclic adenosine monophosphate (cAMP) in the sensory cell. The cAMP signals the neuron to release more glutamate, thus temporally strengthening its connection to the motor neuron (Brunelli et al., 1976) (also known as *activity-dependent enhancement of synaptic facilitation*; for an extensive review the reader is referred to Kandel et al. (2014)).

Generally speaking, long-term memory, but not short-term memory formation, requires the synthesis of new proteins (Lisman et al., 2012). However, proteins themselves are ‘unstable’, as they come and go in shorter time scales than memory. Thus, in order for long-term changes to occur, serotonin stimulation needs to be repeated several times, so that the increase of cAMP persists, causing cAMP-dependent proteins (for instance, the protein kinase-A, PKA; and mitogen-activated protein kinase, MAPK) to move to the nucleus of the cell where they activate the gene expression mechanisms required for long-term memory (Martin et al., 1997).

The mechanisms of synaptic facilitation involve PKA and postsynaptic Ca^{2+}. In particular, the intermediate phase of consolidation begins with PKA in the presynaptic neuron mediating an increase of glutamate release. This increase acts in the molecular machinery of the postsynaptic cell and induces the initial steps of synaptic growth: activation of glutamate receptors cause release of calcium stored in the postsynaptic cell; then, calcium leads to the insertion of new copies of α-amino-3-hydroxy-5-methyl-4-isoxazolepropionic acid (AMPA) receptors in the postsynaptic cell (Kandel et al., 2014).

In the hippocampus, as well as in other brain areas, long-term potentiation (LTP) of synaptic transmission is widely considered a model of activity-dependent synaptic plasticity (Kandel et al., 2014). Standard protocols for inducing LTP in the hippocampus come in two main types: high-frequency stimulation (~100 Hz) in which several pulses are delivered (Bliss and Lømo, 1973); and low-frequency stimulation close to the theta-range delivered in the form of bursts (~200 Hz) (Staubli and Lynch, 1987). LTP induction has been documented in different regions of the hippocampus. For instance, in CA1, 100 Hz stimulation induces a form of LTP dependent on N-methyl-D-aspartate (NMDA) receptor activation. NMDA receptors require depolarization of the postsynaptic membrane as well as simultaneous release of glutamate from the pre-synaptic terminal. Thus, NMDA receptors are functional only at active synapses. Moreover, activated NMDA receptors produce postsynaptic Ca^{2+} influx required to produce LTP, and Ca^{2+} can activate several molecular signaling pathways (including PKA, MAPK and Ca^{2+} /calmodulin-dependent protein kinase II, CaMKII) implicated in LTP and its stabilization (e.g. see Lisman et al. (2012)). Indeed, deletion of the CaMKII gene in mice triggers severe deficits in hippocampus-dependent forms of learning (Grant et al., 1992), whereas selective elimination of NMDA receptors only in the DG leads to a loss of performant-path LTP associated with pattern discriminability (McHugh et al., 2007).

Recent investigations have sought to identify the source of LTP associated with REM sleep, which may depend on several specific anatomical pathways. One predominant view is that such source of sleep-dependent and LTP-inducing stimulation comes from the structures of the brainstem. That is, the structures that generate and transfer potentials to forebrain structures via multiple anatomical tracts. Such activity is often associated with the occurrence of PGO waves, whose transmission has been suggested to be purely glutamatergic, while at the same time modulated by endogenous release of ACh (Datta, 2006; Steriade et al., 1990a,b). PGO-wave generating cells discharge high-frequency spike bursts (>500 Hz) on a background of tonically increased firing rates (30-40 Hz) during the states of pre-REM and REM sleep (Datta and Hobson, 1994). In addition, activation of PGO-generating cells can be attained by cholinergic agonists, such as carbachol, prompting changes in the characteristics of PGO waves and increasing the number of bursts in a single PGO wave (Datta et al., 1992). The effects of cholinergic stimulation-induced potentiation last for seven to ten days (Datta, 2012).

REM-PGO waves co-occur with hippocampal theta and neocortical activation (Datta, 1997), in line with increased cholinergic tone, and seem to contribute to the enhancement of theta activity in both hippocampus and amygdala (Karashima et al., 2005, 2010). This evidence seems to correspond with the fact that ‘information-specific’ input to the hippocampus during theta states comes from thalamic and thalamo-cortical systems, where PGO have been observed in cats and non-human primates (Steriade et al., 1990b; Vuillon-Cacciuttolo et al., 1978). Concordantly, as punctuated earlier, interruption of the theta-generating pathway in hippocampus during REM sleep correlates with impaired memory retention (Boyce et al., 2016), and also selective inactivation of pontine PGO-wave generating cells has been paired to similar memory impairments (Mavanji and Datta, 2003; Mavanji et al., 2004).

On top of the previous experimental evidence, the findings reported in the third paper of this dissertation suggest that PGO waves not only co-occur with increases of theta-like activity in the hippocampus (by analogy to Karashima et al. (2004, 2005)), but also co-occur –strikingly in almost equal proportion– with hippocampal SWR complexes (Ramirez-Villegas et al., 2017a). Because of their time-frequency characteristics, SWR episodes are good candidates to generate plasticity in target structures (in line with brief >100 Hz stimulation-inducing LTP) (Bliss and Lømo, 1973). Correlative evidence suggests that SWR are important for early-consolidating memories related to a novel environment, but not maintenance of memories associated with familiar enclosures (Kovacs et al., 2016; van de Ven et al., 2016). Moreover, SWR-associated 'memory replay' is thought to establish reinstatement of distinct movement- and immobility-associated experiences in rodents (Yu et al., 2017; Rothschild et al., 2016).

On the basis of the previous evidence, a PGO-associated input may transiently increase hippocampal excitability, prompting the emergence of SWR complexes at a higher rate (in line with Grosmark et al. (2012)). This prediction is also in line with the sharp increase in pontine MUA likely signaling an increase in glutamatergic neurotransmission at the time of PGO-wave occurrence. I speculate that such activity would release glutamate in the hippocampus (and activate NMDA receptors), which could lead to release of calcium stored in postsynaptic cells; then, calcium could lead to the insertion of new copies of AMPA receptors in the postsynaptic cells. A similar process may occur in the neocortex, where sleep spindles, together with ripples in associative cortices, may also bear a role in triggering or modulating consolidation (Latchoumane et al., 2017; Khodagholy et al., 2017). The question as to whether PGO activity controls directly or indirectly the behaviourally-relevant 'replay' contents during hippocampal and neocortical ripples remains to be addressed in future investigations.

As mentioned before, activation of cAMP, Ca^{2+}, PKA, and cAMP response element binding (CREB) proteins are involved in the induction of gene expressions that lead to long-term memory formation. Several studies support the idea that activation of the PGO-wave generator (P-wave generator in rodents) is correlated with increases in CREB, brain-derived nerve growth factor (BDNF) and activity-regulated cytoskeletal protein (Arc) in the hippocampus and amygdala. In particular, during the post-training three-hour sleep recording session, PGO wave density correlated with the time-dependent levels of CREB, BDNF and Arc in hippocampus, amygdala, and neocortex (specifically frontal and occipital) (Ulloor and Datta, 2005). Furthermore, selective inactivation of the

PGO-generating cells of the rat abolished avoidance training-induced expression of the aforementioned proteins in the hippocampus and amygdala. Notably, the levels of the proteins fell below baseline control conditions in which the animals were not exposed to the conditioning stimulus (Ulloor and Datta, 2005). Concordantly, whereas suppression of PGO-generating cells decreased trial-induced mRNA expression in hippocampus and amygdala, cholinergic stimulation increased its expression, together with that of Arc and BDNF (Datta et al., 2008), and test-trial performance (Datta et al., 2004). It is worth noting that task acquisition was not affected by these experimental manipulations, whose main effect was only on memory retrieval (Datta et al., 2004, 2008). These results suggest that memory processing-specific gene activation through protein synthesis may be initiated or mediated by PGO wave-generating sites. In a similar vein, these data suggest that the PGO wave generator may signal the primary mechanism for REM sleep-dependent memory consolidation processes.

3.4 Limitations of this study

Throughout this dissertation I have demonstrated several properties associated with neural events, that constitute the physiological activity of the hippocampus and other centres in the intact brain. Our findings reveal how the activity of these brain structures is linked to naturalistic off-line states, when sleep-dependent memory consolidation processes likely happen. The function of these off-line states is thought to be recuperative and regulatory of the brain activity (Tononi and Cirelli, 2014). These regulation processes are instantiated by changes in brain-wide neuronal excitability, ascribed to the activity of several systems located in the brainstem that control the global state of the brain. As mentioned in all papers of this dissertation (Ramirez-Villegas et al., 2017a), all experimental data used in this project were obtained from anaesthetised preparations. Although many reviewers have seen this fact as one of the major ‘drawbacks’ of our investigations (Logothetis et al., 2012; Ramirez-Villegas et al., 2015), none of the results reported here are the product of fluctuations in the level of anaesthetics in our experiments. This concern likely originates from a misconception on the effects of several types of anaesthesia in the rodent brain. The anaesthesia protocols used in our laboratory are based on opioids (Logothetis et al., 2012). More specifically, remifentanil, a μ-receptor agonist, has been shown to have no effect on acetylcholine release in the pontine cholinergic cell bodies and cholinergic terminals of cats (Mortazavi et al., 1999). In the same study, however, opioid-dependent reduction of acetylcholine levels suggested a μ-receptor modulation that was accompanied with REM-sleep disruption by other anaesthetic drugs. Importantly, this and similar anaesthesia protocols have shown to only have mild effects on BOLD fMRI signals, making them comparable to that of alert monkeys (Goense and Logothetis, 2008; Logothetis et al., 1999, 2001, 2012). Nonetheless, in our experiments we were unable to identify tonic signatures corresponding to different sleep stages, as we had no access to ground-truth markers from naturalistic SWS or REM episodes. These matters remain to be resolved in future research endeavours.

Although our first results provide specific evidence for the existence of diverse SWR complexes, it is likely that the detected events are only a fraction of all SWR episodes. For instance, SWR are known to occur along the whole septo-temporal axis of the rodent hippocampus (posterior-anterior direction in primates) (Patel et al., 2013). In addition, our event detection protocol included several stringent refinements –in line with the requests of anonymous reviewers– that limited the sample of events analysed. The most obvious effect of event selection is the increase of false-negative rate, as a consequence of an increase in sensitivity. However, this did not prevented us from detecting distinct SWR subclasses. Yet, we were unable to ascertain that 'discarded' neural events were fundamentally different in their correlates to the selected *'bona fide'* ones. Beyond these practical issues, in future investigations, there is need to develop principled methodologies to detect and classify events without relying on statistical threshold-based selection (Besserve et al., 2017).

Finally, in the second paper of this dissertation, we devised a simple, multi-compartmental model of the CA3-CA1 network. The approach of other investigations, however, relies on morphologically-realistic models (Schomburg et al., 2012; Linden et al., 2011; Reimann et al., 2013) of several neurons within a neuronal network subfield. One of the questions that emerges is as to whether such biophysical and anatomical levels of detail are necessary to observe and understand the basic phenomena underlying neural events in the LFP, while keeping high biological accountability. There is no definitive answer to this question in the literature, because under certain conditions the differences seem negligible (see Reimann et al. (2013), but see Taxidis et al. (2012); Mazzoni et al. (2015); Ramirez-Villegas et al. (2017b)). Nonetheless, the networks considered in this work can undoubtedly generate distinct dynamics on the basis of their active components, i.e. the neurons. A myriad of interneuron subtypes have been identified in the hippocampus (Klausberger and Somogyi, 2008). These interneurons are known to display specific relationships to field activities such as theta and SWR complexes (Klausberger et al., 2003; Somogyi et al., 2014). In our model, minimalistically, we only included basket cells, as peri-somatic inhibition seems critical for the emergence of physiological SWR activity according to recent experimental evidence (Schlingloff et al., 2014; Stark et al., 2014; Varga et al., 2014; Gan et al., 2017). Furthermore, we only included CA3 and CA1, while not considering the contribution of CA2, which is also involved in triggering SWR according to a recent study (Oliva et al., 2016). It is thus possible that some of the observed SWR neuronal correlates change upon including other types of interneuronal activity and other hippocampal subfields, which could also help to better understand other aspects of our experimental observations (Ramirez-Villegas et al., 2015; Varga et al., 2014).

3.5 Outlook

In this dissertation I have addressed four main scientific questions, encompassed within four specific aims (see Section 1.9). I have advanced our understanding on the extent of the variations in meso- and macroscopic brain dynamics that can be observed during the occurrence of SWR complexes in the hippocampus of primates. In classical studies, these episodes were thought to be homogeneous in their temporo-spectral characteristics. However, not only there are physiological variations of such episodes, but also distinct SWR subtypes may be associated with functionally distinct wide-brain dynamical events. Our findings are in agreement with intact-brain experimental preparations in rodents (Oliva et al., 2016; Karimi et al., 2017; Yu et al., 2017). In addition, our results offer several venues for new experiments in alert and naturally sleeping animals.

For instance, future experiments could establish the relationship between the neural correlates of reactivation of remote and new experiences. This question is both beyond the scope of this dissertation and the primate data available in our laboratory. However, as mentioned in this General Discussion section, the relationship between hippocampal and neocortical activations may change as memories become stable and independent of the hippocampus, where SWR episodes may be useful for modulating the retrieval of information. The possibility that neocortical associative and high-order areas (such as PFC, parietal cortex, ACC, PCC etc) are activated before a SWR event occurs was not explored systematically in our investigation. However, it is reasonable to postulate that neocortex exerts control over hippocampal ensembles and vice versa, in line with processes of retrieval and consolidation, respectively (Rothschild et al., 2016; Place et al., 2016; Karimi et al., 2017). In addition, these processes may be related to SWR episodes with distinct temporo-spectral profiles as I showed in the first paper of this thesis (Ramirez-Villegas et al., 2015), possibly occurring across distinct hippocampal SWR activation pathways (Oliva et al., 2016).

Furthermore, the second paper adds on the current understanding of hippocampal SWR episodes across microscopic and mesoscopic scales. The model introduced in this paper, currently stands as the only one in the literature to account for almost all *in vivo* experimental observations in regard to the dynamics of SWR complexes. Furthermore, from a more general perspective, many studies use LFP as a population measure in order to investigate specific brain circuit functions. However, the LFP is a signal with a high degree of intrinsic ambiguity, reflecting both excitation and inhibition due to complex network interactions (peri-synaptic activities), active cellular processes, amongst other types of neuronal interactions (Buzsaki et al., 2012). Understanding the content of the peri-SWR LFP is challenging and currently there is no agreement on the nature of these contents amongst hippocampologists. We have provided new insights on how SWR complexes are constructed from a neuronal population perspective, and have put forward evidence on the relationship across multiple scales of neuronal processing associated with SWR episodes.

In a similar vein, we identified several network mechanisms associated with SWR episodes. We predict that signals of distinct biophysical nature conflating at a specific time can be associated with specific effectors within a neuronal ensemble. In this sense, in agreement with previous studies (Carr et al., 2012; Ylinen et al., 1995), we found that CA3 populations coordinate their activity with CA1 populations by low-frequency activities. The electrical signature of ripples –in light of our results– is brought about by the concerted action of IPSC, which were largely associated with variations in ripple power and the time course of individual ripples. Furthermore, interneuronal firing is concerted at high-frequencies beyond the ripple itself, a range for which we have coined the term 'supra-ripple'. In light of the current literature, the last two results are more or less as controversial than the SWR-gamma (see Gan et al. (2017), but see Maier et al. (2011)). Moreover, we discovered that the excitation exerted by CA1 pyramidal cells onto CA1 interneurons (resulting in somatic EPSC) may be a specific mechanism that controls the feedback inhibitory loop during SWR and ultimately may determine the specific pyramidal cell assemblies that participate during individual episodes. These findings indicate that somatic EPSC –possibly through specific synaptic links between pyramidal neurons and interneurons (Dupret et al., 2013)– may be necessary for precise behaviourally-relevant SWR memory replay.

Finally, the third paper of this thesis advanced our understanding of PGO waves, and their relationship to neural events in the hippocampus. In this work, we made two striking findings. First, PGO waves manifest themselves in distinct types, which are associated with antagonistic MUA profiles, and distinct peri-event pontine/LGN LFP profiles. Second, PGO waves are differentially associated with hippocampal episodes, namely, SWS-PGO waves (type I) co-occur with SWR complexes, whereas REM-PGO waves (type II) are associated with episodes of hippocampal theta-like oscillations. Investigating the differentiated brain-wide activities associated with PGO waves remains beyond the scope of this thesis. Addressing this question requires analysing the concurrent LFP-fMRI recordings, which will be done in a future investigation. The PGO wave-triggered BOLD maps will likely provide further insights into the dynamics of these episodes and how they are related to each other from the viewpoint of the global metabolic activity of neocortical and subcortical domains. It is also fundamental to further investigate the brainstem-hippocampus synchronisation pathway with direct methods. The interaction between brainstem and hippocampus could result from the coordinated action of many pathways including the MS-DB, SuM nucleus (Vertes, 1992), and several thalamic nuclei (Lara-Vásquez et al., 2016) that are known to express PGO potentials in cats (Datta, 1997). The fact that both SWS-related and REM-related neuronal events are markedly associated with memory formation leads to the question whether the coupling of hippocampal activity with PGO waves, that we address in the third paper, is indeed critical for such purpose, and whether it relates to behaviourally-relevant SWR activity occurring in several association cortices (Khodagholy et al., 2017). Addressing this question will require extensive multi-structure recordings, possibly with direct electrical or optogenetic stimulation/suppression of circuits in unrestrained, behaving animals. I predict that the transition to REM sleep –when SWS-PGO waves co-occur with hippocampal SWR– marks a period of enhanced memory signaling to neocortical ensembles, facilitating consolidation of memories. In addition, plastic changes in brain-wide networks could also occur during REM-related theta in hippocampus, associated with brainstem-generated PGO wave activity.

3.6 Conclusion

This dissertation provides insights on system-level charactersitics and mechanisms of neural events: recurring episodes present in the LFP of several brain structures that signal cooperative microcircuit activities and are thought to underlie cognitive processes such as memory reactivation, transfer, consolidation and retrieval. Altogether, the results of the three studies reported and discussed here provide evidence for local circuit operations in the hippocampus, and the pontine-thalamic-hippocampal system during off-line states, that likely support mnemonic processing. On the basis of both the theoretical and experimental approaches of this thesis, I have demonstrated how neuronal activity is coordinated across multiple spatio-temporal scales and how these scales –at which information is processed– relate to each other. Importantly, the global activity of the brain at times when neural events occur is likely associated with the transfer of information between brain subsystems that are anatomically and functionally connected. Our findings point to specific neural mechanisms of these processes together with novel brain-wide system-level relationships, as an important step toward generating a system-level understanding of the hippocampal system and its interaction with the rest of the brain. Thus, our data and computational modelling hold wide implications for existing mechanistic models of SWR and PGO waves, for future large-scale computational models, together with new experimental directions. In addition, our methodological approaches and results –specifically in the context of the primate animal model– will be instrumental toward understanding brain activity in humans under pathological conditions.

References

Aghajan, Z. M., Schuette, P., Fields, T., Tran, M., Siddiqui, S., Hasulak, N., Tcheng, T. K., Eliashiv, D., Stern, J., Fried, I., and Suthana, N. (2016). Theta oscillations in the human medial temporal lobe during real world ambulatory movement. *bioRxiv*, 1:1–21.

Ahlsen, G. (1984). Brain stem neurons with differential projections to functional subregions of the dorsal lateral geniculate complex in the cat. *Neuroscience*, 12:817–838.

Ajmone-Marsan, C. (1965). Electrical activity of the brain: Slow waves and neuronal activity. *Isr. J. Med. Sci.*, 1:104.

Amaral, D. G., Dolorfo, C., and Alvarez-Royo, P. (1991). Organization of CA1 projections to the subiculum: a PHA-L analysis in the rat. *Hippocampus*, 1:415–435.

Amaral, D. G. and Witter, M. P. (1989). The three-dimensional organization of the hippocampal formation: A review of anatomical data. *Neuroscience*, 31:571–591.

Anastassiou, C. A., Perin, R., Markram, H., and Koch, C. (2011). Ephaptic coupling of cortical neurons. *Nat. Neurosci.*, 14:217–223.

Andersen, P., Morris, R., Amaral, D., Bliss, T., and O'Keefe, J. (2006). *The hippocampus book*. Oxford University Press, New York, USA.

Aston-Jones, G. and Cohen, J. D. (2005). An integrative theory of locus coeruleus-norepinephrine function: Adaptive gain and optimal performance. *Annu. Rev. Neurosci.*, 28:403–450.

Atherton, L. A., Dupret, D., and Mellor, J. R. (2015). Memory trace replay: the shaping of memory consolidation by neuromodulation. *Trends Neurosci.*, 38:560–570.

Axmacher, N., Elger, C. E., and Fell, J. (2008). Ripples in the medial temporal lobe are relevant for human memory consolidation. *Brain*, 131:1806–1817.

Azevedo, F. A. C., Carvalho, L. R., Grinberg, L. T., Farfel, J. M., Ferreti, R. E., Jacob, F. W., Lent, R., and Herculano-Houzel, S. (2009). Equal numbers of neuronal and nonneuronal cells make the human brain an isometrically scaled-up primate brain. *J. Comp. Neurol.*, 513:532–541.

Bailey, C. H. and Chen, M. (1988). Long-term memory in aplysia modulates the total number of varicosities of single identified sensory neurons. *Proc. Natl. Acad. Sci. U. S. A.*, 85:2373–2377.

Battaglia, F. P., Benchenane, K., Sirota, A., Pennartz, C. M., and Wiener, S. I. (2011). The hippocampus: hub of brain network communication for memory. *Trends in Cognitive Science*, 15:310–318.

Bennet, T. L. (1970). Hippocampal EEG correlates of behavior. *Electroencephalogr. Clin. Neurophysiol.*, 28:17–23.

Bennet, T. L., Nunn-Hebert, P., and Moss, D. E. (1973). Hippocampal theta activity and the attention component of discrimination learning. *Behav. Biol.*, 8:173–181.

Berridge, C. W. and Waterhouse, B. D. (2003). The locus coeruleus-noradrenergic system: modulation of behavioral state and state-dependent cognitive processes. *Brain Res. Rev.*, 42:33–84.

Bezaire, M. J. and Soltesz, I. (2013). Quantitative assessment of CA1 local circuits: Knowledge base for interneuron-pyramidal cell connectivity. *Hippocampus*, 23:751–785.

Bland, B. H. and Oddie, S. D. (1998). Anatomical, electrophysiological and pharmacological studies of ascending brainstem hippocampal synchronizing pathways. *Neuroscience and Behavioral Reviews*, 22:259–273.

Bland, B. H., Oddie, S. D., Colom, L. V., and Vertes, R. P. (1994). The extrinsic modulation of medial septal cell discharges by the ascending brainstem hippocampal synchronizing pathway. *Hippocampus*, 4:649–660.

Bland, S. K. and Bland, B. H. (1986). Medial septal modulation of hippocampal theta cell discharges. *Brain Res.*, 375:102–116.

Bliss, T. V. P. and Lømo, T. (1973). Long-lasting potentiation of synaptic transmission in the dentate area of the anaesthetized rabbit following stimulation of the perforant path. *J. Physiol. (Lond.)*, 232:331–356.

Bowker, R. M. (1985). Variability in the characteristics of pontogeniculooccipital spikes during paradoxical sleep. *Exp. Neurol.*, 87:212–224.

Boyce, R., Glasgow, S. D., Williams, S., and Adamantidis, A. (2016). Causal evidence for the role of REM sleep theta rhythm in contextual memory consolidation. *Science*, 352:812–816.

Bragin, A., Jando, G., Nadasdy, Z., Hetke, J., Wise, K., and Buzsaki, G. (1995). Gamma frequency (40-100 Hz) patterns in the hippocampus of the behaving rat. *J. Neurosci.*, 15:47–60.

Brooks, D. C. (1968). Localization and characteristics of the cortical waves associated with eye movements in the cat. *Exp. Neurol.*, 22:603–613.

Brooks, D. C. and Bizzi, E. (1963). Brain stem electrical activity during deep sleep. *Arch. Ital. Biol.*, 101:648–665.

Brunel, N. and Wang, X. J. (2003). What determines the frequency of fast network oscillations with irregular neural discharges? i. synaptic dynamics and excitation-inhibition balance. *J. Neurophysiol.*, 90:415–430.

Brunelli, M., Castellucci, V., and Kandel, E. (1976). Synaptic facilitation and behavioral sensitization in aplysia: possible role of serotonin and cyclic AMP. *Science*, 194:1178–1181.

Buchwald, J. S., Hala, E. S., and Schramm, S. (1965). A comparison of multi-unit activity eeg activity recorded from the same brain site in chronic cats during behavioral conditioning. *Nature*, 205:1012–1014.

Buckmaster, P. S., Wenze, H. J., Kunkel, D. D., and Schwartzkroin, P. A. (1996). Axon arbors and synaptic connections of hippocampal mossy cells in the rat in vivo. *J. Comp. Neurol.*, 366:271–292.

Buzsaki, G. (1986). Hippocampal sharp waves: Their origin and significance. *Brain Res.*, 398:242–252.

Buzsaki, G. (2002). Theta oscillations in the hippocampus. *Neuron*, 33:325–340.

Buzsaki, G. (2015). Hippocampal sharp wave-ripple: a cognitive biomarker for episodic memory and planning. *Hippocampus*, 25:1073–1188.

Buzsaki, G., Anastassiou, C. A., and Koch, C. (2012). The origin of extracellular fields and currents - EEG, ECoG, LFP and spikes. *Nat. Rev. Neurosci.*, 13:407–420.

Buzsaki, G., Horvath, Z., Urioste, R., Hetke, J., and Wise, K. (1992). High-frequency network oscillation in the hippocampus. *Science*, 256:1025–1027.

Buzsaki, G. and Wang, X. J. (2012). Mechanisms of gamma oscillations. *Annu. Rev. Neurosci.*, 35:203–225.

Callaway, C. W., Lydic, R., Baghdoyan, H. A., and Hobson, J. A. (1987). Pontogeniculooccipital waves: Spontaneous visual system activity during rapid eye movement sleep. *Cell. Mol. Neurobiol.*, 7:105–149.

Calvo, J. M. and Fernandez-Guardiola, A. (1984). Phasic activity of the basolateral amygdala, cingulate gyrus and hippocampus during REM sleep in the cat. *Sleep*, 7:202–210.

Carr, M. F., Jadhav, S. P., and Frank, L. M. (2011). Hippocampal replay in the awake state: a potential substrate for memory consolidation and retrieval. *Nat. Neurosci.*, 14:147–153.

Carr, M. F., Karlsson, M. P., and Frank, L. M. (2012). Transient slow gamma synchrony underlies hippocampal memory replay. *Neuron*, 75:700–713.

Cheng, S. and Frank, L. M. (2008). New experiences enhance coordinated neural activity in the hippocampus. *Neuron*, 57:303–313.

Chiovini, B., Turi, G. F., Katona, G., Kaszas, A., Palfi, D., Maak, P., Szalay, G., Szabo, M. F., Szabo, G., Szadai, Z., Kali, S., and Rozsa, B. (2014). Dendritic spikes induce ripples in parvalbumin interneurons during hippocampal sharp waves. *Neuron*, 82:908–924.

Chrobak, J. J. and Buzsaki, G. (1994). Selective activation of deep layer (V-VI) retrohippocampal cortical neurons during hippocampal sharp waves in the behaving rat. *J. Neurosci.*, 14:6160–6170.

Chrobak, J. J. and Buzsaki, G. (1996). High-frequency oscillations in the output networks of the hippocampal-entorhinal axis of the freely behaving rat. *J. Neurosci.*, 16:3056–3066.

Ciocchi, S., Passecker, J., Malagon-Vina, H., Mikus, N., and Klausberger, T. (2015). Selective information routing by ventral hippocampal CA1 projection neurons. *Science*, 348:560–563.

Cohen, B. and Feldman, M. (1968). Relationship to electrical activity in the pontine reticular formation and lateral geniculate body to rapid eye movements. *J. Neurophysiol.*, 31:807–817.

Colgin, L. L. (2016). Rhythms of the hippocampal network. *Nat. Rev. Neurosci.*, 17:239–249.

Colgin, L. L., Denninger, T., Fyhn, M., Hafting, T., Bonnevie, T., Jensen, O., Moser, M. B., and Moser, E. I. (2009). Frequency of gamma oscillations routes flow of information in the hippocampus. *Nature*, 462:353–357.

Cowansage, K. K., Shuman, T., Dillingham, B. C., Chang, A., Golshani, P., and Mayford, M. (2014). Direct reactivation of a coherent neocortical memory of context. *Neuron*, 84:432–441.

Csicsvari, J., Hirase, H., Czurko, A., Mamiya, A., and Buzsaki, G. (1999). Oscillatory coupling of hippocampal pyramidal cells and interneurons in the behaving rat. *J. Neurosci.*, 19:274–287.

Csicsvari, J., Hirase, H., Mamiya, A., and Buzsaki, G. (2000). Ensemble patterns of hippocampal CA3-CA1 neurons during sharp wave-associated population events. *Neuron*, 28:585–594.

Csicsvari, J., Jamieson, B., Wise, K., and Buzsaki, G. (2003). Mechanisms of gamma oscillations in the hippocampus of the behaving rat. *Neuron*, 37:311–322.

Datta, S. (1995). Neuronal activity in the peribrachial area: Relationship to behavioral state control. *Neurosci. Biobehav. Rev.*, 19:67–84.

Datta, S. (1997). Cellular basis of pontine ponto-geniculo occipital wave generation and modulation. *Cell. Mol. Neurobiol.*, 17:341–365.

Datta, S. (2000). Avoidance task training potentiates phasic pontine-wave density in the rat: A mechanism for sleep-dependent plasticity. *J. Neurosci.*, 20:8607–8613.

Datta, S. (2006). Activation of phasic pontine-wave generator: A mechanism for sleep-dependent memory processing. *Sleep and Biological Rhythms*, 4:16–26.

Datta, S. (2012). *Sleep and Brain Activity*, chapter 7, pages 147–164. Elsevier Inc.

Datta, S., Calvo, J. M., Quatrochi, J. J., and Hobson, J. A. (1992). Cholinergic microstimulation of the peribrachial nucleus in the cat. I. immediate and prolonged increases in ponto-geniculo-occipital waves. *Arch. Ital. Biol.*, 130:263–284.

Datta, S. and Hobson, J. A. (1994). Neuronal activity in the caudo-lateral peribrachial pons: Relationship to PGO waves and rapid eye movements. *J. Neurophysiol.*, 71:95–109.

Datta, S. and Hobson, J. A. (1995). Suppression of ponto-geniculo-occipital waves by neurotoxic lesions of pontine caudo-lateral peribrachial cells. *Neuroscience*, 67:703–712.

Datta, S., Li, G., and Auerbach, S. (2008). Activation of phasic pontine-wave generator in the rat: a mechanism for expression of plasticity-related genes and proteins in the dorsal hippocampus and amygdala. *Eur. J. Neurosci.*, 27:1876–1892.

Datta, S. and MacLean, R. R. (2007). Neurobiological mechanisms for the regulation of mammalian sleep-wake behavior: Reinterpretation of historical evidence and inclusion of contemporary cellular and molecular evidence. *Neurosci. Biobehav. Rev.*, 31:775–824.

Datta, S., Mavanji, V., Ulloor, J., and Patterson, E. H. (2004). Activation of phasic pontine-wave generator prevents rapid eye movement sleep deprivation-induced learning impairment in the rat: A mechanism for sleep-dependent plasticity. *J. Neurosci.*, 24:1416–1427.

Datta, S., Pare, D., Oakson, G., and Steriade, M. (1989). Thalamic-projecting neurons in brainstem cholinergic nuclei increases their firing rates one minute in advance of EEG desynchronization associated with REM sleep. *Soc. Neurosci. Abstr.*, 15:452.

Datta, S. and Siwek, D. F. (1997). Excitation of the brain stem pedunculopontine tegmentum cholinergic cells induces wakefulness and REM sleep. *J. Neurophysiol.*, 77:2975–2988.

Debanne, D., Guérineau, N. C., H., G. B., and Thompson, S. M. (1995). Physiology and pharmacology of unitary synaptic connections between pairs of cells in areas CA3 and CA1 of rat hippocampal slice cultures. *J. Neurophysiol.*, 73:1282–1294.

Denlinger, S. L., Patarca, R., and Hobson, J. A. (1988). Differential enhancement of rapid eye movement sleep signs in the cat: a comparison of microinjection of the cholinergic agonist carbachol and the P-adrenergic antagonist propranolol on pontogeniculo-occipital wave clusters. *Brain Res.*, 473:116–126.

Dermietzel, R. and Spray, D. C. (1993). Gap junctions in the brain: Where, what type, how many and why? *Trends Neurosci.*, 16:186–192.

Deshmukh, S. S. and Knierim, J. J. (2011). Representation of non-spatial and spatial information in the lateral entorhinal cortex. *Frontiers in Behavioral Neuroscience*, 5:1–33.

Deshmukh, S. S. and Knierim, J. J. (2013). Influence of local objects on hippocampal representations: landmark vectors and memory. *Hippocampus*, 23:253–267.

Diba, K. and Buzsaki, G. (2007). Forward and reverse hippocampal place-cell sequences during ripples. *Nat. Neurosci.*, 10:1241–1242.

Draguhn, A., Traub, R. D., D., S., and Jefferys, J. G. (1998). Electrical coupling underlies high-frequency oscillations in the hippocampus in vitro. *Nature*, 394:189–192.

Dupret, D., O'Neill, J., and Csicsvari, J. (2013). Dynamic reconfiguration of hippocampal interneuron circuits during spatial learning. *Neuron*, 78:166–180.

Dupret, D., OŠNeill, J., Pleydell-Bouverie, B., and Csicsvari, J. (2010). The reorganization and reactivation of hippocampal maps predict spatial memory performance. *Nat. Neurosci.*, 13:995–1002.

Ego-Stengel, V. and Wilson, M. A. (2010). Disruption of ripple-associated hippocampal activity during rest impairs spatial learning in the rat. *Hippocampus*, 20:1–10.

Eichenbaum, H. (2014). Time cells in the hippocampus: a new dimension for mapping memories. *Nat. Rev. Neurosci.*, 15:732–744.

Eichenbaum, H., Kuperstein, M., Fagan, A., and Nagode, J. (1987). Cue-sampling and goal-approach correlates of hippocampal unit activity in rats performing an odor-discrimination task. *J. Neurosci.*, 7:716–732.

Einevoll, G. T., Kayser, C., Logothetis, N. K., and Panzeri, S. (2013). Modelling and analysis of local field potentials for studying the function of cortical circuits. *Nat. Rev. Neurosci.*, 14:770–785.

Ekstrom, A. D., Caplan, J. B., Ho, E., Shattuck, K., Fried, I., and Kahana, M. J. (2005). Human hippocampal theta activity during virtual navigation. *Hippocampus*, 15:881–889.

Ellender, T. J., Nissen, W., Colgin, L. L., Mann, E. O., and Paulsen, O. (2010). Priming of hippocampal population bursts by individual perisomatic targeting interneurons. *J. Neurosci.*, 30:5979–5991.

English, D. F., Peyrache, A., Stark, E., Roux, L., Vallentin, D., Long, M. A., and Buzsaki, G. (2014). Excitation and inhibition compete to control spiking during hippocampal ripples: Intracellular study in behaving mice. *J. Neurosci.*, 34:16509–16517.

Eschenko, O. and Sara, S. J. (2008). Learning-dependent, transient increase of activity in noradrenergic neurons of locus coeruleus during slow wave sleep in the rat: Brain stem-cortex interplay for memory consolidation? *Cereb. Cortex*, 18:2596–2603.

Euston, D. R., Tatsuno, M., and McNaughton, B. L. (2007). Fast-forward playback of recent memory sequences in prefrontal cortex during sleep. *Science*, 318:1147–1150.

Farber, J., Marks, G. A., and Roffwarg, H. P. (1980). Rapid eye movement sleep PGO-type waves are present in the dorsal pons of the albino rat. *Science*, 209:615–617.

Feldman, M. and Cohen, B. (1968). Electrical activity in the lateral geniculate body of the alert monkey associated with eye movements. *J. Neurophysiol.*, 31:455–466.

Fernandez-Mendoza, J., Lozano, B., Seijo, F., Santamarta-Liebana, E., Ramos-Platon, M. J., Vela-Bueno, A., and Fernandez-Ruiz, A.ndez-Gonzalez, F. (2009). Evidence of subthalamic PGO-like waves during REM sleep in humans: A deep brain polysomnographic study. *Sleep*, 32:1117–1126.

Fernandez-Ruiz, A., Oliva, A., Nagy, G. A., Maurer, A. P., Berenyi, A., and Buzsaki, G. (2017). Entorhinal-CA3 dual-input control of spike timing in the hippocampus by theta-gamma coupling. *Neuron*, 93:1213–1226.

Foster, D. J. and Wilson, M. A. (2006). Reverse replay of behavioural sequences in hippocampal place cells during the awake state. *Nature*, 440:680–683.

Freund, T. F. and Buzsaki, G. (1996). Interneurons of the hippocampus. *Hippocampus*, 6:347–470.

Freund, T. F., Gulyas, A. I., Acsády, L., Goercs, T., and Toth, K. (1990). Serotonergic control of the hippocampus via local inhibitory interneurons. *Proc. Natl. Acad. Sci. U. S. A.*, 87:8501–8505.

Fyhn, M., Molden, S., Witter, M. P., Moser, E. I., and Moser, M. B. (2004). Spatial representation in the entorhinal cortex. *Science*, 305:1258–1264.

Gan, J., Weng, S., Pernia-Andrade, A. J., Csicsvari, J., and Jonas, P. (2017). Phase-locked inhibition, but not excitation, underlies hippocampal ripple oscillations in awake mice in vivo. *Neuron*, 93:308–314.

Gasbarri, A., Verney, B., Innocenzia, R., Campanaa, E., and Pacittia, C. (1994). Mesolimbic dopaminergic-neurons innervating the hippocampal formation in the rat: a combined retrograde tracing and immunohistochemical study. *Brain Res.*, 668:71–79.

Gerrard, J. L., Burke, S. N., McNaughton, B. L., and Barnes, C. A. (2008). Sequence reactivation in the hippocampus is impaired in aged rats. *J. Neurosci.*, 28:7883–7890.

Gervasoni, D., Peyron, C., Rampon, C., Barbagli, B., Chouvet, G., Urbain, N., Fort, P., and Luppi, P. H. (2000). Role and origin of the gabaergic innervation of dorsal raphe serotonergic neurons. *J. Neurosci.*, 20:4217–4225.

Gigg, J. (2006). Constraints on hippocampal processing imposed by the connectivity between CA1, subiculum and subicular targets. *Behav. Brain Res.*, 174:265–271.

Gillespie, A. K., Jones, E. A., Lin, Y. H., Karlsson, M. P., Kay, K., Yoon, S. Y., Tong, L. M., Nova, P., Carr, J. S., Frank, L. M., and Huang, Y. (2016). Apolipoprotein E4 causes age-dependent disruption of slow gamma oscillations during hippocampal sharp-wave ripples. *Neuron*, 90:740–751.

Giocomo, L. M., Stensola, T., Bonnevie, T., Van Cauter, T., Moser, M. B., and Moser, E. I. (2014). Topography of head direction cells in medial entorhinal cortex. *Curr. Biol.*, 24:252–262.

Girardeau, G., Benchenane, K., Wiener, S. I., Buzsaki, G., and Zugaro, M. (2009). Selective suppression of hippocampal ripples impairs spatial memory. *Nat. Neurosci.*, 12:1222–1223.

Goense, J. and Logothetis, N. K. (2008). Neurophysiology of the BOLD fMRI signal in awake monkeys. *Neuron*, 18:631–640.

Gomperts, S. N., Kloosterman, F., and Wilson, M. A. (2015). VTA neurons coordinate with the hippocampal reactivation of spatial experience. *eLife*, 4:e05360.

Grant, S., O'Dell, T., Karl, K., Stein, P., Soriano, P., and Kandel, E. (1992). Impaired long-term potentiation, spatial learning, and hippocampal development in fyn mutant mice. *Science*, 258:1903–1910.

Gray, J. A. and Ball, C. G. (1970). Frequency-specific relation between hippocampal theta rhythm behavior and amobarbital action. *Science*, 168:1246–1248.

Green, J. D. and Arduini, A. A. (1954). Hippocampal electrical activity in arousal. *J. Neurophysiol.*, 17:533Ű557.

Grosmark, A. D., Mizuseki, K., Pastalkova, E., Diba, K., and Buzsaki, G. (2012). REM sleep reorganizes hippocampal excitability. *Neuron*, 75:1001–1007.

Gupta, A. S., van der Meer, M. A., Touretzky, D. S., and Redish, A. D. (2010). Hippocampal replay is not a simple function of experience. *Neuron*, 65:695–705.

Gustafsson, B. (1984). Afterpotentials and transduction properties in different types of central neurones. *Arch. Ital. Biol.*, 122:17–30.

Hafting, T., Fyhn, M., Molden, S., Moser, M. B., and Moser, E. I. (2005). Microstructure of a spatial map in the entorhinal cortex. *Nature*, 436:801–806.

Hahn, T. G., McFarland, J. M., Berberich, S., Sakmann, B., and Mehta, M. R. (2012). Spontaneous persistent activity in entorhinal cortex modulates cortico-hippocampal interaction in vivo. *Nat. Neurosci.*, 15:1531–1538.

Hajos, N., Karlocai, M. R., Nemeth, B., Ulbert, I., Monyer, H., Szabo, G., Erdelyi, F., Freund, T., and Gulyas, A. (2013). Input-output features of anatomically identified ca3 neurons during hippocampal sharp wave/ripple oscillation in vitro. *J. Neurosci.*, 33:11677–11691.

Hallanger, A. E., Levey, A. I., Lee, H. J., Rye, D. B., and Wainer, B. H. (1987). The origins of cholinergic and other subcortical afferents to the thalamus in the rat. *J. Comp. Neurol.*, 262:105–124.

Harada, Y. and Takahashi, T. (1983). The calcium component of the action potential in spinal motoneurones of the rat. *J. Physiol. (Lond.)*, 335:89–100.

Henke, P. (1990). Hippocampal pathway to the amygdala and stress ulcer development. *Brain Res. Bull.*, 25:691–695.

Hitti, F. L. and Siegelbaum, S. A. (2014). The hippocampal ca2 region is essential for social memory. *Nature*, 508:88–92.

Hobson, J. A. (1964). L'activite electrique phasique du cortex et du thalmus au cours du sommeil desynchronise chez le chat. *C. R. Soc. Biol.*, 158:2131–2135.

Hobson, J. A. (1965). The effects of chronic brain.stem lesions on cortical and muscular activity during sleep and waking in the cat. *Electroencephalogr. Clin. Neurophysiol.*, 19:41–62.

Hobson, J. A. (2009). REM sleep and dreaming: towards a theory of protoconsciousness. *Nat. Rev. Neurosci.*, 10:803–813.

Hofer, K. T., Kandraks, A., Ulbert, I., Pal, I., Szabo, C., Heja, L., and Wittner, L. (2014). The hippocampal ca3 region can generate two distinct types of sharp wave-ripple complexes, in vitro. *Hippocampus*, 00:1–8.

Hoffman, K. and McNaughton, B. L. (2002). Coordinated reactivation of distributed memory traces in primate neocortex. *Science*, 297:2070–2073.

Hok, V., Lenck-Santini, P. P., Roux, S., Save, E., Muller, R. U., and Poucet, B. (2007). Goal-related activity in hippocampal place cells. *J. Neurosci.*, 27:472–482.

Hu, B., Steriade, M., and Deschenes, M. (1989a). The cellular mechanisms of thalamic ponto-geniculo-occipital (PGO) waves. *Neuroscience*, 3:25–35.

Hu, B., Steriade, M., and Deschenes, M. (1989b). The effects of brainstem peribrachial stimulation on perigeniculate neurons: the blockage of spindle waves. *Neuroscience*, 3:1–12.

Huang, H. P., Wang, S. R., Yao, W., Zhang, C., Zhou, Y., Chen, X. W., Zhang, B., Xiong, W., Wang, L. Y., and Zheng, L. H. (2007). Long latency of evoked quantal transmitter release from somata of locus coeruleus neurons in rat pontine slices. *Proc. Natl. Acad. Sci. U. S. A.*, 104:1401–1406.

Hulse, B. K., Moreaux, L. C., Lubenov, E. V., and Siapas, A. G. (2016). Membrane potential dynamics of CA1 pyramidal neurons during hippocampal ripples in awake mice. *Neuron*, 89:800–813.

Isaacson, L. G., , and Tanaka, D. (1986). Cholinergic and non-cholinergic projections from the canin pontomesencephalic tegmentum (ch5 area) to the caudal intralaminar thalamic nuclei. *Exp. Brain Res.*, 62:179–188.

Ishizuka, N., Weber, J., and Amaral, D. G. (1990). Organization of intrahippocampal projections originating from CA3 pyramidal cells in the rat. *J. Comp. Neurol.*, 295:580–623.

Isomura, Y., Sirota, A., Ozen, S., Montgomery, S., Mizuseki, K., Henze, D. A., and Buzsaki, G. (2006). Integration and segregation of activity in entorhinal-hippocampal subregions by neocortical slow oscillations. *Neuron*, 52:871–882.

Ito, H. T. and Schuman, E. M. (2012). Functional division of hippocampal area CA1 via modulatory gating of entorhinal cortical inputs. *Hippocampus*, 22:372–387.

Jacobs, J., Weidemann, C. T., Miller, J. F., Solway, A., Burke, J. F., Wei, X. X., Suthana, N., Sperling, M. R., Sharan, A. D., Fried, I., and Kahana, M. J. (2013). Direct recordings of grid-like neuronal activity in human spatial navigation. *Nat. Neurosci.*, 16:1188–1190.

Jadhav, S. P., Kemere, C., German, P. W., and Frank, L. M. (2012). Awake hippocampal sharp-wave ripples support spatial memory. *Science*, 336:1454–1458.

Jahnke, S., Timme, M., and Memmesheimer, R. M. (2015). A unified dynamic model for learning, replay, and sharp-wave/ripples. *J. Neurosci.*, 35:16236–16258.

Ji, D. and Wilson, M. A. (2007). Coordinated memory replay in the visual cortex and hippocampus during sleep. *Nat. Neurosci.*, 10:100–107.

Johnson, L., Euston, D. R., M., T., and McNaughton, B. L. (2010). Stored-trace reactivation in rat prefrontal cortex is correlated with down-to-up state fluctuation density. *J. Neurosci.*, 30:2650–2661.

Jouvet, M. (1965). Paradoxical sleep -a study of its nature and mechanisms. *Prog. Brain Res.*, 18:20–62.

Jouvet, M. (1969). Biogenic amines and the states of sleep. *Science*, 163:32–41.

Jouvet, M. and Michel, F. (1959). Correlations electromyographiques du sommeil chez le chat decortique et mesencephalique chronique. *C. R. Seances Soc. Biol. Fil.*, 153:422–425.

Jouvet, M., Michel, F., and Courjon, J. (1959a). Sur la mise en jeu de deux mecaismes a expression electro-encephalographique differente au cours du sommeil physiologique chez le chat. *Comptes Rendus Hebdomadaires des Seances de l'Academie des Sciences*, 248:3043–3045.

Jouvet, M., Michel, F., and Courjon, J. (1959b). Sur un stade d'activite electrique rapide au cours du sommeil physiologique. *C. R. Seances Soc. Biol. Fil.*, 153:1024–1028.

Jutras, M. J., Fries, P., and Buffalo, E. A. (2013). Oscillatory activity in the monkey hippocampus during visual exploration and memory formation. *Proc. Natl. Acad. Sci. U. S. A.*, 110:13144–13149.

Kamondi, A., Acsady, L., Wang, X. J., and Buzsaki, G. (1998). Theta oscillations in somata and dendrites of hippocampal pyramidal cells in vivo: activity dependent phase-precession of action potentials. *Hippocampus*, 8:244–261.

Kanamori, N. (1985). A spindle-like wave in the cat hippocampus: a novel vigilance level-dependent electrical activity. *Brain Res.*, 334:180–182.

Kandel, E. R., Dudai, Y., and Mayford, M. R. (2014). The molecular and systems biology of memory. *Cell*, 157:163–186.

Kang, J., Jiang, L., Goldman, S. A., and Nedergaard, M. (1998). Astrocyte-mediated potentiation of inhibitory synaptic transmission. *Nat. Neurosci.*, 1:683–692.

Karashima, A., Katayama, N., and Nakao, M. (2010). Enhancement of synchronization between hippocampal and amygdala theta waves associated with pontine wave density. *J. Neurophysiol.*, 103:2318–2325.

Karashima, A., Nakamura, K., Horiuchi, M., Nakao, M., Katayama, N., and Yamamoto, M. (2002). Elicited ponto-geniculo-occipital waves by auditory stimuli are synchronized with hippocampal theta-waves. *Psychiatry Clin. Neurosci.*, 56:343–344.

Karashima, A., Nakamura, K., Watanabe, M., Sato, N., Nakao, M., Katayama, N., and Yamamoto, M. (2001). Synchronization between hippocampal theta waves and PGO waves during REM sleep. *Psychiatry Clin. Neurosci.*, 55:189–190.

Karashima, A., Nakao, M., Honda, K., Iwasaki, N., Katayama, N., and Yamamoto, M. (2004). Theta wave amplitude and frequency are differentially correlated with pontine waves and rapid eye movements during rem sleep in rats. *Neurosci. Res.*, 50:283–289.

Karashima, A., Nakao, M., Katayama, N., and Honda, K. (2005). Instantaneous acceleration and amplification of hippocampal theta wave coincident with phasic pontine activities during REM sleep. *Brain Res.*, 1051:50–56.

Karimi, J., Nazari, M., L., M. B., and Mohajerani, M. H. (2017). Spatiotemporal patterns of cortical voltage activity during sharp wave-ripples: Implications for memory consolidation theory. In *47th Annual Meeting of the Society for Neuroscience (Neuroscience 2017), Washington DC, USA*.

Karlocai, M. R., Kohus, Z., Kali, S., Ulbert, I., Szabo, G., Mate, Z., Freund, T. F., and Gulyas, A. (2014). Physiological sharp wave-ripples and interictal events in vitro: What's the difference? *Brain*, 137:463–485.

Kay, K., Sosa, M., Chung, J. E., Karlsson, M. P., Larkin, M. C., and Frank, L. M. (2016). A hippocampal network for spatial coding during immobility and sleep. *Nature*, 531:185–190.

Kerber, K., Duempelmann, M., Schelter, B., Le Van, P., Korinthenberg, R., Schulze-Bonhage, A., and Jacobs, J. (2014). Differentiation of specific ripple patterns helps to identify epileptogenic areas for surgical procedures. *Clin. Neurophysiol.*, 125:1339–1345.

Khodagholy, D., Gelinas, J. N., and Buzsaki, G. (2017). Learning-enhanced coupling between ripple oscillations in association cortices and hippocampus. *Science*, 358:369–372.

Kirk, I. J. and McNaughton, N. (1993). Mapping the differential effects of procaine on the frequency and amplitude of reticularly elicited rhythmical slow activity. *Hippocampus*, 3:517–526.

Kirk, I. J., Oddie, S. D., Konopacki, J., and Bland, B. H. (1996). Evidence for differential control of posterior hypothalamic, supramammillary, and medial mammillary theta-related cellular discharge by ascending and descending pathways. *J. Neurosci.*, 16:5547–5554.

Klausberger, T., J., M. P., Marton, L. F., Roberts, J. D., Cobden, P. M., Buzsaki, G., and Somogyi, P. (2003). Brain-state- and cell-type-specific firing of hippocampal interneurons in vivo. *Nature*, 421:844–848.

Klausberger, T. and Somogyi, P. (2008). Neuronal diversity and temporal dynamics: The unity of hippocampal circuit operations. *Science*, 321:53–57.

Kloosterman, F., van Haeften, T., and Lopes da Silva, F. H. (2004). Two reentrant pathways in the hippocampal-entorhinal system. *Hippocampus*, 14:1026–1039.

Kocsis, B. and Vertes, R. P. (1994). Characterization of neurons in the supramammillary nucleus and mammillary body that discharge rhythmically with the hippocampal theta rhythm in the rat. *J. Neurosci.*, 14:7040–7052.

Kohler, C. (1985). Intrinsic projections of the retrohippocampal region in the rat brain. i. the subicular complex. *J. Comp. Neurol.*, 236:504–522.

Kovacs, K. A., O'Neill, J., Schoenenberger, P., Penttonen, P. M., Ranguel Guerrero, D. K., and Csicsvari, J. (2016). Optogenetically blocking sharp wave ripple events in sleep does not interfere with the formation of stable spatial representation in the CA1 area of the hippocampus. *PLoS ONE*, 11:e0164675.

Kropff, E., Carmichael, J. E., Moser, M. B., and Moser, E. I. (2015). Speed cells in the medial entorhinal cortex. *Nature*, 523:419–424.

Kudrimoti, H. S., Barnes, C. A., and L., M. B. (1999). Reactivation of hippocampal cell assemblies: Effects of behavioral state, experience, and eeg dynamics. *J. Neurosci.*, 19:4090–4101.

Lara-Vásquez, A., Espinosa, N., Durán, E., Stockle, M., and Fuentealba, P. (2016). Midline thalamic neurons are differentially engaged during hippocampus network oscillations. *Scientific Reports*, 6:29807.

Lasztoczi, B. and Klausberger, T. (2014). Layer-specific GABAergic control of distinct gamma oscillations in the CA1 hippocampus. *Neuron*, 81:1126–1139.

Latchoumane, C. F. V., Ngo, H. V. V., Born, J., and Shin, H. S. (2017). Thalamic spindles promote memory formation during sleep through triple phase-locking of cortical, thalamic, and hippocampal rhythms. *Neuron*, 95:424–435.

Lawson, V. and Bland, B. H. (1993). The role of the septo-hippocampal pathway in the regulation of hippocampal field activity and behavior: Analysis by the intraseptal microinfusion of carbachol, atropine and procaine. *Exp. Neurol.*, 120:132–144.

Le Van Quyen, M., Bragin, A., Staba, R., Crepon, B., Wilson, C. L., and Engel, J. J. (2008). Cell type-specific firing during ripple oscillations in the hippocampal formation of humans. *J. Neurosci.*, 28:6104–6110.

Lee, A. K. and Wilson, M. A. (2002). Memory of sequential experience in the hippocampus during slow wave sleep. *Neuron*, 36:1183–1194.

Lee, S. H., Marchionni, I., Bezaire, M., Varga, C., Danielson, N., Lovett-Barron, M., Losonczy, A., and Soltesz, I. (2014). Parvalbumin-positive basket cells differentiate among hippocampal pyramidal cells. *Neuron*, 82:1129–1144.

Leonard, C. S. and Llinas, R. R. (1994). Serotonergic and cholinergic inhibition of mesopontine cholinergic neurons controlling REM sleep: an in vitro electrophysiological study. *Neuroscience*, 59:309–330.

Leonard, T. K. and Hoffman, K. (2016). Sharp-wave ripples in primates are enhanced near remembered visual objects. *Curr. Biol.*, 27:1–6.

Leonard, T. K., Mikkila, J. M., Eskandar, E. N., Gerrard, G. L., Kaping, D., Patel, S. R., Womelsdorf, T., and Hoffman, K. (2015). Sharp wave ripples during visual exploration in the primate hippocampus. *J. Neurosci.*, 35:14771–14782.

Lesburgueres, E., Gobbo, O. L., Alaux-Cantin, S., Hambucken, A., Trifilieff, P., and Bontempi, B. (2011). Early tagging of cortical networks is required for the formation of enduring associative memory. *Science*, 331:924–928.

Lever, C., Burton, S., Jeewajee, A., O'Keefe, J., and Burgess, N. (2009). Boundary vector cells in the subiculum of the hippocampal formation. *J. Neurosci.*, 29:9771–9777.

Li, X. G., Somogyi, P., Ylinen, A., and Buzsaki, G. (1994). The hippocampal CA3 network: an in vivo intracellular labeling study. *J. Comp. Neurol.*, 339:181–208.

Lim, A. S., Lozano, A. M., Moro, E., Hamani, C., Hutchison, W. D., Dostrovsky, J. O., Lang, A. E., Wennberg, R. A., and Murray, B. J. (2007). Characterization of rem-sleep associated ponto-geniculo-occipital waves in the human pons. *Sleep*, 30:823–827.

Linden, H., Tetzlaff, T., Potjans, T. C., Pettersen, K. H., Grun, S., Diesmann, M., and Einevoll, G. T. (2011). Modeling the spatial reach of the lfp. *Neuron*, 72:859–872.

Lisman, J. (2005). The theta/gamma discrete phase code occuring during the hippocampal phase precession may be a more general brain coding scheme. *Hippocampus*, 15:913–922.

Lisman, J., Yasuda, R., and Raghavachari, S. (2012). Mechanisms of CaMKII action in long-term potentiation. *Nat. Rev. Neurosci.*, 13:169–182.

Lisman, J. E. and Idiart, M. A. P. (1995). Storage of 7+/-2 short-term memories in oscillatory subcycles. *Science*, 267:1512–1515.

Llinas, R. R. (1988). The intrinsic electrophysiological properties of mammalian neurons: insights into central nervous system function. *Science*, 242:1654–1664.

Logothetis, N. K. (2015). Neural-event-triggered fMRI of large-scale neural networks. *Curr. Opin. Neurobiol.*, 31:214–222.

Logothetis, N. K., Eschenko, O., Murayama, Y., Augath, M., Steudel, T., Evrard, H. C., Besserve, M., and Oeltermann, A. (2012). Hippocampal-cortical interaction during periods of subcortical silence. *Nature*, 491:547–553.

Logothetis, N. K., Guggenberger, H., Peled, S., and Pauls, J. (1999). Functional imaging of the monkey brain. *Nat. Neurosci.*, 2:555–562.

Logothetis, N. K., Paus, J., Augath, M., Trinath, T., and Oeltermann, A. (2001). Neurophysiological investigation of the basis of the fMRI signal. *Nature*, 412:150–157.

Logothetis, N. K. and Wandell, B. A. (2004). Interpreting the BOLD signal. *Annu. Rev. Physiol.*, 66:735–769.

Lorente de No, R. (1934). Studies on the structure of the cerebral cortex. ii. continuation of the study of the ammonic system. *J. Psychol. Neurol.*, 46:113Ű177.

Macadar, S. W., Chalupa, L. M., and Lindsley, D. B. (1974). Differentiation of brainstem loci which affect hippoocampal and neocortical activity. *Exp. Neurol.*, 43:499–514.

Magloczky, Z., Acsady, L., and Freund, T. F. (1994). Principal cells are the postsynaptic targets of supramammillary afferents in the hippocampus of the rat. *Hippocampus*, 4:322–334.

Maier, N., Nimmrich, V., and Draguhn, A. (2003). Cellular and network mechanisms underlying spontaneous sharp waveŰripple complexes in mouse hippocampal slices. *J. Physiol. (Lond.)*, 550:873–887.

Maier, N., Tejero-Cantero, A., Dorrn, A. L., Winterer, J., Beed, P. S., Morris, G., Kempter, R., Poulet, J. F., Leibold, C., and Schmitz, D. (2011). Coherent phasic excitation during hippocampal ripples. *Neuron*, 72:137–152.

Manns, J. R. and Eichenbaum, H. (2009). A cognitive map for object memory in the hippocampus. *Learn. Mem.*, 16:616–624.

Marks, G. A., Farber, J., and Roffwarg, H. P. (1980a). Metencephalic localization of ponto-geniculooccipital waves in the albino rat. *Exp. Neurol.*, 69:667–677.

Marks, G. A., Farber, J., Rubinstein, M., and Roffwarg, H. P. (1980b). Demonstration of ponto-geniculo-occipital waves in the albino rat. *Exp. Neurol.*, 69:648–655.

Martig, A. K. and Mizumori, S. J. Y. (2011). Ventral tegmental area disruption selectively affects ca1/ca2 but not ca3 place fields during a differential reward working memory task. *Hippocampus*, 21:172–184.

Martin, K. C., Michael, D., Rose, J. C., Barad, M., Casadio, A., Zhu, H., and Kandel, E. R. (1997). MAP kinase translocates into the nucleus of the presynaptic cell and is required for long-term facilitation in aplysia. *Neuron*, 18:899–912.

Mavanji, V. and Datta, S. (2003). Activation of the phasic pontinewave generator enhances improvement of learning performance: a mechanism for sleep-dependent plasticity. *Eur. J. Neurosci.*, 17:359–370.

Mavanji, V., Ulloor, J., Saha, S., and Datta, S. (2004). Neurotoxic lesions of phasic pontine-wave generator cells impair retention of 2-way active avoidance memory. *Sleep*, 27:1282–1292.

Mazzoni, A., Lindén, H., Cuntz, H., Lansner, A., Panzeri, S., and Einevoll, G. T. (2015). Computing the local field potential (lfp) from integrate-and-fire network models. *PLoS Comput. Biol.*, 11:e1004584.

McCarley, R. W., Winkelman, J. W., , and Duffy, F. H. (1983). Human cerebral potentials associated with REM sleep rapid eye movements: links to PGO waves and waking potentials. *Brain Res.*, 274:359–364.

McClelland, J. L., McNaughton, B. L., and O'Reilly, R. C. (1995). Why there are complementary learning systems in the hippocampus and neocortex: insights from the successes and failures of connectionist models of learning and memory. *Psychol. Rev.*, 102:419–457.

McCormick, D. A. and Bal, T. (1997). Sleep and arousal: thalamocortical mechanisms. *Annu. Rev. Neurosci.*, 20:185–215.

McCormick, D. A. and Prince, D. A. (1986). Acetylcholine induces burst firing in thalamic reticular neurones by activating a potassium conductance. *Nature*, 3:402–405.

McCormick, D. A. and Prince, D. A. (1988). Noradrenergic modulation of firing pattern in guinea pig and cat thalamic neurons in vitro. *J. Neurophysiol.*, 59:978–996.

McHugh, T. J., Jones, M. W., Quinn, J. J., Balthasar, N., Coppari, R., Elmquist, J. K., Lowell, B. B., Fanselow, M. S., Wilson, M. A., and Tonegawa, S. (2007). Dentate gyrus NMDA receptors mediate rapid pattern separation in the hippocampal network. *Science*, 317:94–99.

McNamara, C. G., Tejero-Cantero, A., Trouche, S., Campo-Urriza, N., and Dupret, D. (2014). Dopaminergic neurons promote hippocampal reactivation and spatial memory persistence. *Nat. Neurosci.*, 17:1658–1660.

Memmesheimer, R. M. (2010). Quantitative prediction of intermittent high-frequency oscillations in neural networks with supralinear dendritic interactions. *Proc. Natl. Acad. Sci. U. S. A.*, 107:11092–11097.

Miles, R. and Wong, R. K. (1986). Excitatory synaptic interactions between ca3 neurones in the guinea-pig hippocampus. *J. Physiol. (Lond.)*, 373:397–418.

Mizunuma, M., Norimoto, H., Tao, K., Egawa, T., Hanaoka, K., Tetsuya Sakaguchi, T., Hiroyuki Hioki3, Kaneko, T., Yamaguchi, S., Nagano, T., Matsuki, N., and Ikegaya, Y. (2014). Unbalanced excitability underlies offline reactivation of behaviorally activated neurons. *Nat. Neurosci.*, 17:503–505.

Mizuseki, K., Diba, K., Pastalkova, E., and Buzsaki, G. (2011). Hippocampal CA1 pyramidal cells form functionally distinct sublayers. *Nat. Neurosci.*, 14:1174–1181.

Moita, M. A., Rosis, S., Zhou, Y., LeDoux, J. E., and Blair, H. T. (2003). Hippocampal place cells acquire location-specific responses to the conditioned stimulus during auditory fear conditioning. *Neuron*, 37:485–497.

Montgomery, S., Sirota, A., and Buzsaki, G. (2008). Theta and gamma coordination of hippocampal networks during waking and rapid eye movement sleep. *J. Neurosci.*, 28:6731–6741.

Morison, R. S. and Bassett, D. L. (1945). Electrical activity of the thalamus and basal ganglia in decorrticated cats. *J. Neurophysiol.*, 8:309–314.

Morrison, A. R. and Pompeiano, O. (1966). Vestibular influences during sleep. IV. functional relations between the vestibular nuclei and lateral geniculate nucleus during desynchronized sleep. *Arch. Ital. Biol.*, 104:425–458.

Mortazavi, S., Thompson, J., Baghdoyan, H. A., and Lydic, R. (1999). Fentanyl and morphine, but not remifentanil, inhibit acetylcholine release in pontine regions modulating arousal. *Anesthesiology*, 90:1070–1077.

Moser, M. B., Moser, E. I., Forrest, E., Andersen, P., and Morris, R. G. (1995). Spatial learning with a minislab in the dorsal hippocampus. *Proc. Natl. Acad. Sci. U. S. A.*, 92:9697–9701.

Nakashiba, T., Buhl, D., McHugh, T. J., and Tonegawa, S. (2009). Hippocampal CA3 output is crucial for ripple-associated reactivation and consolidation of memory. *Neuron*, 62:781–787.

Nelson, J. P., McCarley, R. W., and Hobson, J. A. (1983). Rem sleep burst neurons, PGO waves, and eye movement information. *J. Neurophysiol.*, 50:784–797.

Nicholson, C. (1973). Theoretical analysis of field potentials in anisotropic ensembles of neuronal elements. BME-20:278–288.

Nicholson, C. and Freeman, J. A. (1975). Theory of current source-density analysis and determination of conductivity tensor for anuran cerebellum. *J. Neurophysiol.*, 38:356–368.

Nicholson, C. and Llinas, R. R. (1971). Field potentials in the alligator cerebellum and theory of their relationship to Purkinje cell dendritic spikes. *J. Neurophysiol.*, 34:209–531.

Nitz, D. and Siegel, J. M. (1997). Gaba release in the locus coeruleus as a function of sleep-wake state. *Neuroscience*, 78:795–801.

Nokia, M., Penttonen, M., and Wikgren, J. (2010). Hippocampal ripplecontingent training accelerates trace eyeblink conditioning and retards extinction in rabbits. *J. Neurosci.*, 30:11486–11492.

Norimoto, H., Matsumoto, N., Miyawaki, T., Matsuki, N., and Y., I. (2013). Subicular activation preceding hippocampal ripples in vitro. *Science Reports*, 3:2696.

Novitskaya, Y., Sara, S. J., Logothetis, N. K., and Eschenko, O. (2016). Ripple-triggered stimulation of the locus coeruleus during post-learning sleep disrupts ripple/spindle coupling and impairs memory consolidation. *Learn. Mem.*, 23:238–248.

Oddie, S. D., Bland, B. H., Colom, L. V., and Vertes, R. P. (1994). The midline posterior hypothalamic region comprises a critical part of the ascending brainstem hippocampal synchronizing pathway. *Hippocampus*, 4:454–473.

Ohara, S., Sato, S., Tsutsui, K., Witter, M. P., and Iijima, T. (2013). Organization of multisynaptic inputs to the dorsal and ventral dentate gyrus: retrograde trans-synaptic tracing with rabies virus vector in the rat. *PLoS One*, 8:e78928.

O'Keefe, J. (1976). Place units in the hippocampus of the freely moving rat. *Exp. Neurol.*, 51:78–109.

O'Keefe, J. and Dostrovsky, J. (1971). The hippocampus as a spatial map. preliminary evidence from unit activity in the freely-moving rat. *Brain Res.*, 34:171–175.

O'Keefe, J. and Nadel, L. (1978). *The Hippocampus as a Cognitive Map*. Oxford University Press.

O'Keefe, J. and Recce, M. L. (1993). Phase relationship between hippocampal place units and the EEG theta rhythm. *Hippocampus*, 3:317–330.

Oliva, A., Fernandez-Ruiz, A., Buzsaki, G., and Berenyi, A. (2016). Role of hippocampal CA2 region in triggering sharp-wave ripples. *Neuron*, 91:1–14.

O'Mara, S. (2005). The subiculum: what it does, what it might do, and what neuroanatomy has yet to tell us. *J. Anat.*, 207:271–282.

O'Mara, S. M., Commins, S., Anderson, M., and Gigg, J. (2001). The subiculum: a review of form, physiology and function. *Prog. Neurobiol.*, 64:129–155.

Ozen, S., Sirota, A., Belluscio, M. A., Anastassiou, C. A., Stark, E., Koch, C., and Buzsaki, G. (2010). Transcranial electric stimulation entrains cortical neuronal populations in rats. *J. Neurosci.*, 30:11476–11485.

Pace-Schott, E. F. and Hobson, J. A. (2002). The neurobiology of sleep: Genetics, cellular physiology and subcortical networks. *Nat. Rev. Neurosci.*, 3:591–605.

Pan, W. X. and McNaughton, N. (2004). The supramammillary area: its organization, functions and relationship to the hippocampus. *Prog. Neurobiol.*, 74:127–166.

Papale, A. E., Zielinski, M. C., Frank, L. M., Jadhav, S. P., and Redish, A. D. (2016). Interplay between hippocampal sharp-wave-ripple events and vicarious trial and error behaviors in decision making. *Neuron*, 92:1–8.

Patel, J., Schomburg, E. W., Berenyi, A., Fujisawa, S., and Buzsaki, G. (2013). Local generation and propagation of ripples along the septotemporal axis of the hippocampus. *J. Neurosci.*, 33:17029–17041.

Pavlidis, P. and Madison, D. V. (1999). Synaptic transmission in pair recordings from CA3 pyramidal cells in organotypic culture. *J. Neurophysiol.*, 81:2787–2797.

Perenin, M. T., Maeda, T., and Jeannerod, M. (1972). Are vestibular nuclei responsible for rapid eye movements of paradoxical sleep? *Brain Res.*, 43:617–621.

Petsche, H., Stumpf, C., and Gogolak, G. (1962). The significance of the rabbit's septum as a relay station between midbrain and the hippocampus: I. the control of hippocampus arousal activity by the septum cells. *Electroencephalogr. Clin. Neurophysiol.*, 14:202–211.

Peyrache, A., Battaglia, F. P., and Destexhe, A. (2011). Inhibition recruitment in prefrontal cortex during sleep spindles and gating of hippocampal inputs. *Proc. Natl. Acad. Sci. U. S. A.*, 108:17207–17212.

Peyrache, A., Khamassi, M., Benchenane, K., Wiener, S. I., and Battaglia, F. P. (2009). Replay of rule-learning related neural patterns in the prefrontal cortex during sleep. *Nat. Neurosci.*, 12:919–926.

Pfeiffer, B. E. and Foster, D. J. (2015). Autoassociative dynamics in the generation of sequences of hippocampal place cells. *Science*, 349:180–183.

Place, R., Farovik, A., Brockmann, M., and Eichenbaum, H. (2016). Bidirectional prefrontal-hippocampal interactions support context-guided memory. *Nat. Neurosci.*, 19:992–994.

Quatrochi, J. J. and Hobson, J. A. (1999). Carbachol microinjection into the caudal peribrachial area induces long-term enhancement of PGO wave activity but not REM sleep. *J. Sleep Res.*, 8:281–290.

Quian Quiroga, R. and Panzeri, S. (2013). *Principles of Neural Coding.* CRC Press.

Racz, A., Ponomarenko, A. A., Fuchs, E. C., and Monyer, H. (2009). Augmented hippocampal ripple oscillations in mice with reduced fast excitation onto parvalbumin-positive cells. *J. Neurosci.*, 28:2563–2568.

Ramirez-Villegas, J. F., Logothetis, N. K., and Besserve, M. (2015). Diversity of sharp-wave-ripple LFP signatures reveals differentiated brain-wide dynamical events. *Proc. Natl. Acad. Sci. U. S. A.*, 112:E6379–E6387.

Ramirez-Villegas, J. F., Murayama, Y., Evrard, H. C., Besserve, M., and Logothetis, N. K. (2017a). Ponto-geniculo-occipital (PGO) waves reflect transient competition between brain stem and hippocampus. In preparation.

Ramirez-Villegas, J. F., Willeke, K. F., Logothetis, N. K., and Besserve, M. (2017b). Dissection of the frequency-dependent network to in-vivo hippocampal sharp wave-ripples. Submitted.

Ramon y Cajal, S. (1893). Estructura del asta de ammon y fascia dentata. *Anales de la Sociedad Espanola de Historia Natural*, 22:53–125.

Ramon y Cajal, S. (1984). La fine structure des centres nerveux. *Proc. R. Soc. Lond.*, 55:444–468.

Ray, S. and Maunsell, J. H. R. (2011). Different origins of gamma rhythm and high-gamma activity in macaque visual cortex. *PLoS Biol.*, 9:e1000610.

Reichinnek, S., Kuensting, T., Draguhn, A., and Both, M. (2010). Field potential signature of distinct multicellular activity patterns in the mouse hippocampus. *J. Neurosci.*, 30:15441–15449.

Reimann, M. W., Anastassiou, C. A., Perin, R., Hill, S. L., Markram, H., and Koch, C. (2013). A biophysically detailed model of neocortical local field potentials predicts the critical role of active membrane currents. *Neuron*, 79:375–390.

Reiner, P. B. and Morrison, A. R. (1980). Pontine-geniculate-occipital spikes in the albino rat: Evidence for the presence of the pontine component as revealed by cerebellar lesions. *Exp. Neurol.*, 69:61–73.

Rothschild, G., Eban, E., and Frank, L. M. (2016). A cortical-hippocampal-cortical loop of information processing during memory consolidation. *Nat. Neurosci.*, 20:251–259.

Saito, T., Matsuba, Y., Mihira, N., Takano, J., Nilsson, P., Itohara, S., Iwata, N., and Saido, T. C. (2014). Single App knock-in mouse models of Alzheimer's disease. *Nat. Neurosci.*, 17:661–663.

Sakai, K. and Koyama, Y. (1996). Are there cholinergic and noncholinergic paradoxical sleep-on neurons in the pons? *Neuroreport*, 7:2449–2453.

Schiller, J., Major, G., Koester, H. J., and Schiller, Y. (2000). NMDA spikes in basal dendrites of cortical pyramidal neurons. *Nature*, 404:285–289.

Schlingloff, D., Kali, S., Freund, T. F., Hajos, N., and Gulyas, A. I. (2014). Mechanisms of sharp wave initiation and ripple generation. *J. Neurosci.*, 34:11385–11398.

Schmitz, D., Schuchmann, S., Fisahn, A., Draguhn, A., Buhl, E. H., Petrasch-Parwez, E., Dermietzel, R., Heinemann, U., and Traub, R. D. (2001). Axo-axonal coupling. a novel mechanism for ultrafast neuronal communication. *Neuron*, 31:831–840.

Schomburg, E. W., Anastassiou, C. A., Buzsaki, G., and Koch, C. (2012). The spiking component of oscillatory extracellular potentials in the rat hippocampus. *J. Neurosci.*, 32:11798–11811.

Schomburg, E. W., Fernandez-Ruiz, A., Mizuseki, K., Berenyi, A., Anastassiou, C. A., Koch, C., and Buzsaki, G. (2014). Theta phase segregation of input-specific gamma patterns in entorhinal-hippocampal networks. *Neuron*, 84:470–485.

Schwindel, C. D., Navratilova, Z., Ali, K., Tatsuno, M., and McNaughton, B. L. (2016). Reactivation of rate remapping in CA3. *J. Neurosci.*, 36:9342–9350.

Scoville, W. B. and Milner, B. (1957). Loss of recent memory after bilateral hippocampal lesions. *Journal of Neurology Neurosurgery and Psychiatry*, 20:11–21.

Shouse, N. and Siegel, J. M. (1992). Pontine regulation of REM sleep components in cats: Integrity of the pedunculopontine tegmentum (PPT) is important for phasic events but unnecessary for atonia during REM sleep. *Brain Res.*, 571:50–63.

Siapas, A. G. and Wilson, M. A. (1998). Coordinated interactions between hippocampal ripples and cortical spindles during slow-wave sleep. *Neuron*, 21:1123–1128.

Singer, A. C., Carr, M. F., Karlsson, M. P., and Frank, L. M. (2013). Hippocampal SWR activity predicts correct decisions during the initial learning of an alternation task. *Neuron*, 77:1163–1173.

Singer, A. C. and Frank, L. M. (2009). Rewarded outcomes enhance reactivation of experience in the hippocampus. *Neuron*, 64:910–921.

Sirota, A. and Buzsaki, G. (2005). Interaction between neocortical and hippocampal networks via slow oscillations. *Thalamus Relat. Syst.*, 3:245–259.

Sirota, A., Csicsvari, J., Buhl, D., and Buzsaki, G. (2003). Communication between neocortex and hippocampus during sleep in rodents. *Proc. Natl. Acad. Sci. U. S. A.*, 100:2065–2069.

Siwek, D. F., Knapp, C. M., Kaur, G., and Datta, S. (2014). Dorsal subcoeruleus nucleus (SubCD) involvement in context-associated fear memory consolidation. *Exp. Brain Res.*, 232:1535–1545.

Skaggs, W. E. and McNaughton, B. L. (1996). Replay of neuronal firing sequences in rat hippocampus during sleep following spatial experience. *Science*, 271:1870–1873.

Skaggs, W. E., McNaughton, B. L., Permenter, M., Archibeque, M., Vogt, J., Amaral, D. G., and Barnes, C. A. (2007). EEG sharp waves and sparse ensemble unit activity in the macaque hippocampus. *J. Neurophysiol.*, 98:898–910.

Skaggs, W. E., McNaughton, B. L., Wilson, M. A., and Barnes, C. A. (1996). Theta phase precession in hippocampal neuronal populations and the compression of temporal sequences. *Hippocampus*, 6:149–172.

Solstad, T., Boccara, C. N., Kropff, E., Moser, M. B., and Moser, E. I. (2008). Representation of geometric borders in the entorhinal cortex. *Science*, 322:1865–1868.

Somogyi, P., Katona, L., Klausberger, T., Lasztoczi, B., and Viney, T. J. (2014). Temporal redistribution of inhibition over neuronal subcellular domains underlies state-dependent rhythmic change of excitability in the hippocampus. *Philos. Trans. R. Soc. Lond. Ser. B Biol. Sci.*, 369:20120518.

Sosa, S., Gillespie, A. K., and Frank, L. M. (2016). *Current Topics in Behavioral Neurosciences*, chapter Neural Activity Patterns Underlying Spatial Coding in the Hippocampus, pages 1–58. Springer Berlin Heidelberg.

Spruston, N. (2008). Pyramidal neurons: dendritic structure and synaptic integration. *Nat. Rev. Neurosci.*, 9:206–221.

Staresina, B. P., Bergmann, T. O., Bonnefond, M., van der Meij, R., Jensen, O., Deuker, L., Elger, C. E., Axmacher, N., and Fell, J. (2015). Hierarchical nesting of slow oscillations, spindles and ripples in the human hippocampus during sleep. *Nat. Neurosci.*, 18:1679–1686.

Stark, E., Roux, L., Eichler, R., Senzai, Y., Royer, S., and Buzsaki, G. (2014). Pyramidal cell-interneuron interactions underlie hippocampal ripple oscillations. *Neuron*, 83:467–480.

Staubli, U. and Lynch, G. (1987). Stable hippocampal long-term potentiation elicited by "theta" pattern stimulation. *Brain Res.*, 435:227–234.

Steriade, M., Contreras, D., Curro, D. R., and Nunez, A. (1993a). The slow (<1 Hz) oscillation in reticular thalamic and thalamocortical neurons: scenario of sleep rhythm generation in interacting thalamic and neocortical networks. *J. Neurosci.*, 13:3284–3299.

Steriade, M., Datta, S., Pare, D., Oakson, G., and Currodossi, R. (1990a). Neuronal activities in brain-stem cholinergic nuclei related to tonic activation processes in thalamocortical systems. *J. Neurosci.*, 10:2541–2559.

Steriade, M., Deschenes, M., Domich, L., and Mulle, C. (1985). Abolition of spindle oscillations in thalamic neurons disconnected from nucleus reticularis thalami. *J. Neurophysiol.*, 54:1473–1497.

Steriade, M., Domich, L., Oakson, G., and Deschenes, M. (1987). The deafferented reticular thalamic nucleus generates spindle rhythmicity. *J. Neurophysiol.*, 57:260–273.

Steriade, M., McCormick, D. A., and Sejnowski, T. J. (1993b). Thalamocortical oscillations in the sleeping and aroused brain. *Science*, 262:679–685.

Steriade, M., Pare, D., Datta, S., Oakson, G., and Currodossi, R. (1990b). Different cellular types in mesopontine cholinergic nuclei related to ponto-geniculo-occipital waves. *J. Neurosci.*, 10:2560–2579.

Stern, E. A., Kincaid, A. E., and Wilson, C. J. (1997). Spontaneous subthreshold membrane potential fluctuations and action potential variability of rat corticostriatal and striatal neurons in vivo. *J. Neurophysiol.*, 77:1697–1715.

Stewart, M. and Fox, S. E. (1991). Hippocampal theta activity in monkeys. *Brain Research*, 538:59–63.

Sullivan, D., Csicsvari, J., Mizuseki, K., Montgomery, S., Diba, K., and Buzsaki, G. (2011). Relationships between hippocampal sharp waves, ripples, and fast gamma oscillation: Influence of dentate and entorhinal cortical activity. *J. Neurosci.*, 31:8605–8616.

Sullivan, D., Mizuseki, K., Sorgi, A., and Buzsaki, G. (2014). Comparison of sleep spindles and theta oscillations in the hippocampus. *J. Neurosci.*, 34:662– 674.

Sun, Y., Nguyen, A. Q., Nguyen, J. P., Le, L., Saur, D., Choi, J., Callaway, E. M., and Xu, X. (2014). Cell-type-specific circuit connectivity of hippocampal CA1 revealed through cre-dependent rabies tracing. *Cell Reports*, 7:269–280.

Takacs, V. T., Klausberger, T., Somogyi, P., Freund, T. F., and Gulyas, A. I. (2012). Extrinsic and local glutamatergic inputs of the rat hippocampal CA1 area differentially innervate pyramidal cells and interneurons. *Hippocampus*, 22:1379–1391.

Tamamaki, N., Abe, K., and Nojyo, Y. (1988). Three-dimensional analysis of the whole axonal arbors originating from single CA2 pyramidal neurons in the rat hippocampus with the aid of a computer graphic technique. *Brain Res.*, 452:255–272.

Taube, J. S., Muller, R. U., and Ranck, J. B. (1990a). Head-direction cells recorded from the postsubiculum in freely moving rats. I. Description and quantitative analysis. *J. Neurosci.*, 10:420–435.

Taube, J. S., Muller, R. U., and Ranck, J. B. (1990b). Head-direction cells recorded from the postsubiculum in freely moving rats. II. Effects of environmental manipulations. *J. Neurosci.*, 10:436–447.

Taxidis, J., Coombes, S., Mason, R., and Owen, M. R. (2012). Modeling sharp wave-ripple complexes through a CA3-CA1 network model with chemical synapses. *Hippocampus*, 22:995–1017.

Teyler, T. J. and DiScenna, P. (1986). The hippocampal memory indexing theory. *Behavioural Neuroscience*, 100:147–154.

Teyler, T. J. and Rudy, J. W. (2007). The hippocampal indexing theory and episodic memory: Updating the index. *Hippocampus*, 17:1158–1169.

Timofeev, I. and Steriade, M. (1996). Low-frequency rhythms in the thalamus of intactcortex and decorticated cats. *J. Neurophysiol.*, 76:4152–4168.

Tononi, G. and Cirelli, C. (2014). Sleep and the price of plasticity: From synaptic and cellular homeostasis to memory consolidation and integration. *Neuron*, 81:12–34.

Torterolo, P., Sampogna, T., and Chase, M. H. (2011). A restricted parabrachial pontine region is active during non-rapid eye movement sleep. *Neuroscience*, 190:184–193.

Traub, R. D. and Bibbig, A. (2000). A model of high-frequency ripples in the hippocampus based on synaptic coupling plus axon-axon gap junctions between pyramidal neurons. *J. Neurosci.*, 20:2086–2093.

Traub, R. D., Schmitz, D., Maier, N., Whittington, M. A., and Draguhn, A. (2012). Axonal properties determine somatic firing in a model of in vitro ca1 hippocampal sharp wave/ripples and persistent gamma oscillations. *Eur. J. Neurosci.*, 36:2650–2660.

Ul Haq, R., Anderson, M., Hollnagel, J. O., Worschech, F., Sherkheli, M. A., Behrens, C., and Heinemann, U. (2016). Serotonin dependent masking of hippocampal sharp wave ripples. *Neuropharmacology*, 101:188–203.

Ul Haq, R., Liotta, A., Kovacs, R., Rosler, A., Jarosch, M., Heinemann, U., and Behrens, C. (2012). Adrenergic modulation of sharp wave-ripple activity in rat hippocampal slices. *Hippocampus*, 22:516–533.

Ulanovsky, N. and Moss, C. F. (2007). Hippocampal cellular and network activity in freely moving echolocating bats. *Nat. Neurosci.*, 10:224–233.

Ulloor, J. and Datta, S. (2005). Spatio-temporal activation of cyclic AMP response element-binding protein, activity-regulated cytoskeletal-associated protein and brain-derived nerve growth factor: a mechanism for pontine-wave generator activation-dependent two-way active-avoidance memory processing in the rat. *J. Neurochem.*, 95:418–428.

van de Ven, G. M., Trouche, S., McNamara, C. G., Allen, K., and Dupret, D. (2016). Hippocampal offline reactivation consolidates recently formed cell assembly patterns during sharp wave-ripples. *Neuron*, 92:968–974.

van Strien, N. M., Cappaert, N. L., and Witter, M. P. (2009). The anatomy of memory: an interactive overview of the parahippocampal-hippocampal network. *Nat. Rev. Neurosci.*, 10:272–282.

Vandecasteele, M., Varga, V., Berenyi, A., Papp, E., Bartho, P., Venance, L., Freund, T. F., and Buzsaki, G. (2014). Optogenetic activation of septal cholinergic neurons suppresses sharp wave ripples and enhances theta oscillations in the hippocampus. *Proc. Natl. Acad. Sci. U. S. A.*, 111:13535–13540.

Vanderwolf, C. H. (1969). Hippocampal electrical activity and voluntary movement in the rat. *Electroencephalogr. Clin. Neurophysiol.*, 26:407–418.

Varga, C., Golshani, P., and Soltesz, I. (2012). Frequency-invariant temporal ordering of interneuronal discharges during hippocampal oscillations in awake mice. *Proc. Natl. Acad. Sci. U. S. A.*, 109:E2726–E2734.

Varga, C., Oijala, M., Lish, J., Szabo, G. G., Bezaire, M., Marchionni, I., Golshani, P., and Soltesz, I. (2014). Functional fission of parvalbumin interneuron classes during fast network events. *eLife*, 3:04006.

Varga, V., Losonczy, A., Zemelman, B. V., Borhegyi, Z., Nyiri, G., Domonkos, A., Hangya, B., Holderith, N., Magee, J. C., and Freund, T. F. (2009). Fast synaptic subcortical control of hippocampal circuits. science. *Science*, 326:449–453.

Vass, L. K., Copara, M. S., Seyal, M., Shahlaie, K., Farias, S. T., and Shen, P. Y. (2016). Oscillations go the distance: low-frequency human hippocampal oscillations code spatial distance in the absence of sensory cues during teleportation. *Neuron*, 89:1180–1186.

Vertes, R. (1981). An analysis of ascending brain stem systems involved in hippocampal synchronization and desynchronization. *J. Neurophysiol.*, 46:1140–1159.

Vertes, R. P. (1982). Brain stem generation of the hippocampal EEG. *Prog. Neurobiol.*, 19:159–186.

Vertes, R. P. (1992). PHA-L analysis of projections from the supramammillary nucleus in the rat. *J. Comp. Neurol.*, 326:595–622.

Vertes, R. P., Colom, L. V., Fortin, W. J., and Bland, B. H. (1993). Brainstem sites for the carbachol elicitation of the hippocampal theta rhythm in the rat. *Exp. Brain Res.*, 96:419–429.

Vertes, R. P., Hoover, W. B., and Viana Di Prisco, G. (2004). Theta rhythm of the hippocampus: Subcortical control and functional significance. *Behav. Cogn. Neurosci. Rev.*, 3:173–200.

Vertes, R. P. and McKenna, J. T. (2000). Collateral projections from the supramammillary nucleus to the medial septum and hippocampus. *Synapse*, 38:281–293.

Vincent, S. R., Satoh, K., Armstrong, D. M., Panula, P., Vale, W., and Fibiger, H. C. (1986). Neuropeptides and nadph-diphorase activity in the ascending cholinergic reticular system of the rat. *Neuroscience*, 17:167–182.

Vuillon-Cacciuttolo, G., , and Seri, B. (1978). Effets de la section des nerfs optiques chez le babouin sur l'activite A Type de pointes genouilles et corticales au cours des divers etats de vigilance. *Electroencephalogr. Clin. Neurophysiol.*, 44:754–768.

Wang, D. V., Yau, H. J., Broker, C. J., Tsou, J. H., Bonci, A., and Ikemoto, S. (2015). Mesopontine median raphe regulates hippocampal ripple oscillation and memory consolidation. *Nat. Neurosci.*, 18:728–735.

Wang, S., Wang, I. Z., Bulacio, J. C., Mosher, J. C., Gonzalez-Martinez, J., Alexopoulos, A. V., Najm, I. M., and So, N. K. (2013). Ripple classification helps to localize the seizure-onset zone in neocortical epilepsy. *Epilepsia*, 54:370–376.

Wang, Y., Roth, Z., and Pastalkova, E. (2016). Synchronized excitability in a network enables generation of internal neuronal sequences. *eLife*, 5:e20697.

Whittingstall, K. and Logothetis, N. K. (2013). *Principles of Neural Coding*, chapter Physiological Foundations of Neural Signals, pages 3–14. CRC Press.

Wierzynski, C. M., Lubenov, E. V., Gu, M., and Siapas, A. G. (2009). State-dependent spike-timing relationships between hippocampal and prefrontal circuits during sleep. *Neuron*, 61:587–596.

Wilber, A. A., Skelin, I., Wu, W., and L., M. B. (2017). Laminar organization of encoding and memory reactivation in the parietal cortex. *Neuron*, 95:1406–1419.

Williams, J. A., Comisarow, J., Day, J., Fibiger, H. C., and Reiner, P. B. (1994). State-dependent release of acetylcholine in rat thalamus measured by in vivo microdialysis. *J. Neurosci.*, 14:5236–5242.

Wilson, M. A. and McNaughton, B. L. (1994). Reactivation of hippocampal ensemble memories during sleep. *Science*, 265:676–679.

Witter, M. P. and Amaral, D. G. (2004). *The Rat Nervous System*, chapter Hippocampal Formation, pages 635–704. Elsevier Academic Press, Burlington.

Witter, M. P., Naber, P. A., van Haeften, T., Machielsen, W. C. M., Rombouts, S. A. R. B., Barkhof, F., Scheltens, P., and Lopes da Silva, F. H. (2000). Cortico-hippocampal communication by way of parallel parahippocampal-subicular pathways. *Hippocampus*, 10:398–410.

Wu, C., Asl, M. N., Gillis, J., Skinner, F. K., and Zhang, L. (2005). An in vitro model of hippocampal sharp waves: Regional initiation and intracellular correlates. *J. Neurophysiol.*, 94:741–753.

Yang, S., Yang, S., Moreira, T., Hoffman, G., Carlson, G. C., Bender, K. J., Alger, B. E., and Tang, C. M. (2014). Interlamellar CA1 network in the hippocampus. *Proc. Natl. Acad. Sci. U. S. A.*, 111:12919–12924.

Yavich, L., Jakala, P., and Tanila, H. (2005). Noradrenaline overflow in mouse dentate gyrus following locus coeruleus and natural stimulation: Real-time monitoring by in vivo voltammetry. *J. Neurochem.*, 95:641–650.

Ylinen, A., Bragin, A., Nadasdy, Z., Jando, G., Szabo, I., Sik, A., and Buzsaki, G. (1995). Sharp wave-associated high-frequency oscillation (200 Hz) in the intact hippocampus: network and intracellular mechanisms. *J. Neurosci.*, 15:30–46.

Yu, J. Y., Kay, K., Liu, D. F., Grossrubatscher, I., Loback, A., Sosa, M., Chung, J. E., P., K. M., Larkin, M. C., and Frank, L. M. (2017). Distinct hippocampal-cortical memory representations for experiences associated with movement versus immobility. *eLife*, 6:e27621.

Zaldivar, D. (2016). *Effects of Neuromodulation on Neurovascular Coupling.* PhD thesis, Medizinischen Fakultät der Eberhard-Karls-Universität Tübingen.

Zaldivar, D., Rauch, A., Whittingstall, K., Logothetis, N. K., and Goense, J. (2014). Dopamine-induced dissociation of BOLD and neural activity in macaque visual cortex. *Curr. Biol.*, 24:2805–2811.

Zhang, S. J., Ye, J., Miao, C., Tsao, A., Cerniauskas, I., Ledergerber, D., Moser, M. B., and Moser, E. I. (2013). Optogenetic dissection of entorhinal-hippocampal functional connectivity. *Science*, 340:1232627.

Appendix A

Paper 1

Diversity of sharp-wave–ripple LFP signatures reveals differentiated brain-wide dynamical events

Juan F. Ramirez-Villegas[a,b], **Nikos K. Logothetis**[a,c,1], **and Michel Besserve**[a,d,1]

[a]Department of Physiology of Cognitive Processes, Max Planck Institute for Biological Cybernetics, 72076 Tübingen, Germany; [b]Graduate School of Neural and Behavioral Sciences, International Max Planck Research School, Eberhard-Karls University of Tübingen, 72074 Tübingen, Germany; [c]Centre for Imaging Sciences, Biomedical Imaging Institute, The University of Manchester, Manchester M13 9PT, United Kingdom; and [d]Department of Empirical Inference, Max Planck Institute for Intelligent Systems, 72076 Tübingen, Germany

Contributed by Nikos K. Logothetis, September 21, 2015 (sent for review May 21, 2015)

Sharp-wave–ripple (SPW-R) complexes are believed to mediate memory reactivation, transfer, and consolidation. However, their underlying neuronal dynamics at multiple scales remains poorly understood. Using concurrent hippocampal local field potential (LFP) recordings and functional MRI (fMRI), we study local changes in neuronal activity during SPW-R episodes and their brain-wide correlates. Analysis of the temporal alignment between SPW and ripple components reveals well-differentiated SPW-R subtypes in the CA1 LFP. SPW-R–triggered fMRI maps show that ripples aligned to the positive peak of their SPWs have enhanced neocortical metabolic up-regulation. In contrast, ripples occurring at the trough of their SPWs relate to weaker neocortical up-regulation and absent subcortical down-regulation, indicating differentiated involvement of neuromodulatory pathways in the ripple phenomenon mediated by long-range interactions. To our knowledge, this study provides the first evidence for the existence of SPW-R subtypes with differentiated CA1 activity and metabolic correlates in related brain areas, possibly serving different memory functions.

hippocampus | memory | in vivo electrophysiology | fMRI | local field potential

Memory processes require mechanisms for large-scale integration of neuronal activity, in which information processing is precisely coordinated at multiple scales. A prominent example of such phenomenon is the replay of specific sequences of action potentials of hippocampal and neocortical neurons, reflecting previous experiences during wakefulness (1–7). Sharp-wave–ripple (SPW-R) complexes observed in the hippocampal CA1 local field potential (LFP) mark the reactivation of these sequences by the simultaneous occurrence of two distinct but related phenomena: a strong LFP deflection, known as sharp wave (SPW), and a high-frequency oscillation known as ripple (8, 9). SPW-R episodes are thought to reflect brain-wide processes mediating memory consolidation (10–13). However, the large-scale cooperative mechanisms associated to these episodes and their relationship to the observed SPW-R electrical signature remain largely unknown. Investigating this relationship is critical for understanding memory processes at a system level and may provide new insights into the mechanisms of pathological fast ripples observed during epilepsy (14).

Although they were initially thought to occur during slow-wave sleep and quiescence periods, later on SPW-R and sequence replay were also observed during or shortly after active behavior (15–17). Moreover, many SPW-Rs occur at path choice points (18, 19), which are also locations where vicarious trial and error are reported (20). Thus, reactivation of memory sequences during SPW-Rs could provide a convenient mechanism not only for consolidation of long-term memory (4) but also for quickly recalling memories during awake state, serving various cognitive functions (21). The generation of SPW-R complexes in these various contexts likely involves brain-wide network mechanisms, and as a consequence, SPW-R–related brain dynamics may vary, reflecting different types of interactions with cortical and subcortical systems. These interactions may in turn affect the underlying dynamics of hippocampal circuits, thus modifying the observed SPW-R–associated functional activity at multiple scales.

In this work, we investigate how the LFP signature of SPW-R events varies during ongoing activity at a given CA1 recording site, and whether these variations reflect differences in the coordination of neural activity at multiple scales, possibly related to different functions. We test our hypothesis by studying the SPW-R correlates at mesoscopic and macroscopic scales. Specifically, using multisite hippocampal LFP recordings and functional MRI (fMRI) in anesthetized rhesus monkeys (*Macaca mulatta*), we examine the spatiotemporal properties of SPW-R complexes with a multivariate clustering approach. This approach revealed that recorded multisite SPW-R LFP activity can be classified in four subtypes differing in the temporal SPW-to-ripple coupling and low-frequency SPW pattern. On the one hand, SPW-R–triggered fMRI statistical maps suggest that ripples synchronized to the positive peak of their SPWs mark enhanced neocortical activations. On the other hand, ripples occurring at the trough of their SPWs reveal weak or absent down-regulation in subcortical structures, especially in two neuromodulatory structures: dorsal raphe nucleus and locus coeruleus. Altogether, our results show that hippocampal episodes displaying specific SPW temporal patterns and distinct couplings between SPWs and ripples may instantiate cortico- and subcortico-hippocampal interactions of different nature, possibly associated with specific memory-related functions.

Significance

Sharp-wave–ripple (SPW-R) episodes observed in the electrical activity of mammalian hippocampus are traditionally associated to memory consolidation during sleep but have been recently observed during active behavior. Their involvement in various cognitive functions suggests the existence of SPW-R subtypes engaged in distinct neuronal activity patterns at multiple scales. We use concurrent electrophysiological and functional MRI (fMRI) recordings in macaque monkeys to investigate this hypothesis. We discover several subtypes of SPW-R with distinct electrophysiological properties. Importantly, fMRI recordings reveal differences between the large-scale signatures of SPW-R subtypes, indicating differentiated interactions with neocortex, and contributions of neuromodulatory pathways to the SPW-R phenomenon. Understanding the detailed properties of hippocampal SPW-Rs at multiple scales will provide new insights on the function of memory systems.

Author contributions: M.B. designed research; J.F.R.-V. performed research; J.F.R.-V., N.K.L., and M.B. contributed new reagents/analytic tools; J.F.R.-V. analyzed data; and J.F.R.-V. and M.B. wrote the paper.

The authors declare no conflict of interest.

[1]To whom correspondence may be addressed. Email: michel.besserve@tuebingen.mpg.de or nikos.logothetis@tuebingen.mpg.de.

This article contains supporting information online at www.pnas.org/lookup/suppl/doi:10.1073/pnas.1518257112/-/DCSupplemental.

Results

Four Subtypes of SPW-R Complexes. To study the variability of SPW-R complexes, we analyzed extracellular recordings and characterized the temporal and frequency profile of LFPs of the macaque hippocampus. Multicontact recording electrodes were positioned in CA1 on the basis of high-resolution structural MRI scans and on-line tracking of stereotypical hippocampal neuronal response profiles (see *Materials and Methods* for details). Fig. 1 depicts a schematic representation of the recording configuration and typical electrode penetration (Fig. 1*A*), together with an example of a typical SPW-R complex signature across multiple electrode tips (Fig. 1 *B* and *C*). SPW-R amplitude, duration (~100 ms) (Fig. 1*B*), current source density (CSD) profile (Fig. 1*D*), and spectrogram (Fig. 1*E*) are consistent with previous studies in macaque monkeys (22). To check the stability of the level of anesthesia, we monitored the power of hippocampal LFP in the theta frequency band (4–8 Hz) (23). Each experiment of a given session was divided into two blocks (5 min each). The distribution of theta power in these two blocks was assessed by randomly choosing time intervals of 1 min (for a total of 50 time intervals) within the block and computing its theta power using Morlet-wavelet spectrograms (see *Materials and Methods*). Our analysis revealed no significant differences between the first block and second block of each experiment ($n = 242$ experiments; $P > 0.69$, paired-samples permutation t test). Theta activity was thus stable across experiments of single-recording sessions, reflecting no putative fluctuations on the anesthesia levels (Fig. S1 *A* and *B*).

To study the dynamics of SPW-Rs, we have initially identified candidate events using the process described in ref. 24, coupled with several refinements. Briefly, oscillatory events were initially detected as peaks in the envelope of the broadband LFP (10–250 Hz). Candidate events were clustered on the basis of their spectral signatures, and only events exhibiting increases in their spectra above 80 Hz were identified as ripples. Detection of ripples was further refined by quantifying the Z-scored power in the ripple frequency band (80–180 Hz) and ripple localization in time. Only events satisfying stringent localization and power profile criteria were taken into account for further processing steps (see full procedure in *SI Section A*).

To quantify the variability in hippocampal LFP during SPW-R events, we first compared their spatiotemporal signature. We asked whether this variability supported the existence of well-differentiated SPW-R event types, possibly reflecting distinct microcircuit dynamics and functional roles. As a preliminary step, we first aligned perievent waveforms with respect to the averaged ripple power peak across recording sites. We next used a two-step procedure to cluster the detected and aligned SPW-R events as illustrated in Fig. S2. The cluster analysis procedure was performed for each experimental session separately. First, we grouped the spatiotemporal SPW-R series into 200 representative signals using a growing neural gas (GNG) algorithm (25). Each representative signal is the average of a group of raw perievent signals with similar time courses (Fig. S2 *A* and *B*). It is worth noting that GNG does not extract particular features of the signals but represents them solely based on their corresponding time courses in an unsupervised manner. In the second step (Fig. S2*C*), we clustered these representative signals based on their cosine similarity using the normalized cuts algorithm (26) (see *SI Section A* for details).

We applied this two-step algorithm to 12 experimental sessions (a total of ~11,000 detected SPW-R complexes). The results of the clustering procedure were consistent across all experimental sessions and animals, and did not vary significantly due to recording channel selection (the algorithm was amenable to one or multiple recording channels). However, it was difficult to determine whether SPW-R complexes were truly clustered or they only existed as part of some continuum. To address this question, we devised two procedures: clustering quality analysis, and cluster consistency analysis (see *SI Section A* for methodological details, and Fig. S3). The first analysis revealed that the population of SPW-R complexes in the CA1 field is best represented by four LFP signatures. Furthermore, the second procedure revealed that clustering consistency across experimental sessions was significantly higher than chance ($P < 10^{-6}$, t test; mean value with 95% confidence interval for clustering consistency, 74.17% ± 1.63%).

Fig. 2*A* depicts the SPW-R LFP grand averages of the resulting clusters ($n = 12$ experimental sessions, 4 animals), showing that ripple oscillations may follow (subtype 1), precede (subtype 2), or be located at the peak of dendritic depolarization (subtype 3). Additionally, ripples may be deprived from a clear SPW depolarization signature (subtype 4). For brevity, we refer to ripple oscillations located near the peak of the SPW (subtypes 2 and 3) as "classical" (SPW-R patterns with the strongest visual resemblance to those first reported in ref. 22). The remaining SPW-Rs (subtypes 1 and 4) will be referred to as "nonclassical." In correspondence with each SPW-R subtype, typical raw signal traces (0.5–300 Hz) are illustrated in Fig. 2*B* (*Top*) (monkey *i11*), together with their SPW (0–20 Hz) and ripple (80–180 Hz) filtered traces (Fig. 2*B*, *Top* and *Middle*, respectively), a colored dotted line shows the SD threshold for the event in the ripple band. Finally, single-event (broadband) Z-scored Morlet-wavelet spectrograms for every example event are given in Fig. 2*B* (*Bottom*), displaying significant and localized ripple-band power

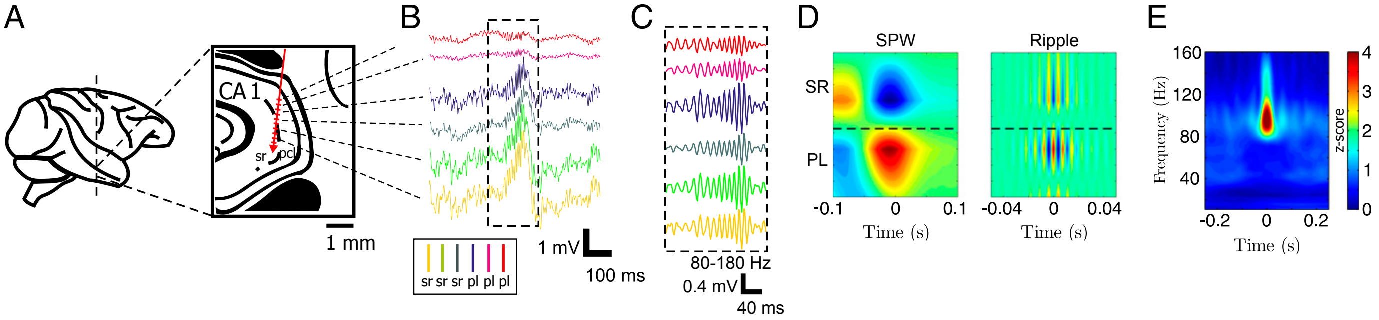

Fig. 1. Electrode position, recordings in the hippocampus, and SPW-Rs. (*A*) Schematic representation of our hippocampal recordings. The diagram of the electrode position is superimposed on an *Inset* of the MRI histology atlas (49) indicating the approximate thickness of the pyramidal cell layer in the CA1 field. (*B*) Raw multisite LFP traces (0.5–250 Hz). Labels indicate the site targeted by each electrode tip: "sr" for stratum radiatum, "pl" for pyramidal layer. (*C*) LFP traces depicted in *B* filtered in the ripple band (80–180 Hz). (*D*) Averaged current source density (CSD) maps (50) for SPW (*Left*) and ripple (*Right*) for a typical experimental session ($n = 1,020$, monkey *i11*). In the CSD plots, warm colors (red) indicate sources, whereas cold colors (blue) indicate sinks. (*E*) Averaged ripple-triggered Morlet-wavelet spectrogram for a typical recording session ($n = 1,020$, monkey *i11*).

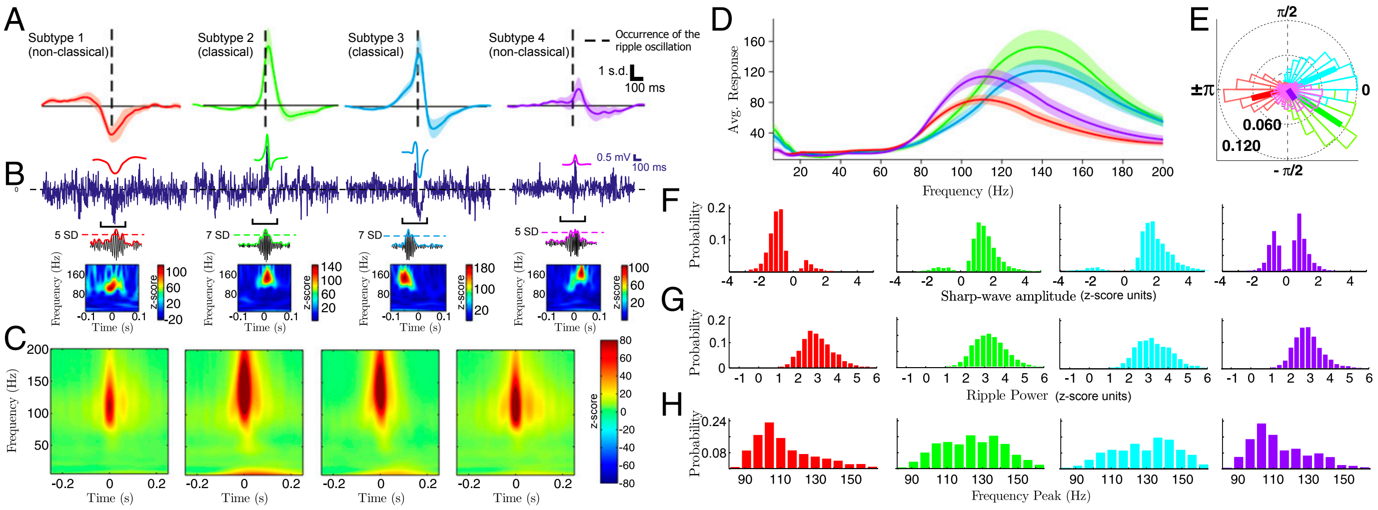

Fig. 2. Classification of SPW-R complexes across 12 experimental sessions in anesthetized macaque monkeys. (*A*) Grand averages of ripple power-triggered SPW-R field potential signatures, from one representative stratum radiatum recording site. Occurrence of the ripple oscillation is marked by dashed lines. Shaded areas indicate SEM. (*B*) Representative single-trial events for each subtype. (*Top*) SPW and related raw signals of each event subtype (monkey *i11*). Note that shapes correspond to the average patterns presented in *A*. (*Middle*) Filtered, *Z*-scored LFP in the ripple frequency range (80–180 Hz), illustrating that all SPW-R classes present a significant power increase in this range. Dashed lines indicate ripple amplitude in SD units. (*Bottom*) *Z*-scored single-event spectrogram of the broadband signal presented in the top rows. (*C*) Spectrogram grand averages, in correspondence with each of the SPW-R signatures depicted in *A*. Averages are computed across all recording sites. (*D*) Averaged clusterwise spectra. Shaded areas indicate SEM. (*E*) Phase coupling of the ripple to the SPW of dendritic depolarization for each cluster. Thick lines indicate the circular mean of the phase-coupling values. (*F*–*H*) Empirical distribution of SPW and ripple subtypes properties. (*F*) SPW amplitude. (*G*) Ripple power. (*H*) Ripple frequency peak. Colors indicate SPW-R subtype.

increases. We found that results were very consistent from one experimental session to another. As additional evidence, Fig. S4 shows results from another anesthetized experimental session (monkey *e10*). As previous results have shown, single-event ripple band traces and spectrograms show that nonclassical ripples appear localized in line with our selection criteria (*Materials and Methods*), and in good agreement with ripple events reported in the literature (9, 27). It is worth noting that each SPW-R subtype occurred concomitantly across all recording sites, displaying little depth-dependent differences. Furthermore, SPW-R episodes usually maintained the same polarity across all channels.

In addition to average waveforms, we asked whether SPW-R subtypes showed differences in the frequency content of peri-event LFP. Population complex Morlet-wavelet spectrograms corresponding to each SPW-R type are depicted in Fig. 2*C* (n = 12 experimental sessions, 4 animals). This time–frequency analysis shows a clearer low-frequency peak for classical SPW-Rs, suggesting they have higher-power sharp waves than nonclassical SPWs. In addition, the spectral profiles at ripple onset extracted from the middle vertical line of each spectrogram (Fig. 2*D*) show that classical ripples have higher frequency peaks [mean values with 95% confidence intervals, 110.56 ± 1.09, 127.14 ± 0.91, 125.35 ± 0.95, and 115.53 ± 0.83, respectively; pairwise bootstrapped Kolmogorov–Smirnov (KS) test, $P < 10^{-6}$, for the difference between frequency peaks, Bonferroni corrected] and spectral power (*SI Section B* and *SI Section C*, and Fig. S5; specifically note that Fig. S5*H* shows a clear bimodal empirical distribution of the ripple frequency peaks) compared with nonclassical ripples.

A characteristic of our results is the different coupling of average SPW waveforms to the ripple onset. To quantify precisely this relationship in individual events, we measured the phase of the sharp wave (0–20 Hz) at each ripple occurrence. The results, grouped by SPW-R subtypes, are shown as polar histograms on Fig. 2*E*. Classical ripple signatures and only one nonclassical signature (subtype 1, depicted in red) presented statistically significant coupling to the sharp wave (mean values with 95% confidence interval, -2.9126 ± 0.060, -0.53 ± 0.034, and 0.548 ± 0.025; $P < 10^{-10}$, permuted KS test). In contrast, the nonsignificant coupling of the last cluster (subtype 4) (mean value with 95% confidence interval, -0.74 ± 0.091; $P > 0.8$, permuted KS test) is attributable to the lack of clear SPW signature. Notably, ripple-to-SPW coupling was statistically different among all SPW-R subtypes ($P < 0.0001$, permuted KS test; see also Fig. S5*E*, where histograms show clear multimodality). In line with this analysis, the empirical distributions illustrated in Fig. 2*F* show mostly positive SPW amplitude distributions for classical SPW-Rs, whereas nonclassical events show negative distribution or distribution around zero. As illustrated by Fig. 2 *G* and *H*, all SPW-R subtypes have their main spectral support in the frequency range of 80–180 Hz and have similar ripple power profiles (Fig. S5). Altogether, these results suggest that SPW-R subtypes are distinct in several ways, likely reflecting a discrete set of modes for the underlying hippocampal dynamics (e.g., mediated by differentiated inputs to CA1), rather than reflecting a continuum of variations of the same phenomenon. Furthermore, these differences observed at local scales are further supported by subsequent analyses on recording sessions from one unanesthetized animal (*SI Section B* and Fig. S6).

Some of the SPW-R patterns described here are in close correspondence with signatures reported in a previous macaque monkey study (22). Our results extend previous observations on the variability of the time course of SPW-R complexes across species (9, 22, 28). In fact, Skaggs et al. (22) suggested that ripple oscillations come before the largest deflection of SPW in macaque monkeys. Here, we demonstrate that SPWs and ripples exhibit a variety of couplings. Moreover, our findings show that SPWs also come in different shapes. In *SI Section B*, we further characterize SPWs and ripples of distinct type. In particular, we report comparable ripple power, and higher ripple peak frequency for classical SPW-Rs with respect to their nonclassical counterparts (see the overall ripple and SPW statistics across experimental sessions in Fig. S5). These differences may be related to changes in neuronal synchrony (recruitment of pyramidal neurons and interneurons) and modifications of the *E*–*I* balance resulting in a higher neuronal excitability during classical SPW-Rs. Interestingly, we also report that, although subtypes have comparable rates and appear at similar timescales (Fig. S7

A and B), classical sharp waves have larger autocorrelation density ($P < 0.01$; t test; $n = 12$ experimental sessions), suggesting larger burstiness for these subtypes (Fig. S7C and *SI Section B*), and consistent with previous studies reporting that ripples tend to occur at comparable timescales, in time windows of increased multiunit spiking activity (29). We now investigate the coupling of SPW-R signatures to multiunit spiking activity.

Spike-Field Coherence Reflects Differences in Population Synchrony During SPW-R Subtypes. Ripples are correlated with single-unit and multiunit spiking activity from the CA1 pyramidal layer (9, 27). We asked whether this was the case for the identified SPW-R subtypes. Using the recorded multiunit spiking activity, we computed perievent time histograms (5-ms bins) for each SPW-R subtype across experimental sessions. For such a purpose, we limited our analysis to the electrode tip with the largest ripple oscillation power located in stratum pyramidale (see *SI Section A* for details). Our first analysis revealed a significant increase in spiking activity from baseline (Fig. 3*A*; $n = 12$ experimental sessions) concomitant with the ripple occurrence. Broadly, spiking activity of all SPW-R event types peaked at the same time.

Ripple events have a characteristic phase relationship to the firing of participating units (8). We thus asked whether this relationship was the same for differentiated SPW-R subtypes. We assessed precisely the relationship between multiunit spikes and LFP phase using cross-correlation. For this analysis, the SPW-R signal was bandpass filtered in the ripple range (80–180 Hz), and we used the location of the largest trough of the oscillation as event onset reference for the cross-correlation. We then computed the ripple trough-triggered perievent time histograms (bins of 2 ms; $n = 12$ experimental sessions). Our results not only indicated that neuronal assemblies increase their discharge probability (Fig. 3*A*) during the occurrence of SPW-Rs but also revealed that unit discharges occur preferentially at the negative peaks of the ripple oscillations (ripple trough) (Fig. 3*B*), in agreement with previous studies in rats (8, 9). This finding was consistent across all SPW-R event subtypes, displaying virtually identical cross-correlograms (Fig. 3*B*, *Top*). In addition, the average ripple oscillation signature was almost identical among SPW-R subtypes.

Differences in the relationship between multiunit spikes and LFP across SPW-R subtypes may also span over the entire frequency axis, instead of remaining localized to a particular frequency band (such as the ripple range). Hence we further studied the LFP–spike relationship of SPW-R subtypes using spike-field coherence (SFC) of each SPW-R cluster across all frequencies in the [0–200 Hz] range (30) (see *SI Section A*). We computed this quantity for the four SPW-R signatures independently, across all experimental sessions. SFC group results are shown in Fig. 3*C* for each SPW-R subtype ($n = 12$ experimental sessions). Absolute values reported in Fig. 3*C* reveal coherency peaks both in the ripple and sharp-wave frequency bands. Classical SPW-Rs have the highest coherence values. Furthermore, the ripple-band peak of coherency of nonclassical events was consistently below that of classical SPW-Rs, in agreement with previous analyses (Fig. 2 and Fig. S6).

We further investigated whether spikes had a consistent phase relationship to LFP at different frequencies. Phase-locking values and circular mean phase of the coherence maps are reported in Fig. 3*D*. Consistent with our preliminary analysis, we found that multiunit spikes were phase-locked approximately to the trough of the ripple oscillation (corresponding to a phase of π radians or 180°; Fig. 3*D*, middle map plots; mean phase with 95% circular confidence interval -2.84 ± 0.04 radians or $197.28 \pm 2.29°$ for subtype 2; -2.62 ± 0.02 radians or $209.78 \pm 1.25°$ degrees for subtype 3). However, in our SFC result, this relationship holds more precisely for classical ripples (nonclassical ripples mean phase with 95% circular confidence interval -2.32 ± 0.04 radians or $227.07 \pm 2.29°$; -2.52 ± 0.05 radians or $215.61 \pm 2.86°$; $P < 10^{-3}$, paired Kuiper test for the difference between phase couplings of all ripple subtypes, Bonferroni corrected). This finding most likely reflects different degrees of neuronal population synchrony 50 ms around the occurrence of the ripple oscillation for different types of SPW-R complexes, which may explain the difference between our preliminary results and those with the SFC. Furthermore, this finding also suggests that nonclassical episodes represent the activity of a less synchronous neuronal population, in agreement with results in Fig. 3*C*.

Finally, SFC analysis shows that multiunit spiking activity is significantly locked to the gamma rhythm. A previous study showed that a gamma rhythm is ubiquitous in the SPW-R phenomenon (31). Notably, the results of this study suggest that SWR-related gamma coordinates CA3 and CA1 assemblies, and could coordinate the reactivation of stored memories. It is worth noting that, in the present work, we only selected "pure" ripple events taking into account a signal-to-noise ratio, thus assuring an almost unimodal ripple band power profile (24) (*SI Section C*). To fully account for the possible influence of putative perievent gamma oscillations, we considered all detected events, namely pure and "nonpure" events in two separate groups. In *SI Section C*, we show that detailed examination of SPW-R episode-related gamma oscillations across all detected nonpure events reveal neither new SPW-R LFP signatures nor distinct electrophysiological features compared with pure events (see Fig. S8 *A–D*). Interestingly, we found a transient increase of power over gamma frequencies concomitant with the occurrence of pure, nonpure, and

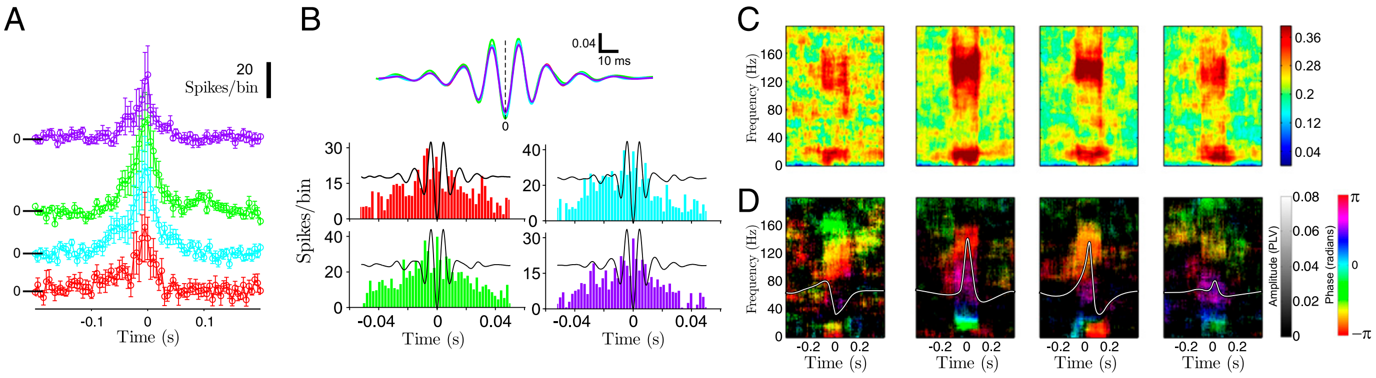

Fig. 3. Relationship between SPW-R complex subtypes and neuronal spiking activity. (*A*) Perievent time histograms of multiunit spiking activity using bins of size 5 ms. Histograms are computed with respect to random point processes of the same rate. (*B*) Cross-correlogram (*Top*) and ripple-trough perievent time histograms (*Bottom*). (*C*) Maps of absolute SFC for each SPW-R subtype defined in Fig. 3. (*D*) Spike-field phase-locking maps corresponding to SFC map displayed in *C*.

all SPW-R subtypes (Fig. S8*E*). These oscillations spread over the slow- and high-gamma range of 25–75 Hz, with a unimodal distribution of instantaneous frequencies peaking at ∼50 Hz (see Fig. S8*C*, *Insets*). We found that individual SPW-R episodes can be predicted—to a certain extent—from this transient increase in gamma power, but not their specific subtype (Fig. S8*F*). Furthermore, in line with our SFC analysis, the relationship between gamma LFP and multiunit spikes displays significant differences in phase-coupling and phase-locking value among SPW-R subtypes, further supporting our hypothesis that these episode subtypes are functionally different (Fig. S8*G*). Importantly, these results demonstrate that our observations are invariant to SPW-R event detection protocols, and most likely reflect the intricate hippocampal dynamics. Furthermore, in line with ref. 31, our data suggest that macaque SPW-Rs are also mediated by a gamma rhythm (see *SI Section C* and *SI Section D* for further discussion).

Brain-Wide Signatures During Distinct SPW-R Episodes. To investigate the differentiated signature of each SPW-R subtype on brain-wide activity, we measured neural event-triggered fMRI (NET-fMRI) for a set of regions of interest (ROIs) (24). The occurrence of each SPW-R complex was used as a reference (trigger) to align and average the time course of the blood oxygenation level-dependent (BOLD) fMRI signal (see *Materials and Methods*). We defined the ROIs according to previously established functional specificity criteria (24). We analyzed the averaged *Z*-scored BOLD maps for each experimental session, across four animals. Because classical SPW-R (subtypes 2 and 3) have virtually identical ripple-triggered fMRI signature, they were averaged together. First, we tracked qualitative differences in brain-wide activations for the three remaining SPW-R subtypes (subtype 1, subtype 2–3, and subtype 4). As shown in the population analysis across all experimental sessions ($n = 12$ experimental sessions, 4 monkeys, Fig. 4*A*; see Fig. S9 *A* and *B* for examples in individual animals), the overall NET-fMRI time courses of all subtypes matches previously reported observations: cortical up-regulation and subcortical down-regulation. However, BOLD responses related to classical SPW-Rs exhibit the largest cortical up-regulations and subcortical down-regulations. In agreement with these observations, significant differences between BOLD activations of classical and nonclassical subtypes are observed in both neocortical and subcortical domains (KS test, $P < 0.02$; Fig. 4*B*), with larger effect over subcortical domains in the case of event subtype 1 (Fig. S9*C*).

We found no significant deactivation of subcortical structures associated with SPW-R subtype 1 (*t* test, Bonferroni-corrected, $P > 0.36$), with very low amplitude or no negative deviation from zero. Interestingly, SPW-R subtype 1 was related to increased neocortical BOLD responses compared with SPW-R subtype 4, the last being associated with weak cortical up-regulation, and subcortical down-regulations qualitatively comparable to that of subtypes 2–3. The grand average NET-fMRI results are shown in Fig. 5*A* for a large number of ROIs. We assessed how subtype 1 and subtype 4 differed from classical SPW-Rs (subtypes 2–3) in each ROI. Because ROI-associated NET-fMRI responses exhibit similar shapes across subtypes, presenting differences mostly in magnitude, we extracted the average NET-fMRI response over the full width at half absolute maximum and compared the magnitude of up- or down-regulation for each ROI across subtypes with univariate statistical tests corrected for multiple comparisons. We found significantly higher up-regulation during classical SPW-Rs than during nonclassical SPW-Rs within the hippocampal formation, and in cortical associative areas (posterior

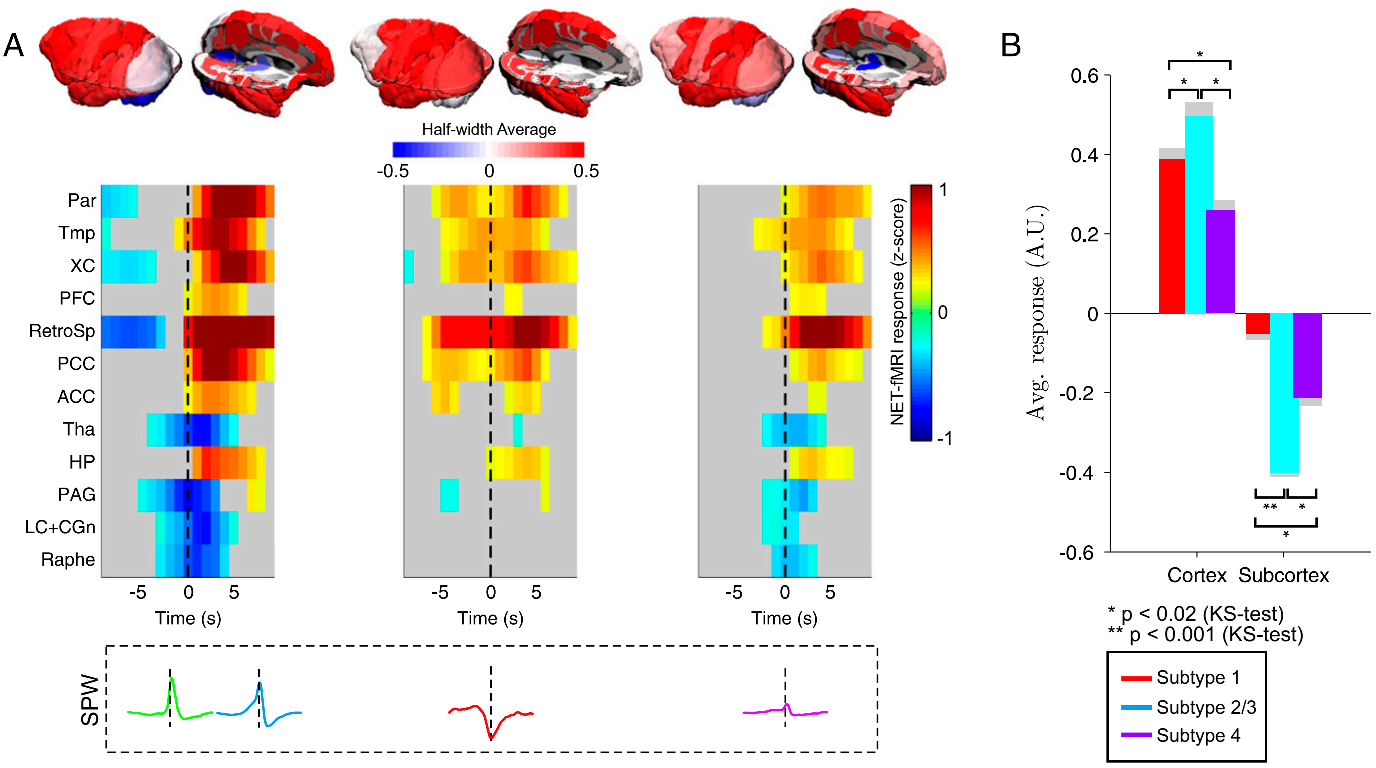

Fig. 4. Ripple-triggered NET-fMRI associated with SPW-R subtypes. (*A*) Absolute averaged BOLD full-width at half absolute maximum, illustrating that significant activation related to subtype 1 occurs almost exclusively for neocortex. Event subtypes 2 and 4 present heterogeneous activations across all brain domains (*Top*). Averaged BOLD time courses show differentiated neocortical activations and subcortical deactivations for distinct event subtypes in *Z*-score units across 12 experimental sessions, 4 animals. The gray regions in the previous plots represent activations below a 0.3-*Z*-score-units threshold to ease visualization (*Bottom*). (*B*) Averaged cortical and subcortical BOLD responses computed using the first singular-value decomposition (SVD) component (Fig. S9).

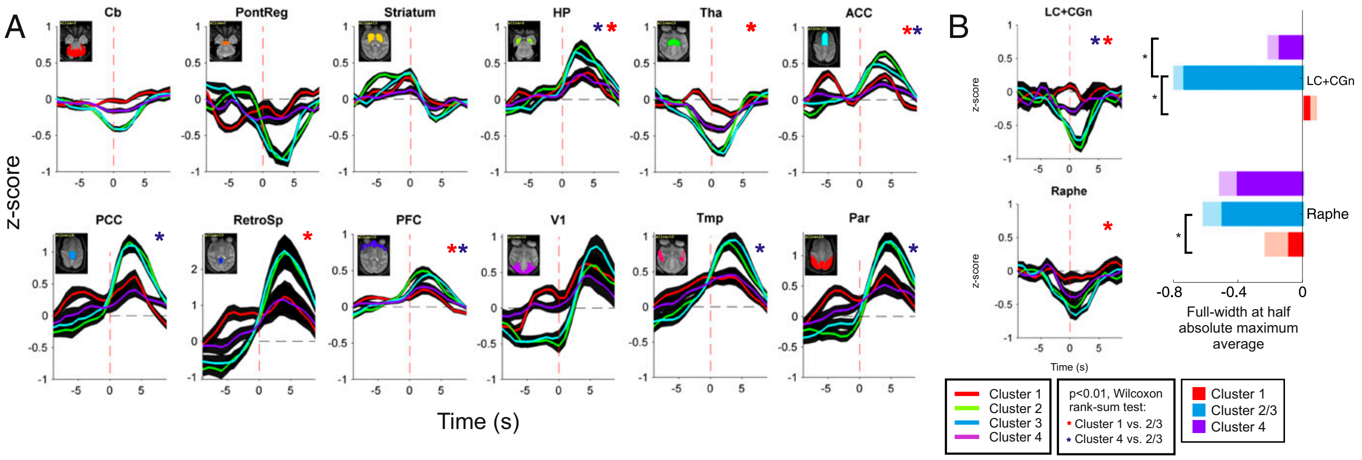

Fig. 5. Population ripple-triggered NET-fMRI time course in ROIs for each SPW-R subtype. (*A*) Average BOLD response show differentiated activations (all experimental sessions) of hippocampus (HP), thalamus (Tha), posterior and anterior cingulate cortices (PCC, ACC), retrosplenial area (RetroSp), and prefrontal (PFC) and parietal (Par) cortical areas (significant differences are indicated by asterisks). Black-shaded areas indicate SEM. (*B*) Average NET-fMRI responses (full width at half-maximum) show differentiated contributions of two neuromodulatory structures, dorsal raphe nucleus (serotonergic) and locus coeruleus (noradrenergic), to the SPW-R phenomenon (Fig. S10).

and anterior cingulate cortex, retrosplenial area, prefrontal, temporal, and parietal cortices) (Fig. 5*A*).

In support of previous analyses, nonclassical SPW-Rs gave rise to differences between subcortical down-regulation profiles. Detailed statistical analysis of all subcortical ROIs showed that differentiated BOLD activations occur in periaqueductal gray (PAG), thalamus, mesencephalon, locus coeruleus (LC), and dorsal raphe nucleus (Fig. S10*B*). The last two areas are neuromodulatory structures known to exert control on the overall brain state, and may influence the emergence of SPW-Rs. Notably, we found that, compared with classical SPW-Rs, subtype 1 (Fig. 5*B*, red curves) was associated with weaker deactivation of LC and raphe [$P < 0.002$, pairwise Wilcoxon rank-sum test, false-discovery rate (FDR) corrected with $q_{FDR} < 0.05$] (Fig. 5*B*, red bars). In contrast, during the occurrence of SPW-R subtype 4, deactivation of the raphe was comparable to that of classical SPW-Rs ($P > 0.1$, Wilcoxon rank-sum test, FDR corrected with $q_{FDR} < 0.05$), but LC down-regulation was significantly weaker ($P < 0.002$, pairwise Wilcoxon rank-sum test, FDR corrected with $q_{FDR} < 0.05$) (Fig. 5*B*, purple bars).

Discussion

In the present study, we identified—for the first time (to the best of our knowledge)—distinct subtypes of in vivo SPW-R patterns in a single recording site, displaying qualitative and quantitative electrophysiological differences. Our procedure reliably clusters the perievent time series into a number of event subtypes; examines their characteristic properties, such as their frequency content, amplitude, and frequency of occurrence; and maps the topology and dynamics of brain-wide metabolic activity at the time of event occurrence.

This approach revealed the existence of four hippocampal SPW-R subtypes with differentiated mesoscopic and brain-wide dynamics. Subtype identification relied on the presence of a SPW pattern in the LFP trace and its shape. The characteristics of SPW patterns and ripple oscillations in the hippocampal CA1 subfield suggested differences in subthreshold activity of the underlying neural populations. Importantly, such differences at the mesoscopic level were complemented by differences in brain-wide signatures mapped with NET-fMRI. Our results demonstrate significant modulation of two brain-wide networks linked to hippocampal-dependent memory functions: one involving associative neocortex, and another one involving subcortical and specifically neuromodulatory structures.

It is unlikely that our results are an effect of fluctuations in the levels of anesthesia (in the case of the four anesthetized animals), because the low-frequency LFP activity over the theta range was stable over time for each experimental session. Furthermore, the occurrences of SPW-R complex subtypes showed no apparent clustering in time for different event types and were comparable to those observed in experimental sessions from one drug-free animal, recorded during quiet wakefulness.

Identification of Four Subtypes of the SPW-R Phenomenon. We have demonstrated that hippocampal LFP dynamical variability during SPW-Rs can be summarized into four typical signatures. Each signature corresponds to a specific relationship between SPWs and ripple oscillations: high-frequency oscillations preceding, following, or coinciding with the peak of the SPW of dendritic depolarization, as well as high-frequency oscillations with no clear SPW signature. Such highly structured variability suggests differentiated underlying neural mechanisms, possibly associated with different memory-related functions.

Some SPW-R subtypes reported in the present work are in agreement with recently reported SPW-R signatures in slice models (32, 33). However, Hofer et al. (32) report only two event classes based on the SPW polarity in CA3. In contrast, Reichinnek et al. (33) have also observed two SPW-R event classes, differing only in SPW amplitude. The discrepancy between previously reported results and ours may be due to the chosen SPW-R detection protocol, solely based on SPW amplitude and visual inspection (33), and also to the limitations inherent to slice models, unable to reproduce the effect of long-range brain interactions.

The observed variability of LFP profiles during ripples suggests a different spatiotemporal repartition of extracellular currents in the CA1 microcircuits, possibly resulting from the differences in the recruitment of—and interactions between—the underlying neuronal subgroups. Indeed, several inhibitory and excitatory subgroups of neurons interact during SPW-R episodes, and their nonhomogenous spatial configuration can affect the spatial distribution of extracellular activity. For instance, Mizuseki et al. (34) report differential involvement of the two CA1 pyramidal sublayers, having distinct phase shifting with respect to the theta rhythm during rapid eye movement (REM) sleep, and they further indicate that REM shifting cells were more strongly associated with SPW-R activity, compared with that of non-REM shifting cells. Whether these two sublayers are differentially involved during SPW-R subtypes and are at the origin of the observed LFP characteristics remains an open question.

Another candidate for modulating the physiological properties of SPW-R is the influence of CA3. In particular, gamma oscillations during SPW-R are assumed to play a central role in coordinating CA3 and CA1 cell assemblies during memory replay (31). We discovered that a gamma rhythm is ubiquitous in all SPW-R subtypes. Specifically, we found a transient increase in gamma power concomitant with the occurrence of SPW-R episodes, and barring the detailed single-unit analysis, we found similar SWR-gamma correlates as those reported in ref. 31. Thus, gamma-related mechanisms mediating CA3–CA1 interactions during SPW-R episodes seem to be independent from the mechanisms generating the SPW-R diversity.

Additional discussion about the possible influence of the recording locations and the local circuits in stratum pyramidale within CA1 in relation to our results can be found in *SI Section D*. Although the above comments discuss modifications of hippocampal neural activity that might explain our LFP observations, we hypothesize that these changes may in turn result from the influence of other brain structures.

SPW-R Subtypes Relate to Differentiated Neuromodulatory Activities. Modulations in amplitude of the BOLD responses in subcortical domains suggest the involvement of two neuromodulatory structures directly connected to hippocampus in the SPW-R phenomenon, namely dorsal raphe nucleus and LC. Due to the transient nature of the examined neuronal events, the lack of clustering of the SPW-R subtypes, and their NET-fMRI correlates, it is likely that our study reflects short-duration "phasic" changes, rather than tonic neuromodulatory effects spanning over 10 s or larger timescales.

A dense noradrenergic and serotonergic innervation is present in the hippocampus proper, exerting modulatory effects in the activity of microcircuits. For instance, LC deactivation is involved in switching cortex and hippocampus to inactive states (35). However, LC neurons exhibit also phasic modes of activity, with bursts of activity of 15- to 70-ms duration, followed by a 300- to 700-ms period of suppression (36). Experimental evidence suggests that the timescales of interactions between LC and hippocampus (~1–2 s) (37) are compatible with the scale of occurrence of individual ripple episodes. Although the hypothesis that differentiated SPW-R complexes emerge partly as a result of LC inputs remains to be tested using more direct methods, it has been shown that decision making under uncertainty involves LC (38). Moreover, SPW-Rs are more frequent after task modifications, such as exposing an animal to a second novel environment (18).

In addition, nonclassical SPW-R subtypes may mark a differentiated involvement of the ascending serotonergic system. Notably, raphe projects to several subtypes of hippocampal GABAergic interneurons and may exert control on the *E–I* balance over local circuitry engaged during ripples via fast synapses (39). Moreover, the capacity of raphe projections to selectively influence well-segregated groups of hippocampal parvalbumin (PV) expressing interneurons has been recently stressed (40), raising the possibility of serotonergic control of neuronal circuits over timescales spanning the occurrence of single ripples (~200 ms). This view is further supported by a recent study where groups of the three major PV cell classes are differentially modulated during ripples, suggesting that fast network episodes involve distinct inhibitory circuits (41), modulated at timescales at which raphe–hippocampal modulations may occur.

Hippocampal–Neocortical Interactions May Contribute to SPW-R Variability. We showed that SPW-R subtypes 1 and 4 (nonclassical SPW-Rs) in the hippocampus consistently led to lesser activation across different cortical domains compared with SPW-R subtypes 2 and 3 (classical SPW-Rs). Because our experiments were performed in anesthetized macaque monkeys without any previous behavioral training, the robustness of our results across sessions suggests that these differentiated signatures reflect different types of brain-wide dynamical processes involving memory traces, not necessarily accounting for differences in memory content per se.

Differentiated activations were detected in the posterior and anterior cingulate (PCC, ACC) (42), PFC (43), and parietal cortices (44). One possible explanation for these results is that increased cortical activity marks enhanced recurrent interactions between neocortex and hippocampus during classical SPWs. Taking into account hippocampal connectivity, two recurrent mechanisms might account for differentiated SPW-R patterns. First, entorhinal cortex (EC) input may modulate CA1 activity by episodes of persistent activity that occur concomitantly with neocortical up-down state transitions (45). These neocortical–EC episodes develop at timescales similar to those of a typical burst of ripples, i.e., series of ripples with relatively short delays. Second, reentry may also be achieved at the scale of a single SPW-R event, through projections of medial entorhinal cortex (MEC) to CA1 stratum lacunosum moleculare (SLM) (46). Layer-specific activation of MEC would be followed by a local depolarization of SLM with the delay of a single synapse, thus influencing the time course of single SPW-Rs (46). In both scenarios, hippocampal activity could be controlled by recurrent activity within the local microcircuits and through cortico-hippocampal dialogue. These mechanisms might serve many purposes, such as volitional reactivation of a set of related memory traces or controlling the consolidation of new memories according to their relevance to preexisting memories and their reward value.

A Repertoire of Memory-Related Brain-Wide Events. To the best of our knowledge, the present study shows for the first time the existence of in vivo SPW-R subtypes occurring in the same recording site, and reflecting qualitative differences in brain activity within hippocampus and across cortical and subcortical domains. Processes such as memory reactivation, retrieval, and consolidation could exploit these brain-wide differences to fulfill different functions. Locally, the described SPW-R signatures may be the result of selective interactions between neuronal groups, involving varying degrees of network synchrony and dynamical *E–I* balance. This balance may be mediated by cortico-parahippocampal-hippocampal and subcortico-hippocampal interactions. Our results suggest these dynamical properties of local microcircuits are strongly intertwined with brain-wide interactions during SPW-R, possibly establishing distinct modes of selective processing and routing of information across multiple scales (*SI Section D*). The presented pattern classification will enable the characterization of SPW-Rs in behaving and natural sleep preparations and establish the functional role of each subtype. Finally, our approach could be used to better understand the underlying mechanisms of epileptiform events and more generally pathological phenomena (see ref. 47 for a perspective).

Materials and Methods

Surgical Procedures, Electrophysiology, and fMRI Recordings. Experimental and surgical procedures have been detailed in a previous study (27). In summary, a total of 242 experiments (10 min each) spread over 12 sessions were carried out in anesthetized male rhesus monkeys (*Macaca mulatta*). Head holders and recording chambers were located stereotaxically based on high-resolution anatomical MRI scans. Recordings were conducted in the anterior part of the hippocampus in the right hemisphere of each animal. All recording hardware, including the electrodes and amplifiers for simultaneous fMRI and multisite electrophysiological recordings, was developed at the Max Planck Institute for Biological Cybernetics. Custom-made, multicontact, NMR-compatible recording electrodes were made from a carbon fiber composite baton with 500-μm diameter (R&G). The 2.6-mm-long tip grounded down to a diameter of 250 μm. Electrodes contained 10 contacts spaced 150 μm apart, with 6–10 targeting the structure of interest. Recording electrodes were positioned around the pyramidal layer of the hippocampal CA1 subfield (8–14 mm anterior of the interaural line). Fine adjustment of the recording electrode was achieved by intermediate MRI anatomical scans. Functional imaging was carried out in a vertical 4.7-T scanner with a 40-cm-diameter bore (BioSpec 47/40v; Bruker BioSpin), in which each animal was positioned in a custom-made chair [see Logothetis et al. (24) for details on the gradient coil]. Typically, 22 axial slices were acquired, covering the entire brain (voxel size, $0.75 \times 0.75 \times 2$ mm^3). BOLD activity was acquired at a resolution of 2 s with two-shot gradient-echo echo-planar imaging images (repetition time/echo time, 1,000/20 ms; bandwidth, 150 kHz; flip angle, 53°; field of view, 96 × 96 mm; matrix, 96 × 96; 2-mm slice thickness). MRI data were analyzed off-line. During all experiments, anesthesia was maintained with remifentanil (0.5–2 $\mu g \cdot kg^{-1} \cdot min^{-1}$) in combination with a fast-acting paralytic mivacurium chloride (5–7 $mg \cdot kg^{-1} \cdot h^{-1}$), known to only mildly affect the magnitude and time course of neural and vascular responses (24, 48). All experimental and surgical procedures were approved by the local authorities (Regierungspraesidium, Tübingen Referat 35, Veteriärwesen) and were in full compliance with the guidelines of the European Community (EUVD 86/609/EEC) for the care and use of laboratory animals.

Processing and Analysis of Neural Data. Analyses of electrophysiology and fMRI data were performed using MATLAB (The MathWorks). Signal denoising, electromagnetic interference elimination, and frequency band isolation procedures have been described in detail in a previous study (24). In *SI Section A*, we describe the main signal processing and neuronal data analysis performed on the denoised broadband extracellular signals (0.05 Hz to 7 kHz).

ACKNOWLEDGMENTS. We acknowledge A. Ramírez-Cárdenas and D. Zaldivar for insightful comments and discussions on previous versions of this manuscript. J. Werner and M. Schnabel provided excellent technical support during the development of this work. This research was supported by the Max Planck Society.

1. Euston DR, Tatsuno M, McNaughton BL (2007) Fast-forward playback of recent memory sequences in prefrontal cortex during sleep. *Science* 318(5853):1147–1150.
2. Johnson LA, Euston DR, Tatsuno M, McNaughton BL (2010) Stored-trace reactivation in rat prefrontal cortex is correlated with down-to-up state fluctuation density. *J Neurosci* 30(7):2650–2661.
3. Kudrimoti HS, Barnes CA, McNaughton BL (1999) Reactivation of hippocampal cell assemblies: Effects of behavioral state, experience, and EEG dynamics. *J Neurosci* 19(10):4090–4101.
4. Lee AK, Wilson MA (2002) Memory of sequential experience in the hippocampus during slow wave sleep. *Neuron* 36(6):1183–1194.
5. Nádasdy Z, Hirase H, Czurkó A, Csicsvari J, Buzsáki G (1999) Replay and time compression of recurring spike sequences in the hippocampus. *J Neurosci* 19(21): 9497–9507.
6. Skaggs WE, McNaughton BL (1996) Replay of neuronal firing sequences in rat hippocampus during sleep following spatial experience. *Science* 271(5257):1870–1873.
7. Wilson MA, McNaughton BL (1994) Reactivation of hippocampal ensemble memories during sleep. *Science* 265(5172):676–679.
8. Buzsáki G, Horváth Z, Urioste R, Hetke J, Wise K (1992) High-frequency network oscillation in the hippocampus. *Science* 256(5059):1025–1027.
9. Ylinen A, et al. (1995) Sharp wave-associated high-frequency oscillation (200 Hz) in the intact hippocampus: Network and intracellular mechanisms. *J Neurosci* 15(1 Pt 1): 30–46.
10. Ego-Stengel V, Wilson MA (2010) Disruption of ripple-associated hippocampal activity during rest impairs spatial learning in the rat. *Hippocampus* 20(1):1–10.
11. Gerrard JL, Burke SN, McNaughton BL, Barnes CA (2008) Sequence reactivation in the hippocampus is impaired in aged rats. *J Neurosci* 28(31):7883–7890.
12. Girardeau G, Benchenane K, Wiener SI, Buzsáki G, Zugaro MB (2009) Selective suppression of hippocampal ripples impairs spatial memory. *Nat Neurosci* 12(10): 1222–1223.
13. Nakashiba T, Buhl DL, McHugh TJ, Tonegawa S (2009) Hippocampal CA3 output is crucial for ripple-associated reactivation and consolidation of memory. *Neuron* 62(6): 781–787.
14. Karlócai MR, et al. (2014) Physiological sharp wave-ripples and interictal events in vitro: What's the difference? *Brain* 137(Pt 2):463–485.
15. Foster DJ, Wilson MA (2006) Reverse replay of behavioural sequences in hippocampal place cells during the awake state. *Nature* 440(7084):680–683.
16. Singer AC, Carr MF, Karlsson MP, Frank LM (2013) Hippocampal SWR activity predicts correct decisions during the initial learning of an alternation task. *Neuron* 77(6): 1163–1173.
17. Dupret D, O'Neill J, Pleydell-Bouverie B, Csicsvari J (2010) The reorganization and reactivation of hippocampal maps predict spatial memory performance. *Nat Neurosci* 13(8):995–1002.
18. Karlsson MP, Frank LM (2009) Awake replay of remote experiences in the hippocampus. *Nat Neurosci* 12(7):913–918.
19. Jadhav SP, Kemere C, German PW, Frank LM (2012) Awake hippocampal sharp-wave ripples support spatial memory. *Science* 336(6087):1454–1458.
20. Muenzinger KF (1938) Vicarious trial and error at a point of choice: I. A general survey of its relation to learning efficiency. *Pedagog Semin J Genet Psychol* 53(1):75–86.
21. Carr MF, Jadhav SP, Frank LM (2011) Hippocampal replay in the awake state: A potential substrate for memory consolidation and retrieval. *Nat Neurosci* 14(2):147–153.
22. Skaggs WE, et al. (2007) EEG sharp waves and sparse ensemble unit activity in the macaque hippocampus. *J Neurophysiol* 98(2):898–910.
23. Bland BH, et al. (2003) Effect of halothane on type 2 immobility-related hippocampal theta field activity and theta-on/theta-off cell discharges. *Hippocampus* 13(1):38–47.
24. Logothetis NK, et al. (2012) Hippocampal–cortical interaction during periods of subcortical silence. *Nature* 491(7425):547–553.
25. Fritzke B (1995) A growing neural gas network learns topologies. *Adv Neural Inf Process Syst* 7:625–632.
26. Shi J, Malik J (2000) Normalized cuts and image segmentation. *IEEE Trans Pattern Anal Mach Intell* 22(8):888–905.
27. Csicsvari J, Hirase H, Mamiya A, Buzsáki G (2000) Ensemble patterns of hippocampal CA3-CA1 neurons during sharp wave–associated population events. *Neuron* 28(2): 585–594.
28. Patel J, Schomburg EW, Berényi A, Fujisawa S, Buzsáki G (2013) Local generation and propagation of ripples along the septotemporal axis of the hippocampus. *J Neurosci* 33(43):17029–17041.
29. Ji D, Wilson MA (2007) Coordinated memory replay in the visual cortex and hippocampus during sleep. *Nat Neurosci* 10(1):100–107.
30. van der Meer MA, Redish AD (2009) Low and high gamma oscillations in rat ventral striatum have distinct relationships to behavior, reward, and spiking activity on a learned spatial decision task. *Front Integr Neurosci* 3:9.
31. Carr MF, Karlsson MP, Frank LM (2012) Transient slow gamma synchrony underlies hippocampal memory replay. *Neuron* 75(4):700–713.
32. Hofer KT, et al. (2015) The hippocampal CA3 region can generate two distinct types of sharp wave-ripple complexes, in vitro: Hippocampal sharp-waves in vitro. *Hippocampus* 25(2):169–186.
33. Reichinnek S, Künsting T, Draguhn A, Both M (2010) Field potential signature of distinct multicellular activity patterns in the mouse hippocampus. *J Neurosci* 30(46): 15441–15449.
34. Mizuseki K, Diba K, Pastalkova E, Buzsáki G (2011) Hippocampal CA1 pyramidal cells form functionally distinct sublayers. *Nat Neurosci* 14(9):1174–1181.
35. Aston-Jones G, Bloom FE (1981) Activity of norepinephrine-containing locus coeruleus neurons in behaving rats anticipates fluctuations in the sleep-waking cycle. *J Neurosci* 1(8):876–886.
36. Aston-Jones G, Cohen JD (2005) An integrative theory of locus coeruleus-norepinephrine function: Adaptive gain and optimal performance. *Annu Rev Neurosci* 28(1): 403–450.
37. Yavich L, Jäkälä P, Tanila H (2005) Noradrenaline overflow in mouse dentate gyrus following locus coeruleus and natural stimulation: Real-time monitoring by in vivo voltammetry. *J Neurochem* 95(3):641–650.
38. Payzan-LeNestour E, Dunne S, Bossaerts P, O'Doherty JP (2013) The neural representation of unexpected uncertainty during value-based decision making. *Neuron* 79(1):191–201.
39. Freund TF, Gulyás AI, Acsády L, Görcs T, Tóth K (1990) Serotonergic control of the hippocampus via local inhibitory interneurons. *Proc Natl Acad Sci USA* 87(21): 8501–8505.
40. Varga V, et al. (2009) Fast synaptic subcortical control of hippocampal circuits. *Science* 326(5951):449–453.
41. Varga C, et al. (2014) Functional fission of parvalbumin interneuron classes during fast network events. *Elife* 3:e04006.
42. Maddock RJ, Garrett AS, Buonocore MH (2001) Remembering familiar people: The posterior cingulate cortex and autobiographical memory retrieval. *Neuroscience* 104(3):667–676.
43. Wierzynski CM, Lubenov EV, Gu M, Siapas AG (2009) State-dependent spike-timing relationships between hippocampal and prefrontal circuits during sleep. *Neuron* 61(4):587–596.
44. Salazar RF, Dotson NM, Bressler SL, Gray CM (2012) Content-specific fronto-parietal synchronization during visual working memory. *Science* 338(6110):1097–1100.
45. Isomura Y, et al. (2006) Integration and segregation of activity in entorhinal-hippocampal subregions by neocortical slow oscillations. *Neuron* 52(5):871–882.
46. Kloosterman F, van Haeften T, Lopes da Silva FH (2004) Two reentrant pathways in the hippocampal-entorhinal system. *Hippocampus* 14(8):1026–1039.
47. Kerber K, et al. (2014) Differentiation of specific ripple patterns helps to identify epileptogenic areas for surgical procedures. *Clin Neurophysiol* 125(7):1339–1345.
48. Goense JBM, Logothetis NK (2008) Neurophysiology of the BOLD fMRI signal in awake monkeys. *Curr Biol* 18(9):631–640.
49. Saleem KS, Logothetis NK (2007) *A Combined MRI and Histology Atlas of the Rhesus Monkey Brain in Stereotaxic Coordinates* (Academic, London).
50. Łęski S, et al. (2011) Inverse current source density method in two dimensions: Inferring neural activation from multielectrode recordings. *Neuroinformatics* 9(4): 401–425.
51. Kortelainen J, Väyrynen E, Seppänen T (2011) Depth of anesthesia during multidrug infusion: Separating the effects of propofol and remifentanil using the spectral features of EEG. *IEEE Trans Biomed Eng* 58(5):1216–1223.
52. Battaglia FP, Sutherland GR, McNaughton BL (2004) Hippocampal sharp wave bursts coincide with neocortical "up-state" transitions. *Learn Mem* 11(6):697–704.
53. Seber GAF, Wild CJ (1989) Computational methods for nonlinear least squares. *Nonlinear Regression* (Wiley, Hoboken, NJ), pp 619–660.

54. Fritzke B (1994) Growing cell structures—a self-organizing network for unsupervised and supervised learning. *Neural Netw* 7(9):1441–1460.
55. Martinetz TM, Berkovich SG, Schulten KJ (1993) Neural-gas' network for vector quantization and its application to time-series prediction. *IEEE Trans Neural Netw* 4(4):558–569.
56. Yu SX, Shi J (2003) Multiclass spectral clustering. *Proceedings of the Ninth IEEE International Conference on Computer Vision* (IEEE, Washington, DC), pp 313–319.
57. Smola AJ, Kondor R (2003) Kernels and regularization on graphs. *Learning Theory and Kernel Machines,* Lecture Notes in Computer Science, eds Schölkopf B, Warmuth MK (Springer, Berlin), Vol 2777, pp 144–158.
58. Desgraupes B (2013) *Clustering Indices*. Available at https://cran.r-project.org/web/packages/clusterCrit/vignettes/clusterCrit.pdf. Accessed February 17, 2014.
59. Bokil H, Andrews P, Kulkarni JE, Mehta S, Mitra PP (2010) Chronux: A platform for analyzing neural signals. *J Neurosci Methods* 192(1):146–151.
60. Hájos N, et al. (2013) Input-output features of anatomically identified CA3 neurons during hippocampal sharp wave/ripple oscillation in vitro. *J Neurosci* 33(28):11677–11691.
61. Sullivan D, et al. (2011) Relationships between hippocampal sharp waves, ripples, and fast gamma oscillation: Influence of dentate and entorhinal cortical activity. *J Neurosci* 31(23):8605–8616.
62. Buzsáki G, et al. (2003) Hippocampal network patterns of activity in the mouse. *Neuroscience* 116(1):201–211.
63. Schölkopf B, Smola AJ (2001) *Learning with Kernels: Support Vector Machines, Regularization, Optimization, and Beyond* (MIT, Cambridge, MA).
64. Lee S-H, et al. (2014) Parvalbumin-positive basket cells differentiate among hippocampal pyramidal cells. *Neuron* 82(5):1129–1144.
65. Sørensen JC, Tønder N, Slomianka L (1993) Zinc-positive afferents to the rat septum originate from distinct subpopulations of zinc-containing neurons in the hippocampal areas and layers. A combined fluoro-gold tracing and histochemical study. *Anat Embryol (Berl)* 188(2):107–115.

Supporting Information

Ramirez-Villegas et al. 10.1073/pnas.1518257112

SI Section A: Neural Data Analysis Methods

Estimate of Changes in the Level of Anesthesia. The theta LFP band was used to estimate changes in the level of anesthesia during individual experimental sessions in anesthetized animals (23, 51). Raw data experiments were divided into two parts (5 min each). Signals were filtered in the theta frequency band (4–8 Hz) and were then rectified using the Hilbert transform and averaged across recording sites (only for plotting purposes). Spectral power, on the other hand, was estimated using the nonfiltered signal (0.5–300 Hz) across 15 frequencies in this band using Morlet-wavelet spectrograms. Power estimates from 50 randomly chosen time windows of 1 min were compared statistically using a paired-samples permutation t test. This statistical test was performed in 242 experiments separately. A P value of 0.05 was considered a statistically significant difference.

Selection of SPW-R Events. Following a methodology presented in Logothetis et al. (24), we examined changes of power in the broadband signal (10–250 Hz). In addition to anatomical criteria, we classified the electrode recording tips into stratum radiatum (SR) and stratum pyramidale (PL) tips, based on visual tracking of oscillations with distinct frequency contents (complex spike features, ripple or gamma-like high-frequency events and low-frequency sharp waves) and observing synchronous activity across recording sites. The broadband signal was rectified, low-pass filtered at 20 Hz, and then normalized. Candidate events were detected as epochs during which the signal exceeded a 3.5 SD threshold. Because increases in power may result from oscillations occurring in different frequency bands, we clustered the spectra using nonnegative matrix factorization (NNMF), an unsupervised algorithm that creates data decompositions for a user-defined number of components. Stable representation of the data was achieved using three components, corresponding to increases over different frequency bands, namely sigma (8–22 Hz), gamma (25–75 Hz), and ripple (80–180 Hz).

Ripple events clustered using the NNMF procedure were considered "candidate ripples." All candidate ripple events must be highly localized in time and distinguish themselves from any spurious baseline ripple-band activity or brief oscillatory episode. To ensure that all selected events were genuine ripples, a higher threshold was applied for ripple event selection. To this end, all candidate ripples were filtered in the ripple band (80–180 Hz) with a fourth-order Butterworth bandpass filter. We selected ripples exceeding a threshold of 5 SD, a higher threshold than that reported in previous research in rats and monkeys (16, 22, 27, 28, 52). We further refined the procedure with a "ripple time-localization criterion": a Gaussian function was fitted to the envelope of the signal filtered in the ripple band using nonlinear least squares (53). Only events with a fitted width of 50 ms $\leq \sigma \leq$ 150 ms and r^2 greater than 0.6 ($r \geq 0.77$) were taken into account for further processing.

Clustering of SPW-R LFP Time Series. Cluster analysis was applied to each experimental session separately. Perievent SPW signal time courses were used for clustering. After low-pass filtering with a cutoff frequency of 20 Hz, distortion of waveforms induced by hardware filtering was corrected by numerical temporal integration of the wave form (given that our hardware filtering acted as a temporal derivative in this frequency band). For the first stage of the clustering approach, the spatiotemporal SPW-R series were grouped in 200 representative signals using a growing neural gas (GNG) algorithm (25) (see *SI Section B* for mathematical details). Each representative signal (also called "node") corresponds to the average of a group of raw perievent signals with similar time courses (reduced pairwise Euclidean distance). Because representative signals are easier to cluster due to noise reduction, in the second step, we clustered these representative signals based on their pairwise cosine similarity matrix using the normalized cuts algorithm, a clustering technique that creates partitions in the data by maximizing the overall similarity of the signals to be included in a given cluster (26). SPW-Rs were sorted and then averaged across sessions.

This procedure was performed for SPW-R data from each experimental session (~11,000 SPW-R complexes) using up to 14 cluster partitions and 200 repetitions. We chose the optimal number of cluster partitions based on how well separated the distinct clusters were. We devised a cluster validity measure to have an objective measure of the clustering quality across clustering partitions. This measure quantifies the ratio of the pairwise intracluster similarity to the pairwise intercluster similarity, in the following referred to as the normalized cuts index (NCI). In addition, we used well-known clustering quality measures that typically compare the distances between signals belonging to a given cluster to those belonging to distinct clusters. Because all clustering quality values are normalized measures, across-sessions statistics were computed by pulling together the values obtained for each session ($n = 12$ experimental sessions). Finally, we devised a consistency procedure to validate the results of the clustering (see details below).

The GNG Network. The GNG, originally proposed by Fritzke (25, 54), is an incremental self-organizing network of "codebook" vectors that fits an arbitrary topology, incorporating a growing mechanism. Connections between the vectors in the network are developed dynamically as the number of vectors in the network grows over time.

The network topology is initialized with randomly generated codebook vectors connected by edges and covering the input space (matching the number of dimensions of the input data). During one iteration of the network's training stage, a data point is randomly selected and the closest codebook vector is iteratively updated following a simple learning rule:

$$w_j(t+1) = w_j(t) + \varepsilon_b\left[x^\mu - w_j(t)\right], \qquad \textbf{[S1]}$$

where w_j is the closest codebook vector to the μth input data point and $\varepsilon_b \in [0,1]$ is a constant learning rate.

The topological arrangement of the network is represented by edges connecting codebook vectors, thus defining "topological neighborhoods." A connection between two nodes is created (or "strengthen") if the two nodes happen to be the nearest to a given input signal. These topological neighborhoods allow us to cluster the data more easily, because data points with similar time courses tend to be connected.

GNG is a graph of connected data points (representative vectors) that grows over time. The insertion policy of the GNG based on tracking representative vectors with large error variables along with the establishment of a topological neighborhood adaptation is somewhat equivalent to a stochastic gradient descent rule: vectors move in the input space together with their topological neighbors, and new vectors are inserted over large-error areas, i.e., over areas where the network has not yet fitted adequately the input data (55).

Clustering the GNG (Connection to Normalized Cuts Criterion). The codebook vectors obtained by the GNG are clustered as follows: let $G(V,E)$ be a neural network forming a graph, with codebook vector as vertices in the set V and edges in the set E. If we add a weight on each edge, denoted W_{ij} as a function of the cosine similarity between the codebook vectors i and j being linked by the edge, we may denote the weighted graph as $G(V,E,W)$. The normalized cuts criterion seeks to partition the set of codebook vectors (vertices of the graph) into several sets, such that we maximize the fraction of total weights within a group with respect to the total weights of all member nodes in the graph (26, 56). Thus, given a partition of V, $\Gamma_V^K = \{V_1, .., V_K\}$, the objective function to maximize is:

$$\varepsilon\left(\Gamma_V^K\right) = \frac{1}{K}\sum_{l=1}^{K}\frac{\sum\limits_{i\in V_l, j\in V_l} W(i,j)}{\sum\limits_{i\in V_l, j\in V} W(i,j)}. \qquad \textbf{[S2]}$$

In practice, an N-by-K partition matrix X is used to represent Γ_V^K, where $X = [X_1, ..., X_K]$ and $X(i,l) = 1$ if $i \in V_l$, i.e., if the codebook vector i belongs to the cluster V_l; otherwise $X(i,l) = 0$. We can notice that there is an implicit exclusion constraint on $X : X1_K = 1_N$, where 1_N denotes a N-by-1 vector of all 1's. The neural network graph clustering problem is then formulated as follows:

$$\text{maximize } \varepsilon\left(\Gamma_V^K\right) = \frac{1}{K}\sum_{l=1}^{K}\frac{X_l^T W X_l}{X_l^T D X_l}, \qquad \textbf{[S3]}$$

$$\text{subject to } X \in \{0,1\}^{NxK}$$

$$X1_K = 1_N,$$

where $D = \text{diag}(W1_N)$ is the degree matrix, i.e., gathering on its diagonal the total weight of connections of each codebook vector. The computational solution of the above problem reduces to a generalized eigenvalue system.

Validation of the Clustering Procedure. To help determine whether SPW-R complexes were truly clustered, or they only existed as part of some continuum, we used two procedures: (*i*) clustering quality analysis, and (*ii*) clustering consistency analysis (see details below).

i) After running the clustering algorithm for several numbers of clusters (for up to 14 clusters), we compared the quality of the outcome quantitatively and qualitatively using clustering quality indices, together with low-dimensional projections of the original datasets (via Laplacian Eigenmaps, described in detail in ref. 57), respectively.

To assess the quality of the outcome of the Normalized Cut approach, we use the NCI, which corresponds to the value of the objective function described in Eq. **S3** at its optimum (when the Normalized Cut Algorithm has converged). NCI is used to estimate the quality of the clustering for different numbers of clusters.

We also assessed the clustering quality using the following classical indices: silhouette index, Davies–Bouldin (DB) index, and C index (58). Briefly, the silhouette for each cluster (or across clusters) is a measure defined in the range [−1, 1] and the best clustering partition is achieved when the silhouette index approaches 1. Furthermore, the DB index is a classical index suited to compact and well-separated clusters; we note that good clustering partitions are obtained as $DB \rightarrow 0$, because this measure is the ratio of the intracluster distances to the distances between the clusters' barycenters. Finally, the C index compares the total sum of the pairwise distances in each cluster and the smallest pairwise distances in the data against an equivalent number of the largest pairwise distances. An optimal cluster partition is obtained when $C \rightarrow 0$.

ii) To check the stability of our clustering results, we devised an internal consistency procedure amenable to single experimental sessions, and several repetitions per session. To this end, 75% of each SPW-R dataset was taken as training set, and the remaining 25% was taken as test set. Training and test groups were balanced on the basis of the original cluster labels established a priori for the whole dataset, so that the marginal probabilities of ripple types remained equal. Training sets were further divided in two halves to train two GNGs independently, for each session. Clustering consistency of both GNGs was then measured on remaining test set, using the following equation:

$$Q^{\mu} = 1 - \frac{1}{N}\sum_{i=1}^{N} F\left(x_i^{\mu} - y_i^{\mu}\right), \qquad \textbf{[S4]}$$

where x_i^{μ} and y_i^{μ} are the ith cluster labels of the μth repetition, N is the total number of signals in the test set, and $F(x)$ is described by the following function:

$$F(x) = \begin{cases} 0 & x = 0 \\ 1 & \text{otherwise} \end{cases}. \qquad \textbf{[S5]}$$

Thus, when the sets cluster labels $X^{\mu} = \{x_1^{\mu}, x_2^{\mu}, ..., x_N^{\mu}\}$ and $Y^{\mu} = \{y_1^{\mu}, y_2^{\mu}, ..., y_N^{\mu}\}$ are identical, the consistency takes value 1 (or 100% consistency).

SPW-R Features and Morlet-Wavelet Spectrograms. Four different features were computed for each of the SPW-R signatures from the previous clustering procedure, namely normalized SPW amplitude, ripple power, number of oscillations exceeding 50% of the peak of the ripple oscillation, and frequency peak in the ripple band. Ripple power was computed as the average of the squared, filtered signal in the ripple band (80–180 Hz). In addition, spectral analysis was performed using Morlet-wavelet spectrograms. The spectrograms were Z scored with respect to spectrograms computed using the same number of events with randomized inter-event intervals. Ripple-band frequency peaks for each event were extracted using this spectral technique. Barring the number of oscillations feature, all features and spectra were Z scored with respect to baseline activity. In addition, we measured correlations between the aforementioned features using the standard Spearman rank correlation coefficient; a value of $P < 0.05$ was considered a statistically significant correlation.

Multiunit Spikes Analysis. Multiunit spike times were detected by threshold crossing (3 SD) of the high-pass–filtered extracellular signal (1,000-Hz cutoff frequency). Single units were not isolated due to constraints of the recording hardware. Spikes around each perievent SPW-R signal were pooled together and perievent time histograms were computed (bin size, 5 and 2 ms, as indicated in main text) with respect to random point processes of the same rate. Thus, only above-baseline activity is reported in the main text of this work. Perievent cross-correlation analysis between LFPs and spikes was performed for each event subtype using the cumulative number of multiunit spike events (9).

Spike-Field Coherence. Spike-field coherence (SFC) was computed for all recording sites located in the CA1 stratum pyramidale, across all SPW-R broadband signal events using a tapering window duration of 200 ms with an increment of 10 ms, using the Chronux toolbox available at chronux.org (59). This process outputs a complex-valued matrix $F \times n_t \times M$, where n_t refers to the length of the perievent time windows, F is the number of frequencies (regularly spaced between 0 and 200 Hz), and M is the total number of ripple events. Complex-valued coefficients of this matrix account for the entrainment between LFP and spikes at particular frequency and time points. Average absolute SFCs values within the same cluster label were averaged, resulting in four $F \times n_t$ absolute coherence matrices. To study the phase-locking properties of spikes to the LFP, the complex SFC coefficients were also normalized to an absolute value of 1 and the circular mean of the normalized maps was computed for each cluster subtype, resulting in phase-locking maps described by their magnitude [phase-locking value (PLV)] and phase (in the range $[-\pi, \pi]$ radians).

fMRI Data Processing. Preprocessing of the MRI data has been described in a previous study (24). Briefly, linear trends were removed and bandpass filtering (0.01–0.4 Hz) was applied for temporal noise reduction. Due to the slow nature of the BOLD signal, we excluded events with overlapped BOLD time courses in a time window of $[-5, 5]$ s. Maps from different sessions were computed using Hotelling's T^2 statistic. BOLD activations were subsequently averaged and compared across triggering SPW-R events. For qualitative analysis, contrast maps were computed as the average difference between activations associated with paired event types across experimental sessions. Statistical significance for the differences between full-width at half-maximum BOLD activations was tested later on using the Wilcoxon rank-sum test. All statistical tests were FDR corrected.

SI Section B: Supporting Results on SPW-R Complexes Subtypes

Putative Fluctuations on the Anesthesia Level. To check the influence of the fluctuations of the level of anesthesia on the occurrence of event subtypes, event raster plots were superimposed to the rectified theta-band activity, showing no relationship between the occurrence of different types of SPW-R episodes and changes in the theta activity, used as a marker of the level of anesthesia (Fig. S1*A*, first two panels for anesthetized animals and third panel for one unanesthetized animal) (see also main text).

Clustering Quality Analysis. To measure the quality of the SPW-R clustering partition, we computed four clustering quality measures: NCI, silhouette index, DB index, and C index. Clustering quality analysis measures were consistent across experimental sessions and were put together for population analysis. NCI, on the one hand, was computed as a quality measure for the GNG graph clustering procedure across up to 14 partitions to quantify the optimal number of clusters present in the data. Based on this analysis, we concluded that the optimal number of clusters is 4 (Fig. S3*A*). On the other hand, silhouette, DB and C indexes were used to assess the clustering quality of the raw data points and compare the quality of the two-stage clustering procedure to the quality of a single-stage clustering procedure, i.e., clustering with no neural network as preprocessing stage.

Fig. S3*B* (*Left*) illustrates the silhouette indices for our two-stage clustering methodology, in comparison with the normalized graph cuts alone and to randomly permuted clusters. Positive silhouette values are suggestive of good clustering quality, whereas negative values indicate the opposite. Our two-stage methodology largely outperforms the normalized graph cuts ($P < 10^{-4}$, pairwise Bonferroni-corrected KS test). No significant differences were found across recording sites. Fig. S3*B* (*Middle*) illustrates the clustering quality assessment using DB indices. As in the previous case, we compared the two-stage methodology to the normalized graph cuts alone and to randomly permuted clusters. DB-index values close to zero indicate a good clustering quality and clusters are assumed compact and well separated. The two-stage methodology again outperforms the normalized graph cuts ($P < 10^{-5}$, pairwise Bonferroni-corrected KS test). No significant differences were found across recording sites. Finally, Fig. S3*B* (*Right*) illustrates the C-indices for our two-stage clustering methodology, in comparison with the normalized graph cuts alone and to randomly permuted clusters. C-index values close to zero indicate a good clustering quality, whereas higher values indicate the opposite. The two-stage methodology was deemed better than normalized graph cuts alone ($P < 10^{-5}$, pairwise Bonferroni-corrected KS test). In all of the previous cases, no significant differences were found across recording sites ($P < 0.1$, $P < 0.07$, and $P < 0.4$, respectively).

Finally, a typical GNG similarity matrix is depicted in Fig. S3*C*; the matrix is sorted according to the cluster label of each SPW-R representative. The matrix illustrates the pairwise cosine similarity between SPW-R representatives. Note that SPW-Rs of the same type remain heavily connected and bear strong similarity (greater than 0.7; brightest spots in the matrix account for connections between SPW-R representatives), whereas very few, sparse connections remain between SPW-Rs of distinct type. In addition, Fig. S3*D* depicts the Laplacian Eigenmap (58) (2D representation) of a typical GNG network, where each vertex corresponds to a SPW-R representative. Edges computed by the GNG algorithm (*SI Section A*) are shown as solid black lines. Note that clusters remain well separated, despite their high dimensionality. This result suggests that it is unlikely that distinct SPW-R signatures are a continuum of variations of the same phenomenon.

Consistency of the Clustering Procedure. Clustering consistency was then measured for each experimental session, for a total of 100 repetitions. Session results were averaged individually, and results were pooled together for population statistics. We found that clustering consistency across experimental sessions was significantly higher than chance ($P < 10^{-6}$, t test; mean value with 95% confidence interval for clustering consistency across 12 experimental sessions, 74.17 ± 1.63%).

We next examined the classification changes underlying the performance of the clustering consistency procedure. More specifically, we asked which SPW-R categories most of the inconsistently classified SPW-Rs were associated to. We addressed this question by constructing a "confusion matrix," averaged across cross-validations. Our results show that SPW-R subtypes 2 and 3 were inconsistently classified slightly more often than other subtypes, likely due to their similar time courses (Fig. S3*E*). Likewise, the least inconsistently clustered subtype was subtype 1, probably because its time course is anticorrelated with respect to the time course of other SPW-R signatures.

Variations in Amplitude, Frequency Content, and Statistics of SPW-R Events. We compared the four SPW-R types on the basis of normalized absolute sharp-wave amplitude (Fig. S5*A*), ripple power (defined as the average of the squared, filtered signal) (Fig. S5*B*), number of oscillations above 20% of the ripple oscillation peak (Fig. S5*C*), and frequency peak of the ripple (band, 80–180 Hz) (Fig. S5*D*).

This analysis revealed statistically significant differences across clusters for the Z-scored sharp-wave amplitude (mean values in Z-score units with 95% confidence intervals, -0.9414 ± 0.0609, 1.4279 ± 0.0572, 1.5380 ± 0.0600, 0.4627 ± 0.0425, respectively; pairwise bootstrapped KS test, $P < 10^{-6}$, Bonferroni corrected) and frequency peak of the ripple (mean values with 95% confidence intervals, 110.56 ± 1.09, 127.14 ± 0.91, 125.35 ± 0.95, and 115.53 ± 0.83, respectively; pairwise bootstrapped KS test, $P < 10^{-6}$, Bonferroni corrected). In contrast, no significant differences were observed for ripple power (mean values in Z-score units with 95% confidence intervals, 2.7410 ± 0.0542, 3.0094 ± 0.0604, 2.9230 ± 0.0553, and 2.8120 ± 0.0436, respectively; pairwise bootstrapped KS test, $P > 0.05$, Bonferroni corrected) and the number of oscillations above 50% of the ripple oscillation peak (mean values with 95% confidence intervals, 5.4068 ± 0.0922, 5.7088 ± 0.0704, 5.6842 ± 0.0718, and 5.4615 ± 0.0681, respectively; pairwise bootstrapped KS test, $P < 0.1$).

SPWs and ripples have correlated time courses and correlated features (28, 31, 60, 61). In particular, we studied the relationship between ripple power and sharp-wave amplitude and also between ripple frequency peak and sharp-wave amplitude. We conducted regression analyses to quantify such relationships. Consistent with our spectral analysis reported in the main text, we found that ripple power correlated positively to sharp-wave amplitude ($R = 0.4534$; $P = 0.0001$) and this relationship is observed for each type of SPW-R (Fig. S5 *E* and *F*). Analogously, frequency peak in the ripple band (80–180 Hz) correlated positively to sharp-wave amplitude ($R = 0.3548$; $P = 0.0001$). In all subtypes, both the ripple-band frequency peak and ripple power remained relatively localized (Fig. S5 *E* and *F*).

In addition to their specific amplitude and frequency properties, a vast body of evidence suggests that SPW-R events do not happen randomly (4, 27, 62). First, we examined how different event types occurred over time. Fig. S7*A* shows two typical event raster plots across different experiments of two different experimental sessions. SPW-R events tend to happen with no apparent clustering along the time course of an experimental session. To examine potential differences in "bursting" behavior, we computed the autocorrelation density of each event type (Fig. S7*C*) and found that classical sharp-wave ripples are autocorrelated to a significantly higher extent than other types of sharp-wave ripples. It is noteworthy that the rate of each event subtype across experiments is comparable (Fig. S7*B*).

SPW-R Subtypes in LFP Recordings from One Unanesthetized Animal. We asked whether the same SPW-R classification would apply for drug-free animals. In correspondence with each SPW-R pattern in Fig. 2*A*, Fig. S6*A* shows equivalent SPW-R patterns in one unanesthetized (drug-free) animal (monkey *b04*), recorded during quiet wakefulness. Single-event broadband (0.5–300 Hz) traces show remarkable similarity with those detected in anesthetized animals. Single-event ripples and broadband spectral profiles (Fig. S6*B*, third and bottom panels, respectively) display significant power increase in the ripple band. Both SPW and ripple features were encountered in good agreement with the anesthetized data (Fig. S6 *D* and *E*). Notably, both positive and negative SPW deflections were prevalent and the spectra of fast oscillations were localized in the ripple frequency range. Classical ripples had higher frequency peaks and power as in their anesthetized counter parts (mean values in hertz with 95% confidence intervals, 96.7325 ± 1.8008, 112.5978 ± 3.1107, 113.7546 ± 3.2415, and 98.7585 ± 2.3142, respectively; pairwise bootstrapped KS test, $P < 0.001$, Bonferroni corrected). However, in this case, both classical and nonclassical ripples had more localized ripple-band spectral distributions (Fig. S6*F*). This effect could be explained by state-dependent differences between ripples (31). In this case, quiet wakefulness ripples present lower frequency peak in the ripple frequency band, compared with off-line–state ripples.

Predicting SPW-R Subtypes from BOLD fMRI Time Courses. To assess how different these responses were between subtypes, we first used a multivariate predictive approach. We trained a multiclass linear SVM classifier (63) to predict the SPW-R subtype using the time course of all ROIs averaged over a few experiments. The classifier trained in this way could not distinguish between the BOLD responses related to subtypes 2 and 3, which have virtually identical ripple-triggered fMRI signature. We thus pooled them together for further comparison. We next predicted SPW-R subtype 1, against subtype 4, against pooled SPW-R subtypes 2 and 3, which resulted in an average of 72.87 ± 6.19% (mean with 95% confidence interval) cross-validation accuracy. We then quantified the discriminative power of each ROI by counting the fraction of time points from each ROI that were attributed a large coefficient by the classifier for distinguishing between all subtypes. We found that largest differences between the classical and nonclassical SPW-R subtypes mostly involve associative cortical areas and neuromodulatory systems. Furthermore, the largest differences between subtype 1 and subtype 4 involve solely associative cortical areas, consistent with previous analysis (*Results* in the main text).

It is worth noting that the SVM classifier trained in this way is not in a one-to-one correspondence to predicting the occurrence of SPW-R complexes from ongoing BOLD fMRI activity. Addressing such a question goes beyond the scope of the present work and shall be part of a future investigation.

SI Section C: Supporting Results on SWR-Related Gamma Oscillations

Since ripple oscillations from CA3 and CA1 are largely incoherent (61), it is unlikely that synchronization in this band coordinates the activity in both subfields during memory replay. Instead, gamma oscillations during SPW-R have been recently suggested to play this role in a recent study (31). In the following sections, we address whether such oscillations are present in our monkey recordings, and how they relate to specific SPW-R subtypes, possibly reflecting differentiated levels of coordination between CA3 and CA1.

SPW-R Detection Procedure, "Pure" and "Nonpure" Events. In the present work, detection of oscillatory events is first performed using the following procedure [following Logothetis et al. (24)]. Candidate events are detected using the smoothed envelope of the broad-band LFP signal (10–250 Hz) (we set 3.5 SD as threshold). Events' spectral signatures were clustered using the NMF algorithm as explained in *SI Section A*, thus establishing three event groups with distinct spectra. We examined how well a single factor of the NMF could explain the observed power spectrum of individual events. For this, we computed a signal-to-noise (SNR) ratio, defined as the ratio of the sum of the squared power spectrum values to the sum of the squared difference of the spectrum, from its projection on a single factor. Events with unimodal (or close to unimodal spectral distribution) associated to a factor SNR > 3 were selected as pure events. These events are the ones reported in the main text of this work, in correspondence with those reported in ref. 24. However, there are not only ripple events with SNR ≤ 3 but also sigma and gamma episodes with SNR ≤ 3 that may have substantial power in the ripple frequency band (80–180 Hz), even at or above a 5 SD threshold and well localized in time according to our previous ripple selection criteria. The compound of all detected events with SNR ≤ 3 that had substantial power in the ripple band are henceforth referred to as nonpure SPW-R events and were analyzed separately in the present section of *Supporting Information*.

Nonpure SPW-Rs Also Come in Four Subtypes. Following the event detection procedure, we applied the stringent criteria for SPW-R detection described previously in *SI Section A*. We next used our two-step methodology to cluster nonpure SPW-R episodes time series. We applied the algorithm to the nonpure SPW-Rs of 12 experimental sessions (a total of ~10,000 nonpure SPW-R complexes were in compliance with our stringent ripple selection criteria). The results of the clustering were consistent across experimental sessions and animals. Furthermore, our clustering quality analysis revealed that nonpure SPW-R complexes are best represented by four LFP signatures (Fig. S8 *A* and *B*).

Fig. S8*A* depicts the nonpure SPW-R LFP grand averages, in close correspondence with pure SPW-R LFP signatures ($n = 12$ experimental sessions, 4 animals). Population Morlet-wavelet spectra for each pure and nonpure SPW-R subtype are depicted in Fig. S8*C*. Both pure and nonpure SPW-Rs presented enhanced power profiles over gamma frequencies (25–75 Hz), where nonpure events displayed the largest power over such frequency range.

However, spectral profiles of pure and nonpure events were remarkably consistent over the SPW and ripple frequency bands. We found that nonpure classical ripples had higher frequency peaks (mean values with 95% confidence intervals, 106.90 ± 1.0900, 119.4697 ± 1.0260, 118.2110 ± 1.0985, and 105.1701 ± 0.4481, respectively; pairwise bootstrapped KS test, $P < 0.0007$ for the difference between frequency peaks, Bonferroni corrected). Notably, nonpure SPW-R complexes presented virtually the same coupling of the SPW wave form to the ripple onset as their pure counterparts (see polar histograms on Fig. S8*D*). We found that classical ripple signatures and only one nonclassical signature (subtype 1, depicted in red) presented statistically significant coupling to the SPW (mean values with 95% confidence interval, −2.9406 ± 0.0292, −0.2535 ± 0.0137, 0.1091 ± 0.0065, and −1.0074 ± 0.1613; and $P < 10^{-6}$ and $P > 0.05$ permuted KS test for the phase coupling, respectively). Moreover, ripple-to-SPW coupling was statistically different among all nonpure SPW-R subtypes ($P < 10^{-6}$, permuted KS test). We now investigate the fine properties of nonpure events and the relation of pure and nonpure SPW-R signatures to the observed gamma component.

Variations in Amplitude, Frequency Content, and Statistics of Nonpure SPW-R Events. As in our analysis for pure events, we compared the four SPW-R types on the basis of the normalized absolute SPW amplitude, ripple power, and number of oscillations above 20% of the ripple oscillation peak.

This analysis revealed statistically significant differences across clusters for the *Z*-scored SPW amplitude (mean values in *Z*-score units with 95% confidence intervals, −0.5537 ± 0.0968, 1.4038 ± 0.0664, 1.2835 ± 0.0831, and 0.0808 ± 0.0341, respectively; pairwise bootstrapped KS test, $P < 10^{-10}$, Bonferroni corrected). However, no significant differences were observed for ripple power (mean values in *Z*-score units with 95% confidence intervals, 2.3832 ± 0.0660, 2.6662 ± 0.0470, 2.6976 ± 0.0535, and 2.2102 ± 0.0267, respectively; pairwise bootstrapped KS test, $P > 0.05$, noncorrected) and the number of oscillations above 50% of the ripple oscillation peak (mean values with 95% confidence intervals, 4.9098 ± 0.1042, 5.0149 ± 0.0868, 4.8820 ± 0.0887, and 4.9462 ± 0.0455, respectively; pairwise bootstrapped KS test, $P > 0.2$).

Next, we conducted regression analyses to quantify relationships between ripple power and SPW amplitude and also between ripple frequency peak and SPW amplitude. In line with the quantitative analysis performed for pure events, we found that ripple power and frequency peak in the ripple band (80–180 Hz) correlated positively to SPW amplitude ($R = 0.4534$, $P = 0.0001$; $R = 0.3548$, $P = 0.0001$, respectively).

Transient Increase of Gamma Power (25–75 Hz) During Pure and Nonpure SPW-R Events. Ripple-triggered spectrograms show that both pure and nonpure SPW-Rs present somewhat enhanced power profiles over gamma frequencies (25–75 Hz), in addition to the expected increases in SPW and ripple frequency bands (<20 and 80–180 Hz, respectively). To identify the increased gamma band, we followed the procedure reported in ref. 31 with a slight modification. We filtered the perievent pure and nonpure SPW-R signals in the range 15–80 Hz with a fourth-order Butterworth filter, i.e., covering all of the gamma frequencies until the beginning of the ripple band. We estimated the instantaneous frequency by measuring the inverse of the time between the peaks of this signal in a [−0.1 0.1]-s time window around the occurrence of each event. From this somewhat broadband signal, we could expect one or various peaks to emerge (e.g., in the low-gamma band [25–49 Hz], or high-gamma band [50–79 Hz]) (24). However, we found that pure, nonpure, and all SPW-R event subtypes presented virtually identical gamma-band distributions with peaks around 50 Hz (in between low-gamma and high-gamma; $P > 0.4$, pairwise permutation KS test for the comparison between gamma instantaneous frequency distributions). Notably, pure and nonpure gamma distributions were largely unimodal ($P > 0.4$, Hartigan's dip test) and ranged from 25 to 80 Hz, approximately (Fig. S8*C*, *Insets*). To avoid conflating gamma with ripple-band oscillations, we performed all following gamma-band analyses in the 25- to 75-Hz frequency band, which captures ∼99% of the gamma empirical probability density function.

Altogether, these results suggest that concomitant with the occurrence of the SPW-R complexes, there is an increase in power over gamma frequencies, in correspondence with previously published data (31). We discover, however, that the gamma rhythm is in the range of 25–75 Hz in macaques, covering the slow- and high-gamma ranges simultaneously. We now investigate whether this increase in power is exclusive to SPW-R complexes or it is simply an effect of ongoing baseline activity intermingled with the occurrence of such events.

Occurrence of Pure and Nonpure SPW-R Events Can Be Predicted by Gamma Power Increases. We asked how systematic is the relationship between gamma-power increases and SPW-R complexes in single trials. To partly address this question, we computed SWR-triggered gamma-power averages, by bandpass filtering the raw LFP perievent signal in the range of 25–75 Hz, and then computed the absolute value of its Hilbert transform. Gamma power increased significantly above baseline concomitant during both pure and nonpure SPW-R episodes, and presented its largest increase at the ripple power peak (Fig. S8*E*). This analysis revealed that the gamma-power increase was largely transient, decaying to baseline in about 100 ms from the ripple peak. Notably, the peak of gamma power was not significantly different among pure and nonpure events ($P > 0.1$, KS test). Furthermore, "classical" SPW-R subtypes presented higher average peak perievent gamma power compared with "nonclassical" SPW-Rs; however, this difference was not significant ($P > 0.4$, pairwise KS test, noncorrected). Thus, increases in gamma power were transient, concomitant with the occurrence of SPW-R episodes, and spanning the duration of a single episode. These results demonstrate that gamma is concurrent with SPW and does not reflect putative fluctuations of baseline activity, nor a gamma tail following SPW-R occurrence.

We next asked whether a power increase over the gamma frequency range (25–75 Hz) was predictive of the occurrence of a SPW-R episode. We learned linear SVM classifiers to predict the presence (or absence) of a SPW-R complex (pure, nonpure, and SPW-R subtypes were analyzed separately for each experimental session). To this end, periripple gamma-power signals were intended to be discriminated against surrogate (randomly chosen) baseline events in time windows of [−0.1 0.1] s around the event. The classifiers performed significantly above chance, with 66.89 ± 4.03% and 64.22 ± 3.19% (mean with 95% confidence interval, 10-fold cross-validation) prediction accuracy for pure and nonpure events, respectively ($P > 0.3$, two-sample *t* test, for the comparison between pure and nonpure SPW-R prediction accuracy). We found no significant difference in the prediction accuracy among SPW-R subtypes (Fig. S8*F*), in line with our previous analysis. Furthermore, individual SPW-R subtypes could not be discriminated from their underlying gamma-power profiles, resulting in ∼25% prediction accuracy.

These results suggest that gamma oscillations reflect an intrinsic mechanism of SPW-R episodes, common to all SPW-Rs subtypes discovered in this work. This phenomenon is invariant to event detection protocols, suggesting that it can only be attributed to network mechanisms underlying SPW-R episodes themselves. We speculate, in line with observations from a previous study in rats (31), that SPW-Rs may occur when CA3 gamma rhythm entrains CA1 assemblies in the macaque hippocampus.

Gamma Rhythm Modulates Local Multiunit Spiking Activity. The transient increase in gamma power during SPW-R complexes covered both slow- and high-gamma frequency ranges (25–75 Hz). If gamma is an intrinsic network rhythm of SPW-R episodes as our results suggest, it is expected that gamma rhythm modulates the spiking activity of participating neuronal ensembles during such events within CA1. Indeed, our SFC analysis suggests that spiking activity is locked not only to the ripple and SPW bands but also to the gamma range. To quantify this relationship, we filtered the perievent SPW-R signals in the range of 25–75 Hz using a fourth-order bandpass Butterworth filter. For this analysis, we referred to the recording tip with the largest gamma power. We computed the largest-gamma-trough–triggered perievent histograms (bins of 2 ms; $n = 12$ experimental sessions). Our results revealed that multiunit spiking activity was phase-locked to the gamma rhythm underlying pure and nonpure SPW-R complexes. Notably, neuronal discharges occur preferentially at the falling phase or rising phase of gamma (Fig. S8*G*). These findings were consistent across all SPW-R subtypes. Importantly, SPW-R subtype-related multiunit spikes showed significantly different gamma-rhythm phase preference (mean values with 95% confidence intervals, 2.7941 ± 0.06; 4.5972 ± 0.0882; 3.4514 ± 0.1162; 4.8442 ± 0.0830 radians; $P < 10^{-4}$, pairwise bootstrapped KS test). Furthermore, subtypes 2 and 3 presented the largest PLVs, suggesting that multiunit spikes are more consistently entrained by the gamma rhythm at a given phase in such cases ($P < 0.0001$, pairwise KS test for the comparison between classical and nonclassical SPW-R subtypes PLV).

SI Section D: Supporting Discussion

SPW-R episodes may be initiated over relatively localized neuronal circuitry in hippocampus, presenting different spatial extents and propagation features. Hence, it is expected that SPW-R phenomena would present some variability. Indeed, a previous study has reported that SPW-R events propagate along the septotemporal axis of the CA1 of rats (28), such that the events detected at a given location may be initiated in another region of this subfield. SPW-R complexes may be deprived of a clear SPW pattern, which may indicate a more local spread of neuronal activity in the hippocampus. Patterns with disparate SPW polarity, however, cannot be fully explained in light of the observations of Patel et al. (28). The similarity of the SPW-R waveforms as they propagate reported in their work further supports this view. The patterns observed in the present work may indicate different localizations of the current sources in the first place (32); possibly reflecting a different repartition of the activity over the underlying cell groups.

Previous studies (34, 64) suggest that CA1 pyramidal neurons from deep and superficial layers form two functionally distinct groups. A subgroup of CA1 pyramidal cells (located in deep layers) presents differentiated coupling to intrinsic LFP rhythms such as theta and gamma. Notably, the coupling of modulated cells strongly depends on the behavioral state (namely, REM sleep or awake exploration), suggesting that pyramidal cells from functionally distinct sublayers can influence targets jointly or differentially in a brain state-dependent way. Although modulated cells during REM sleep respond more strongly to CA3 inputs (34, 64), a parsimonious explanation to our results is that distinct CA1 sublayers may be active during different SPW-R subtypes. Although this question remains open, in this work we show that SPW-R subtype-related multiunit spiking activity synchronizes differently to ripple- and gamma-band LFP oscillations, suggesting that activity of CA1 subcircuits is differentially organized (64). These changes are a possible indication of differentiated afferent inputs from upstream structures originating in both cortical and subcortical domains. For instance, entorhinal cortex may drive more strongly some of the discovered SPW-R patterns, thus shifting the coupling between LFP gamma and spikes, which in turn may be fired mostly by deep sublayer cells (i.e., REM-modulated cells). The fact that deep and superficial CA1 sublayers have different targets as suggested by anatomical data (65) is in line with the hypothesis that SPW-R subtypes may arise from the population activity of distinct local sublayers, and further supports our hypothesis that SPW-R subtypes are functionally distinct as pointed out by our fMRI data.

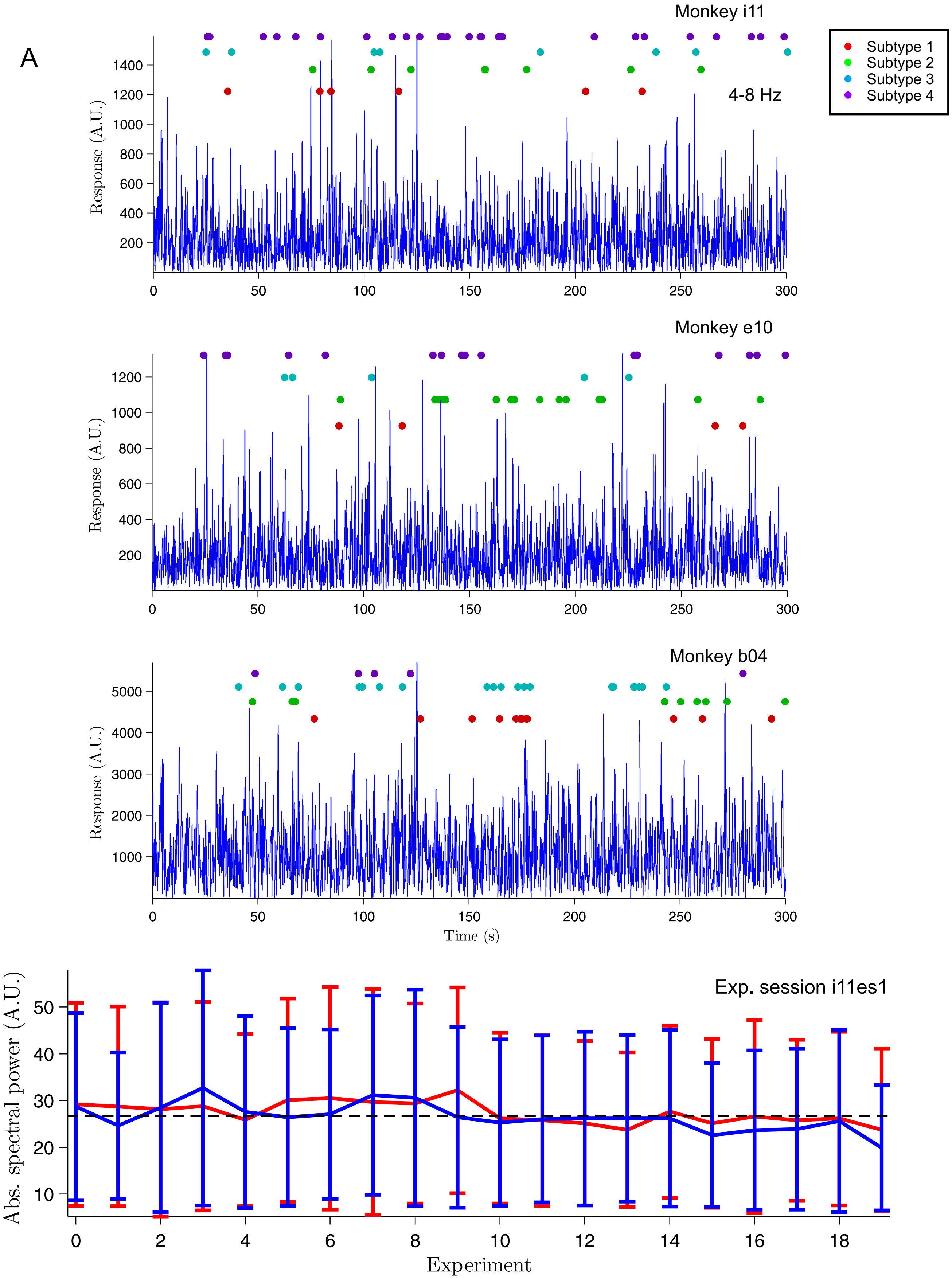

Fig. S1. Theta LFP activity during different states. (*A*) Hilbert-rectified theta (4–8 Hz) frequency band LFP amplitude (blue) with superimposed SPW-R raster plots. Different colors indicate different SPW-R event subtypes as clustered using the procedure showed in Fig. 2. Two anesthetized animals (monkey *i11* and

Legend continued on following page

monkey *e10*, *Top* and *Middle*) show comparable traces and SPW-R raster plots to one unanesthetized animal (monkey *b04*, *Bottom*). (*B*) Absolute average spectral power in the theta band as computed using wavelet-Morlet spectrograms is stable over time. Only one example experimental session (monkey *i11*) is shown. Error bars indicate SD.

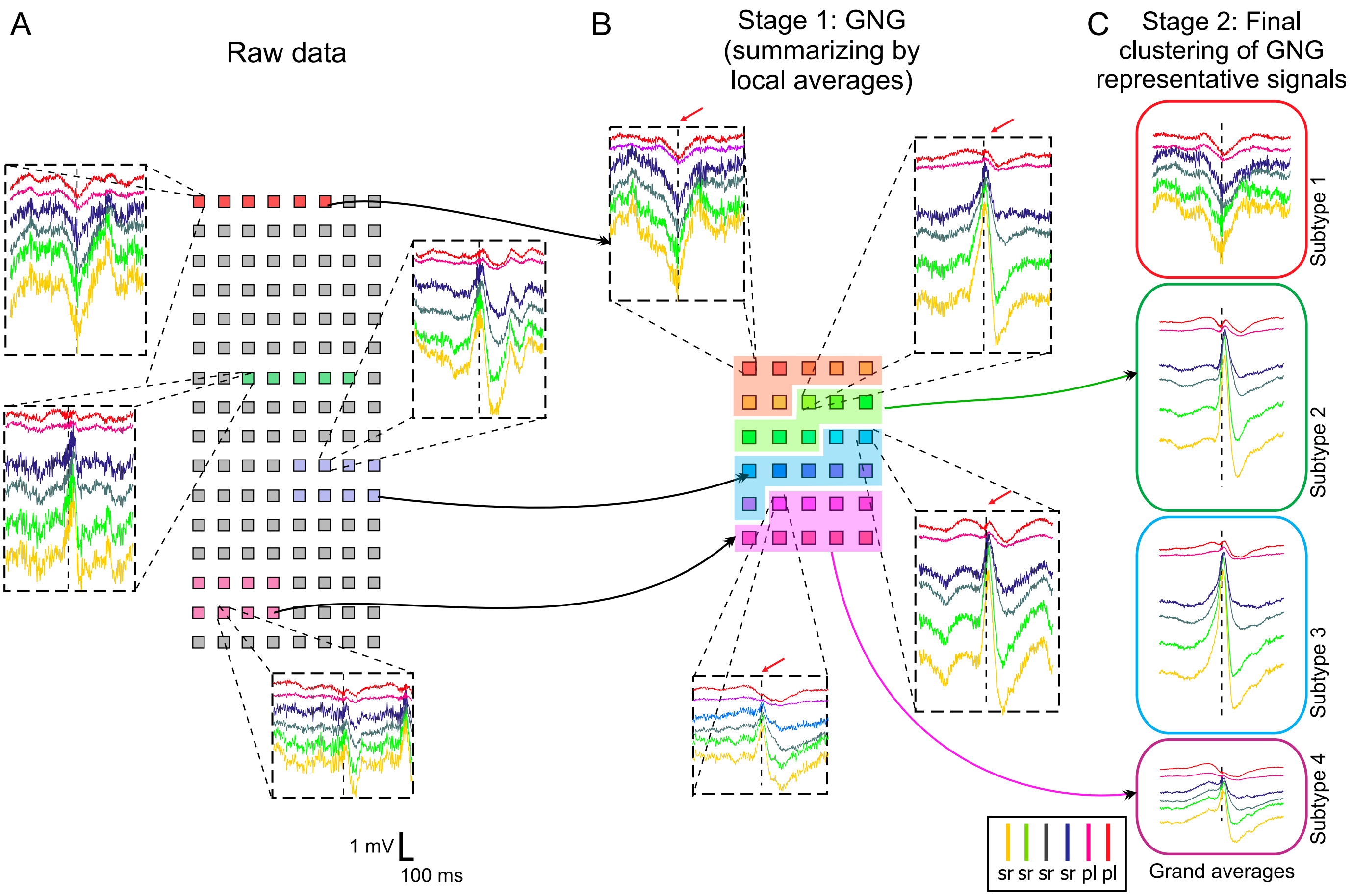

Fig. S2. Diagram of the SPW-R clustering methodology. (*A*) Multichannel, raw perievent SPW-Rs are represented by squares. Groups of contiguous colored squares represent ripple events with similar time courses (*Insets*). (*B*) Stage 1 of the clustering procedure builds an intermediate representation of the multichannel data points by averaging over the groups exemplified in *A*. (*C*) Stage 2 of the clustering procedure consists in grouping the representative signals into four SPW-R subtypes based on pairwise cosine similarities (see Fig. S3 for clustering quality analysis). Dotted, thin black lines mark the center of each exemplary SPW-R, defined as the peak of power of the ripple-band LFP trace (80–180 Hz).

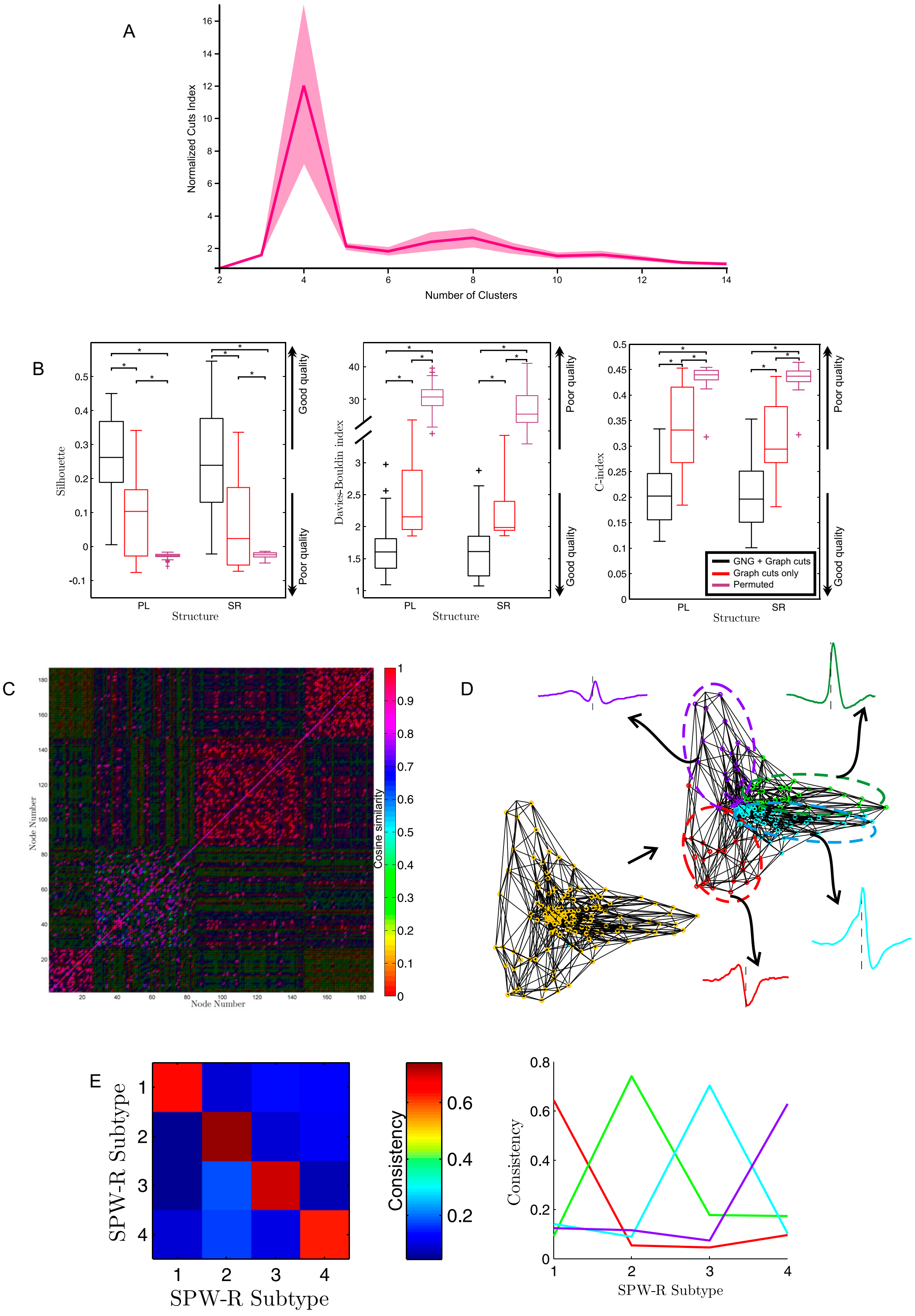

Fig. S3. Clustering quality measures and 2D projection of SPW-Rs. (*A*) Normalized cuts index (NCI) for different cluster partitions. The optimal clustering partition is four, corresponding to the maximum NCI. Results are computed for 200 runs of the clustering algorithm across all experimental sessions; shaded area indicates SE across experimental sessions. (*B*) Four-cluster partition given by the GNG and normalized graph cuts compared with normalized graph cuts alone and to randomly assigned clusters. Clustering quality is evaluated by various measures. (*Left*) Silhouette index. (*Middle*) Davies–Bouldin (DB) index. (*Right*) C index. Asterisks indicate paired significant differences, according to a two-sample Kolmogorov–Smirnov test (KS test). On each box, the top and bottom are the 25th and 75th percentiles of the samples, respectively; the line in the middle of each box is the sample median; the dashed lines extending below and above each box are drawn from the ends of the interquartile ranges to the furthest observation (extreme points); crosses (if any) in the diagrams are the outliers of the samples. (*C*) Cosine similarity matrix of a representative GNG, sorted according to the cluster labels (1–4) for a single experimental session. Spots that pop-out denote connected (neighboring) SPW-R complexes (GNG representative signals). Note that SPW-Rs of a given subtype remain closely connected to each other, whereas connections between clusters remain very sparse. (*D*) Two-dimensional projection of the representative GNG in *C* using Laplacian Eigenmaps. Here, SPW-R complexes (GNG representative signals) are represented by open circles of different colors. Note that clusters remain relatively well separated in the projection, despite the high dimensionality of the real data. Ripple-triggered LFP averages are indicated schematically by arrows. (*E*) Confusion matrix of the cluster consistency procedure. Note that most of the SPW-Rs are classified consistently across experimental sessions (only test datasets are reported).

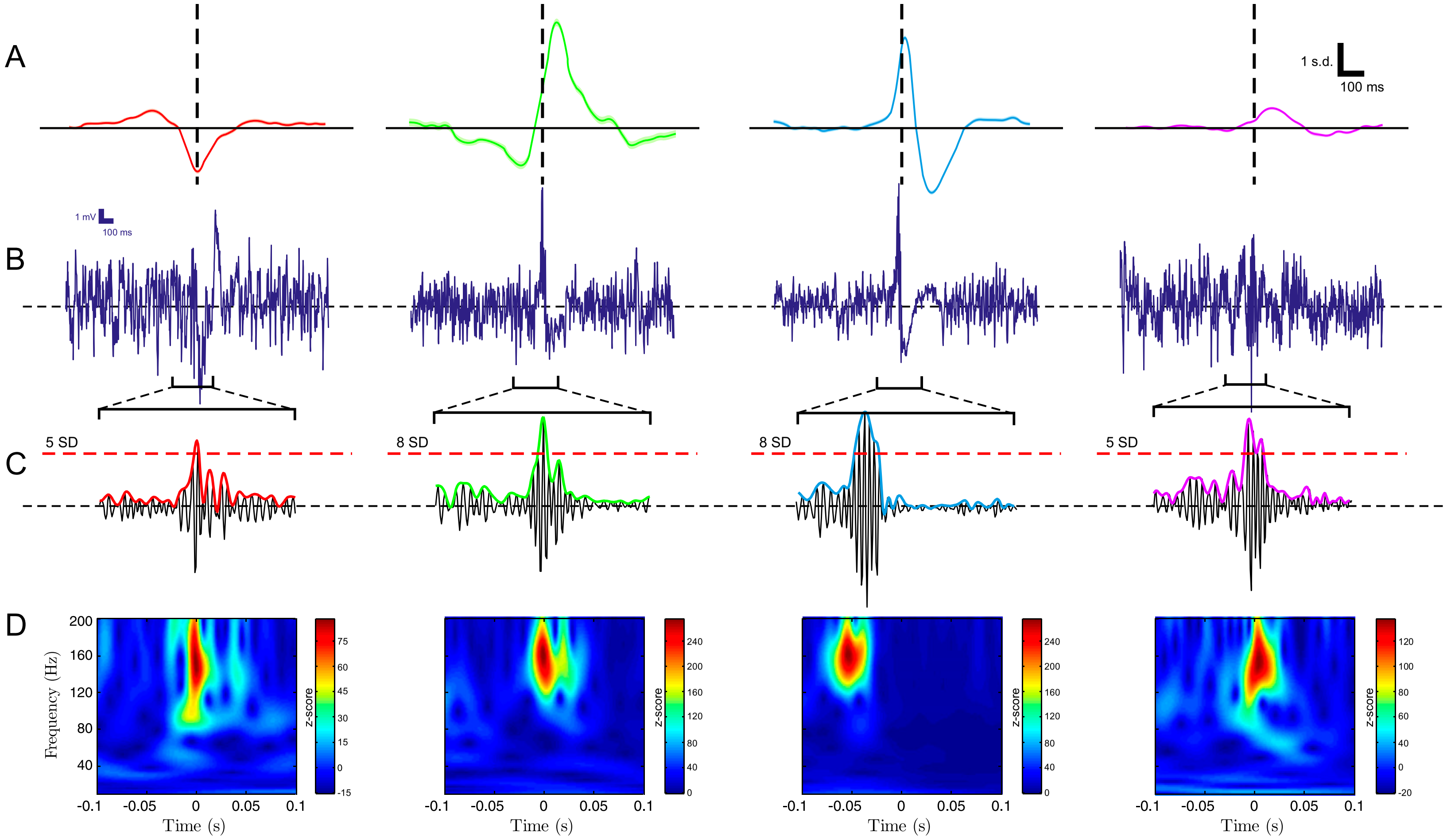

Fig. S4. Raw SPW-R complexes with different signatures in time and frequency domain from an example anesthetized animal (monkey *e10*). (*A*) Average SPW waveform for each subtype for this monkey, computed from one representative stratum radiatum recording site. (*B*) Randomly chosen representative raw signals (0–300 Hz) of each event subtype. (*C*) Filtered, *Z*-scored LFP in the ripple frequency range (80–180 Hz), illustrating that all SPW-R classes present a "genuine" power increase in this range, above event detection threshold. Dashed lines indicate ripple amplitude in SD units. (*D*) *Z*-scored single-event time–frequency spectrum of the broadband signal (0.5–330 Hz) presented in the top rows. Spectra have been *Z*-scored with respect to random baseline events.

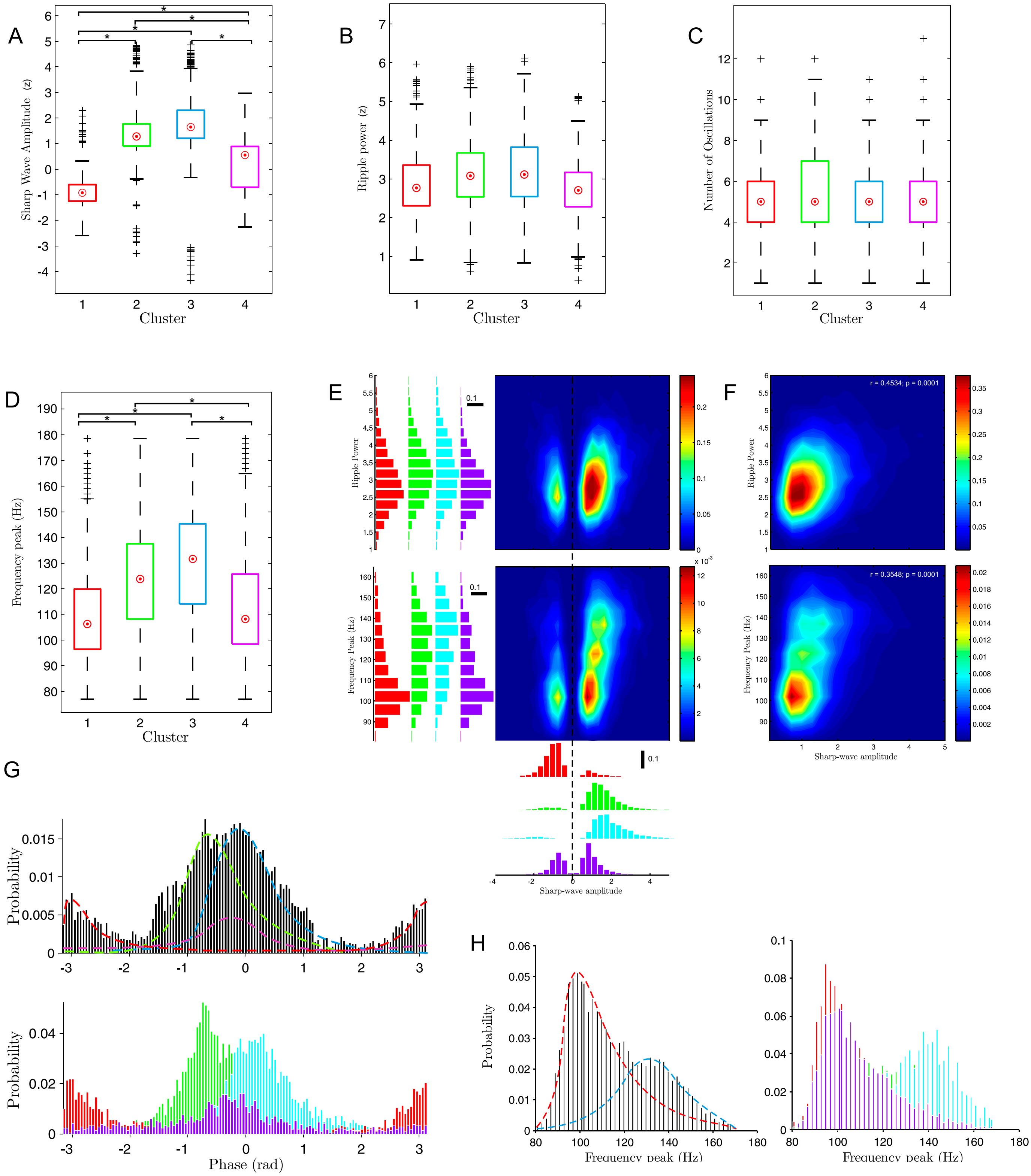

Fig. S5. Distribution of SPW-R field potential signatures' properties. (*A*) Normalized absolute SPW amplitude. (*B*) Ripple power. (*C*) Number of oscillations above 50% of the maximum ripple oscillation peak. (*D*) Frequency peak in the ripple band (80–180 Hz). (*E*) Empirical probability density functions for frequency peak in the ripple band (80–180 Hz) vs. normalized absolute SPW amplitude; and ripple power vs. normalized absolute SPW amplitude. Histograms were taken from Fig. 2 *F* and *H* and illustrate the empirical probability density functions for each feature. (*F*) Empirical probability density functions in *E*, but in absolute SPW *Z*-scored values. Correlation values are given at the *Top*. (*G*) Empirical probability density function of SPW-to-ripple coupling phase: Raw, mixed density function (*Top*); density functions computed for each SPW-R subtype separately (*Bottom*). (*H*) Empirical probability density function of ripple frequency peak: raw density function (*Left*); density functions computed for each SPW-R subtype. Note that all raw distributions present multiple modes, corresponding to the discovered SPW-R subtypes. Colors indicate the SPW-R subtypes shown in Fig. 2; asterisks indicate significant differences between clusters for a given feature,

Legend continued on following page

according to a pairwise bootstrapped Kolmogorov–Smirnov test (KS test). On each box, the top and bottom are the 25th and 75th percentiles of the samples, respectively; the red dot of each box is the sample median; the dashed lines extending below and above each box are drawn from the ends of the interquartile ranges to the furthest observation (extreme points); crosses (if any) in the diagrams are the outliers of the samples.

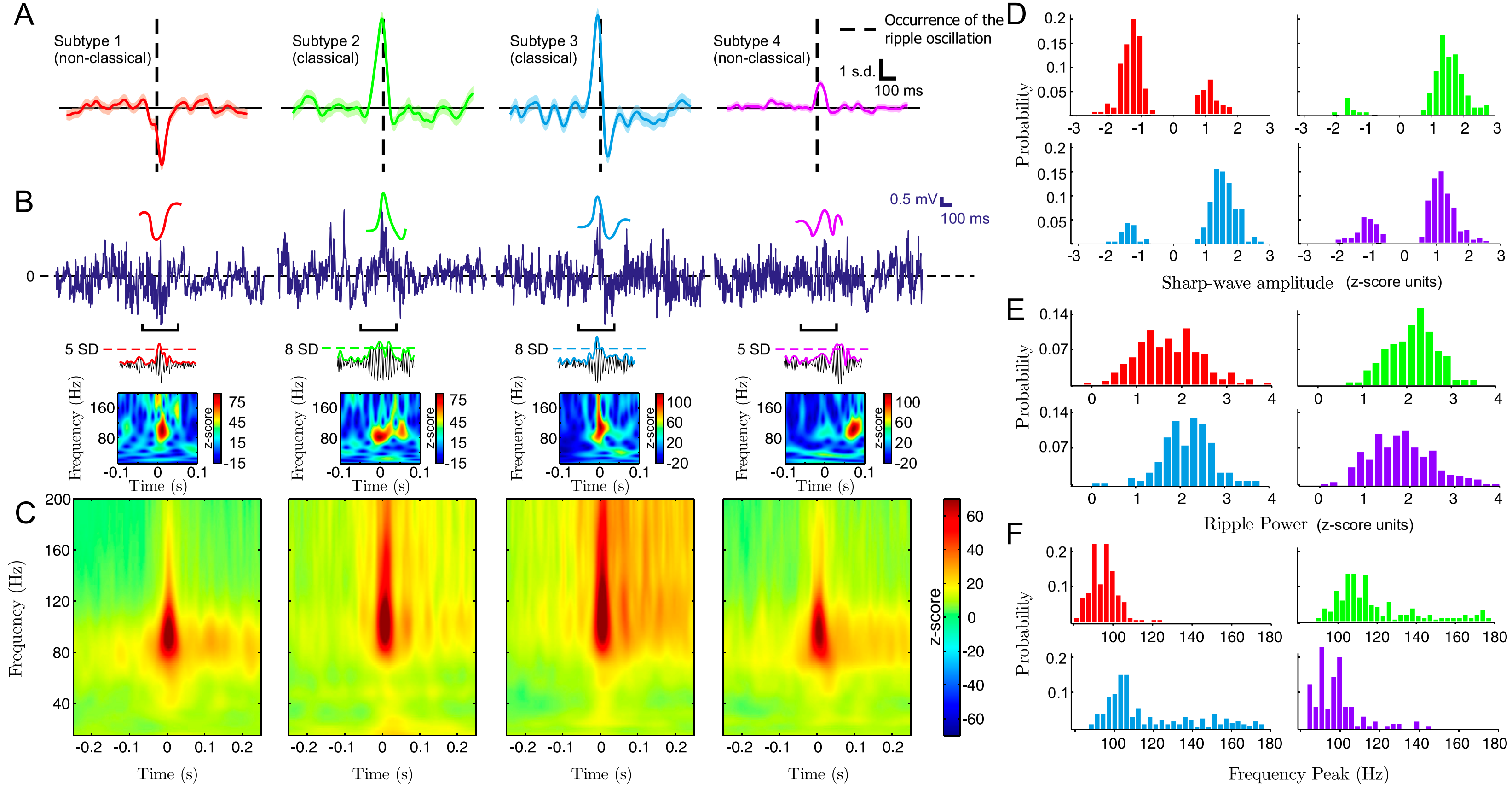

Fig. S6. Classification of SPW-R complexes across four experimental sessions in unanesthetized macaque monkeys. (*A*) Grand averages of ripple power-triggered SPW-R field potential signatures, from one representative stratum radiatum recording site. Occurrence of the ripple oscillation is marked by dashed lines. Shaded areas indicate SEM. (*B*, *Top*) Representative SPWs and related raw signals of each event type. (*B*, *Middle*) Filtered, *Z*-scored LFP in the ripple frequency range (80–180 Hz). Dashed lines indicate ripple amplitude in SD units. (*B*, *Bottom*) *Z*-scored single-event time–frequency spectrum of the broadband signal presented in the top rows. (*C*) Spectrogram grand averages, in correspondence with each of the SPW-R signatures depicted in *A*. Averages are computed across all recording sites. (*D*–*F*) SPW and ripple subtypes statistics. (*D*) SPW amplitude. (*E*) Ripple power. (*F*) Ripple frequency peak. Colors denote the distinct SPW-R signatures.

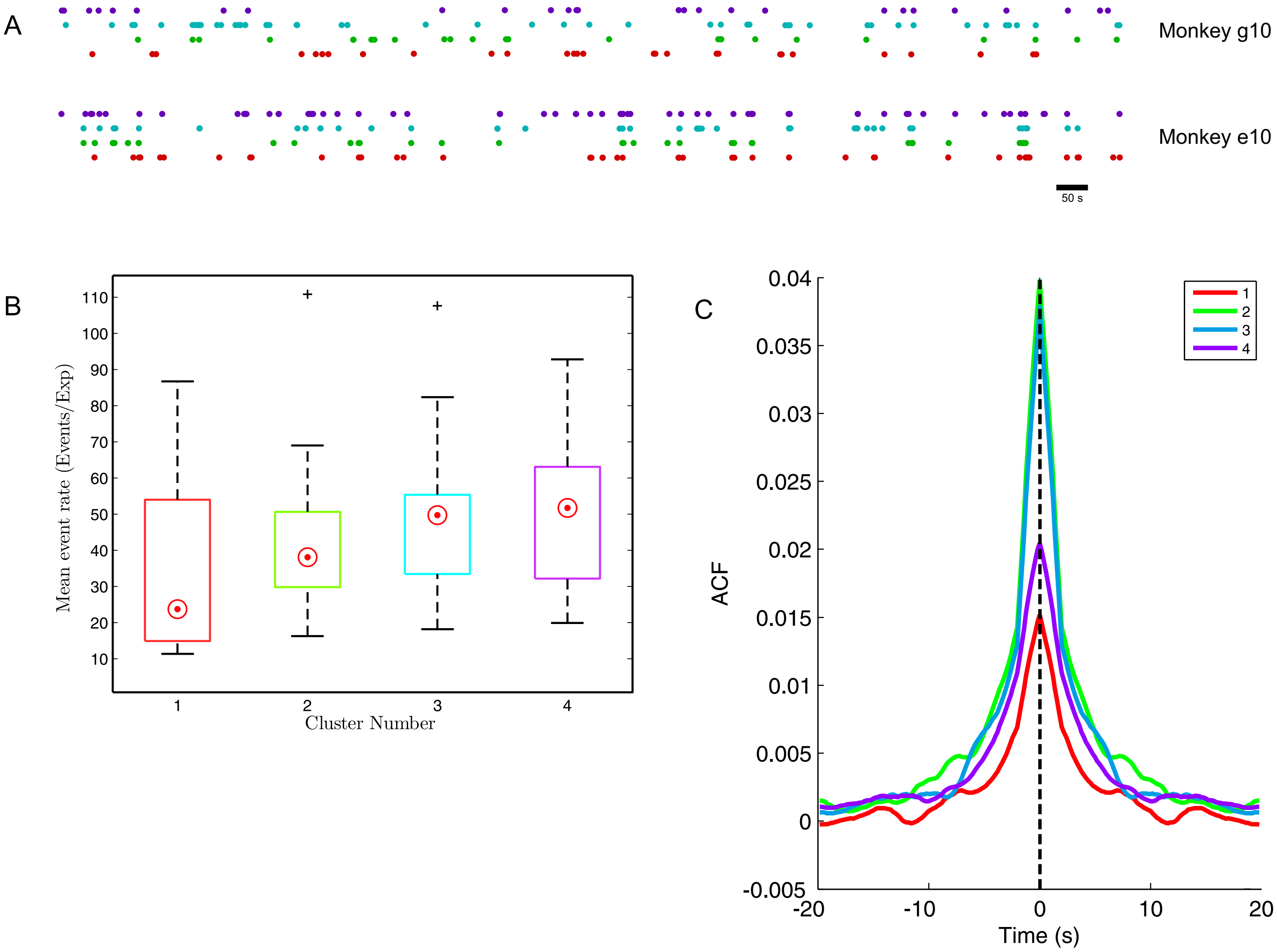

Fig. S7. SPW-R events timing dynamics. (*A*) Typical SPW-R event subtype raster plots. (*B*) Mean event rate (in events per experiment) for each of the reported SPW-R clusters. No significant differences were found between clusters, according to a paired Kolmogorov–Smirnov test (KS test). For a detailed description of the box plots, see legend of Fig. S5. (*C*) Autocorrelation functions corresponding to each type of SPW-R. Events associated to strong sharp waves (2, 3) exhibit more autocorrelation than other event types ($P < 0.01$, t test).

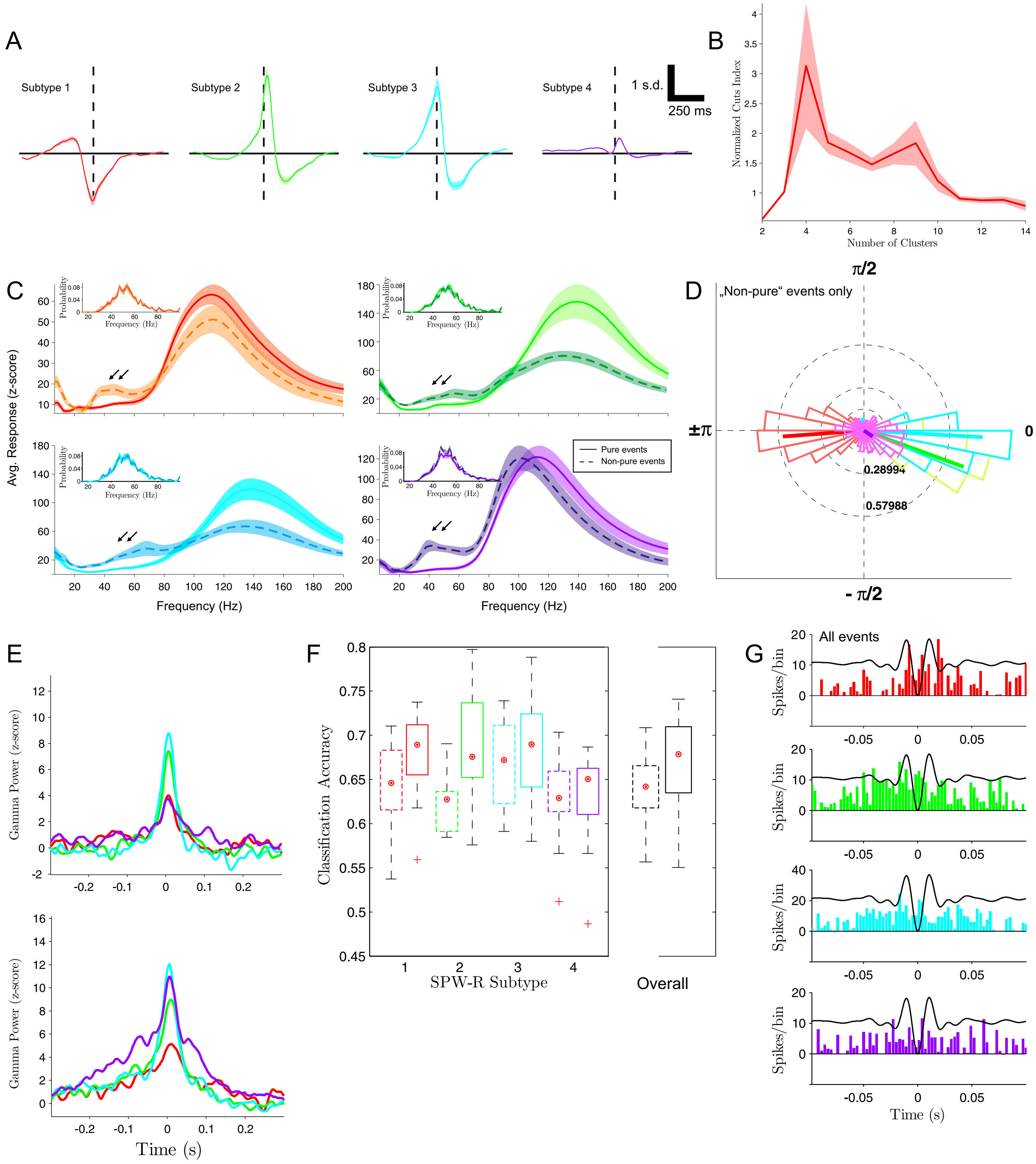

Fig. S8. Classification of SPW-R complexes across 12 experimental sessions in anesthetized macaque monkeys (nonpure events). (*A*) Grand averages of ripple power-triggered SPW-R field potential signatures, from one representative stratum radiatum recording site. Occurrence of the ripple oscillation is marked by dashed lines. Shaded areas indicate SEM. (*B*) Normalized cuts index (NCI) for different cluster partitions. The optimal clustering partition is four, corresponding to the maximum NCI. Results are computed for 200 runs of the clustering algorithm across all experimental sessions; shaded area indicates SE across experimental sessions. (*C*) Overlaid averaged clusterwise spectra for pure (continuous lines) and nonpure (dashed lines) SPW-Rs. Note that gamma instantaneous frequency distributions are unimodal and virtually identical (*Insets*). Shaded areas indicate SEM. (*D*) Phase coupling of the ripple to the SPW of dendritic depolarization for each cluster. Thick lines indicate the circular mean of the phase coupling values. (*E*) SPW-R–triggered gamma power (25–75 Hz) of pure (*Top*) and nonpure (*Bottom*) events reveals nonsignificant differences between SPW-R subtypes. (*F*) Accuracy of a linear SVM classifier in predicting the occurrence of a SPW-R complex by its underlying gamma-power signal. Note that performance is significantly above chance. (*G*) Perievent time histograms of multiunit spiking activity using bins of 2 ms. Histograms are computed taking the maximum perievent gamma-trough as a reference. Colors indicate SPW-R subtype.

Legend continued on following page

Box plots: top and bottom are the 25th and 75th percentiles of the samples, respectively; the red dot of each box is the sample median; the dashed lines extending below and above each box are drawn from the ends of the interquartile ranges to the furthest observation (extreme points); crosses (if any) in the diagrams are the outliers of the samples.

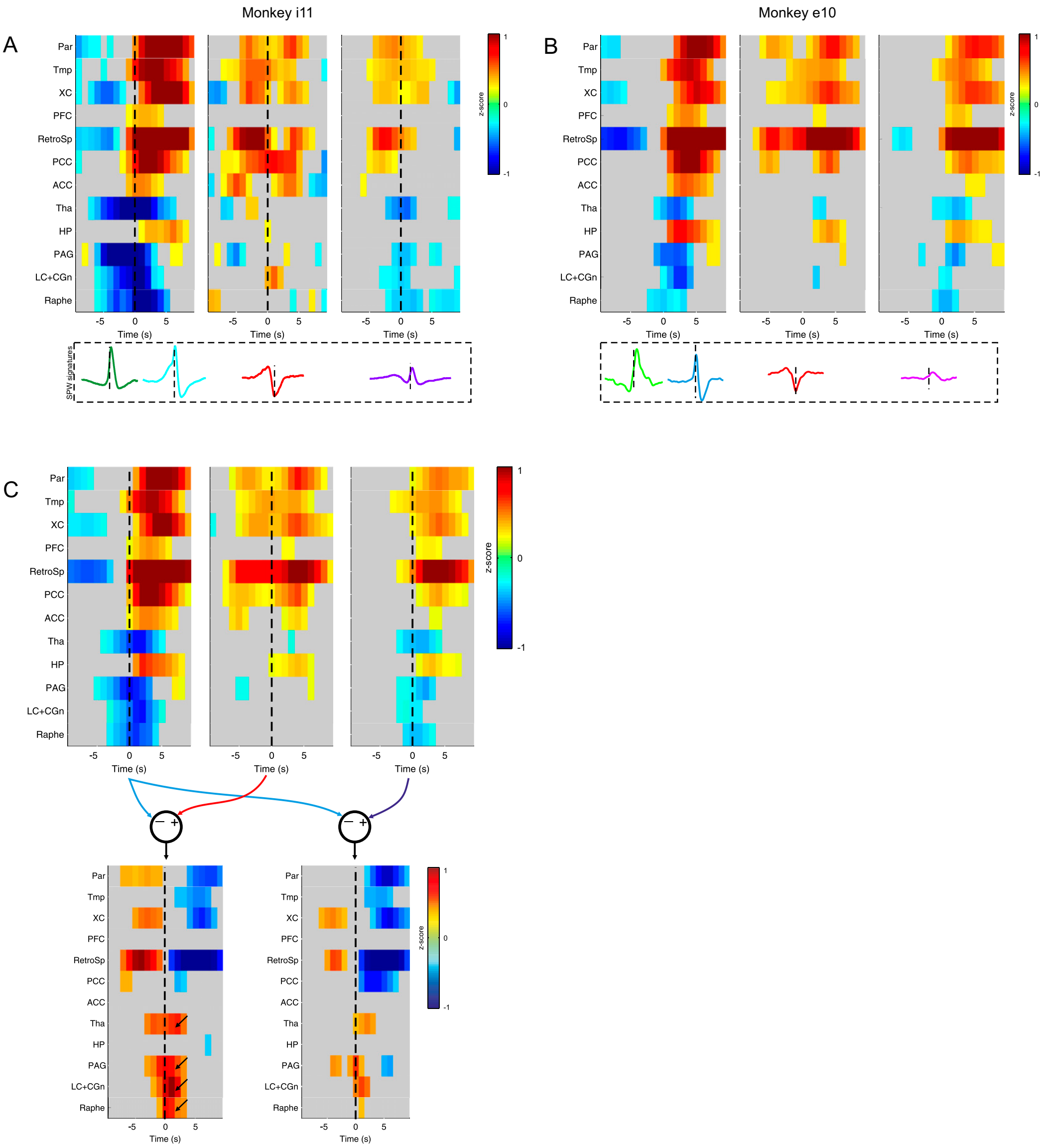

Fig. S9. Ripple-triggered NET-fMRI associated with SPW-R subtypes. Averaged BOLD time courses showing differentiated neocortical activations and subcortical deactivations for distinct event types in *Z*-score units: (*A*) Only monkey *i11*. (*B*) Only monkey *e10*. (*C*) Across 12 experimental sessions, 4 animals. Gray regions in the previous plots represent activations below a 0.3-*Z*-score-units threshold. Population contrast maps (*Bottom*) show differences between subtypes in both neocortical and subcortical domains. Note that subtype 1 relates to the lowest subcortical down-regulations, whereas subtype 4 presents down-regulation comparable to that of classical SPW-Rs. In *A*–*C*, listed ROIs are as follows: Parietal (Par), temporal (Tmp), prefrontal (PFC) cortical areas, extrastriate occipital areas (XC), posterior and anterior cingulate cortices (PCC, ACC, respectively), retrosplenial area (RetroSp), thalamus (Tha), hippocampus (HP), periaqueductal gray (PAG), locus coeruleus (LC), and raphe.

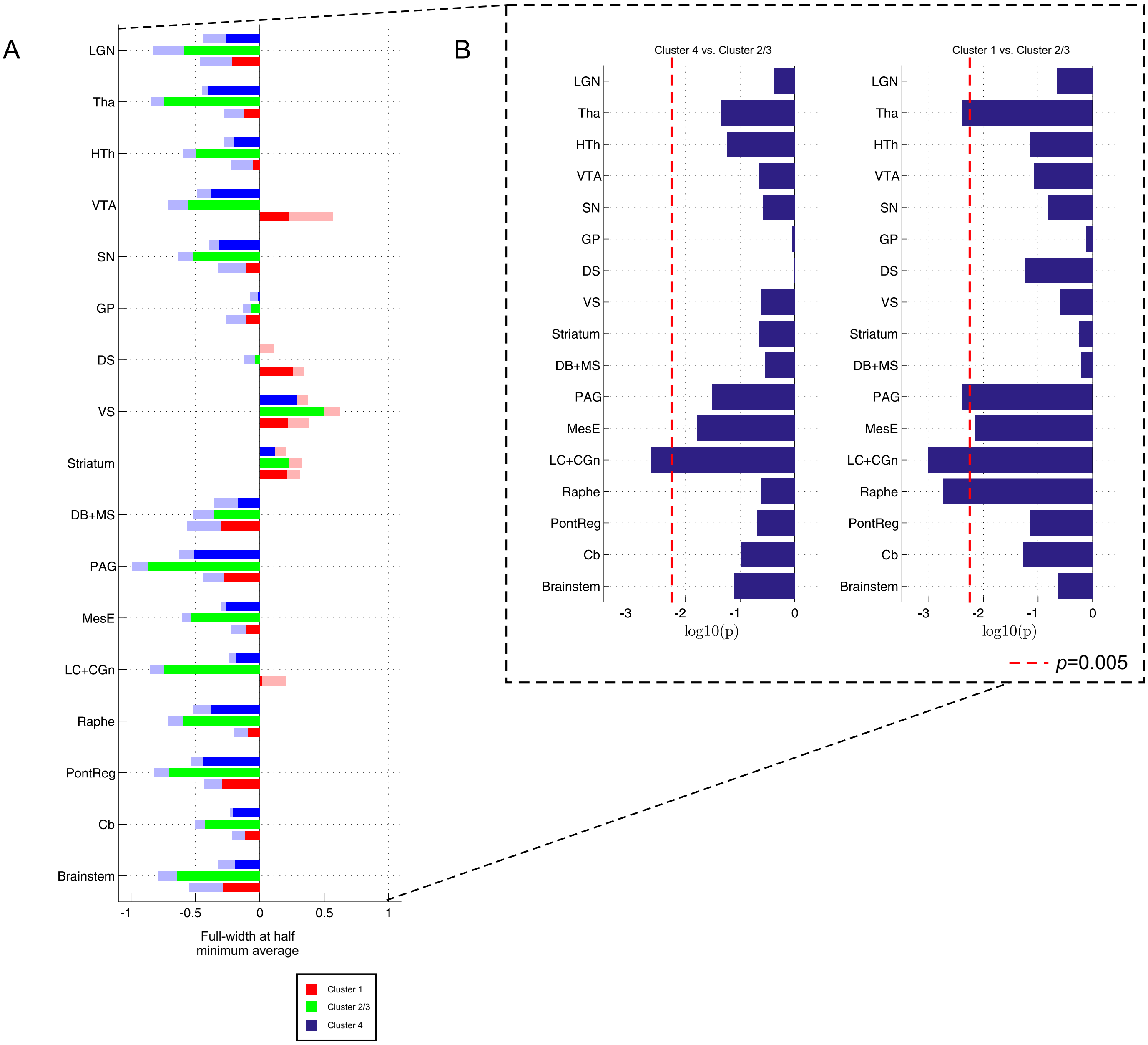

Fig. S10. Statistical analysis of subcortical structures' NET-fMRI results. (*A*) Average over the full width at half-minimum of all subcortical regions, related to classical (pooled subtypes 2 and 3) and nonclassical (subtypes 1 and 4) SPW-Rs (grayed areas indicate SE). (*B*) *P* values from the pairwise Wilcoxon rank-sum test (note logarithmic scale), showing that differences in subcortical activations relate to locus coeruleus, dorsal raphe nucleus, thalamus, and periaqueductal gray (PAG). In contrast, modest differences were observed in lateral geniculate nucleus (LGN), ventral tegmental area (VTA), substantia nigra (SN), globus pallidus (GP), striatum (putamen and caudate nucleus), diagonal band of Broca and medial septum (DB+MS), inferior and superior colliculus (InfCol, SC), pons (PontReg), cerebellum (Cb), and brainstem. The dashed red line is drawn to indicate a FDR-corrected significance threshold of $P = 0.005$ ($P_{FDR} < 0.05$).

Appendix B

Paper 2

Dissecting the frequency-dependent network mechanisms of *in vivo* hippocampal sharp wave-ripples

Juan F. Ramirez-Villegas[1,2], Konstantin F. Willeke[2,5], Nikos K. Logothetis[1,4] & Michel Besserve[1,3,*]

[1]Department of Physiology of Cognitive Processes, Max Planck Institute for Biological Cybernetics, Max Planck Ring 8, 72076 Tübingen, Germany

[2]Graduate School of Neural & Behavioral Sciences, International Max Planck Research School, Eberhard-Karls University of Tübingen, Österbergstrasse 3, 72074 Tübingen, Germany

[3]Department of Empirical Inference, Max Planck Institute for Intelligent Systems and Max Planck ETH Center for Learning Systems, Max Planck Ring 4, 72076 Tübingen, Germany

[4]Centre for Imaging Sciences, Biomedical Imaging Institute, The University of Manchester, Manchester M13 9PT, United Kingdom

[5]Werner-Reichardt Centre for Integrative Neuroscience, Ottfried-Müller-Strasse 25, 72076 Tübingen, Germany

[*]Lead Contact

Abstract

Sharp wave-ripples in the hippocampal region CA1 are transient network phenomena thought to organize the sequential replay of firing patterns for memory consolidation and retrieval. However, the role of afferent CA3 rhythmic inputs and recurrent CA1 activities in precisely coordinating these events remains debated. We designed a multi-compartmental model of the CA3-CA1 network able to generate biophysically-realistic dynamics at the cellular and local field potential (LFP) levels. In this model, ripples emerge locally from the driving of CA1 pyramidal cell by interneurons' recurrent somatic inhibition, whereas somatic excitation controls the amount of pyramidal cells involved in each ripple. Furthermore, CA3 input provides the necessary transient modification of inhibition-excitation balance initiating the phenomenon, and coordinates its interactions with CA1 assemblies through slow gamma oscillations. As it reproduces a broad range of characteristics of *in vivo* activity, this model offers key insights to establish the hippocampal network mechanisms supporting memory-related functions.

Introduction

The hippocampus is essential to the formation of new episodic memories (Scoville and Milner, 1957). Once encoded, reactivating a specific memory trace likely requires precise network mechanisms to select and coordinate the activity of the cell assemblies involved (Wilson and McNaughton, 1994). Such mechanisms are thought to be at play during sharp wave-ripple (SWR) complexes (Lee and Wilson, 2002), transient episodes occurring in the Local Field Potential (LFP) of the hippocampal CA1 subfield in several mammalian species (Buzsáki, 2015). SWRs combine a slow potential deflection (the sharp wave, SW) and a high-frequency oscillation (the ripple) (Ylinen et al., 1995). SWRs have been largely associated with memory consolidation (Ego-Stengel and Wilson, 2009; Girardeau et al., 2009; Nakashiba et al., 2009; van de Ven et al., 2016), and neuronal ensemble activities during these episodes indeed correspond to spike sequences associated with awake exploration (Diba and Buzsáki, 2007; Foster and Wilson, 2006; Karlsson and Frank, 2009; Lee and Wilson, 2002). Although these phenomena are known to involve neuronal ensemble interactions within the *cornu ammonis* hippocampal subfields (Buzsaki et al., 1992; Oliva et al., 2016; Sullivan et al., 2011), the underlying microcircuit dynamics governing them are not yet fully understood. Specifically, computational and experimental studies have pointed to a number of candidate mechanisms for hippocampal dynamics during different brain states (Cutsuridis and Hasselmo, 2011; Memmesheimer, 2010; Schomburg et al., 2012, 2014; Taxidis et al., 2012; Traub and Bibbig, 2000; Wang and Buzsáki, 1996), but the contribution of these mechanisms and of the variety of neuronal types to the observed SWR episodes remains elusive.

In vivo studies suggest that hippocampal SWRs are governed by CA3-ensemble synchronous bursts (inducers) (Csicsvari et al., 2000), and that of other structures of the hippocampal formation (Chrobak and Buzsáki, 1996; Isomura et al., 2006; Oliva et al., 2016). Long-range mechanisms also seem to play a role in the emergence of this phenomenon (Gomperts et al., 2015; McNamara et al., 2014; Wang et al., 2015), and its temporal variability (Ramirez-Villegas et al., 2015). These fine network-level interactions are hypothesized to instantiate changes in the observed SWR extracellular signature and shape its time-frequency properties (Carr et al., 2012; Ramirez-Villegas et al., 2015). For instance, recent experimental evidence suggests that a slow gamma oscillatory component –ubiquitous in several structures of the hippocampus– coordinates the activity of CA3 and CA1 ensembles (Gillespie et al., 2016), and may be a clocking signal that underlies coordinated replay of previous experiences (Carr et al., 2012).

Although remote inputs are partly responsible for the compound of observed CA1 population activities during SWRs, local CA1 effectors themselves play a major role in shaping physiological SWR activity

(Schlingloff et al., 2014; Stark et al., 2014). A number of *in vivo*, *in vitro* and computational studies have suggested that interneurons are crucial for the genesis of fast network oscillations (Hajos, 2004; Mann et al., 2005; Oren et al., 2006; Taxidis et al., 2012; Wang and Buzsáki, 1996; Whittington et al., 1995). In particular, due to their fast kinetic properties, they are hypothesized to pace ripple oscillations (Ellender et al., 2010; English et al., 2014; Gan et al., 2017; Stark et al., 2014). SWRs are also associated with increased excitability of selected principal cells (Ellender et al., 2010; Mizunuma et al., 2014). Excitatory activity is thought to be controlled by feedback inhibition of fast-spiking perisomatic-targeting interneurons, which in turn may be controlled by interneuron-interneuron synapses (Stark et al., 2014). In addition, fine time-scale and strata-specific neuronal interactions within CA1 are likely associated with dynamical changes in excitation-inhibition (E-I) balance during the time course of SWR complexes (Mizunuma et al., 2014; Schlingloff et al., 2014).

In order to understand the neuronal ensemble mechanisms of SWR episodes, we investigated the relationship between CA3 and CA1 ensemble activity at meso- and microscopic scales. We thus designed a multi-compartmental model of the CA3-CA1 network that reproduces *in vivo* intermittent SWR-related activity in both fields. We performed a detailed frequency analysis of transmembrane activities at the population level to isolate the network mechanisms at play, and related them to the features of LFP recordings. We first dissociated the activity caused by upstream CA3 network –locally segregated to CA1 *stratum radiatum*– from the current signatures originated due to post-synaptic processing of CA1 pyramidal cells and interneurons. We found that sharp wave (<20 Hz) and slow gamma (30-55 Hz) components originate due to CA3 activity impinging on CA3 *stratum radiatum* (Schaffer pathway). A SWR-related slow gamma activity was generated within CA3 but propagated to CA1's cell soma, allowing it to coordinate CA3 and CA1 ensembles. Furthermore, ripple oscillations (80-180 Hz) reflected not only concerted somatic inhibitory post-synaptic currents (IPSCs) but also synchronous somatic excitatory post-synaptic currents (EPSCs) in CA1, resulting from reciprocal interactions between local pyramidal cells and interneurons. Finally, the frequency spectrum of CA1 interneuron network dynamics spread largely beyond the ripple band, resulting in identifiable supra-ripple LFP activity (> 180 Hz). Our findings account for a large number of experimental studies covering multiple spatio-temporal scales of the phenomenon, and are compatible with hippocampal LFP recordings from anesthetized rhesus monkeys (*Macaca mulatta*) recorded in our laboratory. Overall, this model sheds light on the detailed mechanisms underlying *in vivo* SWR genesis and the relationship between neuronal activity at meso- and microscopic scales during these events. This opens new avenues for the experimental and computational studies of memory retrieval and consolidation processes at the system level.

Results

SWR complexes in a simple compartmental model of the macaque CA3-CA1 network

We propose a simple model of the CA3-CA1 network that predicts a number of physiological properties observed in macaque monkeys' hippocampal SWR complexes (Logothetis et al., 2012). We modeled two arrays of neurons accounting for the CA3 and CA1 neuronal populations, respectively. The electrical properties of cell membranes were modeled across multiple compartments in a similar way to the approach of Taxidis et al. (2012). Similarly, pyramidal neurons were modeled by the two-compartmental model proposed by Pinsky & Rinzel (Pinsky and Rinzel, 1994), a simplified version of Traub's model of the CA3 pyramidal neuron (Traub et al., 1991). In addition, we developed a simplified two-compartment interneuron on the basis of a model proposed by Traub et al. (1995) that originally consisted of 51 compartments (Traub and Miles, 1995; Traub et al., 1994). Briefly, our simplification stands on the basis of minimal active ionic currents (potassium and sodium) in one axo-somatic compartment and one dendrite-like compartment. An in-depth mathematical description of the model is available in the STAR Methods of this work. CA3 and CA1 neuron models were considered identical, however, the network connectivity within each field was different, after well-documented anatomical constraints (Andersen, 2007; Bezaire and Soltesz, 2013). Whereas CA3 was characterized by strong recurrent auto-associational connections, together with pyramidal neuron-interneuron connections (Andersen, 2007), CA1 connectivity –inspired by recent findings– was implemented as a "feedback and reciprocal inhibition" circuit (Stark et al., 2014), dominated by recurrent inhibition, reciprocal pyramidal cells-interneurons synapses and interneuron-interneuron synapses (Figure 1A; see also Figure S1A and B for diagrams of the subfield canonical circuits, and the network; and see STAR Methods for all mathematical details).

For each hippocampal field we simulated 150 units (135 pyramidal cells and 15 interneurons) in order to limit computational load. We observed no substantial changes in the results when adding a greater number of simulated neurons. The hippocampal extracellular potential was computed following previous modeling work (Nicholson, 1973; Schomburg et al., 2012). The mean extracellular field potential (mEFP; <50 kHz, sampling time 0.02 ms) signal is considered proportional to the transmembrane currents across cells and compartments (including capacitive currents). All transmembrane currents from all cells are assumed to superpose linearly in two simulated multi-site electrodes of 32 tips covering simulated CA1 and CA3 strata (one electrode per field). In addition to the full mEFP, we divided the mEFP activity into the following components: the synaptic field potential (LFPsyn) that only accounts for the signature of synaptic currents, and the active membrane current-dependent field potential (referred here to as LFPt) that accounts for the remaining (non-synaptic) transmembrane currents (see STAR Methods). LFP signals (<330 Hz) were derived from the broad-band mEFP as well as the procedure for detection of oscillatory events are detailed in STAR Methods. In summary, events were selected based on their elevated ripple band power (greater than 3 SD). All experiments in the following subsections are computed for 3,250 SWR episodes, obtained in 25 simulation sessions, unless otherwise specified.

We first observed that SWR-like episodes can emerge spontaneously from the CA3-CA1 network: Episodes of short-lived high-frequency oscillations (ripples) on top of a depolarization (< 25 Hz) with visual and quantitative characteristics consistent with those observed experimentally (exemplary raw LFP traces are shown in Figure 1B, top subpanels; see also Figure S2A-B, D) (Logothetis et al., 2012; Skaggs et al., 2007). Notably, both CA1 SWR traces and SWR-related synaptic currents are in correspondence with previous studies (Ramirez-Villegas et al., 2015; Schlingloff et al., 2014; Stark et al., 2014) (Figure 1B). On average, full-LFP sharp waves (< 20 Hz) and ripples (80-200 Hz) had durations of 146.59±1.73 ms and 28.46±0.26 ms (roughly 5 complete oscillation periods on average), respectively (mean full-width at half-maximum with 95% confidence intervals; Figure 1C, top-middle subpanel), with ripples associated with a peak frequency of 122.07±1.05 Hz (Figure 1C, top-rightmost subpanel). We found that concurrently with the CA1-SWR, CA3 presents episodes of field activity in the form of gamma-like episodes (~20-100 Hz) together with less prominent high-frequency oscillations (>100 Hz) (Figure 1B, bottom subpanel; see also Figure S2D for the population averaged spectrogram) (Sullivan et al., 2011). In addition, our modeled SWR episodes display biologically-plausible peri-SWR recruitment of pyramidal cells and interneuron populations in CA1 (proportion of SWR-participating pyramidal cells and interneurons 0.11±0.001, and 0.72±0.003; Figure 1C, bottom-left subpanel). In particular, SWR episodes correlated with increases in firing probability of both pyramidal cells and interneurons as demonstrated by Peri-Event Time Histograms (PETH), and cell discharges were ripple-coherent as illustrated by spike-field coherence (SFC) and detailed PETH analysis (Figure S2E-2F; Figure 1D, E, respectively). Significant spike-to-LFP locking was observed at the rising phase of the ripple for interneurons, and at the ripple trough for pyramidal neurons (Figure 1D, E) (Buzsaki et al., 1992).

As sharp waves and ripples have correlated features (Hajos et al., 2013; Patel et al., 2013; Ramirez-Villegas et al., 2015), we also investigated the relationship between ripple power and sharp wave amplitude in our model. Interestingly, we found that ripple power significantly correlates with sharp-wave amplitude (r=0.37; $p<10^{-50}$ bootstrapped statistics), and both SW amplitude and ripple power (Figure 1C, bottom-right subpanel). These results support that simulated sharp waves and ripples of our model are related phenomena resulting from CA3 synchronous bursting, and that these episodes –on the basis of their electrical properties– reflect well-known properties of in vivo SWR complexes as recorded from primates (Leonard et al., 2015; Logothetis et al., 2012; Ramirez-Villegas et al., 2015).

Low- and high-frequency dynamical sources of SWR-associated LFP activity

Local properties of SWR events reveal different degrees of synchrony of participating neuronal populations to the LFP, as quantified by spike-field coherence (SFC) maps (Figure S2F). Interestingly, SFC not only shows synchronization of action potentials in the ripple band (80-180 Hz) of the LFP, concomitant with the SPW activity, but also prominent phase locking of the spiking activity to gamma (25-75 Hz) and beyond ripple (>180 Hz) LFP frequencies in a magnitude comparable to that of the ripple (80-180 Hz) and SPW components (<20 Hz) (Figure S2F). This observation suggests that the information contained in peri-event LFPs about the underlying population activity during SWR may span over the broad-band spectrum, instead of remaining localized to a particular frequency band (such as the ripple range as it has been classically assumed). Multiple frequency bands of the SWR spectrum may thus reflect different information about the underlying network dynamics. These coupling patterns may emerge as a result of a combination of synaptic current signatures exerted by the axosomatic and dendritic segments of pyramidal cells, the firing of different cell types (as indicated by Figure 1C) and the incoming excitatory drive from CA3 during SWR episodes (Carr et al., 2012; Ellender et al., 2010; Stark et al., 2014).

If peri-event LFP during SWR episodes is a mixture of distinct “dynamical components” reflecting the activity of different synaptic and transmembrane mechanisms of the network, these components might be retrieved by separating the currents corresponding to such mechanisms. Thus we sought to determine: first, whether the model exhibits distinct peri-SWR dynamical components; and second, if present, whether these components come about by specific extracellular current contributions in the CA1 network. These questions were addressed by isolating the contribution of each type of synapse to LFPsyn and of each compartment to LFPt of each cell type. It is worth noting that in all these cases, we simulated the dynamics of the network with all neuron types and compartments, and we only isolated the non-synaptic and synaptic currents of each population when computing their corresponding peri-SWR LFP signal. In accordance with our previous reasoning, the synaptic component of the LFP revealed that low frequencies are predominant in the dendritic segments of the model. In particular, sharp wave and slow-gamma frequency components (<50 Hz) arose in such compartments to a larger extent than in somatic ones ($p<10^{-6}$ Wilcoxon’s ranksum test, Bonferroni-corrected, for the comparison between somatic and dendritic averaged spectral power, Figure 2A, bottom-left subpanels; and Figure S3A, leftmost subpanels). Interestingly, ripple-related power was prominent in IPSC-related potentials of both interneuron-pyramidal cell and interneuron-interneuron synapses ($p<10^{-6}$ Wilcoxon’s ranksum test, Bonferroni-corrected for the comparison between somatic and dendritic averaged spectral power; Figure 2A top-left and bottom-right subpanels; Figure S3A, rightmost subpanels). Notably, interneuron-interneuron synaptic currents displayed more widespread influence over high-frequency LFP activity, reaching supra-ripple (>180 Hz) frequencies (p = 0.026 Wilcoxon's ranksum test for the comparison between E-I and I-I supra-ripple-related normalised spectral power; Figure S3B).

Conversely, analysis of the LFPt indicates that pyramidal cells' axo-somatic compartments together with fast-spiking GABAergic interneurons present significant ripple-power (>80 Hz) (Figure 2B, left and bottom subpanels, respectively). Furthermore, similar to the synaptic component of the LFP (LFPsyn), apical dendrites (stratum radiatum) elicit increases in SPW and gamma frequency bands for LFPt (Figure 2B, middle-left subpanel; see bottom-left panel for zero-lag frequency profiles), reflecting transmembrane currents resulting from the propagation of the CA3 Schaffer inputs. Supra-ripple frequencies (>180 Hz) originate from the activity of interneurons reflected by the simulated field activity (Figure 2B, bottom-right panel). Interestingly, the supra-ripple component reaches a frequency peak higher than that of synaptic currents alone (i.e. somatic IPSCs and EPSCs), which may be attributed to the expression of interneuronal spiking currents ($p<10^{-6}$ Wilcoxon's ranksum test for the comparison between the peri-SWR frequency peak of pyramidal- and interneuron-associated LFPt; Figure 2C).

These results show that SWR comprise several dynamical components with distinct spectral signatures. Notably, these components do not reflect activity independently generated by each modeled compartment or synapse, since their activities are tightly intertwined due to network-level interactions during the occurrence of SWR episodes. Next, we examined the laminar distribution of each component in the total LFPt and LFPsyn.

Laminar distribution of peri-SWR dynamical components in the full LFP

Due to the non-homogenous repartition of different compartments and synapses across hippocampal layers, the various spectral profiles associated to these elements should result in non-homogenous distributions of the LFP power in various bands across laminar recording sites. We thus quantified the spatial contribution of several representative frequency bands (SW and gamma in the ranges 5-20 Hz and 30-55, respectively; and ripple and supra-ripple in the ranges 80-180 Hz and 190-300 Hz, respectively) to the power of the simulated CA1 LFP.

The power in these bands was computed for all modeled SWR and their spectra were averaged and baseline-subtracted across all simulation sessions (N=25 simulation sessions). The results (Figure 3A) are in good agreement with our previous analysis: Ripple and supra-ripple components (mean peak frequency with 95%

confidence interval 136.39 ± 1.69 Hz; 246.02 ± 2.78 Hz, respectively) are significantly segregated to stratum pyramidale (Figure 3B, bottom subpanels; Figure 3C, bottom subpanels; $p<10^{-5}$ ranksum test for the comparison of stratum pyramidale and stratum radiatum LFP power), whereas gamma and sharp-wave components (mean peak frequency with 95% confidence interval 15.06 ± 0.74 Hz; 36.85 ± 0.56 Hz, respectively) are mostly observed in the apical dendrites of CA1 (Figure 3B, top subpanels; Figure 3C, top subpanels; $p<0.01$ ranksum test for the comparison of stratum pyramidale and stratum radiatum LFP power; N=25 simulation sessions, 3,250 SWR episodes). Crucially, similar results were obtained when using the synaptic component of the LFP (LFPsyn) (see also Figure 2A and Figure S3). These results confirm that the spatial distribution of SWR-associated LFP power across bands reflects the contribution of differentiated synaptic and transmembrane mechanisms to SWR phenomena. Next, we investigated the contribution of CA3 input to these mechanisms.

CA1-associated neuronal correlates of CA3 input

Experimental evidence suggests that the sharp-wave in CA1 LFP represents incoming CA3 synchronous depolarizations onto the apical dendritic field of CA1. In addition, SWR related CA3 activity presents spectrogram increases that spread to the ripple-band (see Figure S2D) and followed by CA1 ripples. Thus, we asked to which extent the activities of CA1 reflect CA3 synaptic input during SWR. In order to address this question, we used field-PSC coherence analysis between CA3 full LFP and CA1-associated population synaptic currents. For this purpose, peri-SWR population dendritic EPSCs to pyramidal neurons (dEPSCs), somatic IPSCs (sIPSCs) and somatic EPSCs to interneurons (sEPSCs) were computed by linear summation of PSCs across neurons. First, we observed that CA3 field and CA1 dEPSCs were coherent throughout the broad-band spectrum; that is, over gamma (<100 Hz), and high-frequency oscillations (>100 Hz) (Figure 4A, lower subpanels). Furthermore, CA3 and CA1 (ripple) high-frequencies were largely incoherent for both pyramidal cells- and interneuron-associated PSCs, but their activity was coordinated in the gamma band (>25 Hz) (Figure 4A, upper subpanels). These findings suggest that CA3 and CA1 ensembles are coordinated by gamma activity and not in the ripple band although ripples occur simultaneously (Carr et al., 2012).

Next, we investigated whether this gamma input would manifest itself in the coordinated dynamics of populations within CA1. Thus, we divided CA1 pyramidal cells and interneurons into two groups and re-computed the peri-SWR sub-population dEPSCs, sIPSCs and sEPSCs. In line with our reasoning, these CA1 population PSCs were coherent at ripple frequencies (80-180 Hz) (Figure 4B). Interestingly, we found that these PSC were also coherent in the gamma range (approximately 50 Hz). Furthermore, whereas the increase in gamma coherence was more prominent between sEPSCs and sIPSCs, sIPSCs associated with interneurons and pyramidal cells were found incoherent in this band (Figure 4B, leftmost subpanel). Overall, intrinsic CA1 activity, that is the activity that coordinates CA1 ripples, is also modulated at slow gamma frequencies.

We further checked whether peri-SWR CA3-gamma oscillations were associated with transient increases in gamma-modulation of spiking activity. We addressed this question by computing CA3 gamma-triggered time histograms of both CA3 and CA1 spiking activity. We found that both CA3 and CA1 discharges were coordinated by CA3 gamma LFP (Figure 4C), with CA3 spikes occurring close to the peak of the LFP gamma oscillation (mean phase with 95% confidence interval -10.37±3.70; Z = 5.3627, $p<4.08*10^{-21}$, bootstrapped Rayleigh test; Figure 4D, blue circular histogram), and CA1 spikes occurring almost one-quarter period afterward (mean phase with 95% confidence interval 47.0212±5.57; Z = 4.7598, $p<0.0027$, bootstrapped Rayleigh test; Figure 4D, red circular histogram). Furthermore, as expected, both CA1 and CA3 displayed significantly increased spike modulation depths (see STAR Methods, Quantification and Statistical Analysis Section) during SWR as compared to that of surrogate (non-SWR) epochs ($p<0.01$ ranksum test for the comparison between SWR gamma discharge modulation vs. non-SWR gamma discharge modulation; Figure 4E). Our results suggest that transient gamma oscillatory activity, but not ripples, may establish a communication channel between CA3 and CA1 in the hippocampus. Furthermore, SWR-gamma oscillations are highly transient, and modulate both CA3 and CA1 ensemble discharges. Interestingly, I-E and I-I ensemble interactions in CA1 are clearly coupled in gamma and ripple bands, suggesting that both rhythms play a role in shaping the underlying sequences of action potentials occurring during ripples. We next investigated the microscopic determinants of ripple coordination.

Coordinated somatic excitation and inhibition underlie ripple oscillations

SWR episodes are thought to be mediated by precise network E-I balance (Brunel and Wang, 2003). In particular, ripple dynamics is defined by coordinated synaptic interactions. However, whether ripples are shaped by the dynamics of EPSCs or IPSCs is still controversial (see (Maier et al., 2011) and the recent investigation reported in (Gan et al., 2017)). We sought to add more evidence to this question by analyzing CA1 population dEPSC, sIPSC and sEPSCs. To this end, using a first-order temporal derivative (Gan et al., 2017; Maier et al., 2011), we generated binary signals (point-processes) with the detected 10% largest synaptic events (see STAR Methods, Quantification and Statistical Analysis Section), then we computed the PSC-triggered CA1 ripple-band LFP (80-180 Hz) average (Figure 5A displays an example event). This analysis was performed across all events and simulation sessions.

Consistent with (Gan et al., 2017), PSC-triggered full-LFP averages revealed that unlike dEPSC, sIPSC were locked to the ripple oscillation (Figure 5B, top and bottom panels). Crucially, we found that sEPSC were also rhythmically locked at ripple frequencies (Figure 5B, middle panel), suggesting that not only concerted sIPSCs, but also sEPSCs are associated to the ripple oscillation. It is worth noting that the contribution of sEPSCs to the ripple power of the LFP is low in the simulated CA1 (see Figure S3A), as connections to interneurons are sparse and excitatory-to-excitatory associational collaterals are absent in the transverse axis of this hippocampal subfield (Andersen, 2007; Bezaire and Soltesz, 2013). Finally, phase analysis revealed that sIPSCs occur with largest probability at the rising phase of the ripple (mean phase with 95% circular confidence interval -81.41±3.95 degrees; $Z = 55.29$, $p < 10^{-28}$ bootstrapped Rayleigh test; Figure 5C, bottom subpanel), whereas sEPSCs tend to occur closer to the trough of the ripple oscillation, where we expect the peak of glutamatergic neurotransmission to happen, that is, coinciding with the firing phase of pyramidal cell populations (mean phase with 95% circular confidence interval -127.36±5.43 degrees; $Z = 24.82$, $p < 10^{-11}$ bootstrapped Rayleigh test; Figure 5C, middle subpanel). Furthermore, dEPSCs are not significantly coupled to ripples ($Z = 0.023$, $p < 0.97$ bootstrapped Rayleigh test; Figure 5C, top subpanel). Thus, rhythmic somatic excitation and inhibition, but not dendritic excitation due to CA3 activity, coordinate CA1 ripple oscillations.

Interneurons pace CA1 membrane potentials during SWR episodes

Previous *in vivo* and *in vitro* experimental findings suggest that the activity of interneurons is critical for the occurrence of SWR complexes (Schlingloff et al., 2014; Stark et al., 2014). Our previous results are in agreement with this possibility. However, instead of being the sole generators of SWR complexes, it has been suggested that both pyramidal cells and interneurons are necessary to generate SWR, and that interneurons have the specific role of pacing activity of pyramidal cells. Yet, this hypothesis has not been directly demonstrated experimentally. In order to test it in our model, we examine the membrane potentials of individual CA1 cells and investigate how subthreshold events that do not result in an action potentials relate to PSCs in the same cell (English et al., 2014; Hulse et al., 2016).

First, we observed that the fluctuations in membrane potential of CA1 pyramidal cells and interneurons were correlated with the occurrence of ripples in CA1. The time course of peri-SWR membrane potentials was composed of three successive parts, reported by previous experimental work (English et al., 2014): a depolarization due to incoming CA3 activity, a high-frequency oscillation generated by peri-synaptic activity, and a post-ripple hyperpolarization (Figure 6A; Figure S4A). We next observed that the LFP and the membrane potential (Vm, see also STAR Methods) had a specific ripple-band phase relationship (Figure S4B). Detailed quantification of this phase shift revealed that peri-ripple Vm leads the peri-ripple LFP by approximately 90 degrees (mean phase value with 95% circular confidence interval 85.81±3.35 degrees; Z

= 18.72, $p<3.7*10^{-11}$ Bootstrapped Rayleigh test; Figure S4C), reflecting the capacitive coupling between the membrane potential and the summed membrane currents.

Given our above analysis of synaptic currents, these last results suggest the membrane potential of pyramidal cells and interneurons may be paced by population inhibitory and/or excitatory currents. Indeed, single-cell membrane potentials seem largely modulated by population PSCs (Figure 6A, bottom panel). Thus, we asked two key questions: first, whether the ripple-band activities of the membrane potentials correlated to that of the PSCs; and second, whether their time relationship was systematic. To this end, using again derivative-based methods, we generated binary signals (point-processes) with the detected largest synaptic events, and the 10% largest Vm positive slope fluctuations occurring in the soma of non-participating cells in the CA1 network during the occurrence of individual ripples (see Figure 6B for a schema; and STAR Methods for details). We then performed Vm-PSC binary-signals cross-correlation analysis, averaged across all cells and then across all ripple events. We found that neither sEPSCs, nor dEPSCs were correlated with Vm of both pyramidal cells and interneurons (Figure 6C, blue and red curves). Interestingly, only sIPSCs displayed a large correlation with interneurons and pyramidal Vm, with largest correlation occurring significantly before zero time-lag ($p<10^{-5}$ bootstrapped sign test; Figure 6C, black curves and insets), indicating that a sIPSC peak occurs consistently after a peak of Vm fluctuation. These results suggest that interneuronal discharges and the resulting inhibitory PSCs onto target cells pace both pyramidal cells and other interneurons by preventing Vm fluctuations to turn into action potentials during SWR. Furthermore, the peri-ripple peak sIPSC, but not the peri-ripple peak dEPSC was correlated with the magnitude of post-ripple hyperpolarization (r=-0.6513, $p=1.19*10^{-17}$; r=-0.1604, p=0.063, respectively, N = 150 cells; Figure 6E), indicating that local interneuronal activity, but not that incoming CA3 excitation, affects the magnitude of post-ripple hyperpolarization. As sIPSC amplitude correlates with ripple power, this result is in line with previous experimental work (English et al., 2014; Gan et al., 2017). In addition, the spectra of Vm-sIPSC cross-correlations displayed a large power modulation at ripple and supra-ripple frequencies (Figure 6D, black curve). In turn, Vm-dEPSC cross correlations showed a similar effect over gamma frequencies, suggesting a gamma-ripple coupling during SWR (Figure 6D, blue curve).

Dynamics of network excitation-inhibition (E-I) balance

Next, we investigated the relationship between excitatory and inhibitory synaptic currents in order to better understand the E-I balance dynamics during SWR. We extracted SWR-related excitatory postsynaptic currents (dEPSCs, sEPSCs) and inhibitory postsynaptic currents (sIPSCs) from the modeled CA1 neuronal populations during SWR episodes. This allowed us to investigate two types of E-I balance: the *exogenous E-I balance* is the ratio of dEPSC to sIPSC activity, and thus focuses on excitation triggered by CA3 afferent activity, while the *endogenous E-I balance* is the ratio of sEPSC to sIPSC, which thus focuses on local recurrent excitation. While the time course of dEPSCs, sEPSCs and sIPSCs bears some similarity due to the driving of CA3 input, we found that dEPSCs consistently preceded sIPSCs during the time course of individual ripples (Figure 7A and its corresponding boxplot in Figure 7C), with the peak of excitation occurring approximately 6 ms before that of inhibition (mean peak time difference with 95% confidence interval 5.96 ± 0.3 ms) (see also Gan et al., 2017). Figure 7A shows that dEPSCs' average amplitude grows fast as the SWR episode reaches its peak and then decays similarly fast as the ripple episode is dampened due to increased inhibitory activity. Specifically, the ratio between normalized average dEPSCs and sIPSCs during individual SWR episodes indicates that, while it is largely inhibited during baseline activity, the CA1 network presents an instantaneous and fast increase in excitation, later decaying exponentially (Figure 7A, right subpanel).

We also observed that sIPSCs slightly preceded sEPSCs, in good agreement with the fact that interneuronal discharges precede that of pyramidal cells during SWR episodes (mean PSC-peak time difference with 95% confidence interval -0.28 ± 0.22 ms) (Figure 7B; see also Figure S2F) (Csicsvari et al., 2000). These results are in line with the hypothesis that SWR episodes result from a transient imbalance in excitation followed by an increase in inhibitory responses due to recurrent excitation by CA1 cells. In addition, ripples are instantiated by sparse local excitatory activity within CA1 that may partly result from interneuron-mediated enhancement (rebound) as suggested by an sEPSC growth upon the first increase in inhibitory conductance up to the peak of power of the ripple (Figure 7B, zero lag in the color bar). Upon this first sEPSC increase, the relationship reverses, as inhibitory activity likely dampens the activity of both pyramidal cells and interneurons, finally extinguishing the SWR-related activity (trajectory in Figure 7B). We also examined the ripple-band sIPSCs vs. sEPSCs (i.e. by filtering in the band 70-120 Hz; note that the band definition changes after the observations in Figure 2A), and concluded that sEPSCs preceded sIPSCs in the ripple-associated phase trajectory (Figure 7D), in contrast to broad band activity. These results are in line with previous experimental and modeling work suggesting that ripples involve an interplay between excitation (provided by sEPSC and dEPSC) and inhibition (provided by sIPSC) (Hulse et al., 2016), where ripple-band excitation precedes ripple-related inhibition (Memmesheimer, 2010). Crucially, in line with this assumption, E-I balance, but neither individual IPSC nor EPSC amplitude, was predictive of the participation of individual CA1 pyramidal cells to a SWR events (Figure 7E).

Due to the differential involvement of synaptic currents in the LFP power at various frequency bands, we reasoned that information about E-I balance may be also inferred from such mesoscopic measurements. Thus, we sought to determine whether specific frequency bands of the broad-band peri-ripple LFP spectrum were predictive of the E-I balance, as computed as the ratio of excitation to inhibition. In order to capture this information, we trained a linear epsilon-support vector machine (ε-SVM) to regress out E-I balance from single-event spectrogram values (see STAR Methods for details). The peri-event time-frequency Morlet wavelet spectrograms (broad-band, 0-300 Hz) of each SWR were used to regress out their underlying population averaged E-I balance values (i.e. <|dEPSC|> / <|sIPSC)|>, and in a separate calculation <|sEPSC|> / <|sIPSC)|>). In order to capture differentially the low- and high-frequency components of the LFP with comparable regression coefficients, we z-scored each peri-SWR spectrogram.

Interestingly, in line with previous analyses (Figure 4), analysis of regression coefficients reveals that a large spectral power over CA1-local gamma (>55 Hz), ripple and supra-ripple frequencies is predictive of a stronger CA1 local inhibitory drive with respect to exogenous excitation (Figure 7F, cold colors), because a power increase in these bands leads to a decrease in E-I balance. Interestingly, we found that larger recurrent excitation is more specifically associated with larger ripple band power (Figure 7G, warm colors), in line with our previous analysis (see Figure 5). Furthermore, sharp wave and slow gamma activity are related to excitatory components (dEPSCs and sEPSCs) (Figure 7G, see SVM coefficients over low frequencies). The overall prediction of the SVM across all simulation sessions was associated with a correlation coefficient $r = 0.6712$ for dEPSC-to-sIPSC (p=0 for the pooled dataset; 20-fold cross-validation; $N = 25$ model sessions; Figure 7F, lower subpanel). Conversely, the overall prediction of the SVM was associated with a correlation coefficient $r = 0.2574$ for sEPSC-to-sIPSC (p=3.03*10^{-45} for the pooled dataset; 20-fold cross-validation; $N = 25$ model sessions; Figure 7G, lower subpanel). Thus, power spectral variability of modeled LFP during SWR predicts better exogenous than endogenous E-I balance. However, the spectral profile of regression coefficients shows that the ripple oscillation is more specifically related to endogenous E-I balance, further supporting the idea that both local excitation and inhibition are necessary to shape this rhythm. Our results suggest that although LFP activity is inherently ambiguous, its power spectrum carries information on elementary network phenomena that shape E-I balance at the local network level during SWR-associated events.

Inactivation of phasic excitation of CA1 pyramidal cells onto interneurons enhances SWRs

As shown in the above section, sEPSCs may partly mediate ripple coordination. Thus, we asked whether these peri-somatic excitatory synapses onto interneurons were required for SWR complexes to occur. We addressed this question by selectively blocking sEPSCs onto all CA1 interneurons. Surprisingly, this circuit manipulation did not abolish ripples (Figure 8A, B). Rather, it enhanced their time-frequency characteristics (e.g., spectral power in the ripple band). SWR generated without sEPSC dynamics were also associated with larger recruitment of pyramidal cells (from ~10% with upper limit of 15% in control condition, to ~15%, reaching an upper limit of ~30%). Pyramidal cells also tended to display more peri-SWR bursts

(Figure 8C, D). These findings were in general agreement with previous work, where genetically-suppressed synaptic excitation did not abolish ripples, but somewhat enhanced them, together with SWR-associated burstiness of pyramidal cells (Racz et al., 2009).

In addition, we found that pyramidal cells that were driven to spike had changed E-I balance during sEPSC-blockade with respect to control conditions, displaying less prominent inhibition during sEPSC-blockade after the phase of enhanced excitation (Figure 8E; $p = 0.002$, two-sample Kolmogorov-Smirnov test for the comparison between the two conditions). These results further support enhanced pyramidal cell participation and a tendency toward bursting during selective blockade of recurrent excitation results from the suppression of phasic feedback inhibition. Whereas these results suggest that sEPSCs are not causally involved in the genesis of the ripple oscillation itself, they also suggest that they implement a feedback inhibition mechanism that guarantees the selection of a sparse subset of pyramidal cell to take part in the ripple event, and limits the bursting of these cells. This may be key to control the selective emergence of well-defined cell assemblies associated to memory traces and the associated memory consolidation mechanisms (Diba and Buzsáki, 2007; Lee and Wilson, 2002). Following the same approach, we further tested whether selective blockade of the various CA1 synaptic interactions were critical for SWR emergence. In order to validate that the generation of ripple oscillations requires I-I driven excitation in addition to inhibition, we investigated the network dynamics when somatic inhibition of excitatory neurons was blocked. The results (Figure 8F) show that ripples are replaced by high-frequency oscillations (>200Hz) together with a broad recruitment of the pyramidal cells (only 25 exemplary pyramidal cells are shown in the plot to ease visualization of individual bursts), supporting that feedback inhibition is needed to bound the ripple frequency and limit CA1 pyramidal cell participation. We examined two additional cases: When reciprocal (I-I) inhibition was blocked; and finally, when CA3 input to CA1 was blocked (see Supplemental Experimental Procedures for details). In both cases, SWR complexes were again abolished. From the resulting network activities, we can conclude that reciprocal inhibition is needed to control inhibitory cell participation and dynamics (Figure S5A). Furthermore, in absence of excitatory input from CA3, CA1 is dominated by gamma activity resulting from I-I interactions (Taxidis et al., 2012; Wang and Buzsáki, 1996), and limited pyramidal cell participation (Figure S5B).

Comparison to *in vivo* LFP recordings from the macaque hippocampus

In order to further validate and investigate the dynamics of the discovered SWR-related components, we used LFP recordings of the CA1 hippocampal subfield of macaque monkeys. Multi-contact recording electrodes were positioned based on high-resolution anatomical MRI scans and visual assessment of hippocampal electrical activity. Electrode tips targeted the CA1 stratum radiatum and stratum pyramidale. Classification of electrode tips was based on visual detection of oscillations (LFP deflections and high-frequency oscillations), inspection of synchronous spiking activity and high-resolution MRI scans. A simplified schema of our electrophysiological recordings together with a typical electrode penetration, are presented in Figure 9A. Time courses and time-frequency characteristics of SWR episodes were in agreement with our model (Figure 9A) (Logothetis et al., 2012; Ramirez-Villegas et al., 2015).

The average time course and baseline-subtracted spectrograms of the LFP filtered in previously selected frequency bands (SW/gamma, ripple and supra-ripple) are depicted in Figure 9B-C (average across N=15 experimental sessions, 4 animals). We then asked how the energy in these bands was distributed across structures. We then computed peri-SWR power signals for each component (see STAR Methods). Power profiles were z-scored and peri-event power maxima for each recording channel were extracted. Whereas the ripple and supra-ripple components have larger power at recording tips putatively located in stratum pyramidale (Figure 9E rightmost columns; $p<0.02$, Wilcoxon's ranksum test for the comparison between power in stratum radiatum and stratum pyramidale), gamma and SPW power remained evenly distributed across recording sites ($p>0.15$, Wilcoxon's ranksum test for the comparison between power in stratum radiatum and stratum pyramidale). In comparison to our simulations, these results confirm the somatic origin of ripple and supra-ripple frequencies. Moreover it suggests a broader spread of low and gamma frequencies along a dendritic tree that would extend closer to the soma than in the geometric configuration of our model. However, it is worth noting that the recording configuration in the macaque anterior hippocampus (that does not guarantee a penetration normal to CA1 strata) may have an effect in identifying the spatial localization of these sources and their associated power profiles.

Importantly, like in modeled SWR (Figure S2G), we observed that SWR events recorded experimentally reveal different degrees of synchrony of participating neuronal populations to the LFP, as quantified by spike-field coherency (SFC) maps (Figure 9D) (Ramirez-Villegas et al., 2015). Notably, action potentials synchronize in the ripple (80-180 Hz) and sharp wave (<20 Hz) (Figure 9D, top subpanel). Concordantly, SFC-phase analysis also shows prominent phase locking of cell discharges to gamma (25-79 Hz) and supra-ripple (>180 Hz) LFP frequencies in a magnitude comparable to that of the ripple and sharp wave components (<20 Hz) (see group results in Figure 9D; across-sessions average N=15 experimental sessions, 4 animals).

As supporting analysis, we further characterized the SWR-associated dynamical components in order to compare both modeled and experimental SWR complexes. We found that sharp wave, gamma, ripple and supra-ripple components have similar peri-event instantaneous frequencies (Figure S6A). Furthermore, all dynamical components are associated with power increases above baseline (Figure S6B). Finally, we assessed how predictive of SWR occurrence were the power increases in each frequency bands using linear SVM classifiers (see also STAR Methods and Supplemental Experimental Procedures). The observed prediction performance across bands (Figure S6C) ranked similarly for experimental and modeled data, differing significantly from chance level classification.

Finally, although time and frequency features SWR complexes from our experimental recordings were in general agreement with modeled ones, in vivo SWRs are often accompanied by a post-ripple low-frequency hyperpolarization in the LFP (Figure S7A) absent from simulated traces. As such component is present solely in sharp waves associated with "fast" ripples (Ramirez-Villegas et al., 2015; Varga et al., 2014), we hypothesized that the post-ripple LFP hyperpolarization, where likely bistratified cells play a key role (Varga et al., 2014), resulted from dendritic inhibition onto the principal cells of CA1. We tested this hypothesis by simulating input IPSCs into the dendritic compartments (dIPSCs) of modeled CA1 pyramidal cells (see Supplemental Experimental Procedures for details). In summary, this resulted in raw LFPs with intermingled negative deflections, sometimes associated with ripple oscillations despite the low pyramidal cell participation (3% to 5% of active cells; Figure S7B-C); alongside, we found that during these SWR episodes, the amplitude of the dIPSCs was precisely timed and correlated with the LFP amplitude decrease associated with the post-ripple hyperpolarization (Figure S7D-E). Thus, the observed LFP post-ripple hyperpolarization may be mediated specifically by dendritic inhibition, which can be accounted for by including more neuronal types into our model.

Discussion

In this study, we presented a biophysical model encompassing a wide-range of specific neural mechanisms underlying SWR episodes across multiple scales. At the cellular level, we used minimal conductance-based compartmental neural models, with a single dendritic and synaptic compartment per cell. The modeled network spanned both CA1 and CA3 hippocampal subfields, with one type of pyramidal cell and one type of interneuron in each region. This allowed us to dissect dendritic from somatic activities in CA1, associated with CA3 input and CA1 recurrent activity respectively, and to model the spatio-temporal properties of LFP in CA1. We observed that CA3-induced dendritic depolarizations manifest themselves by SW and slow gamma (<55Hz) activity in CA1. Interestingly, coherency analysis revealed that CA3 network oscillations in the slow gamma band specifically could be observed beyond the dendrites and reach CA1 somatic activity. Local post-synaptic processing in CA1 generated the ripple oscillations and involved both somatic EPSC and IPSC. Both PSCs seem involved in selecting firing ensembles in CA1, possibly establishing specific synaptic mechanisms that mediate sequence replay. Our results –validated with *in vivo* recordings from the macaque hippocampus– provide detailed evidence that emergence of SWR activity depends on elaborated frequency-specific interactions of remote and local neuronal activity in CA1. These rhythmic activities may be critical for the emergence of *in vivo* SWR activity, and therefore for the formation of hippocampus-dependent memory representations, and other memory-related functions such as retrieval (Carr et al., 2011).

In vivo CA3-CA1 SWR dynamics predicted by a simple multi-compartment model

The modelling study reported in this work aimed at gaining better understanding on the nature of the SWR complexes, and the meso- and microscopic scale hippocampal dynamics during these episodes. Notably, the model network of compartmental neurons predicts several features of SWR dynamics as observed *in vivo* in our experimental preparations on macaque monkeys (Logothetis et al., 2012; Ramirez-Villegas et al., 2015), by relying on local synaptic interactions between inhibitory and excitatory neurons as suggested by recently published data (Stark et al., 2014). Simulated LFP recordings were in close correspondence with experimental data in many respects: LFP traces are a compound of irregular background activity intermingled with episodes of highly synchronous neuronal activity in the SWR range (<20 Hz concomitant with 80-180 Hz oscillations) as indicated by spectral analysis. SWR duration, cell participation and ripple-SW correlation are in correspondence with previous investigations (Csicsvari et al., 2000; Logothetis et al., 2012; Patel et al., 2013). During SWR episodes, incoming activity from CA3 was dominated by bursts of lower frequency associated with LFP gamma-like oscillations (Sullivan et al., 2011). CA3 bursts were not coherent with the ripple activity in CA1, suggesting the *de novo* generation of CA1 ripples as supported by previous experimental studies (Sullivan et al., 2011). Concordantly, CA3 and CA1 activities were only coordinated by their low frequency LFP, namely, up to the upper bound of the slow gamma band (~55 Hz) (Carr et al., 2012). Furthermore, the relationship between CA1 spiking activity and peri-event LFPs was very similar to that of *in vivo* recordings reported previously (Ramirez-Villegas et al., 2015). Peaks of coherent activity in relation to spiking activity were found for SW and ripple frequency bands, with pyramidal neurons' and interneurons' spiking activity occurring preferentially close to the trough and at the rising phase of the ripple oscillation, respectively.

Dissection of frequency specific sources of peri-SWR LFPs

Our results indicate that gamma and sharp wave components dominate the LFP in stratum radiatum due to incoming synchronous activity from CA3 and subsequent SW-related dendritic depolarization (Carr et al., 2012). Furthermore, oscillatory activity in the ripple (80-180 Hz) as well as supra-ripple (>180 Hz) frequency bands originate in stratum pyramidale. Ripple oscillations were present in both interneuronal and pyramidal currents. In particular, local somatic IPSCs and EPSCs were specifically phase-locked to CA1 ripple oscillations, but not dendritic EPSCs originating from CA3 input. These results are consistent with recent *in vivo* findings (Gan et al., 2017) probing the dynamics of peri-ripple IPSC and EPSC. Interestingly, these observations differ from *in vitro* studies (Maier et al., 2011), which have been the basis to ascribe a key roles to axo-axonic electrical coupling or recurrent synaptic excitatory interactions between pyramidal neurons in ripple generation (Maier et al., 2003). Furthermore, in this study we found that inhibitory network activity generates high-frequencies in the LFP power spectrum, spanning largely beyond the ripple band.

Ripple oscillogenesis

The involvement of pyramidal cells and interneurons in hippocampal ripple oscillogenesis has been extensively investigated during the last years (Ellender et al., 2010; English et al., 2014; Hajos, 2004; Karlocai et al., 2014; Le Van Quyen et al., 2008; Mann et al., 2005; Oren et al., 2006; Schlingloff et al., 2014; Stark et al., 2014). Fast oscillations may come about by strong recurrent excitatory synapses (Memmesheimer, 2010; Traub and Bibbig, 2000), recurrent inhibition (Brunel and Wang, 2003; Geisler et al., 2005; Wang and Buzsáki, 1996; Whittington et al., 1995) and the combination of both in form of E-I loops (Brunel and Wang, 2003; Memmesheimer, 2010; Schomburg et al., 2012; Taxidis et al., 2012). In line with recent evidence (Ellender et al., 2010; Gan et al., 2017; Schlingloff et al., 2014; Stark et al., 2014), our modeling experiments suggest that interneuronal activity is of great importance for the occurrence of physiological SWR activity. Our results indicate that absence of inhibition and inhibitory-inhibitory synapses is associated with abolishment of ripples (due to interneuron hyperactivity) and induce major changes in the SWR-associated dynamics beyond physiological regimes, in line with results on interictal epileptiform discharges (Karlocai et al., 2014).

Interneurons are likely the fastest control elements of CA1 network activity, with faster spikes than that of pyramidal cells in addition to high-frequency population peri-synaptic activity. Since ripple activity is only weakly modulated by incoming somatic EPSCs from CA1 pyramidal neurons, we suggest that interneuronal populations pace ripple oscillations mediated mainly by fast local interactions with other interneurons. Indeed, we directly tested this hypothesis, and discovered that ripple-related membrane potentials of interneurons and pyramidal cells are paced by inhibitory, but not excitatory synaptic events or the combination of both. This pacing however does not imply that I-I interactions entrain the network at their own oscillation frequency. *In vivo* experimental evidence suggests that ripple oscillations cannot emerge by entraining populations of interneurons alone (Hulse et al., 2016; Stark et al., 2014), which is confirmed by our own attempt to suppress I-I synaptic interactions in the model, leading to higher frequency oscillations of low amplitude due to inhibitory activity alone. The excitatory population is thus entrained at a lower frequency than the inhibitory network pacing it, and bounds the dominant frequency of the phenomenon to the ripple band.

Low-frequency discharges and sEPSC: two ingredients for coordinated sequences replay

SWR have been associated to coordinated sequence replay, and how these sequences are precisely selected remains a major question. Two features may play a key role in this selection: the CA3 input, and a recurrent control of the sparsity of excitatory spiking within CA1. In line with experimental studies, although each pyramidal neuron receives a number of synaptic inputs from CA3 and CA1 neuronal populations, most CA1 principal cells in our model remain silent during a single SWR burst (Csicsvari et al., 2000). Interestingly, our analysis suggests that the exogenous E-I balance can determine the participation of each pyramidal cell to the SWR, and the timing of these components may control spike timing to precisely represent a replayed sequence, corresponding to a specific memory trace. One element of control of the exogenous E-I balance is the spatio-temporal pattern of CA3 input. As CA3 is also able to replay precise sequences (Karlsson and Frank, 2009), its inputs to CA1 may –to some extent– play a role in the selection of CA1 cells involved in replay. Our model supports this hypothesis, because the CA3 slow gamma activity modulates specifically the peri-SWR somatic activity in CA1, suggesting slow gamma oscillations could transiently coordinate the CA3-CA1 network and possibly memory-replay as well. Although the current experimental evidence favors this possibility (Carr et al., 2012; Gillespie et al., 2016), it remains to be further tested in an extended version of our model.

Finally, our results suggest that somatic EPSC onto interneurons have a direct influence on the strength of the I-to-E feedback inhibition loop, limiting pyramidal cell participation and bursting. Thus, we hypothesize that somatic EPSC due to pyramidal synaptic collaterals –whereas not critical for SWR emergence– may be important for generating physiological SWR with their associated replay, by allowing the precise selection of a small number SWR-participating pyramidal cells. Therefore, these findings hold a key implication for memory-associated SWR replay, and hence for consolidation and retrieval processes previously ascribed to SWR complexes (Girardeau et al., 2009; van de Ven et al., 2016).

LFP correlates of network E-I balance

Due to the frequency specific signature of inhibitory and excitatory mechanisms, SWR modulated E-I balance can be inferred to a certain extent from the LFP spectral properties. Our results suggest that the relationship between SW, gamma, ripple and supra-ripple components carries information about CA1 E-I balance. In particular, the supra-ripple components –to a certain extent– could be a predictor of inhibitory activity within CA1 during SWR episodes, while slow frequencies reflect the level of exogenous excitation from CA3. Interestingly, the ratio between ripple and supra-ripple power relates to endogenous E-I balance is in line with the idea that CA1 pyramidal cells are necessary to shape ripple oscillations. Furthermore, our analysis of E-I balance during these episodes and its correspondence with peri-event LFP traces may be further generalized in a model taking into account a larger number of local populations and exogenous inputs to CA1. This could bring a better understanding of the mechanisms underlying the already documented diversity of SWR LFP signatures, as explained in the next subsection.

Towards brain-wide models of SWR

Indeed, it is worth noting that in this work we did not consider the network mechanisms involved in the dynamics of distinct subtypes of SWR complexes as reported in our previous work (Ramirez-Villegas et al., 2015). In this regard, our experimental recordings did not reveal major differences between SWR-subtypes beyond modulations in power and ripple frequency peak (as previously reported in (Ramirez-Villegas et al., 2015); not shown in the current results). Recordings with a greater spatial extent, however, may help to better understand their correlates and network-level mechanisms (notably, see (Oliva et al., 2016)). Indeed, CA1 activity may be modulated by other structures of the hippocampal formation such as the CA2 subfield (Kay et al., 2016; Oliva et al., 2016), or entorhinal cortex inputs (Hahn et al., 2012) thus selectively enhancing or possibly adding other oscillatory components to the extracellular potentials over distinct spatial locations, likely associated with different neuronal targets. In a similar vein, a recent study indicates that the three major PV cell classes (basket, bistratified and axo-axonic cells) activate differently during SWR episodes, suggesting that fast network episodes with distinct electrophysiological characteristics involve different inhibitory circuits (Varga et al., 2014) . We found support for this hypothesis with our model by showing the putative effect of bistratified cells on post-ripple hyperpolarisation. It is likely that differential recruitment of interneurons also depends on long-range mechanisms involving neocortical and transient changes in subcortical neuromodulatory activity (Varga et al., 2009), ultimately altering microscopic and mesoscopic SWR dynamics. This could be accounted for in further extensions of the present model.

Supplemental Information

Supplemental Information includes ten figures and text accounting for Supplemental Experimental Procedures.

STAR Methods

Detailed methods are provided in this manuscript and include the following:

- Key resources table
- Contact for reagent and resource sharing
- Experimental model and subject details
- Method details
    1. Single neuron models
    2. Network models connectivity and synapses
    3. Determining unitary-PSP amplitudes
    4. Synapse probabilities
    5. Estimating the transmembrane currents of the model
    6. Non-synaptic transmembrane currents
    7. Recording sites and Local Field Potential (LFP) estimation
    8. Intracortical electrophysiological recordings
- Quantification and statistical analysis
    1. Simulations and SWR event detection
    2. Frequency analyses
    3. Post-synaptic current analyses
    4. Processing of experimental neural data
- Data and software availability

Author Contributions

JFR-V and MB conceived and designed the research; JFR-V performed research; MB supervised the research; KFW, NKL and MB contributed new reagents/analytic tools; JFR-V analyzed the data; JFR-V and MB wrote the manuscript with contributions from the other authors.

Acknowledgements

JFR-V wishes to acknowledge Maria Constantinou and Araceli Ramirez-Cardenas for insightful comments and discussions on previous versions of this manuscript. MB acknowledges funding from the Max Planck ETH Center for Learning Systems. Joachim Werner and Michael Schnabel provided excellent technical support during the development of this work. This research was supported by the Max Planck Society.

References

Andersen, P. (2007). The hippocampus book (Oxford; New York: Oxford University Press).

Bezaire, M.J., and Soltesz, I. (2013). Quantitative assessment of CA1 local circuits: Knowledge base for interneuron-pyramidal cell connectivity: Quantitative Assessment Of Ca1 Local Circuits. Hippocampus *23*, 751–785.

Brunel, N., and Wang, X.-J. (2003). What Determines the Frequency of Fast Network Oscillations With Irregular Neural Discharges? I. Synaptic Dynamics and Excitation-Inhibition Balance. J. Neurophysiol. *90*, 415–430.

Buzsáki, G. (2015). Hippocampal sharp wave-ripple: A cognitive biomarker for episodic memory and planning: Hippocampal sharp wave-ripple. Hippocampus *25*, 1073–1188.

Buzsaki, G., Horvath, Z., Urioste, R., Hetke, J., and Wise, K. (1992). High-frequency network oscillation in the hippocampus. Science *256*, 1025–1027.

Carr, M.F., Jadhav, S.P., and Frank, L.M. (2011). Hippocampal replay in the awake state: a potential substrate for memory consolidation and retrieval. Nat. Neurosci. *14*, 147–153.

Carr, M.F., Karlsson, M.P., and Frank, L.M. (2012). Transient Slow Gamma Synchrony Underlies Hippocampal Memory Replay. Neuron *75*, 700–713.

Chrobak, J.J., and Buzsáki, G. (1996). High-frequency oscillations in the output networks of the hippocampal–entorhinal axis of the freely behaving rat. J. Neurosci. *16*, 3056–3066.

Csicsvari, J., Hirase, H., Czurkó, A., Mamiya, A., and Buzsáki, G. (1999). Oscillatory coupling of hippocampal pyramidal cells and interneurons in the behaving rat. J. Neurosci. *19*, 274–287.

Csicsvari, J., Hirase, H., Mamiya, A., and Buzsáki, G. (2000). Ensemble patterns of hippocampal CA3-CA1 neurons during sharp wave–associated population events. Neuron *28*, 585–594.

Cutsuridis, V., and Hasselmo, M. (2011). Spatial Memory Sequence Encoding and Replay During Modeled Theta and Ripple Oscillations. Cogn. Comput. *3*, 554–574.

Diba, K., and Buzsáki, G. (2007). Forward and reverse hippocampal place-cell sequences during ripples. Nat. Neurosci. *10*, 1241–1242.

Ego-Stengel, V., and Wilson, M.A. (2009). Disruption of ripple-associated hippocampal activity during rest impairs spatial learning in the rat. Hippocampus NA-NA.

Ellender, T.J., Nissen, W., Colgin, L.L., Mann, E.O., and Paulsen, O. (2010). Priming of Hippocampal Population Bursts by Individual Perisomatic-Targeting Interneurons. J. Neurosci. *30*, 5979–5991.

English, D.F., Peyrache, A., Stark, E., Roux, L., Vallentin, D., Long, M.A., and Buzsaki, G. (2014). Excitation and Inhibition Compete to Control Spiking during Hippocampal Ripples: Intracellular Study in Behaving Mice. J. Neurosci. *34*, 16509–16517.

Foster, D.J., and Wilson, M.A. (2006). Reverse replay of behavioural sequences in hippocampal place cells during the awake state. Nature *440*, 680–683.

Gan, J., Weng, S., Pernía-Andrade, A.J., Csicsvari, J., and Jonas, P. (2017). Phase-Locked Inhibition, but Not Excitation, Underlies Hippocampal Ripple Oscillations in Awake Mice In Vivo. Neuron *93*, 308–314.

Geisler, C., Brunel, N., and Wang, X.-J. (2005). Contributions of Intrinsic Membrane Dynamics to Fast Network Oscillations With Irregular Neuronal Discharges. J. Neurophysiol. *94*, 4344–4361.

Gillespie, A.K., Jones, E.A., Lin, Y.-H., Karlsson, M.P., Kay, K., Yoon, S.Y., Tong, L.M., Nova, P., Carr, J.S., Frank, L.M., et al. (2016). Apolipoprotein E4 Causes Age-Dependent Disruption of Slow Gamma Oscillations during Hippocampal Sharp-Wave Ripples. Neuron *90*, 740–751.

Girardeau, G., Benchenane, K., Wiener, S.I., Buzsaki, G., and Zugaro, M.B. (2009). Selective suppression of hippocampal ripples impairs spatial memory. Nat Neurosci *12*, 1222–1223.

Gomperts, S.N., Kloosterman, F., and Wilson, M.A. (2015). VTA neurons coordinate with the hippocampal reactivation of spatial experience. ELife *4*.

Hahn, T.T.G., McFarland, J.M., Berberich, S., Sakmann, B., and Mehta, M.R. (2012). Spontaneous persistent activity in entorhinal cortex modulates cortico-hippocampal interaction in vivo. Nat. Neurosci. *15*, 1531–1538.

Hajos, N. (2004). Spike Timing of Distinct Types of GABAergic Interneuron during Hippocampal Gamma Oscillations In Vitro. J. Neurosci. *24*, 9127–9137.

Hajos, N., Karlocai, M.R., Nemeth, B., Ulbert, I., Monyer, H., Szabo, G., Erdelyi, F., Freund, T.F., and Gulyas, A.I. (2013). Input-Output Features of Anatomically Identified CA3 Neurons during Hippocampal Sharp Wave/Ripple Oscillation In Vitro. J. Neurosci. *33*, 11677–11691.

Hulse, B.K., Moreaux, L.C., Lubenov, E.V., and Siapas, A.G. (2016). Membrane Potential Dynamics of CA1 Pyramidal Neurons during Hippocampal Ripples in Awake Mice. Neuron *89*, 800–813.

Isomura, Y., Sirota, A., Özen, S., Montgomery, S., Mizuseki, K., Henze, D.A., and Buzsáki, G. (2006). Integration and segregation of activity in entorhinal-hippocampal subregions by neocortical slow oscillations. Neuron *52*, 871–882.

Karlocai, M.R., Kohus, Z., Kali, S., Ulbert, I., Szabo, G., Mate, Z., Freund, T.F., and Gulyas, A.I. (2014). Physiological sharp wave-ripples and interictal events in vitro: what's the difference? Brain *137*, 463–485.

Karlsson, M.P., and Frank, L.M. (2009). Awake replay of remote experiences in the hippocampus. Nat. Neurosci. *12*, 913–918.

Kay, K., Sosa, M., Chung, J.E., Karlsson, M.P., Larkin, M.C., and Frank, L.M. (2016). A hippocampal network for spatial coding during immobility and sleep. Nature *531*, 185–190.

Klausberger, T., and Somogyi, P. (2008). Neuronal Diversity and Temporal Dynamics: The Unity of Hippocampal Circuit Operations. Science *321*, 53–57.

Klausberger, T., Magill, P.J., Márton, L.F., Roberts, J.D.B., Cobden, P.M., Buzsáki, G., and Somogyi, P. (2003). Brain-state-and cell-type-specific firing of hippocampal interneurons in vivo. Nature *421*, 844–848.

Le Van Quyen, M., Bragin, A., Staba, R., Crepon, B., Wilson, C.L., and Engel, J. (2008). Cell Type-Specific Firing during Ripple Oscillations in the Hippocampal Formation of Humans. J. Neurosci. *28*, 6104–6110.

Lee, A.K., and Wilson, M.A. (2002). Memory of sequential experience in the hippocampus during slow wave sleep. Neuron *36*, 1183–1194.

Leonard, T.K., Mikkila, J.M., Eskandar, E.N., Gerrard, J.L., Kaping, D., Patel, S.R., Womelsdorf, T., and Hoffman, K.L. (2015). Sharp Wave Ripples during Visual Exploration in the Primate Hippocampus. J. Neurosci. *35*, 14771–14782.

Li, X.-G., Somogyi, P., Ylinen, A., and Buzsáki, G. (1994). The hippocampal CA3 network: An in vivo intracellular labeling study. J. Comp. Neurol. *339*, 181–208.

Logothetis, N.K., Eschenko, O., Murayama, Y., Augath, M., Steudel, T., Evrard, H.C., Besserve, M., and Oeltermann, A. (2012). Hippocampal–cortical interaction during periods of subcortical silence. Nature *491*, 547–553.

Maier, N., Nimmrich, V., and Draguhn, A. (2003). Cellular and Network Mechanisms Underlying Spontaneous Sharp Wave-Ripple Complexes in Mouse Hippocampal Slices. J. Physiol. *550*, 873–887.

Maier, N., Tejero-Cantero, Á., Dorrn, A.L., Winterer, J., Beed, P.S., Morris, G., Kempter, R., Poulet, J.F.A., Leibold, C., and Schmitz, D. (2011). Coherent Phasic Excitation during Hippocampal Ripples. Neuron *72*, 137–152.

Mann, E.O., Suckling, J.M., Hajos, N., Greenfield, S.A., and Paulsen, O. (2005). Perisomatic Feedback Inhibition Underlies Cholinergically Induced Fast Network Oscillations in the Rat Hippocampus In Vitro. Neuron *45*, 105–117.

McNamara, C.G., Tejero-Cantero, Á., Trouche, S., Campo-Urriza, N., and Dupret, D. (2014). Dopaminergic neurons promote hippocampal reactivation and spatial memory persistence. Nat. Neurosci. *17*, 1658–1660.

Memmesheimer, R.-M. (2010). Quantitative prediction of intermittent high-frequency oscillations in neural networks with supralinear dendritic interactions. Proc. Natl. Acad. Sci. *107*, 11092–11097.

Mizunuma, M., Norimoto, H., Tao, K., Egawa, T., Hanaoka, K., Sakaguchi, T., Hioki, H., Kaneko, T., Yamaguchi, S., Nagano, T., et al. (2014). Unbalanced excitability underlies offline reactivation of behaviorally activated neurons. Nat. Neurosci. *17*, 503–505.

Nakashiba, T., Buhl, D.L., McHugh, T.J., and Tonegawa, S. (2009). Hippocampal CA3 output is crucial for ripple-associated reactivation and consolidation of memory. Neuron *62*, 781–787.

Nicholson, C. (1973). Theoretical Analysis of Field Potentials in Anisotropic Ensembles of Neuronal Elements. Biomed. Eng. IEEE Trans. On *BME-20*, 278–288.

Nicholson, C., and Llinas, R. (1971). Field potentials in the alligator cerebellum and theory of their relationship to Purkinje cell dendritic spikes. J. Neurophysiol. *34*, 509–531.

Oliva, A., Fernández-Ruiz, A., Buzsáki, G., and Berényi, A. (2016). Role of Hippocampal CA2 Region in Triggering Sharp-Wave Ripples. Neuron *91*, 1342–1355.

Oren, I., Mann, E.O., Paulsen, O., and Hajos, N. (2006). Synaptic Currents in Anatomically Identified CA3 Neurons during Hippocampal Gamma Oscillations In Vitro. J. Neurosci. *26*, 9923–9934.

Patel, J., Schomburg, E.W., Berenyi, A., Fujisawa, S., and Buzsaki, G. (2013). Local generation and propagation of ripples along the septotemporal axis of the hippocampus. J. Neurosci. *33*, 17029–17041.

Pinsky, P.F., and Rinzel, J. (1994). Intrinsic and network rhythmogenesis in a reduced Traub model for CA3 neurons. J. Comput. Neurosci. *1*, 39–60.

Racz, A., Ponomarenko, A.A., Fuchs, E.C., and Monyer, H. (2009). Augmented Hippocampal Ripple Oscillations in Mice with Reduced Fast Excitation onto Parvalbumin-Positive Cells. J. Neurosci. *29*, 2563–2568.

Ramirez-Villegas, J.F., Logothetis, N.K., and Besserve, M. (2015). Diversity of sharp-wave–ripple LFP signatures reveals differentiated brain-wide dynamical events. Proc. Natl. Acad. Sci. *112*, E6379–E6387.

Schlingloff, D., Kali, S., Freund, T.F., Hajos, N., and Gulyas, A.I. (2014). Mechanisms of Sharp Wave Initiation and Ripple Generation. J. Neurosci. *34*, 11385–11398.

Schomburg, E.W., Anastassiou, C.A., Buzsaki, G., and Koch, C. (2012). The Spiking Component of Oscillatory Extracellular Potentials in the Rat Hippocampus. J. Neurosci. *32*, 11798–11811.

Schomburg, E.W., Fernández-Ruiz, A., Mizuseki, K., Berényi, A., Anastassiou, C.A., Koch, C., and Buzsáki, G. (2014). Theta Phase Segregation of Input-Specific Gamma Patterns in Entorhinal-Hippocampal Networks. Neuron.

Scoville, W.B., and Milner, B. (1957). Loss of recent memory after bilateral hippocampal lesions. J. Neurol. Neurosurg. Amp Psychiatry *20*, 11.

Skaggs, W.E., McNaughton, B.L., Permenter, M., Archibeque, M., Vogt, J., Amaral, D.G., and Barnes, C.A. (2007). EEG sharp waves and sparse ensemble unit activity in the macaque hippocampus. J. Neurophysiol. *98*, 898–910.

Stark, E., Roux, L., Eichler, R., Senzai, Y., Royer, S., and Buzsáki, G. (2014). Pyramidal Cell-Interneuron Interactions Underlie Hippocampal Ripple Oscillations. Neuron *83*, 467–480.

Sullivan, D., Csicsvari, J., Mizuseki, K., Montgomery, S., Diba, K., and Buzsaki, G. (2011). Relationships between hippocampal sharp waves, ripples, and fast gamma oscillation: influence of dentate and entorhinal cortical activity. J. Neurosci. *31*, 8605–8616.

Taxidis, J., Coombes, S., Mason, R., and Owen, M.R. (2012). Modeling sharp wave-ripple complexes through a CA3-CA1 network model with chemical synapses. Hippocampus *22*, 995–1017.

Traub, R.D., and Bibbig, A. (2000). A Model of High-Frequency Ripples in the Hippocampus Based on Synaptic Coupling Plus Axon–Axon Gap Junctions between Pyramidal Neurons. J. Neurosci. *20*, 2086–2093.

Traub, R.D., and Miles, R. (1995). Pyramidal cell-to-inhibitory cell spike transduction explicable by active dendritic conductances in inhibitory cell. J. Comput. Neurosci. *2*, 291–298.

Traub, R.D., Wong, R.K., Miles, R., and Michelson, H. (1991). A model of a CA3 hippocampal pyramidal neuron incorporating voltage-clamp data on intrinsic conductances. J. Neurophysiol. *66*, 635–650.

Traub, R.D., Jefferys, J.G., Miles, R., Whittington, M.A., and Tóth, K. (1994). A branching dendritic model of a rodent CA3 pyramidal neurone. J. Physiol. *481*, 79–95.

Van Der Meer, M.A., and Redish, A.D. (2009). Low and high gamma oscillations in rat ventral striatum have distinct relationships to behavior, reward, and spiking activity on a learned spatial decision task. Front. Integr. Neurosci. *3*, 9.

Varga, C., Oijala, M., Lish, J., Szabo, G.G., Bezaire, M., Marchionni, I., Golshani, P., and Soltesz, I. (2014). Functional fission of parvalbumin interneuron classes during fast network events. ELife.

Varga, V., Losonczy, A., Zemelman, B.V., Borhegyi, Z., Nyiri, G., Domonkos, A., Hangya, B., Holderith, N., Magee, J.C., and Freund, T.F. (2009). Fast synaptic subcortical control of hippocampal circuits. Science *326*, 449–453.

van de Ven, G.M., Trouche, S., McNamara, C.G., Allen, K., and Dupret, D. (2016). Hippocampal Offline Reactivation Consolidates Recently Formed Cell Assembly Patterns during Sharp Wave-Ripples. Neuron *92*, 968–974.

Wang, X.-J., and Buzsáki, G. (1996). Gamma oscillation by synaptic inhibition in a hippocampal interneuronal network model. J. Neurosci. *16*, 6402–6413.

Wang, D.V., Yau, H.-J., Broker, C.J., Tsou, J.-H., Bonci, A., and Ikemoto, S. (2015). Mesopontine median raphe regulates hippocampal ripple oscillation and memory consolidation. Nat. Neurosci. *18*, 728–735.

Whittington, M.A., Traub, R.D., and Jefferys, J.G.R. (1995). Synchronized oscillations in interneuron networks driven by metabotropic glutamate receptor activation. Nature *373*, 612–615.

Wilson, M., and McNaughton, B. (1994). Reactivation of hippocampal ensemble memories during sleep. Science *265*, 676–679.

Ylinen, A., Bragin, A., Nadasdy, Z., Jando, G., Szabo, I., Sik, A., and Buzsaki, G. (1995). Sharp wave-associated high-frequency oscillation (200 Hz) in the intact hippocampus: network and intracellular mechanisms. J. Neurosci. *15*, 30–46.

Figures

Figure 1

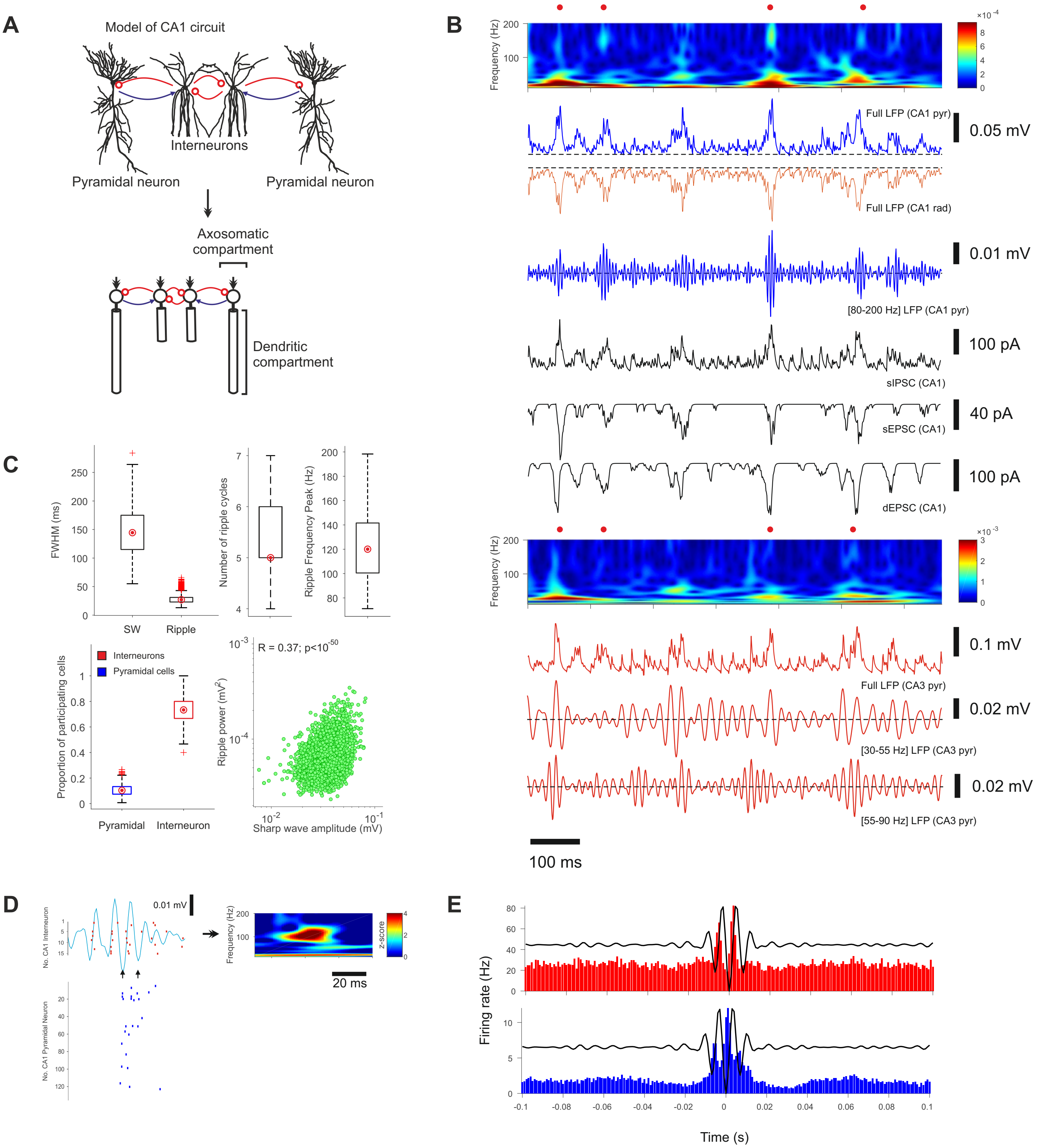
A
Model of CA1 circuit
Interneurons
Pyramidal neuron
Pyramidal neuron
Axosomatic compartment
Dendritic compartment
B
Frequency (Hz)
200
100
×10^-4
8
6
4
2
0
Full LFP (CA1 pyr)
0.05 mV
Full LFP (CA1 rad)
0.01 mV
[80-200 Hz] LFP (CA1 pyr)
100 pA
sIPSC (CA1)
40 pA
sEPSC (CA1)
100 pA
dEPSC (CA1)
×10^-3
3
2
1
0
0.1 mV
Full LFP (CA3 pyr)
0.02 mV
[30-55 Hz] LFP (CA3 pyr)
0.02 mV
[55-90 Hz] LFP (CA3 pyr)
100 ms
C
FWHM (ms)
250
200
150
100
50
0
SW
Ripple
Number of ripple cycles
7
6
5
4
Ripple Frequency Peak (Hz)
200
180
160
140
120
100
80
Interneurons
Pyramidal cells
Proportion of participating cells
1
0.8
0.6
0.4
0.2
0
Pyramidal
Interneuron
R = 0.37; p<10^-50
Ripple power (mV^2)
10^-3
10^-4
10^-2
10^-1
Sharp wave amplitude (mV)
D
0.01 mV
No. CA1 Interneuron
1
5
10
15
No. CA1 Pyramidal Neuron
20
40
60
80
100
120
Frequency (Hz)
200
100
z-score
4
2
0
20 ms
E
Firing rate (Hz)
80
60
40
20
0
10
5
0
-0.1
-0.08
-0.06
-0.04
-0.02
0
0.02
0.04
0.06
0.08
0.1
Time (s)

Figure 1. Neurophysiological nature of SWR complexes revealed by distinct network dynamical components. (A) Canonical circuit of the CA1 network illustrating the feedback and reciprocal inhibition circuit in line with recent experimental evidence (Stark et al., 2014). (B) Spectrogram, broad-band and ripple band-pass filtered trace of the CA1 LFP displaying power increases in the SWR frequency ranges (four three subpanels from top to bottom, blue indicate recordings in stratum pyramidale, orange in stratum radiatum). Averaged sIPSC and sEPSC and dEPSC (black traces). Changes in the electrical activity of CA1 co-occur with changes in CA3 (broad band, low- and high-gamma LFP traces in red), displaying gamma-like oscillatory activities concurrent with CA1 SWR. (C) Statistics of SWR features. Top: full-width at half-maximum (FWHM), number of ripple cycles, and ripple peak frequency. Bottom: proportion of peri-SWR participating pyramidal neurons and interneurons, and correlation between ripple power and sharp wave amplitude. (D) Exemplary ripple oscillation (80-180 Hz) and associated raster plot for interneurons (black) and pyramidal neurons (red). (E) Peri-event time histograms across SWR complexes at the neuronal population level for inhibitory (red) and excitatory neurons (blue). See also Figure S1-S2.

Figure 2

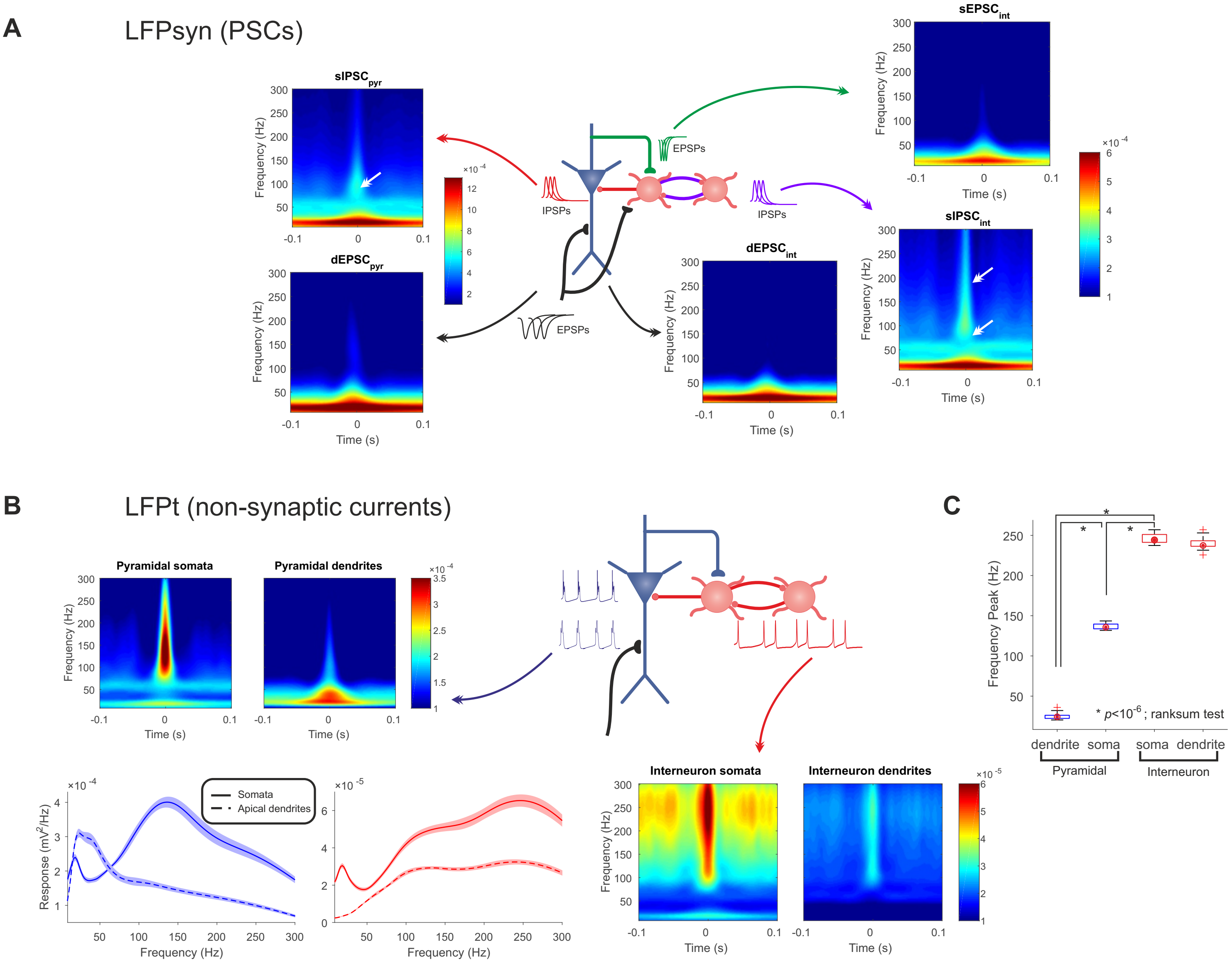
A
LFPsyn (PSCs)
sIPSC$_{pyr}$
Frequency (Hz)
300
250
200
150
100
50
-0.1
0
0.1
×10^{-4}
12
10
8
6
4
2
dEPSC$_{pyr}$
Time (s)
IPSPs
EPSPs
sEPSC$_{int}$
sIPSC$_{int}$
dEPSC$_{int}$
×10^{-4}
6
5
4
3
2
1
B
LFPt (non-synaptic currents)
Pyramidal somata
Pyramidal dendrites
×10^{-4}
3.5
3
2.5
2
1.5
1
Response (mV^2/Hz)
×10^{-4}
Somata
Apical dendrites
Frequency (Hz)
×10^{-5}
Interneuron somata
Interneuron dendrites
×10^{-5}
C
Frequency Peak (Hz)
250
200
150
100
50
*
* $p<10^{-6}$; ranksum test
dendrite
soma
soma
dendrite
Pyramidal
Interneuron

Figure 2. The synaptic and non-synaptic LFP concomitants of SWR complexes. (A) Averaged SWR-triggered spectrograms for the synaptic component of the LFP (LFPsyn) across distinct simulated network compartments. (B)-(C) Averaged SWR-triggered spectrograms for the non-synaptic component of the LFP (LFPt) for distinct network compartments (i.e. somata; dendrites) and cell types. Spectral profiles (bottom, left subpanel) illustrate the difference in frequency peaks, compared in the boxplots in (C). On each box the top and bottom are the 25th and 75th percentiles of the samples, respectively; the red dot within each box corresponds to the sample median; sample extrema are indicated by the dashed lines below and above each box; crosses, if any, correspond to outliers. See also Figure S3.

Figure 3

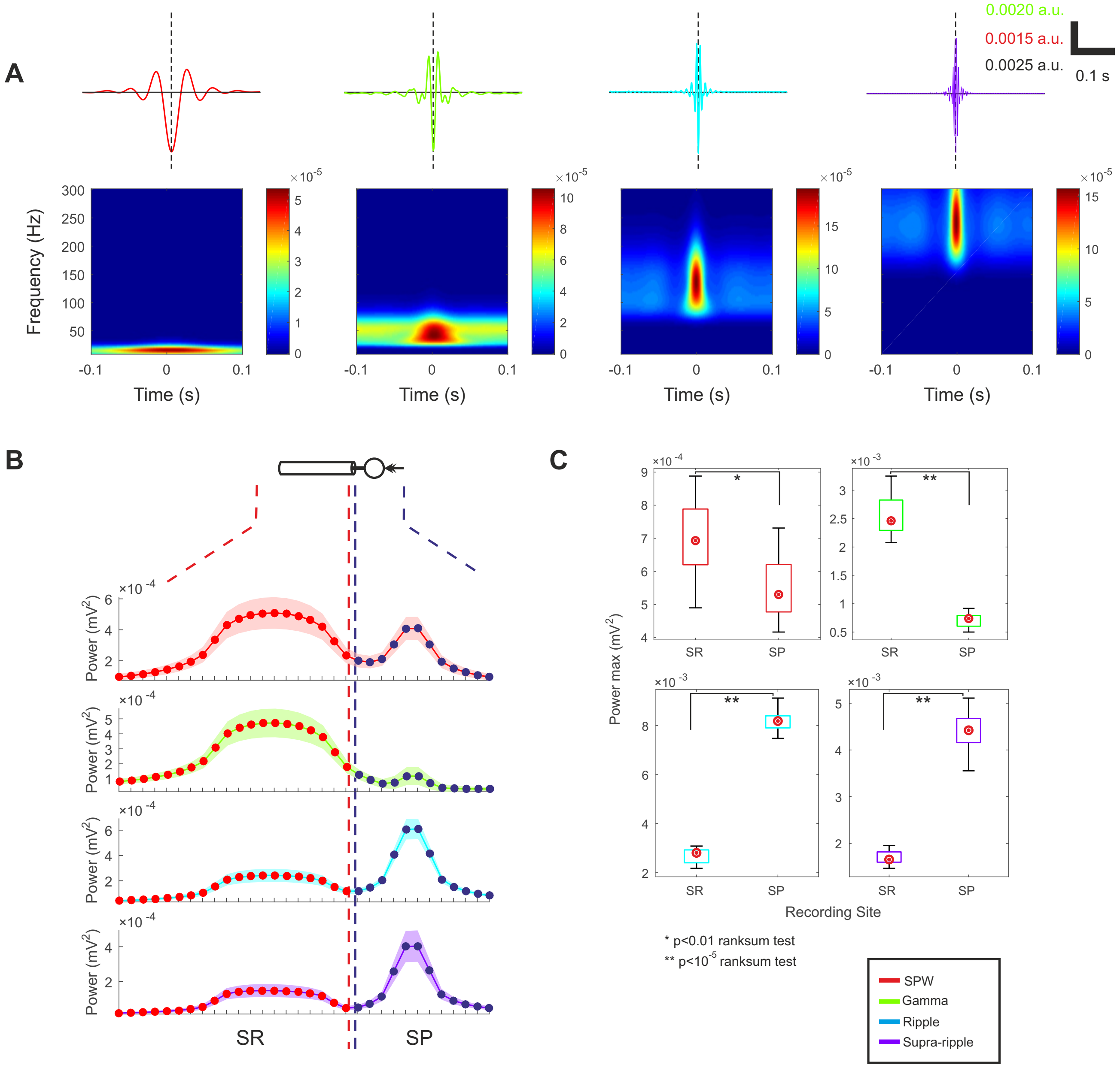
A
0.0020 a.u.
0.0015 a.u.
0.0025 a.u.
0.1 s
Frequency (Hz)
300
250
200
150
100
50
-0.1
0
0.1
Time (s)
×10^-5
B
×10^-4
Power (mV²)
SR
SP
C
×10^-4
×10^-3
*
**
Power max (mV²)
SR
SP
Recording Site
* p<0.01 ranksum test
** p<10^-5 ranksum test
SPW
Gamma
Ripple
Supra-ripple

Figure 3. Frequency band decomposition of modeled peri-event SWR complexes and corresponding laminar power distribution. (A) Averaged spectrograms and time course profiles associated with modeled SWR-related oscillatory components: SW (5-20 Hz; red curve), gamma (30-55 Hz; green curve), ripple (80-180 Hz; cyan curve) and supra-ripple (190-300 Hz; violet curve). (B) Averaged power corresponding to each oscillatory component, as a function of laminar position (given by the location of recording tips in the CA1 model). Power profiles are shown for both strata. (C) Statistical comparison of averaged power profiles across recording sites.

Figure 4

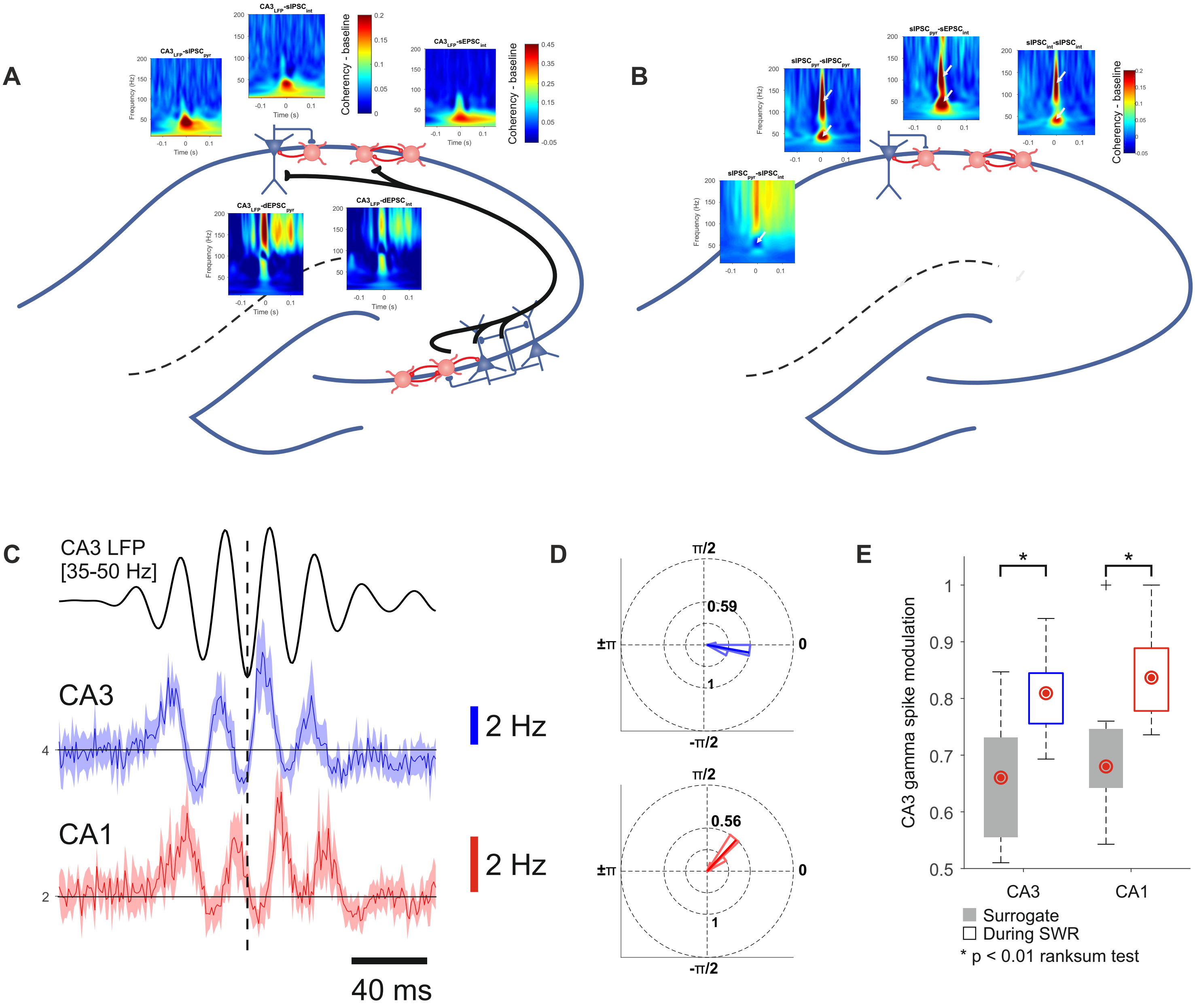
A
CA3$_{LFP}$-sIPSC$_{pyr}$
CA3$_{LFP}$-sIPSC$_{int}$
CA3$_{LFP}$-sEPSC$_{int}$
CA3$_{LFP}$-dEPSC$_{pyr}$
CA3$_{LFP}$-dEPSC$_{int}$
Frequency (Hz)
Time (s)
200
150
100
50
-0.1
0
0.1
Coherency - baseline
0.2
0.15
0.1
0.05
0
0.45
0.35
0.25
0.15
0.05
-0.05
B
sIPSC$_{pyr}$-sIPSC$_{pyr}$
sIPSC$_{pyr}$-sEPSC$_{int}$
sIPSC$_{int}$-sIPSC$_{int}$
sIPSC$_{pyr}$-sIPSC$_{int}$
Frequency (Hz)
Coherency - baseline
C
CA3 LFP
[35-50 Hz]
CA3
CA1
4
2
2 Hz
2 Hz
40 ms
D
π/2
±π
0
-π/2
0.59
0.56
1
E
CA3 gamma spike modulation
1
0.9
0.8
0.7
0.6
0.5
CA3
CA1
*
Surrogate
During SWR
* p < 0.01 ranksum test

Figure 4. Neurophysiological correlates of SWR-associated transient gamma oscillations. (A) Coherency analysis (baseline coherency-subtracted) in the CA3-CA1 network between CA3 field and CA1 synaptic currents. The schema of the hippocampus illustrates the synaptic links to ease interpretation. (B) Coherency analysis between somatic synaptic currents of CA1. CA1 currents are coordinated in the ripple and gamma frequencies, in line with *de novo* ripple generation. (C) CA3 gamma-triggered CA3 (blue curve) and CA1 (red curve) pyramidal cell time histograms illustrating the discharge rate of the populations. (D) Circular histograms illustrating the phase relationship of CA3 LFP to CA3 (blue histogram) and CA1 (red histogram) cell discharges. (E) CA3 (blue box) and CA1 (red box) modulation depth increases during SWR complexes.

Figure 5

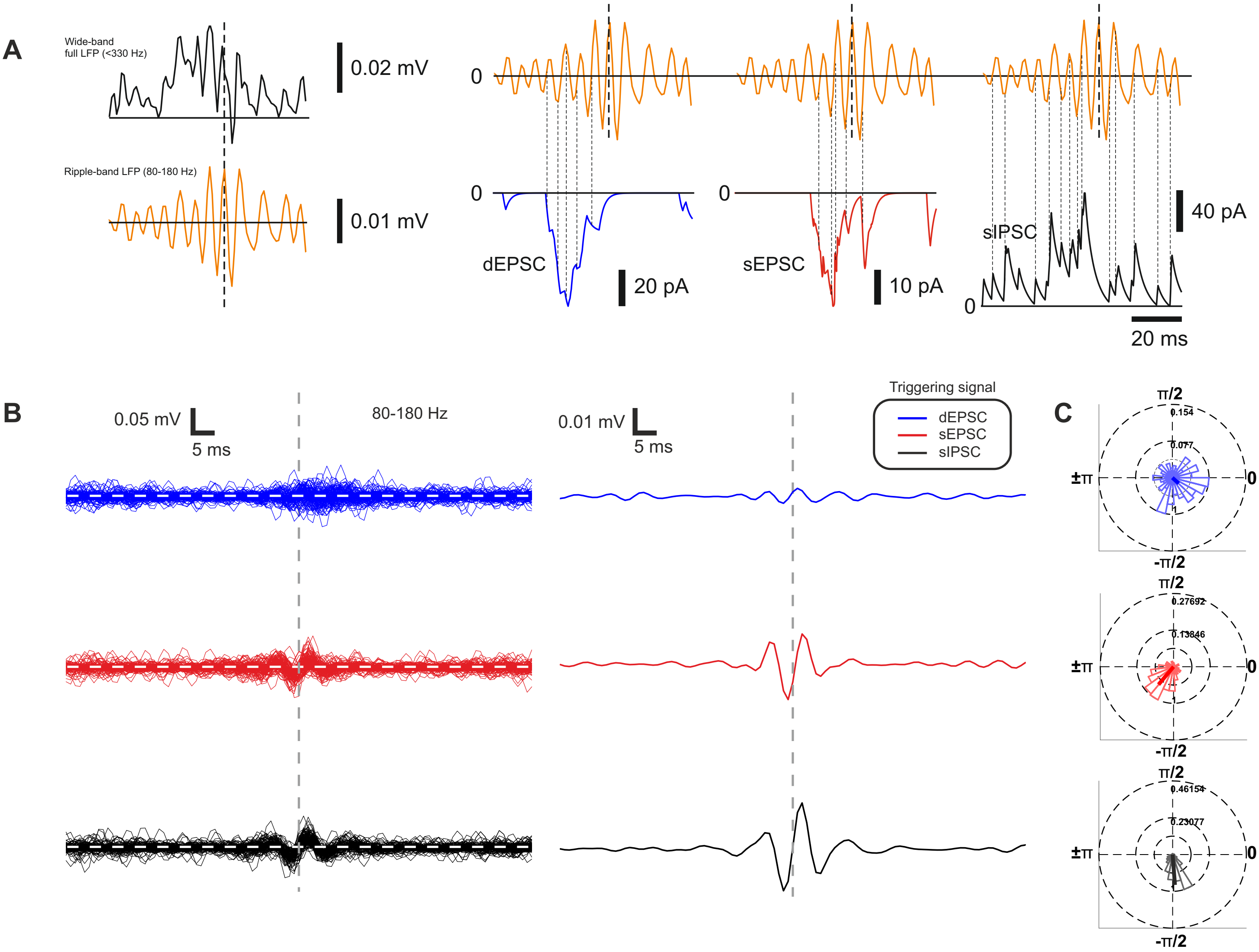
A
Wide-band
full LFP (<330 Hz)
0.02 mV
Ripple-band LFP (80-180 Hz)
0.01 mV
0
0
dEPSC
20 pA
0
sEPSC
10 pA
sIPSC
40 pA
0
20 ms
B
0.05 mV
5 ms
80-180 Hz
0.01 mV
5 ms
Triggering signal
dEPSC
sEPSC
sIPSC
C
π/2
0.154
0.077
±π
0
-π/2
π/2
0.27692
0.13846
±π
0
-π/2
π/2
0.46154
0.23077
±π
0
-π/2

Figure 5. Ripple coordination via sIPSC and sEPSC, but not dEPSC. (A) Example broad-band (<300 Hz) and filtered SWR (80-180 Hz) (left subpanels), and its associated population dEPSC (blue curve), sEPSC (red curve) and sIPSC (black curve). Dashed lines indicate prominent synaptic events at the population level. (B) PSC-triggered ripple-band LFP single trial traces and averages. (C) Circular histograms of the ripple phase at synaptic events.

Figure 6

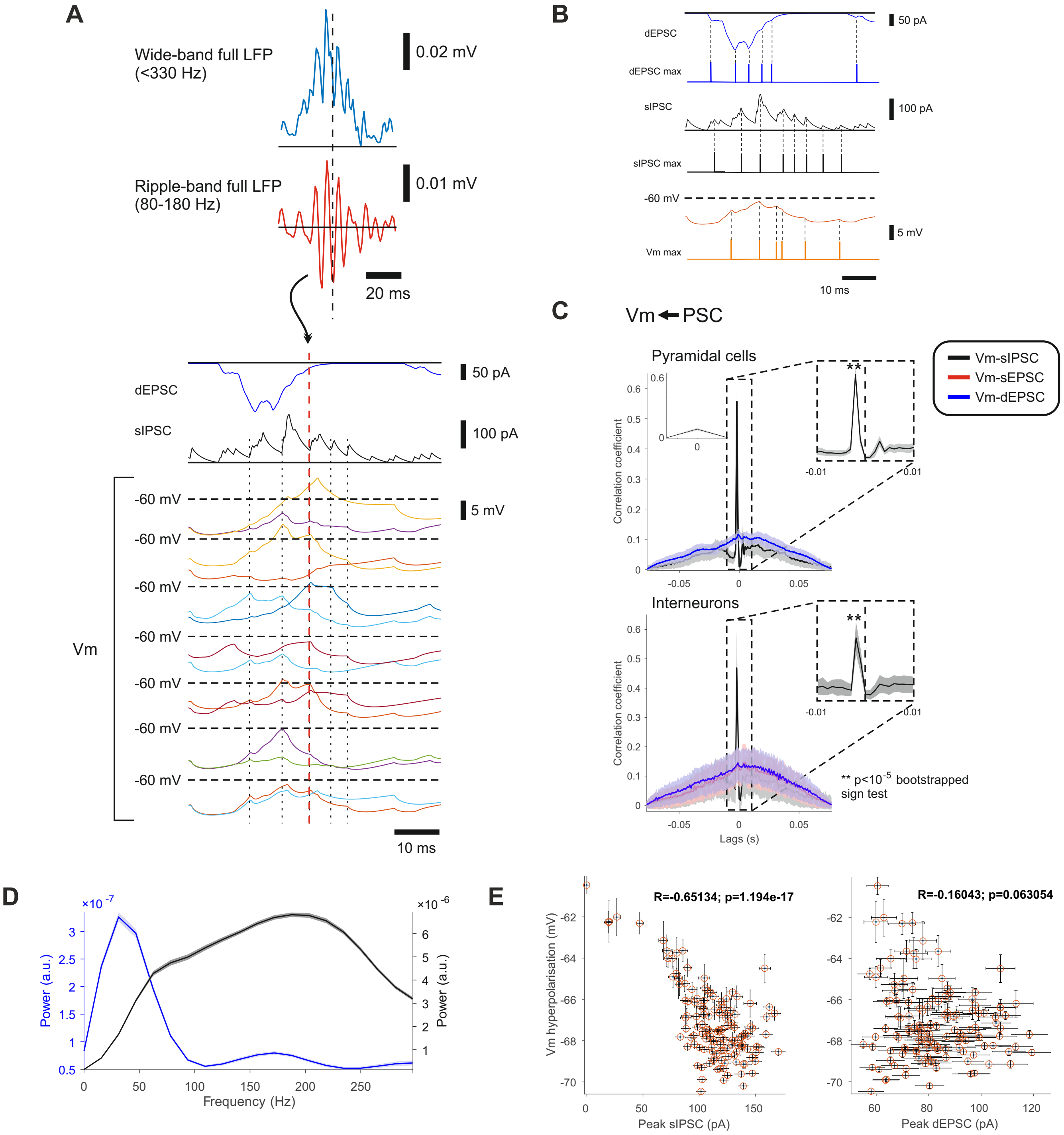
A
Wide-band full LFP
(<330 Hz)
0.02 mV
Ripple-band full LFP
(80-180 Hz)
0.01 mV
20 ms
dEPSC
50 pA
sIPSC
100 pA
-60 mV
5 mV
Vm
10 ms
B
dEPSC
50 pA
dEPSC max
sIPSC
100 pA
sIPSC max
-60 mV
5 mV
Vm max
10 ms
C
Vm ← PSC
Pyramidal cells
Vm-sIPSC
Vm-sEPSC
Vm-dEPSC
**
Correlation coefficient
-0.05
0
0.05
-0.01
0.01
Interneurons
** p<10^-5 bootstrapped sign test
Lags (s)
D
×10^-7
×10^-6
Power (a.u.)
Frequency (Hz)
E
R=-0.65134; p=1.194e-17
R=-0.16043; p=0.063054
Vm hyperpolarisation (mV)
Peak sIPSC (pA)
Peak dEPSC (pA)

Figure 6. Peri-ripple membrane potential pacing by interneurons. (A) Exemplary simulated SWR (wide band <300 Hz, light blue trace; ripple band 80-180 Hz, red trace), together with its associated population dEPSC (dark blue trace), population sIPSC (black trace), and membrane potential (Vm) of several pyramidal neurons (bottom, coloured traces; each trace corresponds to one cell). (B) Schematic of the pre-processing step, wherein we obtain binary signals from the local maxima of the absolute PSC and membrane potential traces. (C) Cross-correlograms between Vm and PSC binary signals, inhibition (black cross-correlogram), but not excitation (blue and red cross-correlograms) paces Vm for both pyramidal cells (top subpanel) and interneurons (bottom subpanel). Top-left subplot in top subpanel illustrates a cross-correlogram between binary singals (point processes) of the same rate, but generated at random. Correlation insets show that Vm consistently lags the sIPSC peak, indicating a notable inhibitory control of excitation. (D) Power spectral density of dEPSC- and sIPSC-related peri-event cross-correlograms for pyramidal cells (blue and black curves, respectively). (E) Raster plot and correlation between peak sIPSC and Vm afterhyperpolarization (left subpanel), and sEPSC and Vm afterhyperpolarization (right subpanel) for pyramidal cells. See also Figure S4.

Figure 7

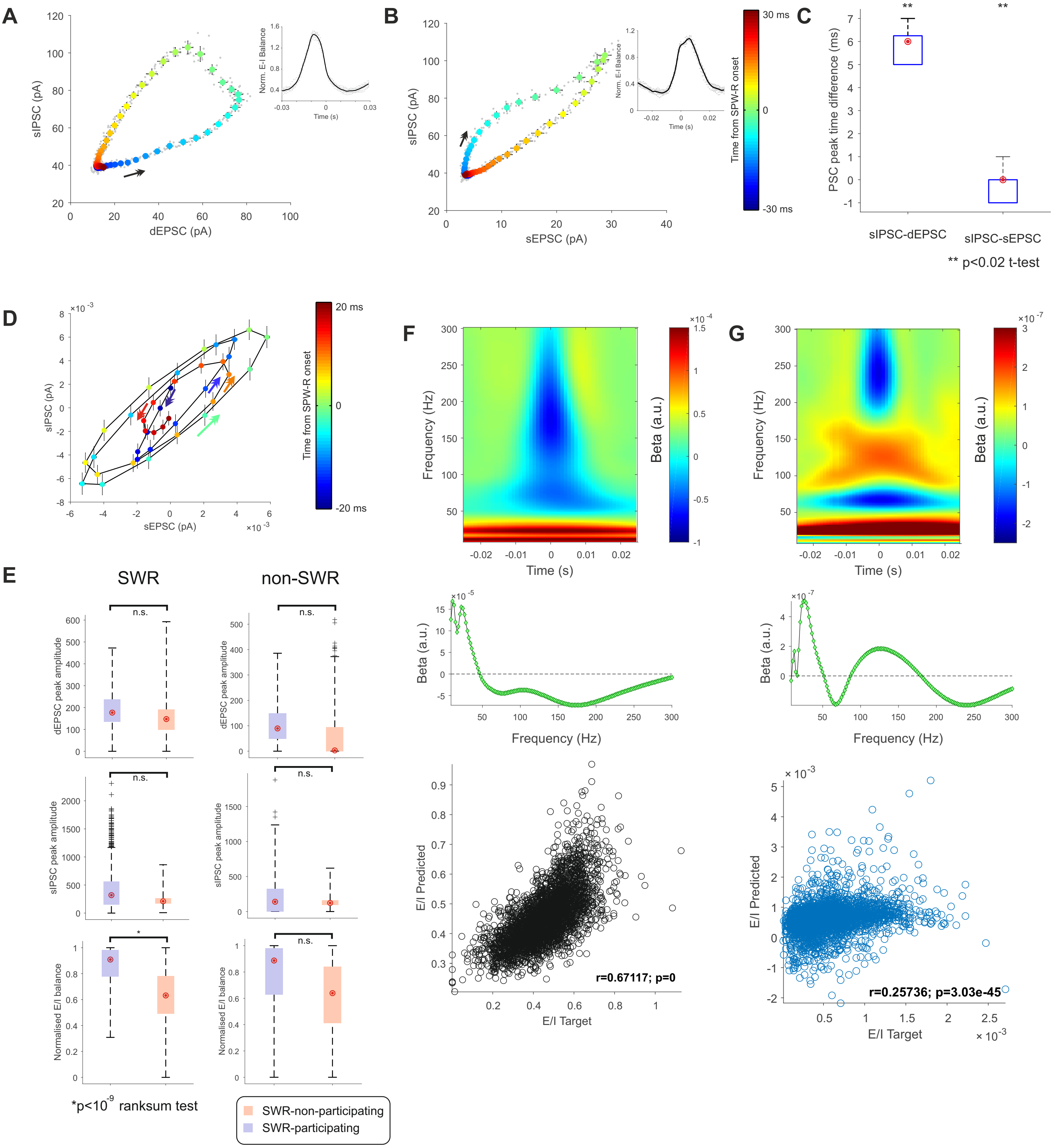
A
sIPSC (pA)
dEPSC (pA)
Norm. E-I Balance
Time (s)
B
sIPSC (pA)
sEPSC (pA)
Norm. E-I Balance
Time (s)
Time from SPW-R onset
30 ms
0
-30 ms
C
PSC peak time difference (ms)
**
**
sIPSC-dEPSC
sIPSC-sEPSC
** p<0.02 t-test
D
×10^-3
sIPSC (pA)
sEPSC (pA)
×10^-3
Time from SPW-R onset
20 ms
0
-20 ms
F
Frequency (Hz)
Time (s)
Beta (a.u.)
×10^-4
Beta (a.u.)
Frequency (Hz)
E/I Predicted
E/I Target
r=0.67117; p=0
G
Frequency (Hz)
Time (s)
Beta (a.u.)
×10^-7
Beta (a.u.)
Frequency (Hz)
E/I Predicted
E/I Target
× 10^-3
r=0.25736; p=3.03e-45
E
SWR
non-SWR
n.s.
*
dEPSC peak amplitude
sIPSC peak amplitude
Normalised E/I balance
*p<10^-9 ranksum test
SWR-non-participating
SWR-participating

Figure 7. SWR-related oscillatory components reflect network excitation/inhibition balance. (A) Averaged time course of sIPSC vs. dEPSC. (B) Averaged time course of sIPSC vs. sEPSC. (C) Statistics of IPSC-to-EPSC peak time difference. Asterisks signify that both peak-time differences are significantly different from zero. (D) Phase-plane trajectory accounting for the oscillatory dynamics of sEPSC and sIPSC (70-120 Hz, see also Figure 2). (E) PSC and E-I balance statistics for SWR (left column) and baseline (right column) for participating (blue) and non-participating (red) neurons. (F) Linear ε-SVM regression coefficients of the peri-event broad-band spectrum for predicting E/I balance (dEPSC/sIPSC). Negative coefficients account for inhibition, whereas positive coefficients account for excitation. Time zero marks the occurrence of the SWR episode (middle subpanel). E/I balance predicted by the SVM as a function of the ground-truth network peri-event E/I balance (bottom subpanel). The overall E-I prediction accuracy is given by $r \approx 0.6712$. (G) Analogous to (F) but for the sEPSC/sIPSC E/I balance. The overall E-I prediction accuracy is given by $r \approx 0.2574$.

Figure 8

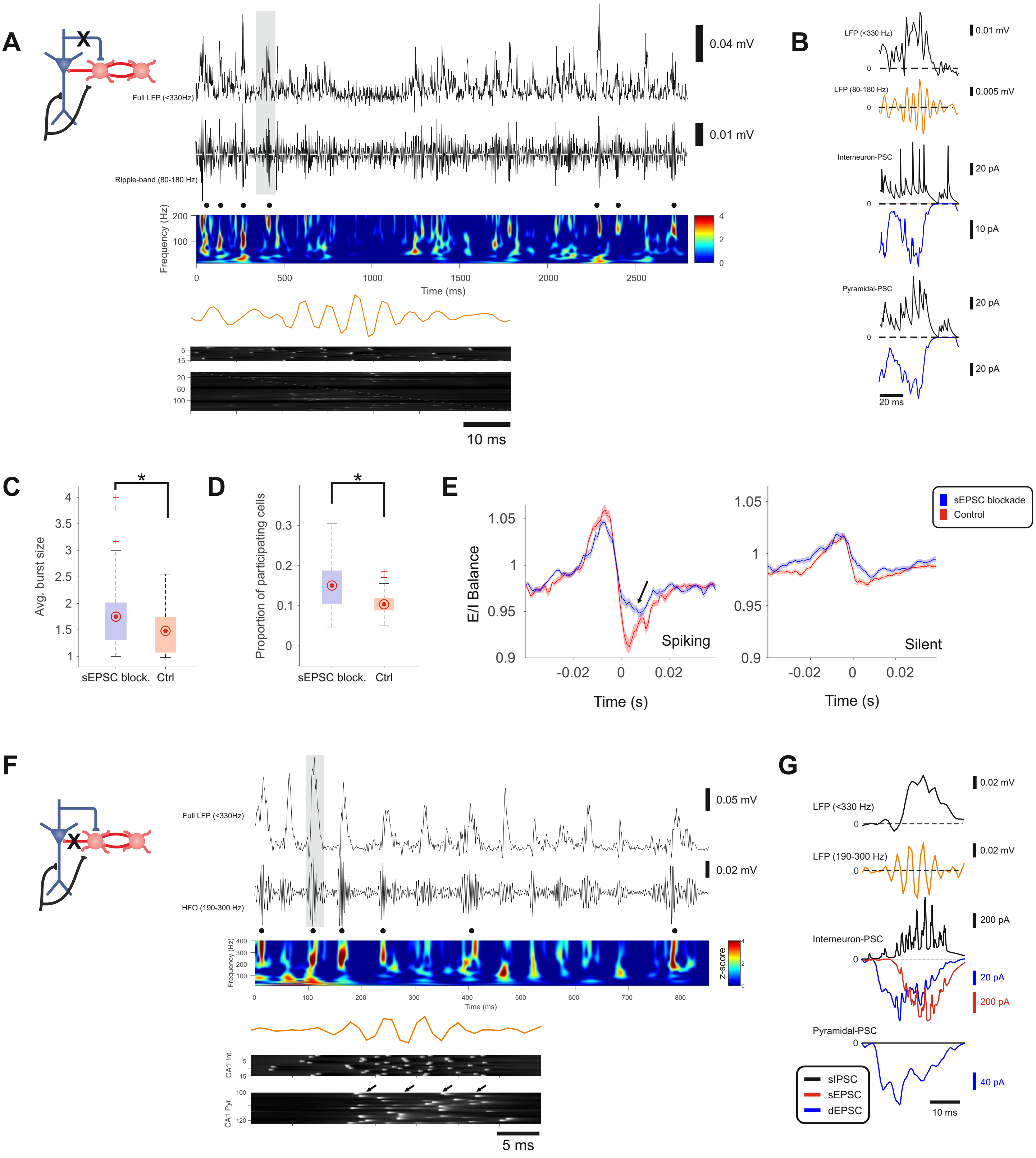
A
Full LFP (<330Hz)
Ripple-band (80-180 Hz)
0.04 mV
0.01 mV
Frequency (Hz)
200
100
0
500
1000
1500
2000
2500
Time (ms)
4
2
0
5
15
20
60
100
10 ms
B
LFP (<330 Hz)
0.01 mV
LFP (80-180 Hz)
0.005 mV
Interneuron-PSC
20 pA
10 pA
Pyramidal-PSC
20 pA
20 pA
20 ms
C
Avg. burst size
4
3.5
3
2.5
2
1.5
1
sEPSC block.
Ctrl
*
D
Proportion of participating cells
0.3
0.2
0.1
0
sEPSC block.
Ctrl
*
E
E/I Balance
1.05
1
0.95
0.9
-0.02
0
0.02
Time (s)
Spiking
Silent
sEPSC blockade
Control
F
Full LFP (<330Hz)
HFO (190-300 Hz)
0.05 mV
0.02 mV
Frequency (Hz)
400
300
200
100
0
100
200
300
400
500
600
700
800
Time (ms)
z-score
4
2
0
CA1 Int.
5
15
CA1 Pyr.
100
120
5 ms
G
LFP (<330 Hz)
0.02 mV
LFP (190-300 Hz)
0.02 mV
Interneuron-PSC
200 pA
20 pA
200 pA
Pyramidal-PSC
40 pA
sIPSC
sEPSC
dEPSC
10 ms

Figure 8. Selective inactivation of phasic synaptic excitation of CA1 pyramidal cells onto interneurons enhances SWR complexes and increases SWR-associated bursting. (A) Resulting CA1 LFP time course upon selective blockade of feedback inhibition onto pyramidal neurons (left schema). Wide-band (<330 Hz, middle column, top subpanel), high-frequency filtered (80-180 Hz), time-frequency spectrogram and peri-event raster plots (right column) correspond with SWR-like events. (B) SWR episode shaded in (A) (top traces) and associated PSC (four bottom traces) display signatures similar to that of standard conditions. (C) Average burst size across simulated pyramidal cells during blockade of synaptic excitation onto interneurons (blue box), and during standard conditions (red box). (D) Proportion of participating pyramidal neurons across simulated pyramidal cells during the two conditions in (C). (E) Averaged E-I balance across participating (left) and non-participating (right) pyramidal neurons. (F-G) Same as (A-B) upon a selective blockade of somatic inhibition onto pyramidal neurons (left schema), displaying very-high-frequency events (>200 Hz) due to the release of pyramidal cells from inhibition (see peri-ripple exemplary raster plots in the bottom, white ticks mark the spike occurrence). See also Figure S5.

Figure 9

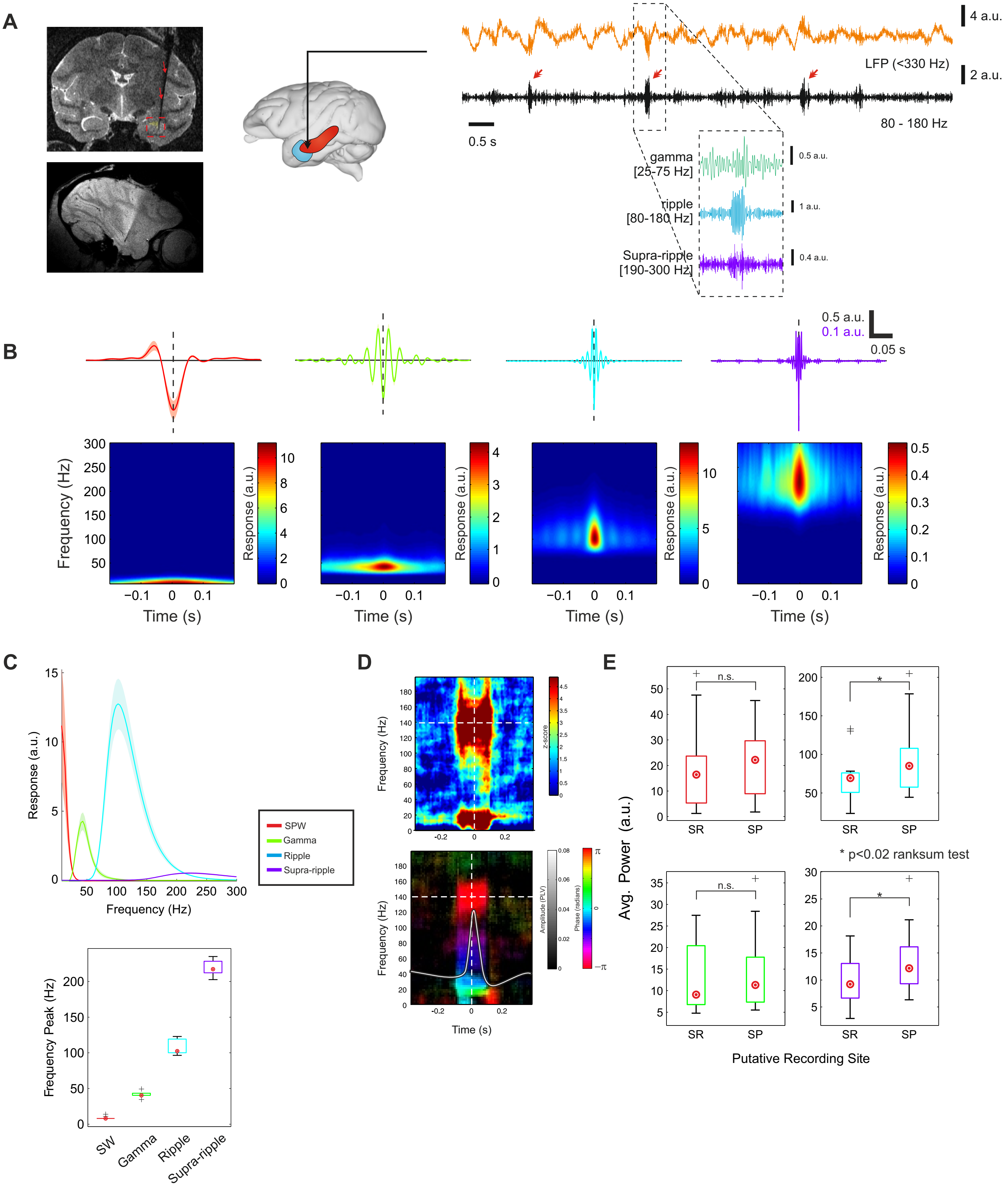
A
4 a.u.
LFP (<330 Hz)
2 a.u.
80 - 180 Hz
0.5 s
gamma
[25-75 Hz]
0.5 a.u.
ripple
[80-180 Hz]
1 a.u.
Supra-ripple
[190-300 Hz]
0.4 a.u.
B
0.5 a.u.
0.1 a.u.
0.05 s
Frequency (Hz)
300
250
200
150
100
50
Response (a.u.)
Time (s)
−0.1
0
0.1
C
Response (a.u.)
Frequency (Hz)
SPW
Gamma
Ripple
Supra-ripple
Frequency Peak (Hz)
SW
Gamma
Ripple
Supra-ripple
D
Frequency (Hz)
z-score
Amplitude (PLV)
Phase (radians)
π
0
−π
Time (s)
E
n.s.
*
SR
SP
* p<0.02 ranksum test
Avg. Power (a.u.)
Putative Recording Site

Figure 9. Electrode position, *in vivo* extracellular recordings and decomposition of peri-event SWR complexes across 15 experimental sessions, 4 animals. (A) Left images depict a T2-weighted (RARE) scan showing the electrode position in sagittal and coronal slices, respectively (electrode trajectory is marked by red arrows). The diagram (middle) shows a schematic of the electrode penetration in the anterior part of the hippocampus. Raw LFP traces (right) show large deflections corresponding to SPWs (top), accompanied by high-frequency oscillations (ripples) (bottom). The inset shows an exemplary SWR filtered in the frequency bands of interest. (B) Averaged spectrograms and time course profiles associated with each identified SWR-related bands: SPW (red curve), gamma (green curve), ripple (cyan curve) and supra-ripple (violet curve). Shaded areas indicate standard error of the mean (SEM). (C) Averaged power spectral density profiles and statistics of the component-wise peak frequency. (D) Maps of absolute spike-field coherence over all SWR episodes (*N*=15 experimental sessions, 4 animals) (left). Spike-field phase locking maps (right). (E) Statistical comparison of averaged power profiles across putative recording sites illustrating that power across stratum radiatum and stratum pyramidale differs significantly for ripple and supra-ripple components. On each box, the top and bottom are the 25th and 75th percentiles of the samples, respectively; the red dot of each box is the sample median; the dashed lines extending below and above each box are drawn from the ends of the interquartile ranges to the furthest observation (extreme points). Outliers are indicated by crosses. See also Figure S6-S7.

STAR METHODS

KEY RESOURCES TABLE

REAGENT or RESOURCE	SOURCE	IDENTIFIER
Experimental Models: Organisms/strains		
Non-human primate: Macaca Mulatta	Silabe ADUEIS (FR); BioPrim (FR)	N/A
Software and Algorithms		
MATLAB	MathWorks	https://www.mathworks.com/
Chronux Toolbox	Partha Mitra	https://chronux.org/
Multi-compartmental models	MPI for Biol. Cybern., Germany	Available upon publication
Anaesthetics		
Remifentanil	GlaxoSmithKline (GSK)	https://www.gsk.com/
Mivacurium chloride	GlaxoSmithKline (GSK)	https://www.gsk.com/
Other		
Carbon fiber (NMR-compatible electrodes)	R&G, Waldenbuch, Germany	https://www.r-g.de/
16-bit AD card (PCI-6052E)	National Instruments	https://www.ni.com/
PowerLab 16/30	ADInstruments, Sydney, Australia	https://www.adinstruments.com/
Polyether etherketone (head-holders)	Ensinger, Inc., Nufringen, Germany	https://www.ensinger-inc.com/
Enrofloxacin (antibiotic) (Baytril$^{\mathrm{TM}}$)	Bayer	https://www.bayer.com/
Flunixin (analgesic) (Meflosyl)	Pfizer	https://www.pfizer.com/

CONTACT FOR REAGENT AND RESOURCE SHARING

Further information and requests for reagents and resource may be derected to and will be fullfiled by the Lead Contact, Dr. Michel Besserve (michel.besserve@tuebingen.mpg.de).

EXPERIMENTAL MODEL AND SUBJECT DETAILS

Male rhesus monkeys were used in this study. MRI-compatible head holders and chambers were made out of PEEK (TecaPEEK, Ensinger, Inc., Nufringen, Germany), and implanted stereotaxically on the cranium of four monkeys using standard clinical aseptic techniques. Implants were secured with custom-made ceramic screws (zirconium oxide; Pfannenstiel, Germany). Postoperatively, animals were placed in large, specially designed recovery chairs for 3 days, during which they were taken for walks by the animal caretakers 2 to 3 times per day. The chairs allowed the animals to freely move body and hands, but prevented them from touching the implants. As a prophylactic measure, antibiotics (enrofloxacin) and analgesics (flunixin) were administered for 5 days. All surgical procedures were carried out under general balanced anaesthesia, whose induction and maintenance was done by trained and qualified personnel. Detailed descriptions of our procedures can be also found in the website of our institute: http://hirnforschung.kyb.mpg.de/en/methoden/. All experimental and surgical procedures were approved by the local authorities (Regierungspraesidium, Tübingen Referat 35, Veteriärwesen) and were in full compliance with the guidelines of the European Community (EUVD 86/609/EEC) for the care and use of laboratory animals.

METHOD DETAILS

1 Single Neuron Models

The models described in this section represent pyramidal neurons and interneurons in the CA3 and CA1 subfields of the hippocampal formation of the macaque monkey. Pyramidal cells, on the one hand, are modeled by the two-compartmental Pinsky-Rinzel model (Pinsky & Rinzel, 1994). Following their conventions, all membrane potentials are represented by their deviation from a reference potential of -60mV, and constants (e.g. reversal potentials) are updated accordingly in the entirety of this paper. On the other hand, we developed a simplified two-compartment interneuron on the basis of a model proposed by Traub et al. (1995) originally with 51 compartments (Traub & Miles, 1995). Our simplification stands on the basis of minimal active ionic currents (potassium and sodium) in one axo-somatic compartment and one dendrite-like compartment, following the simplification approach of Pinsky & Rinzel (Pinsky & Rinzel, 1994). For simplicity, interneurons are considered perisomatic basket cells, i.e. targeting only the axosomatic compartment of pyramidal cells. The two models closely reproduce the firing properties of hippocampal cells. Free parameters values are taken as they are in the original models (see also Table S1 and Table S2 for the full list of variables, free parameters and values). All simulations reported in this work were performed in MATLAB with custom routines. All systems of equations were solved numerically using the fourth-order Runge-Kutta method with an integration time step of 0.02 ms.

CA1/CA3 Two-compartmental Pyramidal Neuron

Each pyramidal neuron is described by two compartments. The first compartment describes the somatic dynamics and the remaining compartment accounts for dendritic dynamics. The two compartments obey the following current balance equations:

$$C_m \frac{dV_s}{dt} = -I_{L-S} - I_{Na} - I_{K-DR} - {}^{I_{Syn-S}}/_{p} + ({}^{g_c}/_{p})\,(V_d - V_s) + {}^{I_s}/_{p}\,, \tag{1}$$

$$C_m \frac{dV_d}{dt} = -I_{L-D} - I_{Ca} - I_{K-AHP} - I_{K-C} - {}^{I_{Syn-D}}/_{(1-p)} + [{}^{g_c}/_{(1-p)}]\,(V_s - V_d) + {}^{I_d}/_{(1-p)}\,, \tag{2}$$

where V_s and V_d are deviations of the somatic and dendritic membrane potentials from a reference potential of -60 mV. I_s and I_d are the injected currents to the somatic and dendritic compartment, respectively. The parameter $p = 0.5$ is the proportion of cell area taken by the soma. The membrane capacitance is $C_m = 3{}^{\mu F}/_{cm^2}$. C_a is the intracellular free calcium level (in arbitrary units) in a submembrane portion of the dendritic compartment. The ionic currents in each equation are described by the following equations (variable dependencies are omitted for simplicity and clarity):

$$I_{L-S} = g_L \cdot (V_s - E_L)\ , \tag{3}$$

$$I_{L-D} = g_L \cdot (V_d - E_L)\ , \tag{4}$$

$$I_{Na} = g_{Na} \cdot m_\infty^2 \cdot h \cdot (V_s - E_{Na})\ , \tag{5}$$

$$I_{K-DR} = g_{K-DR} \cdot n \cdot (V_s - E_K)\ , \tag{6}$$

$$I_{Ca} = g_{Ca} \cdot s^2 \cdot (V_d - E_{Ca})\ , \tag{7}$$

$$I_{K-C} = g_{K-C} \cdot c \cdot \chi \cdot (V_d - E_{Ca})\ , \tag{8}$$

$$I_{K-AHP} = g_{K-AHP} \cdot q \cdot (V_d - E_K)\ . \tag{9}$$

The gating variables h, n, s, c and q take the following forms (variable dependencies are omitted for simplicity and clarity):

$$\frac{dh}{dt} = \frac{1}{\tau_h}(h_\infty - h)\ , \tag{10}$$

$$\frac{dn}{dt} = \frac{1}{\tau_n}(n_\infty - n)\ , \tag{11}$$

$$\frac{ds}{dt} = \frac{1}{\tau_s}(s_\infty - s)\ , \tag{12}$$

$$\frac{dc}{dt} = \frac{1}{\tau_c}\left(c_\infty - c\right) , \tag{13}$$

$$\frac{dq}{dt} = \frac{1}{\tau_q}\left(q_\infty - q\right) . \tag{14}$$

The equation for C_a is described as follows:

$$\frac{dC_a}{dt} = -0.13 I_{\mathrm{Ca}} - 0.075 C_a \, . \tag{15}$$

Finally, the functions m_∞, h_∞, n_∞, s_∞, c_∞ and q_∞ are described by equations of the form $y_\infty = {}^{\alpha_y}\!/_{(\alpha_y+\beta_y)}$ and $\tau_y = {}^{1}\!/_{(\alpha_y+\beta_y)}$, where $\alpha_y$and β_y parameters take the following forms (variable dependencies are omitted for simplicity and clarity):

$$\alpha_m = \frac{0.32\left(13.1 - V_s\right)}{\exp\left[{}^{(13.1 - V_s)}\!/_{4}\right] - 1} , \tag{16}$$

$$\beta_m = \frac{0.28\left(V_s - 40.1\right)}{\exp\left[{}^{(V_s - 40.1)}\!/_{5}\right] - 1} , \tag{17}$$

$$\alpha_n = \frac{0.016\left(35.1 - V_s\right)}{\exp\left[{}^{(35.1 - V_s)}\!/_{5}\right] - 1} , \tag{18}$$

$$\beta_n = 0.25{\cdot}\exp\left(0.5 - 0.025 V_s\right) , \tag{19}$$

$$\alpha_h = 0.128{\cdot}\exp\left[{}^{(17 - V_s)}\!/_{18}\right] , \tag{20}$$

$$\beta_h = \frac{4}{1 + \exp\left[{}^{(40 - V_s)}\!/_{5}\right]} , \tag{21}$$

$$\alpha_s = \frac{1.6}{1 + \exp\left[-0.072\left(V_d - 65\right)\right]} , \tag{22}$$

$$\beta_s = \frac{0.02\left(V_d - 51.1\right)}{\exp\left[{}^{(V_d - 51.1)}\!/_{5}\right] - 1} , \tag{23}$$

$$\alpha_c = \begin{cases} \frac{\exp\left[{}^{(V_d - 10)}\!/_{11} - {}^{(V_d - 6.5)}\!/_{27}\right]}{18.975} , & V_d \leq 50 \\ 2{\cdot}\exp\left[{}^{(6.5 - V_d)}\!/_{27}\right] , & V_d > 50 \end{cases} \tag{24}$$

$$\beta_c = \begin{cases} 2{\cdot}\exp\left[{}^{(6.5 - V_d)}\!/_{27}\right] - \alpha_c \, , & V_d \leq 50 \\ 0 \, , & V_d > 50 \end{cases} \tag{25}$$

$$\alpha_q = \min\left(0.00002 C_a, 0.01\right) , \tag{26}$$

$$\beta_q = 0.001 \, . \tag{27}$$

The standard maximal conductances (in ${}^{\mathrm{mS}}\!/_{\mathrm{cm}^2}$) of the model are: $g_L = 0.1$, $g_{Na} = 30$, $g_{K-DR} = 15$, $g_{Ca} = 10$, $g_{K-AHP} = 0.8$, $g_{K-C} = 15$ (see also Table S2). The reversal potentials (in mV) are: $E_{Na} = 120$, $E_{Ca} = 140$, $E_K = -15$, $E_L = 0$. Typical values for the coupling parameters are $g_c = 2.1 {}^{\mathrm{mS}}\!/_{\mathrm{cm}^2}$ and $p = 0.5$. In addition, the capacitance and the function χ are $3 {}^{\mu F}\!/_{\mathrm{cm}^2}$ and $\chi\left(Ca\right) = \min\left({}^{Ca}\!/_{250}, 1\right)$, respectively.

CA1/CA3 Two-compartmental Interneuron

Interneurons are described by a two-compartmental model that obeys the following current balance equation:

$$C_m \frac{dV_s}{dt} = -I_{\mathrm{Na}} - I_{K-DR} - I_{L-S} - {}^{I_{Syn-S}}\!/_{p} + \left({}^{g_c}\!/_{p}\right)\left(V_d - V_s\right) + {}^{I_s}\!/_{p} \tag{28}$$

$$C_m \frac{dV_d}{dt} = -I_{Ca} - I_{K-C} - I_{L-D} - {}^{I_{Syn-D}}\!/_{(1-p)} + \left[{}^{g_c}\!/_{(1-p)}\right]\left(V_s - V_d\right) + {}^{I_d}\!/_{(1-p)} \tag{29}$$

Following the notation of the previous subsection, V is the deviation of the interneuron's membrane potential from a reference potential of -60mV. I_s and I_d are the injected currents to the somatic and dendritic compartment, respectively. The parameter $p = 0.5$ is the proportion of cell area taken by the soma.

The ionic currents in each equation are described by the following equations (variable dependencies are omitted for simplicity and clarity):

$$I_{L-S} = g_L \left(V_s - E_L\right) \,, \tag{30}$$

$$I_{L-D} = g_L \left(V_d - E_L\right) \,, \tag{31}$$

$$I_{\mathrm{Na}} = g_{\mathrm{Na}} m_{\infty}^2 h \left(V_s - E_{\mathrm{Na}}\right) \,, \tag{32}$$

$$I_{K-DR} = g_{K-DR} n^2 \left(V_s - E_K\right) \,, \tag{33}$$

$$I_{Ca} = g_{Ca} \cdot s^2 \cdot \left(V_d - E_{Ca}\right) \,, \tag{34}$$

$$I_{K-C} = g_{K-C} \cdot c \cdot \chi \cdot \left(V_d - E_{Ca}\right) \,. \tag{35}$$

The gating variables h, n, s, and c take the forms described in subsection 2.1, equations (10)-(13). The equation for C_a writes as

$$\frac{dC_a}{dt} = -0.13 I_{\mathrm{Ca}} - 0.05 C_a \,, \tag{36}$$

and the function χ is described by the following equation: $\chi\left(Ca\right) = \min\left({}^{Ca}/_{250}, 1\right)$. Similar to the case of the pyramidal neuron, the functions m_{∞}, h_{∞}, n_{∞}, s_{∞} and c_{∞} are described by equations of the form $y_{\infty} = {}^{\alpha_y}/_{(\alpha_y+\beta_y)}$ and $\tau_y = {}^{1}/_{(\alpha_y+\beta_y)}$, where $\alpha_y$and β_y parameters are identical to the ones written above for pyramidal cells. The standard values for the maximal conductances (in ${}^{\mathrm{mS}}/_{\mathrm{cm}^2}$) of the interneuron model are: $g_L = 0.1$, $g_{Na} = 100$, $g_{K-DR} = 135$, $g_{Ca} = 1$, $g_{K-C} = 8$ (see also Table S2). The reversal potentials (in mV) are: $E_{Na} = 115$, $E_{Ca} = 140$, $E_K = -25$, $E_L = 0$. Typical values for the coupling parameters are $g_c = 2.1{}^{\mathrm{mS}}/_{\mathrm{cm}^2}$ and $p = 0.5$. In addition, the membrane capacitance is $0.75{}^{\mu F}/_{\mathrm{cm}^2}$. Synaptic interactions throughout the CA3 and CA1 models will be described in detail in the next section.

2 Network Models Connectivity and Synapses

CA3 and CA1 models are considered semi-parallel arrays of two-compartment pyramidal neurons and single-compartment interneurons (models are described in the previous section). No significant variation of the networks dynamics was observed varying the number of simulated pyramidal cells and interneuons. However, we enforce a ratio of 10:1 pyramidal neurons-to-interneurons as it has been estimated for these hippocampal fields (Andersen *et al.*, 2006). Single-layer intercellular distance was set to 10μm in all cases and interneurons were pseudo-randomly distributed in the arrays, enforcing one interneuron every 10 pyramidal neurons on average. For the joint CA3-CA1 network simulations the arrays are assumed parallel and the distance between them was set to 1mm. Leakage reversal potentials were normally distributed with a standard deviation of ±2mV and were refreshed every 5 seconds of simulation time. Finally, all network simulations were limited to 150 units per layer.

CA1/CA3 Network Connectivity

Connections between neurons of the models are assumed Bernoulli trials. The probability of a connection is assumed dependent on the distance between the neurons, and is modeled with a Gaussian function, centered in the source cell with a fixed standard deviation:

$$P_{ij}\left(x_{ij}\right) = \exp\left(-\frac{x_{ij}^2}{2\sigma_i^2}\right) \tag{37}$$

where x_{ij} is the distance from the center of the source cell i to the center of the jth cell of the array. The standard deviation of the Gaussian probability distribution changes according to the cell type. Typically interneurons have narrower range than pyramidal neurons, where $\sigma_{\mathrm{IN}} = 100\mu$m and $\sigma_{\mathrm{PY}} =$ 1mm, respectively. Since auto-synapses are not allowed in the network, we assume $P_{ii} = 0$. This connectivity schema holds for all neuron types, except for CA1, where interneurons were enforced to have stronger inhibitory recurrences by adding a baseline of 0.15 to the probability values. The connectivity of the models is later on constrained by the modeled synaptic interactions (see below).

CA1/CA3 Synaptic Interactions

The CA3 network model is characterized by strong, recurrent excitatory connections and excitation-inhibition (E-I) loops. CA1 synaptic interactions follow a "feedback and recurrent inhibition" model (Figure S1) (Stark *et al.*, 2014). For simplicity only $\mathrm{GABA_A}$receptor-mediated and AMPA-mediated synaptic interactions are considered in this model (see also Taxidis *et al.* (2012); Pinsky & Rinzel (1994)). The synaptic current is described by

$$I_{syn} = g_{syn} s \left(V - E_{syn}\right) , \tag{38}$$

where the maximum synaptic conductance and the synaptic reversal potentials for AMPA and GABA-A are $g_{syn} = 0.1 ^{\mu S}/_{\mathrm{cm}^2}$, $E_{syn}^{AMPA} = 60\mathrm{mV}$, and $E_{syn}^{GABA} = -15\mathrm{mV}$ for all neuron types. We assume that s follows a first-order kinetics:

$$\frac{ds}{dt} = \sum_k \varphi_k H\left(V_k - G_{th}\right) - \frac{s}{\tau_{syn}} , \tag{39}$$

where $H\left(x\right) = \begin{cases} 1 & x \geq 0 \\ 0 & \text{otherwise} \end{cases}$, k is an index that runs over the pre-synaptic neurons, φ_k are the associated synaptic gains and $G_{th} = 20mV$ is a threshold to the membrane potential of the pre-synaptic cells for the synaptic interaction. Note that synaptic parameters change accordingly depending on the subfield (CA3 or CA1) and the neuronal group (interneurons or pyramidal cells) (see also Table S2).

3 Determining unitary-PSP amplitudes

In this model, AMPA synapses target the dendritic compartment of pyramidal cells, wheras they target interneurons in the peri-somatic region, except the CA3 Schaffer input to CA1. $\mathrm{GABA_A}$ synapses are always peri-somatic. . In order to obtain biologically-plausible evoked postsynaptic potentials, we recorded unitary EPSP and IPSP in networks with only one type of synaptic connection and adjusted the synaptic gain φ to match PSP values reported in the literature. Postsynaptic potentials were identified on the basis of local maxima after detecting a pre-synaptic spike. PSPs were recorded at a fixed background membrane potential with the pre-synaptic neuron firing a single spike. Presynaptic bursts (as for the Pinsky-Rinzel model) were excluded from the analysis. Pyramidal cells' and interneurons' background potential was -67.5 mV and -70.1 mV, respectively for CA3, and -69.4 mV and -71.3 mV, respectively for CA1. PSP-amplitude statistics were made on the basis of an average of 8306 unitary PSPs for each type of cell-to-cell synaptic interaction in the network. The main observations regarding these experiments are reported in Table S3.

4 Synapse probabilities

The joint CA3-CA1 network model was simulated with the the full list of network parameters presented in Table S2. As mentioned before, we assume that neurons representing CA3 and CA1 form two parallel pools of cells 1mm apart from each other. The two models are coupled by feed-forward connections mimicking the Shaffer collaterals. The connectivity between CA3 and CA1 cells pools of cells established previously (varying as a function of sigma in equation (37); CA1/CA3 Network Connectivity subsection) results in the following averaged synaptic interaction probabilities: CA1 principal neurons and interneurons are targeted by CA3 pyramidal neurons, with an overall targeting probability of 20% (Li *et al.*, 1994). Likewise, a single CA3 pyramidal neuron targets 35% of the CA3 pyramidal cell population, and 35% of the CA3 interneurons, whereas CA3 interneurons target CA3 pyramidal neurons with average proportion of 40%. Interneuron-interneuron synapses occur in a average proportion of 44% of the interneuron population in CA3. Finally, on average, 25% of the pyramidal cell population in CA1 is postsynaptic to a single CA1 interneuron, and vice versa. There are no pyramidal cell-to-pyramidal cell collaterals in CA1 (Andersen *et al.*, 2006).

5 Estimating the transmembrane currents of the model

Following the early work of Nicholson & Llinas (1971), transmembrane currents -for long, thin dendrites- are determined by the internal and membrane properties of the neuron and are little influenced by the dynamics of the current once it has entered the extracellular medium. We assume that the dendritic and somatic compartments are narrow cables (line sources of current) surrounded by a thin sheath of extracellular medium. The transmembrane current is defined as the sum of all currents derived from solving the equivalent circuit of resistors, capacitors and batteries of each compartment, including the capacitive current. This definition can be reduced to the following general equation:

$$I_t = g_c\left(V_{m+1} - V_m\right) = \left[C_m \frac{\partial V_m}{\partial t} + \sum_j I_j\right] , \tag{40}$$

where V_m is the membrane potential of the compartment underconsideration, V_m is the membrane potential of the neighbor compartment, and I_j is the j^{th} current in the compartment m (including the synaptic input currents) (Nicholson, 1973; Nicholson & Llinas, 1971).

The transmembrane potentials resulting from the dynamical equations of the model are characteristic complex depolarization events from the model of Pinsky & Rinzel (1994), and the reduced two-compartmental interneuron model following Traub & Miles (1995). Typically, pyramidal cell and interneuronal spikes occur first in the axosomatic compartment and then propagate to the dendritic compartment, where a dendritic spike is generated. When this occurs in pyramidal cells, due to the influence of slow dendritic calcium channel activation, a second depolarization event is generated in the axosomatic compartment, thus becoming a complex bursting event.

Thus, in order to compute the field potentials the volume current source density must be known. The term "current density" corresponds to the fact that the currents are the second spatial derivative of the membrane potentials. Since our compartments are one-dimensional core conductors with longitudinal internal resistance R_i (i.e., per unit length), with corresponding extracellular sheath of longitudinal resistance R_e. Customarily we have assumed $R_e = 0$. Cable theory yields the following relations for the internal current I_i and the transmembrane current density I_t: $I_i = {}^{1}\!/_{R_i}\left({}^{\partial V_m}\!/_{\partial t}\right)$, and $I_t = -{}^{\partial I_i}\!/_{\partial z}$, where z is the spatial component along the cable compartments. From these steps, the cable equation $\left({}^{1}\!/_{R_i}\right) {}^{\partial^2 V_m}\!/_{\partial z^2} - C_m {}^{\partial V_m}\!/_{\partial t} - I_i = 0$ is derived. Hence

$$I_t\left(\mathbf{z}, t\right) = -\frac{1}{\lambda^2 R_i} \frac{\partial^2 V_m\left(\mathbf{z}, t\right)}{\partial \mathbf{z}^2} , \tag{41}$$

where the length constant $\lambda = \sqrt{{}^{R_m}\!/_{(R_i+R_e)}}$ $\left[{}^{\Omega\mathrm{cm}}\!/_{\Omega\mathrm{cm}^{-1}}\right]$, and the dimensionless spatial component $\mathbf{z} = {}^{z}\!/_{\lambda}$, following Nicholson & Llinas (1971). This definition is equivalent to equation (40) and follows that there is a current sink (where the current is inward) at the synapse with respect to the extracellular medium and a current source (where the current is outward) elsewhere.

6 Non-synaptic transmembrane currents

In order to address the contribution of synaptic and non-synaptic currents to the full LFP and their time-frequency signatures, we used the population PSC (referred to as LFPsyn), and the non-synaptic currents (referred here to as LFPt). The rationale behind this procedure is to disentangle the peri-SWR frequency-dependent (spatial) distribution of LFP attributable to synaptic activity, with respect to internal neuronal dynamics. In order to compute the frequency-dependent signature of each neuron segment (soma and dendrite) on the peri-SWR LFP we adopted the strategy of separating the LFP into the aforementioned components. On the basis of equation (40), we compute LFPt as follows:

$$I_{LFPt} = g_c\left(V_{m+1} - V_m\right) - I_{syn} = \left[C_m \frac{\partial V_m}{\partial t} + \sum_j I_j^{\mu}\right] , \tag{42}$$

where I_j^{μ} is the j^{th} non-synaptic current in the compartment m.

7 Recording sites and Local Field Potential (LFP) estimation

We assumed a recording electrode with neglegible thickness and cells to be line sources of current (Schomburg *et al.*, 2012). Cells were regularly spaced horizontally, and disposed around the center of a stratum pyramidale of 100μm thickness, with an axosomatic compartments height of 80μm for both pyramidal neurons and interneurons (Traub & Miles, 1995). We assumed a total dendritic arbor height of 200μm corresponding to the CA1 stratum radiatum. Multiple electrode tips (32 sites in total) were set 20μm apart covering the simulated axosomatic and apical dendritic fields of CA1 and CA3 in order to mimick a laminar electrode. Two multi-channel electrodes in such configuration targeted the center of the CA1 and CA3 array of neurons.

Importantly, in our simulations we sought to assess the contribution of interneurons taking into consideration their increased radial symmetry as compared to pyramidal cells (see Traub *et al.* (1994), but see Traub & Miles (1995)). To this end, whereas pyramidal neurons shared a common orientation (long axis perpendicular to the stratum), each interneuron was randomly rotated by an angle in the range $[-\pi, \pi]$. As this choice minimises the contribution of interneurons to the LFP, it is worth noting, nonetheless, that introducing these rotations did not have a noticeable effect on the computed LFP traces, as the overall contribution of interneurons to the LFP is lower than that of pyramidal cells, as pyramidal cells outnumber the interneuronal population. Customarily, the simulations could be performed with all neuron types sharing a common orientation.

We assume a uniform extracellular medium, isotropic and ohmic conductor with resistivity $\rho = 333\Omega$cm. The potential in the extracellular medium is governed by the Poisson equation $\nabla^2\phi = {}^1\!/_{\sigma}{}^{d\xi}\!/_{dt} = -{}^{I_t}\!/_{\sigma}$, where $\sigma = {}^1\!/_{\rho}$ is the conductivity of the extracellular space $[{}^{\mathrm{S}}\!/_{\mathrm{m}}]$. The solution of the Poisson equation leads to an integral that relates the extracellular potential to the radially-flowing volume current density $I(\cdot)$ distributed over volume $\mathbf{u}$: $\phi(\mathbf{p}', t) = {}^1\!/_{4\pi\sigma} \int\int\int_u {}^{I(\mathbf{p},t)}\!/_{|\mathbf{p}'-\mathbf{p}|} \mathrm{d}x\mathrm{d}y\mathrm{d}z$, for a recording electrode placed at $\mathbf{p}' \equiv (x', y', z')$ and $\mathbf{p} \equiv (x, y, z)$ indicating the position of the volume current density under consideration. We assume each compatment is a cylinder whose diameter can be neglected with respect to the distance to the electrode contact. Under these assumption, the potential distribution has a radial symmetry around the cylinder's axis and the problem can be reparametrized by the radial distance r from the axis of symmetry and an algebraic "depth" coordinate z along this axis. Moreover, the volume current density can be turned into a line density, that we assum uniformly distributed along the cylinder's axis. The expression for extracellular potential thus becomes a single integral, measured over the compartment's length limits. Let z_2 be the algebraic depth of the top of the cylindric compartment, and let z_1 be the algebraic depth of the bottom of the cylinder (such that $z_2 - z_1 = L$). At a given time, the expression for the potential $\phi(z_0, r)$ at the algebraic depth z_0 and a radial distance r is: $\phi(\mathbf{z}, r) = {}^1\!/_{4\pi\sigma L} \int_{z_1}^{z_2} {}^{I(t)}\!/_{\sqrt{(\mathbf{z}-z_0)^2+r^2}} \mathrm{d}\mathbf{z}$. After solving the integral with standard algebraic procedures, we account for the contribution of all compartments and cells, then the extracellular potential $\phi(z_0, r, t)$ is

$$\phi(z_0, r, t) = \frac{1}{4\pi\sigma} \sum_i \sum_j \frac{I_t^{ij}(t)}{L_{ij}} \ln\left[\frac{\sqrt{(z_1 - z_0)^2 + r^2} - (z_1 - z_0)}{\sqrt{(z_2 - z_0)^2 + r^2} - (z_2 - z_0)}\right], \tag{43}$$

where the variable L_{ij} is the length and I_t^{ij} is the total transmembrane current corresponding to the j^{th} compartment of the i^{th} cell.

Note that since the neuron models considered in this work are two-compartmental, from equation (40), it follows that the total absolute somatic transmembrane currents equal the absolute of the total dendritic transmembrane currents (which also follows the charge conservation principle), leading to a dipolar distribution of the LFP contribution for each cell.

8 Intracortical Electrophysiological Recordings

Surgical procedures are described in detail elsewhere (Logothetis *et al.*, 2012; Ramirez-Villegas *et al.*, 2015). Briefly, a total of 242 experiments (10 minutes each) spread over 15 experimental sessions were carried out in anesthetized male rhesus monkeys (Macaca mulatta). Head holders and recording chambers were located stereotaxically based on high-resolution anatomical MRI scans. Recordings were conducted in the anterior part of the hippocampus in the right hemisphere of each animal. All recording hardware, including the electrodes and amplifiers, was developed at the Max Planck Institute for Biological Cybernetics. Custom-made, multi-contact, NMR-compatible recording electrodes were made from a carbon fiber composite baton with 500µm diameter (R&G, Waldenbuch, Germany). The 2.6mm long tip grounded down to a diameter of 250µm. Electrodes contained 10 contacts spaced 150µm apart, with 6-10 targeting the structure of interest. Multi-contact recordings were performed around the pyramidal layer of the hippocampal CA1 subfield (8 to 14 mm anterior of the interaural line). The output signals of the laminar electrode were then fed into a PowerLab 16/30 system (ADInstruments, Sydney, Austrialia). Fine adjustment of the recording electrode was achieved by intermediate MRI anatomical scans, in addition to monitoring acoustically and visually the hippocampal neural signals. During these procedures, anesthesia was maintained with remifentanil (0.5-2 µg/kg/min) with a fast-acting paralytic mivacurium chloride (5-7 mg/kg/h), and the physiological state of the animal was monitored continuously and maintained tightly within normal limits (38-39°C body temperature, end-tidal CO_2 33 mmHg, and oxygen saturation over 95%) (Logothetis *et al.*, 2012). In addition, electrophysiological recordings were done with the monkey into the magnet bore for simultaneous acquisition of blood-oxygenation level-dependent (BOLD) fMRI signals. The fMRI recordings were not analyzed in this work (for details see Logothetis *et al.* (2012)). In addition, all neuronal data were analyzed offline.

QUANTIFICATION AND STATISTICAL ANALYSIS

1 Simulations and SWR event detection

of modeled data, a total of 500 independent simulations were performed. These 500 simulations were grouped in a total of 25 simulation sessions, events and spanning a total of 125 seconds. The connectivity of the model was refreshed each 5 seconds of simulation, yielding similar LFP traces. Events were detected as increases in the ripple-band power (80-180 Hz) using a threshold proportional to the standard deviation of the signal (3 SD in this case). Only ripples with more than one oscillation period were selected for further analysis. A total of 3,250 SWR episodes were detected and analyzed for all results in this work, unless otherwise specified.

2 Frequency analyses

Spectral analysis and spike-field coherence (SFC). Spectral analysis was performed using Morlet-wavelet spectrograms. Spectrograms were Z-scored with respect to random baseline events. SFC was computed for all modeled sites located in the CA1 stratum pyramidale, across all SWR broad-band signal events. This analysis was performed using the Chronux toolbox available at http://chronux.org (tapering window duration of 200 ms with an increment of 10 ms). Ripple-related SFC maps were averaged and Z-scored with respect to randomized events. The resulting map was then analyzed in magnitude (absolute value in the range [0, 1]) and in the form of a composite phase map (in the range $[-\pi, \pi]$ rad) with the phase-locking values (PLV).

CA3 gamma-triggered time histograms, phase analysis and cell discharge modulation index. CA3-gamma triggered time histograms were made on the basis of the filtered CA3 LFP (stratum pyramidale contact with largest amplitude) in the band 35-50 Hz, in order to avoid conflating or leaked low-frequency components. Single-trial signals were aligned with respect to the largest gamma trough, and the LFP-aligned CA3 and CA1 pyramidal spike times were used to produce the histograms (at 1 ms bins resolution). This procedure was performed in a single-session basis, session-wise averages were computed, and population (across sessions) averages were performed. Furthermore, LFP-to-histogram phase relationships were computed at the session level, where each time histogram was smoothed first with a Gaussian kernel $\sigma = 15$ms in order to reduce high-frequency noise. Histogram local maxima were detected in a time window of $[-0.05, 0.05]$ s around the largest CA3-gamma trough, the LFP phase (computed via Hilbert transform) corresponding to each maxima was then used to produce the circular histograms across all sessions. Statistical testing was performed across sessions using a standard bootstrapped Rayleigh test. Finally, the modulation indices for both CA3 and CA1 were also computed at the session level, and defined as the difference between the peak and the trough of the spike histogram divided by the sum of the peak and the trough of the spike histogram (after Carr *et al.* (2012)). An analogous procedure was followed for surrogate (non-SWR) epochs for statistical comparison with SWR episodes.

Peri-SWR LFP decomposition by a bank of FIR filters, laminar power profiles and component-wise spectral analysis. We used a bank of filters to separate the activity of elementary components of CA1 activity (Figure 3 and 9). To this end, we applied 4th-order Butterwoth finite impulse response

(FIR) filters in the frequency ranges where we observe sharp waves, gamma (25-75 Hz), ripples (80-180 Hz) and supra-ripple (190-300 Hz). Filtered peri-event SWR complexes were aligned to the largest oscillation trough, and then averaged across sessions. Component-wise spectral analysis was performed using complex Morlet wavelet spectrograms and then baseline-corrected with respect to random surrogate events. Spectral power peak frequencies were extracted from these spectrograms. Finally, component-wise laminar power profiles were computed as the average of each squared peri-event component in a time window of ±50 ms around the event occurrence. Population averages were performed on the basis of the results of each individual experimental or simulation session (N = 15 experimental sessions; M = 25 simulation sessions).

3 Post-synaptic current analyses

Excitation-inhibition balance of single neurons. In this work, we studied the conditions that lead pyramidal neurons and interneurons to spike during individual SWR episodes. We observed that in such cases (when neurons spike), incoming EPSCs were precisely timed with respect to IPSCs from local inhibitory recurrences (Figure 8E of the Main Text). This establishes a transient imbalance in excitation-inhibition ratio. In order to quantify this effect we used the following measure:

$$EI = \frac{|dEPSC + \varepsilon|}{|sIPSC + \varepsilon|}\,, \tag{44}$$

where $\varepsilon = 1$. The constant ε was included in order to avoid by-zero division, at the same time, we obtain a conservative estimate of transient E-I imbalances. In particular, E-I balance above 1 is equivalent to an imbalance toward excitation, whereas E-I balance below 1 is equivalent to an imbalance toward inhibition. Note that we observed the two types of imbalances (Figure 8E of the Main Text). Thus, the global maxima and minima of this measure was obtained for across all cells and events. Then cells were separated according to SWR-participating and SWR-non-participating for further statistical analysis.

PSC-triggered LFP averages and PSC-LFP phase analysis. PSC-triggered LFP averages were made on the full LFP (LFPt + LFPsyn) of CA1, and occassionally CA3 in order to disentangle the coordination mechanisms of CA1 and CA3 ripples, respectively. To this end, a derivative-based method was used in order to detect the largest PSC (Maier *et al.*, 2011; Gan *et al.*, 2017). Peri-SWR PSC were averaged across all cells. Next, first derivatives were computed to these averages in order to detect the largest population synaptic events. We marked the extrema of each derivative depending on whether it was an excitatory or inhibitory current. EPSC were marked in the downward direction (derivative minima), whereas IPSC in the upward direction (derivative maxima). We computed the LFP averages on the basis of the 10% maxima. Likewise, results were robust even when only absolute maxima were considered. Phase values were computed using the Hilbert transform of the ripple-band LFP, and only the phase value corresponding to PSC-derivative top 10% maxima were taken into account for statistical analysis. Finally, circular histograms were computed for 25 bins evenly distributed in the unit circle, and phase locking value was computed as the absolute of the circular mean phase across events.

Computing the relationship between membrane potential (Vm) and LFP. The relationship between Vm and LFP was assessed on the basis of previous experimental work (Hulse *et al.*, 2016). The membrane potential (Vm) associated with each cell and the LFP (in stratum pyramidale) were ripple-band-filtered (80-180 Hz) using a 4th-order Butterworth filter. In order to estimate the instantaneous phase of each signal, we computed the Hilbert transform, and then, computed a PLV in a 25ms window around the SWR occurrence, according to the following equation: $\Gamma_{nm} = {}^{1}\!/_{N}\sum_{t=1}^{N}\left[\exp\left(i\triangle\varphi^{t}_{nm}\right)\right]$, where N is the number of time samples, $\triangle\varphi^{t}_{nm} = \varphi^{t}_{n} - \varphi^{t}_{m}$ accounts for the difference between the phase estimates of the signal corresponding to the SWR n, and Vm of the cell m. This procedure was carried out for each cell and event. Cell-wise averaged PLV was then computed by averaging across events. Finally, circular histograms were computed for 25 bins evenly distributed in the unit circle, and a single PLV and statistical test was computed as the absolute of the circular mean phase across cells.

Next, in a separate condition, 25 randomly chosen pyramidal cells were injected with hyperpolarizing currents ranging from -3.5 to -2.5 nA, resulting in resting membrane potentials from -15 to -25 mV. We then separated these cells from the rest and then computed the ripple Vm-ripple LFP PLV across SWR. Cell-wise averaged PLV was then computed across all SWR episodes from which circular histograms were computed.

Excitation-inhibition balance regression via linear ε-SVM. For the regression analysis, E-I balance in CA1 was computed from the maximum peri-ripple dEPSC and sIPSC. Population PSC were computed as the mean across all CA1 cells. The ratio of the averaged peak IPSC-to-EPSC is referred in this analysis to as the 'ground-truth' peri-event network E-I balance. We then trained a linear ε-SVM in order to predict the peri-SWR network E-I balance, based on the broad-band modeled full LFP signal spectrum (0-300 Hz) at the time of SWR occurrence. Peri-SWR spectrograms were reconstructed on the basis of their first 7 to 15 principal components (retaining an average of 40% to 60% of the variance). For such a purpose, we performed a 10-fold cross-validation: the data set was partitioned in 10 subsamples (test sets), and the rest of the data were used as training set. Each test subsample is used only once for testing the regression model. Finally, we report the averaged performance, resulting from each training/testing stage. This procedure was carried out for each simulation session, then all predictions were pooled together for population analysis and scatter plots. Similarly, session-wise SVM weights were computed according to the following mathematical formalism:

Let $\mathbf{x}^{(s)}$ be a matrix with N_s support vectors and M samples, $\{\alpha_i\}_{i=1}^{N_s}$ the Lagrange multipliers associated with the N support vectors, and $\{\boldsymbol{x}_j, d_j\}_{j=1}^{L}$ be the training sample, where d_j corresponds to the E-I balance to regress out, assigned to the j^{th} M-dimensional data point $\boldsymbol{x}_j$. Here, the M-dimensional data points are long feature vectors comprising the time and frequency components of the peri-SWR Morlet-wavelet spectrogram. Since the support vectors are the most difficult data points to predict, we can compute a weight w for each feature in order to know how predictive of the E-I balance it is. For the linear SVM we have

$$v_j = \boldsymbol{w}^T \boldsymbol{x}_j + b\,, \tag{45}$$

and the weights can be retrieved as: $\boldsymbol{w} = \sum_{i=1}^{N_s} \alpha_i d_i \boldsymbol{x}_i^{(s)}$, and b is the bias term.

Selective suppression of synaptic interactions. In this work, we designed a series of interventions in the CA1 circuitry in order to assess to what extent synaptic excitation or inhibition were necessary for SWR episodes to emerge. We addressed this issue in four conditions: (1) Blockade of feedback inhibition onto CA1 pyramidal cells; (2) Blockade of reciprocal inhibition between CA1 interneurons; (3) Blockade of incoming excitation due to CA3; (4) Blockade of collateral excitation from CA1 pyramidal cells onto interneurons (see neuron schemas in Figure 8 and Figure S5). Each blockade was attained by setting the GABA/AMPA (depending on the condition) synaptic weights φ for all postsynaptic cells to zero.

4 Processing of experimental neural data

of experimental electrophysiology data were performed using MATLAB (The MathWorks). Signal denoising and frequency band isolation procedures have been described in detail in a previous study (Logothetis *et al.*, 2012). In the following we describe the main signal processing and analysis performed on the denoised broad-band signals (0.05-7 kHz). We examined changes of power in the broad band signal (10-250 Hz). We first classified the electrode recording tips into stratum radiatum (SR) and stratum pyramidale (SP) based on several criteria. We visually tracked oscillations with distinct frequency contents (complex spike features, ripple or gamma-like high-frequency events and low-frequency sharp-waves) and inspected synchronous activity across recording sites.

The broad-band signal was rectified, low-pass filtered at 20 Hz and then (z-score) normalized. Candidate events were detected as epochs during which the signal exceeded a 3.5 SD threshold. Since increases in power may result from oscillations occurring in different frequency band, we clustered the spectra using Non-Negative Matrix Factorization (NNMF), an unsupervised algorithm that creates data decompositions for a user-defined number of groups or clusters (Logothetis *et al.*, 2012). Stable representation of the data was attained by a partition in three clusters, corresponding to power increases over different frequency bands, namely hp-sigma (8-22 Hz), gamma (25-75 Hz) and ripple (80-180 Hz). Only events with a significant increase of power in the ripple band (corresponding to SWR complexes) were considered 'candidate ripples', additional criteria such as ripple-associated signal-to-noise ratio were discarded so essentially all ripples were considered initially. All candidate ripples were filtered in the ripple band (80-180 Hz) with a 4th order Butterworth band-pass filter. We selected ripples exceeding a threshold of 5 SD. We further refined the procedure with a 'ripple time-localization criterion' by fitting a Gaussian function to the envelope of the signal filtered in the ripple band. Only events with a fitted width of and greater than 0.6 were considered true ripples and were taken into account for further processing (Ramirez-Villegas *et al.*, 2015). It should be also clarified that other event detection thresholds, such as

3.5 SD or 4 SD, did not alter the results reported in this work, demonstrating the robustness and validity of the results reported here.

Multi-unit spike times of our electrophysiology recordings were detected by threshold-crossing (3 SD) of the high-pass filtered extracellular signal (1000 Hz cutoff frequency). Single units were not isolated due to limitations of the recording hardware, thus all detected spikes were pooled together in a single multi-unit spike vector in order to compute the SFC as described earlier.

DATA AND SOFTWARE AVAILABILITY

The data included in this article will be available upon request to the Lead Contact of this study, Dr. Michel Besserve (michel.besserve@tuebingen.mpg.de).

The MATLAB code used to perform the model simulations will be available immediately upon publication of this article.

Supplemental Tables

Table S1: Related to STAR Methods. List of dynamical variables in the CA3-CA1 model as described by Pinsky & Rinzel (1994), and the two-compartment interneuron developed in this work. Current types apply to both CA3 and CA1 structures.

Neuron Type	Dynamical variable	Description
Pyramidal cell	I_{L-S}	Somatic leakage current
	I_{Na}	Inward sodium current
	I_{K-DR}	Outward delayed-rectified potassium current
	V_s	Somatic potential
	V_d	Dendritic potential
	I_s and I_d	Somatic and dendritic input currents
	I_{L-D}	Dendritic leakage current
	I_{Ca}	Dendritic inward calcium current
	I_{K-AHP}	Dendritic (outward) potassium afterhyperpolarization current
	I_{K-C}	Calcium-activated (outward) potassium current
	I_{syn-S}	Somatic synaptic current
	I_{syn-D}	Dendritic synaptic current
Interneuron	I_{L-S}	Somatic leakage current
	I_{L-D}	Dendritic leakage current
	I_{Na}	Inward sodium current
	I_{K-DR}	Outward delayed-rectified potassium current
	V_s	Somatic potential
	V_d	Dendritic potential
	I_s and I_d	Somatic and dendritic input currents
	I_{Ca}	Dendritic inward calcium current
	I_{K-C}	Calcium-activated (outward) potassium current
	I_{syn-S}	Somatic synaptic current (GABA-A and/or AMPA)
	I_{syn-D}	Dendritic synaptic current (AMPA)

Table S2: Related to STAR Methods. List of parameter values of the CA3-CA1 network model studied in this work across different conditions and neuron types (I: Interneurnons; E: Pyramidal cells).

Neuron type	Parameter (structure, units)	Standard condition
Pyramidal	g_{Na} (CA3/CA1,$\mathrm{mS/cm^2}$)	30
	g_{K-DR} (CA3/CA1,$\mathrm{mS/cm^2}$)	15
	g_{Ca} (CA3/CA1,$\mathrm{mS/cm^2}$)	10
	g_{K-AHP} (CA3/CA1,$\mathrm{mS/cm^2}$)	0.8
	g_{K-C} (CA3/CA1,$\mathrm{mS/cm^2}$)	15
	g_L (CA3/CA1,$\mathrm{mS/cm^2}$)	0.1
	g_C (CA3/CA1,$\mathrm{mS/cm^2}$)	2.1
	p (CA3/CA1,a.u.)	0.5
	C_m (CA3/CA1,$\mathrm{\mu F/cm^2}$)	3
	I_s (CA1,nA)	0
	I_s (CA3,nA)	0.8 ± 0.01
	I_d (CA1,nA)	0
	I_d (CA3,nA)	0
	E_{Na} (CA3/CA1,mV)	120
	E_{Ca} (CA3/CA1,mV)	140
	E_K (CA3/CA1,mV)	-15
	E_L (CA3/CA1,mV)	0
Interneuron	g_L (CA3/CA1,$\mathrm{mS/cm^2}$)	0.1
	g_{Na} (CA3/CA1,$\mathrm{mS/cm^2}$)	100
	g_{K-DR} (CA3/CA1,$\mathrm{mS/cm^2}$)	135
	g_{K-C} (CA3/CA1,$\mathrm{mS/cm^2}$)	8
	g_{Ca} (CA3/CA1,$\mathrm{mS/cm^2}$)	1
	I_s, I_d (CA3/CA1,nA)	0
	C_m (CA3/CA1,$\mathrm{\mu F/cm^2}$)	0.75
	ϕ (CA3/CA1,a.u.)	5
	E_{Na} (CA3/CA1,mV)	115
	E_{Ca} (CA3/CA1,mV)	140
	E_L (CA3/CA1,mV)	0
	E_K (CA3/CA1,mV)	-25
Synaptic interactions	E_{syn} (CA3/CA1,mV) [AMPA, GABA-A]	$[60, -15]$
	φ_{ex}^{CA3} (CA3,a.u.) [E-E; E-I]	$[2.5, 1.25]$
	φ_{inh}^{CA3} (CA3,a.u.) [I-E; I-I]	$[90, 20]$
	G_{th} (CA3/CA1,mV)	20
	τ_{syn} (CA3/CA1,ms) [AMPA, GABA-A]	$[2, 5]$
	g_{syn} (CA3/CA1,$\mathrm{\mu S/cm^2}$)	0.1
	φ_{ex}^{CA1} (CA1,a.u.) [E-E; E-I]	$[0, 0.8]$
	φ_{inh}^{CA1} (CA1,a.u.) [I-E; I-I]	$[60, 30]$
	$\varphi_{ex}^{CA3-CA1}$ (CA1,a.u.) - Schaffer [E-E; E-I]	$[2, 0.8]$

Table S3: Related to STAR Methods. Relation between synaptic parameters and evoked unitary postsynaptic potentials based on simlations.

Synapse	φ (a.u.)	Unitary PSP (mean±std) (mV)	Backgr. V_m (mean±std) (mV)
$CA3_{pyr} \rightarrow CA3_{pyr}$	1.5	0.42±0.060	-66.72±0.69
	2.1	0.61±0.050	-67.38±0.71
	3	0.86±0.050	-67.58±1.07
$CA3_{pyr} \rightarrow CA3_{int}$	1	1.62±0.050	-69.8±0.13
	1.25	2.07±0.410	-70.13±0.10
	1.5	2.37±0.120	-69.9±0.32
$CA3_{int} \rightarrow CA3_{int}$	20	1.13±0.004	-70.23±0.003
	30	1.43±0.005	-70.60±0.006
	35	1.54±0.120	-70.21±0.006
$CA3_{int} \rightarrow CA3_{pyr}$	55	0.59±0.090	-67.11±0.77
	70	0.76±0.080	-67.30±0.53
	85	0.95±0.120	-67.80±0.69
$CA1_{int} \rightarrow CA1_{int}$	25	0.38±0.007	-69.08±0.06
	35	0.48±0.010	-69.40±0.07
	45	0.66±0.010	-69.64±0.06
$CA1_{pyr} \rightarrow CA1_{int}$	0.8	1.32±0.007	-71.78±0.02
	1.1	1.81±0.010	-71.73±0.03
	1.5	2.47±0.010	-71.67±0.04
$CA3_{pyr} \rightarrow CA1_{pyr}$ (Schaffer)	0.5	0.20±0.020	-69.56±0.17
	1	0.42±0.040	-69.23±0.24
	2	0.81±0.040	-69.53±0.24
$CA3_{pyr} \rightarrow CA1_{int}$ (Schaffer)	0.1	0.16±0.004	-71.49±0.01
	0.3	0.48±0.010	-71.35±0.02
	0.5	0.79±0.030	-71.41±0.07

Supplemental Figures

Figure S1

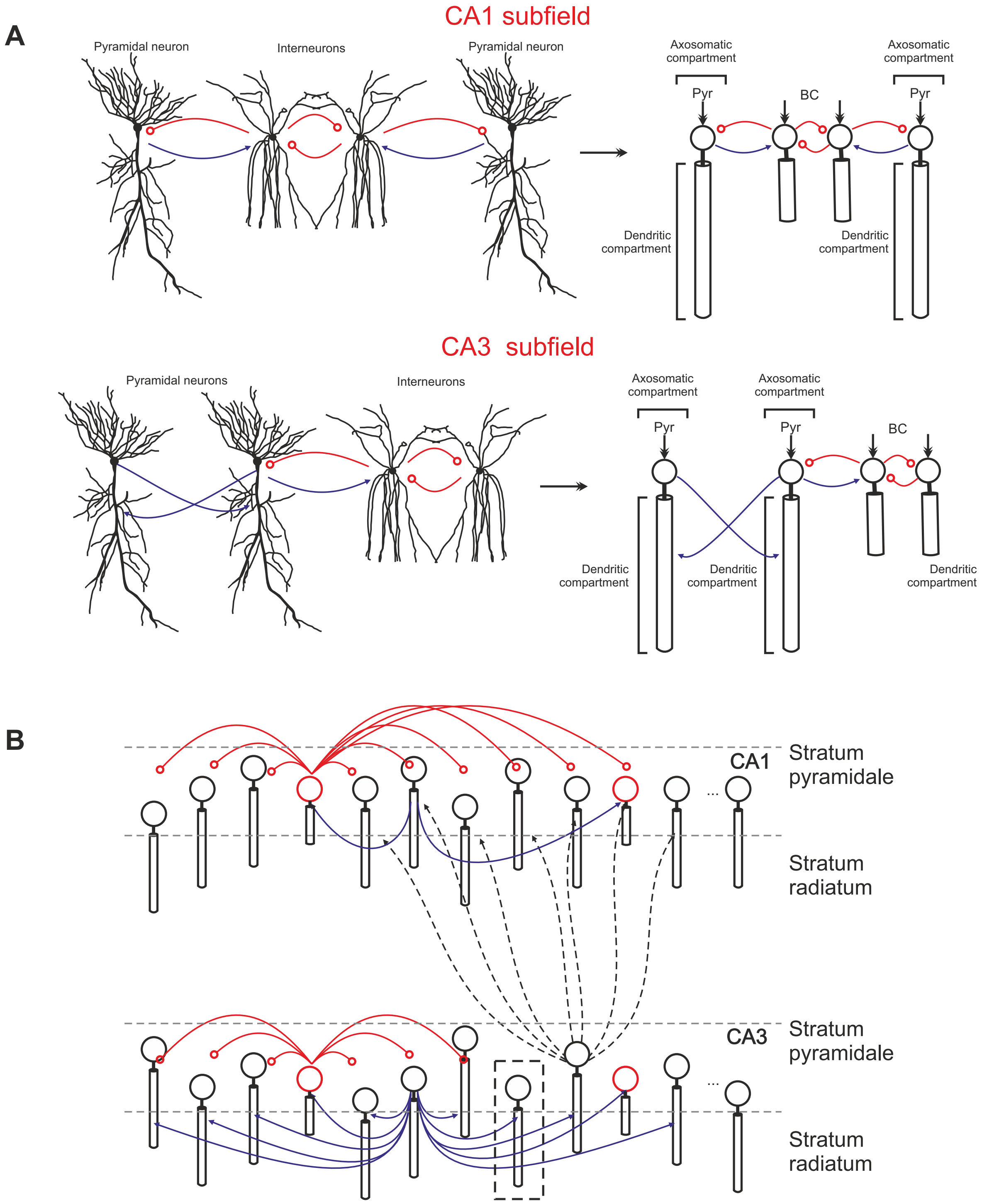
A
CA1 subfield
Pyramidal neuron
Interneurons
Pyramidal neuron
Axosomatic compartment
Axosomatic compartment
Pyr
BC
Pyr
Dendritic compartment
Dendritic compartment
CA3 subfield
Pyramidal neurons
Interneurons
Axosomatic compartment
Axosomatic compartment
Pyr
Pyr
BC
Dendritic compartment
Dendritic compartment
Dendritic compartment
B
CA1
Stratum pyramidale
Stratum radiatum
...
CA3
Stratum pyramidale
Stratum radiatum
...

Figure S1. CA3 and CA1 network multi-compartmental models. Related to Figure 1. (A) Schematic diagram of the possible neuronal interactions between neurons within CA3 and CA1 (left) and their equivalent in our multi-compartment model (right). (B) Schema of the multi-compartment model of the CA3-CA1 network proposed in this work.

Figure S2

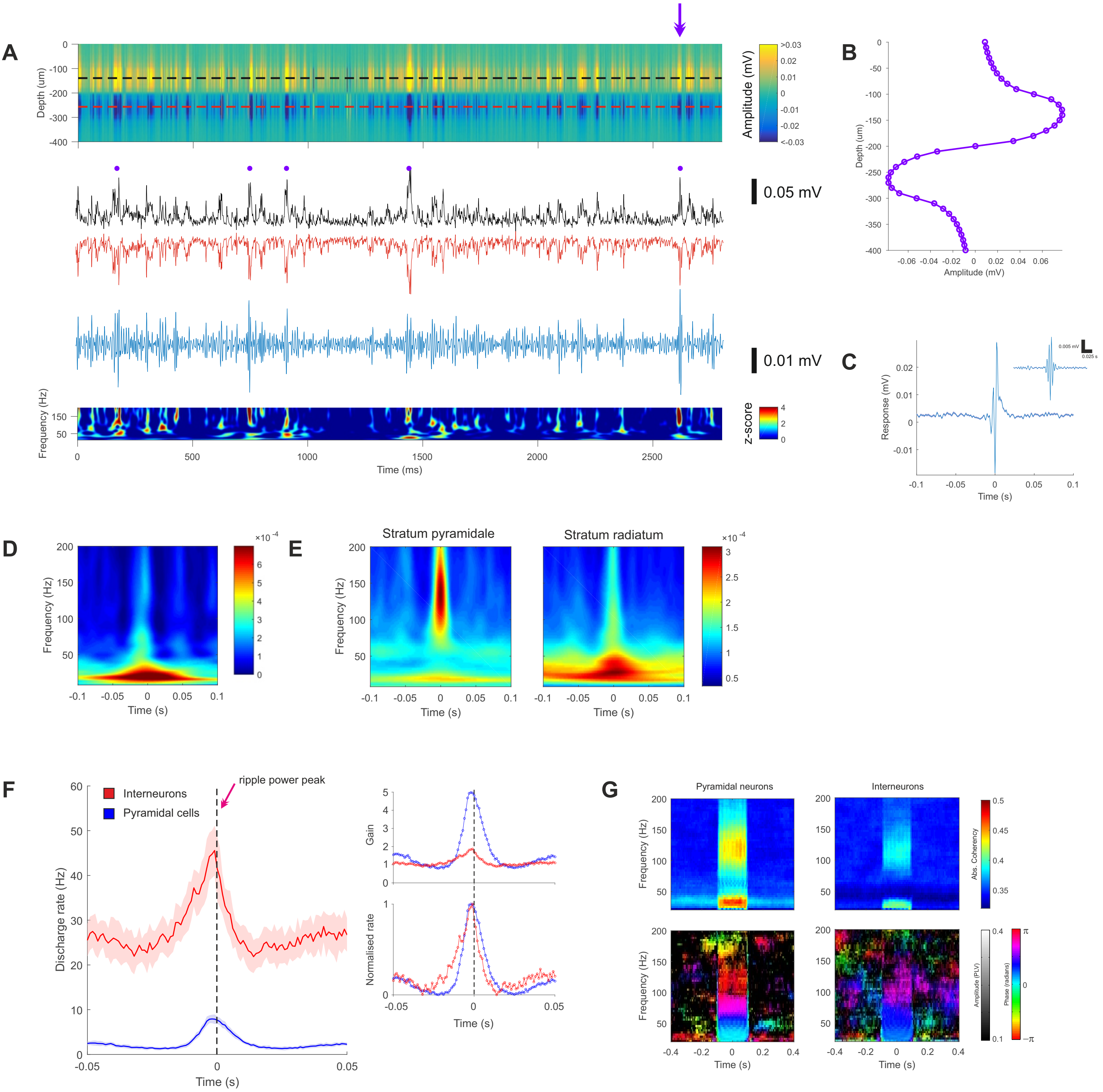
A
0
-100
-200
-300
-400
Depth (um)
Amplitude (mV)
>0.03
0.02
0.01
0
-0.01
-0.02
<-0.03
0.05 mV
0.01 mV
Frequency (Hz)
150
50
z-score
4
2
0
0
500
1000
1500
2000
2500
Time (ms)
B
0
-50
-100
-150
-200
-250
-300
-350
-400
Depth (um)
-0.06 -0.04 -0.02 0 0.02 0.04 0.06
Amplitude (mV)
C
0.005 mV
0.025 s
0.02
0.01
0
-0.01
Response (mV)
-0.1 -0.05 0 0.05 0.1
Time (s)
D
200
150
100
50
Frequency (Hz)
×10⁻⁴
6
5
4
3
2
1
0
-0.1 -0.05 0 0.05 0.1
Time (s)
E
Stratum pyramidale
Stratum radiatum
200
150
100
50
Frequency (Hz)
×10⁻⁴
3
2.5
2
1.5
1
0.5
-0.1 -0.05 0 0.05 0.1
Time (s)
-0.1 -0.05 0 0.05 0.1
Time (s)
F
ripple power peak
Interneurons
Pyramidal cells
60
50
40
30
20
10
0
Discharge rate (Hz)
-0.05 0 0.05
Time (s)
5
4
3
2
1
0
Gain
1
0
Normalised rate
-0.05 0 0.05
Time (s)
G
Pyramidal neurons
Interneurons
200
150
100
50
Frequency (Hz)
Abs. Coherency
0.5
0.45
0.4
0.35
Amplitude (PLV)
0.4
0.1
Phase (radians)
π
0
−π
-0.4 -0.2 0 0.2 0.4
Time (s)
-0.4 -0.2 0 0.2 0.4
Time (s)

Figure S2. The CA3-CA1 network model dynamics during SWR episodes. Related to Figure 1. (A) Laminar distribution and two example traces of wide-band full LFP (LFPt + LFPsyn; first three subpanels, black trace in stratum pyramidale, red trace in stratum radiatum), ripple band-filtered (80-180) LFP (blue trace), and wide band LFP-associated Morlet-wavelet spectrogram of the ongoing LFP activity in a CA1 network of 150 neurons model exhibiting ripples generated spontaneously (indicated by purple dots on top). The channels displayed are representative traces for the center of the simulated stratum pyramidale (black line) and stratum radiatum (red line), as indicated by the dotted lines in the top subpanel. (B) Exemplary spatial (amplitude) profile of the LFP across recording sites (indicated in (A) top subpanel, by the purple arrow). (C) Broad-band SWR average across several detected episodes (N=100 SWR events, inset represents ripple band). (D) Population averaged ripple-triggered CA3 spectrogram displaying significant increases in power over gamma frequencies (<100 Hz). (E) Spectrogram grand averages associated with simulated SWR complexes. The leftmost and rightmost time-frequency spectrograms correspond to the SWR signature in stratum pyramidale and stratum radiatum (only LFPt is shown in these plots in order to illustrate the difference between strata; for an exemplary full LFP in Figure 1B). (F) Peri-SWR spike time histograms for pyramidal cells (blue) and interneurons (red) across modeling sessions (left subpanel) (N = 25 modeling sessions). Excitatory and inhibitory gains with respect to baseline activity accord with experimental evidence (~2-fold for inhibition, ~5-fold for excitation) (Csicsvari et al., 2000). (G) Spike-field coherence absolute value (top) and phase-locking maps (bottom) from pyramidal neurons' spikes (left subpanels), and interneuronal spikes (right subpanels). Note that ripple-related pyramidal neuron's spiking occurs at a phase of *pi* radians, corresponding to the trough of the ripple oscillation. Interestingly, the phase profile of the spike-field coherence closely resembles that of experimental data (Figure 9D).

Figure S3

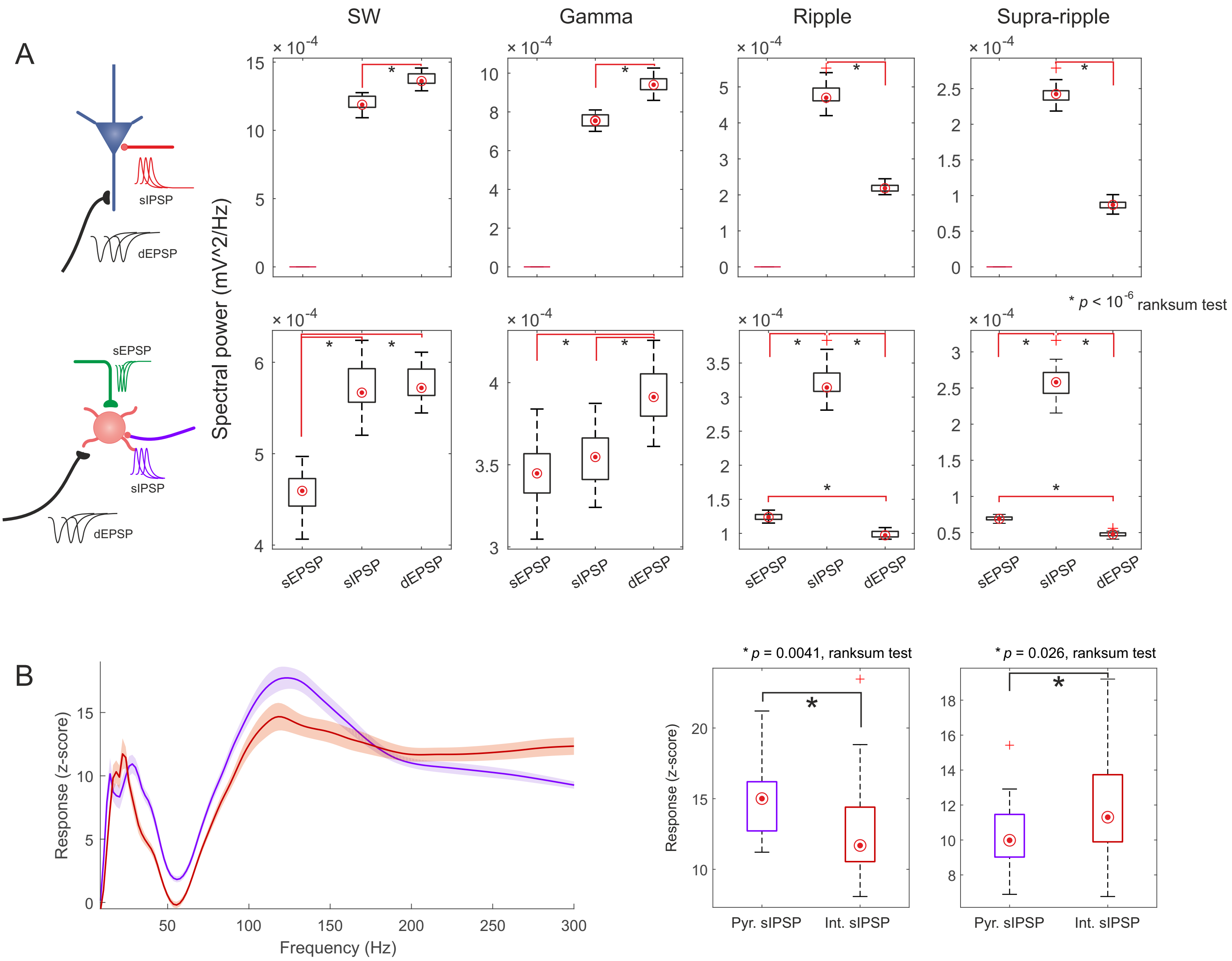
A
SW
Gamma
Ripple
Supra-ripple
sIPSP
dEPSP
sEPSP
sIPSP
dEPSP
Spectral power (mV^2/Hz)
× 10^{-4}
15
10
5
0
10
8
6
4
2
0
5
4
3
2
1
0
2.5
2
1.5
1
0.5
0
*
* $p < 10^{-6}$ ranksum test
6
5
4
3.5
3
3.5
3
2.5
2
1.5
1
3
2.5
2
1.5
1
0.5
sEPSP
sIPSP
dEPSP
B
Response (z-score)
15
10
5
0
50
100
150
200
250
300
Frequency (Hz)
* p = 0.0041, ranksum test
* p = 0.026, ranksum test
Response (z-score)
20
15
10
18
16
14
12
10
8
Pyr. sIPSP
Int. sIPSP
Pyr. sIPSP
Int. sIPSP

Figure S3. Decomposition of the SWR-related synaptic component of the LFP. Related to Figure 2. (A) Statistics of the power of LFPsyn across SWR-related components for pyramidal cell- and interneuron-associated synapses. (B) SWR-triggered spectra of the I-E and I-I synaptic activity (left subpanel), and statistics of the z-scored spectral power of I-E and I-I synaptic activity for ripple (80-180 Hz; middle subpanel) and supra-ripple (190-300 Hz; right subpanel).

Figure S4

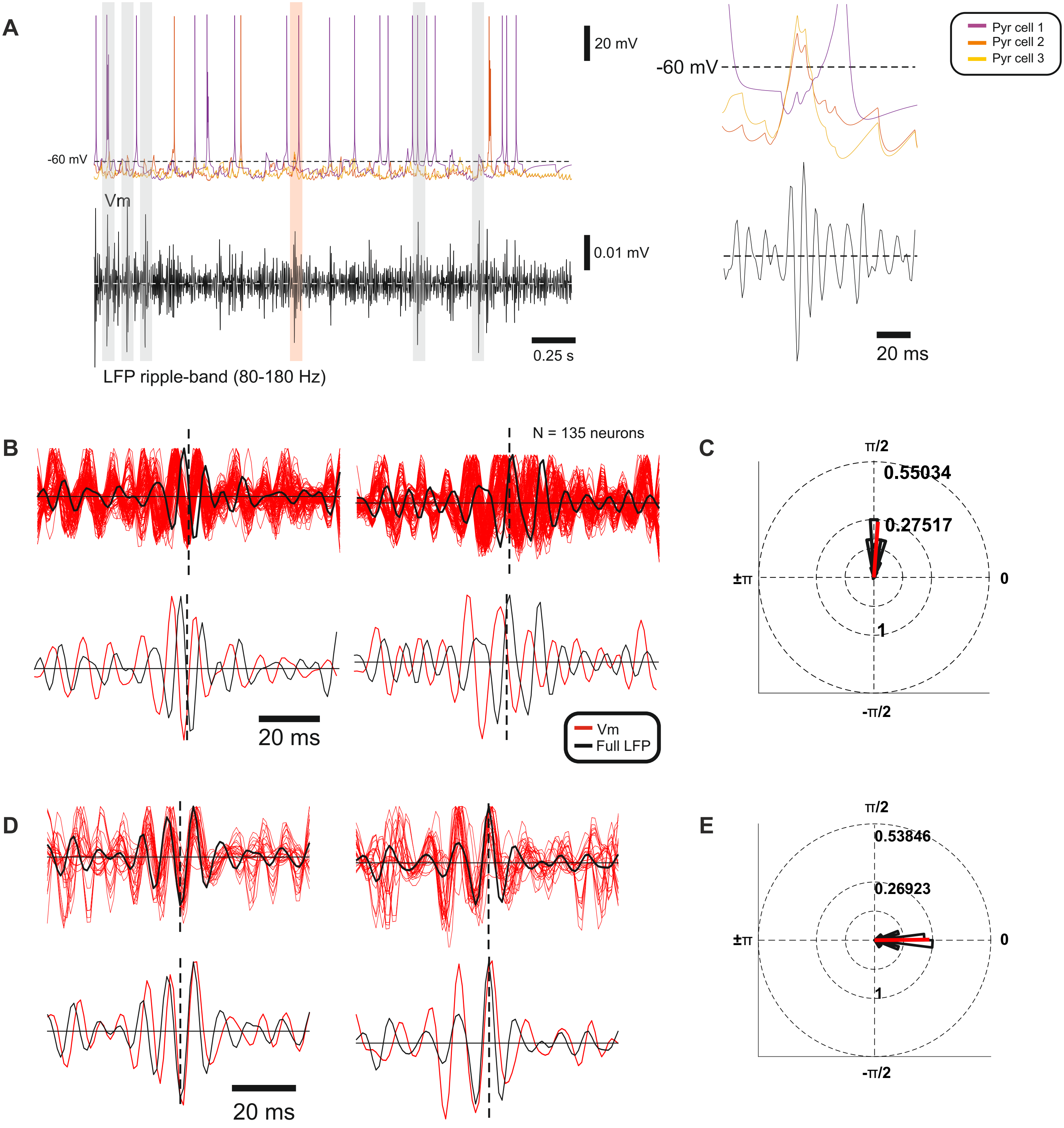
A
-60 mV
Vm
20 mV
0.01 mV
0.25 s
LFP ripple-band (80-180 Hz)
-60 mV
Pyr cell 1
Pyr cell 2
Pyr cell 3
20 ms
B
N = 135 neurons
20 ms
Vm
Full LFP
C
π/2
0.55034
0.27517
±π
0
1
-π/2
D
20 ms
E
π/2
0.53846
0.26923
±π
0
1
-π/2

Figure S4. SWR-associated membrane potential (Vm) dynamics. Related to Figure 6. (A) Exemplary simulated membrane potential (curves of various colors; each curve is one exemplary cell); and ripple-filtered (80-180 Hz) LFP traces (black curve). Grey and red shading indicate detected SWR episodes. A zoomed-in view of the red-shaded event is presented in the right side of the panel. (B) Relationship between Vm and LFP ripples displays a consistent phase lead of Vm across cells (red curves, each curve is one pyramidal cell) with respect to LFP (black thick curves). The averaged Vm-ripple across cells is depicted in the bottom plots. Left and right subpanels depict two exemplary ripples. (C) Circular histogram of the averaged Vm-LFP phase relationship across all simulated CA1 pyramidal cells (*N* = 135 cells). Circular mean is shown by the red line, the length of the line displays the phase-locking value (close to 1). (D) Same as (B), but in independent simulations, for pyramidal cells that received hyperpolarizing currents in the interval [-3.5, -2.5] nA (resulting in Vm roughly from -15 mV to -25 mV below resting; *N* = 25 cells). Cells under standard conditions presented the same phase relationship depicted in (B). (E) Same as (C), but for pyramidal cells that received hyperpolarizing currents in the interval [-3.5, -2.5] nA.

Figure S5

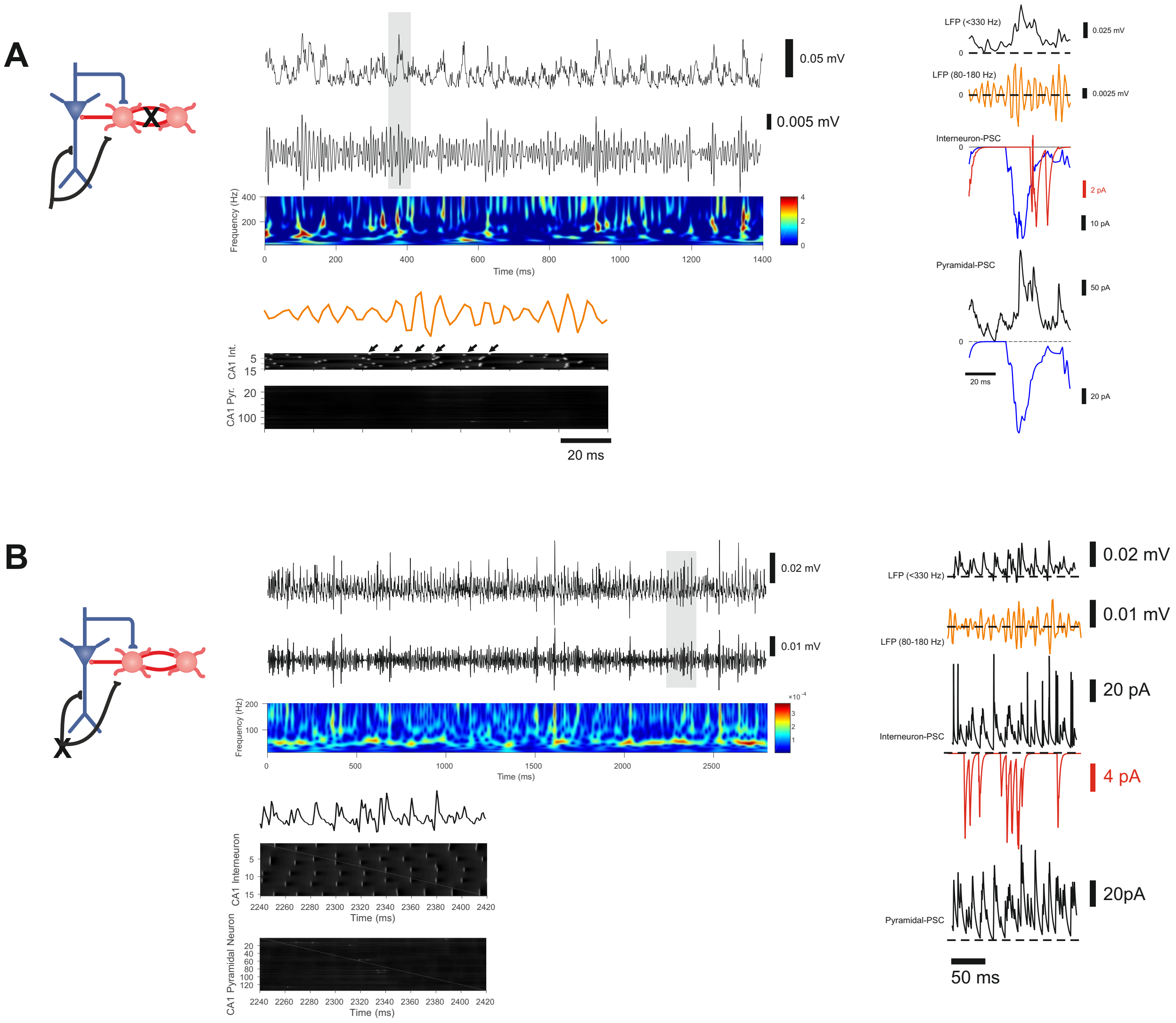
A
0.05 mV
0.005 mV
Frequency (Hz)
400
200
4
2
0
0
200
400
600
800
1000
1200
1400
Time (ms)
CA1 Int.
5
15
CA1 Pyr.
20
100
20 ms
LFP (<330 Hz)
0.025 mV
LFP (80-180 Hz)
0.0025 mV
Interneuron-PSC
2 pA
10 pA
Pyramidal-PSC
50 pA
20 ms
20 pA
B
0.02 mV
0.01 mV
Frequency (Hz)
200
100
×10⁻⁴
3
2
1
0
500
1000
1500
2000
2500
Time (ms)
CA1 Interneuron
5
10
15
2240
2260
2280
2300
2320
2340
2360
2380
2400
2420
Time (ms)
CA1 Pyramidal Neuron
20
40
60
80
100
120
2240
2260
2280
2300
2320
2340
2360
2380
2400
2420
Time (ms)
LFP (<330 Hz)
0.02 mV
LFP (80-180 Hz)
0.01 mV
Interneuron-PSC
20 pA
4 pA
Pyramidal-PSC
20pA
50 ms

Figure S5. Selective inactivation of synaptic excitation and inhibition abolishes SWR complexes. Related to Figure 8. (A) Resulting CA1 LFP time course upon a selective blockade of reciprocal inhibition between interneurons (left schema). Wide-band (<330 Hz, middle column, top subpanel), high-frequency filtered and time-frequency spectrogram (middle column, middle subpanels). Note that SWR are abolished in these LFP traces, with concomitant reduction of the LFP amplitude due to the negligible pyramidal cell participation (see raster plots, bottom panel, white ticks mark the spike occurrence; see also magnification of an exemplary deflection in the right subpanel). (B) Same as (A), but upon selective blockade of CA3-related Schaffer collateral excitation (left schema). Note that SWR are abolished in these LFP traces, with concomitant reduction of the LFP amplitude and prevalent gamma oscillations.

Figure S6

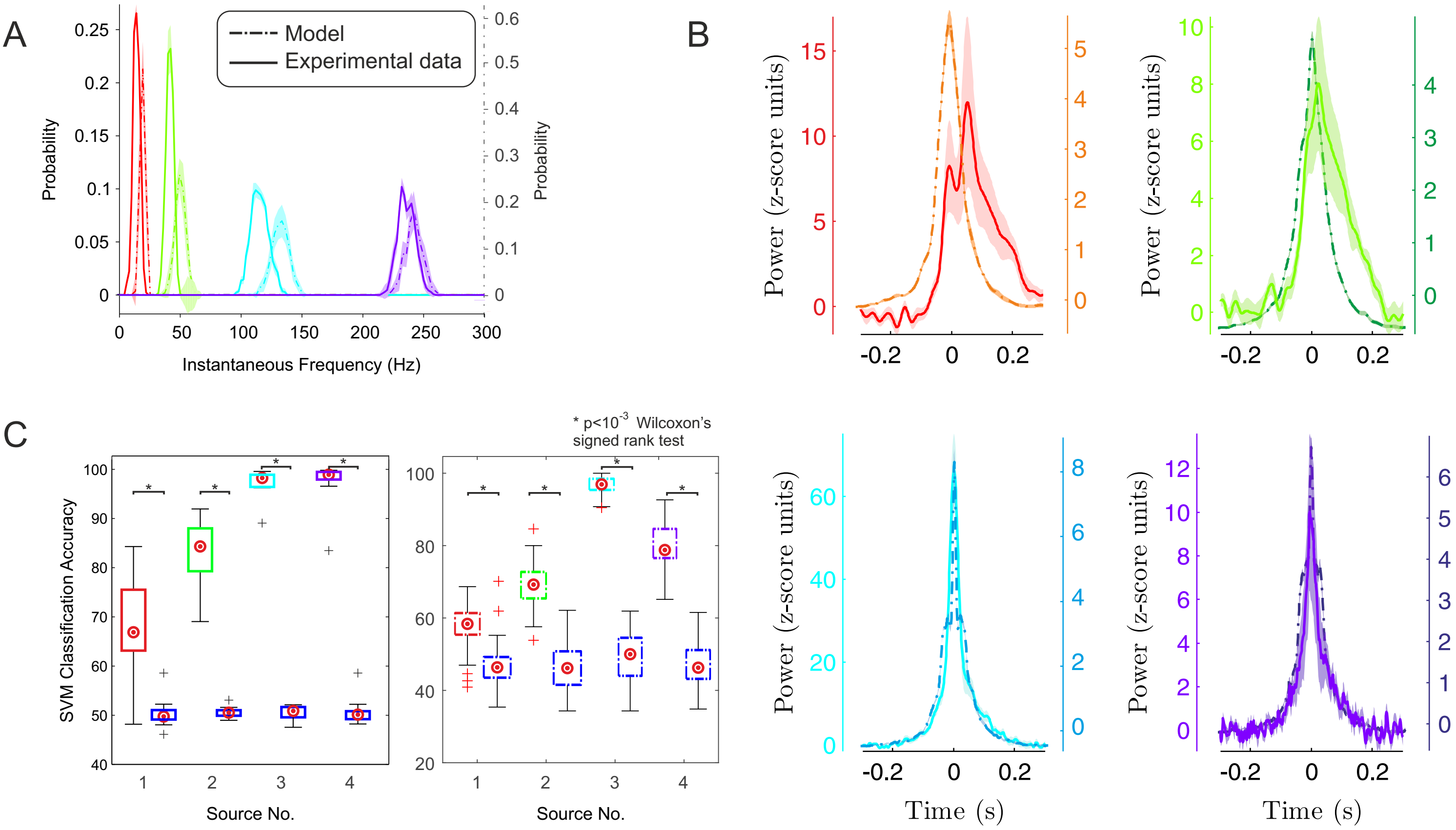
A
Model
Experimental data
Probability
0.25
0.2
0.15
0.1
0.05
0
0
50
100
150
200
250
300
Instantaneous Frequency (Hz)
0.6
0.5
0.4
0.3
0.2
0.1
0
Probability
B
Power (z-score units)
15
10
5
0
5
4
3
2
1
0
-0.2
0
0.2
10
8
6
4
2
0
4
3
2
1
0
60
40
20
0
8
6
4
2
0
12
10
8
6
4
2
0
6
5
4
3
2
1
0
Time (s)
C
SVM Classification Accuracy
100
90
80
70
60
50
40
1
2
3
4
Source No.
* p<10^-3 Wilcoxon's signed rank test
*
100
80
60
40
20

Figure S6. SWR complexes can be predicted from increases in sharp wave, gamma, ripple and supra-ripple power in both experimental and simulated SWR complexes. Related to Figure 9. (A) Empirical distributions of the instantaneous frequency of each SWR-associated dynamical component within a 50 ms time window around the occurrence of each SWR episode. (B) Dynamical components display above-baseline power increases concomitant with the occurrence of a SWR episode for both experimental (solid line) and simulated (dashed line) CA1 recordings. (C) Linear SVM classification accuracy for the prediction of the occurrence of a SWR complex against baseline activity, on the basis of sharp wave (red), gamma (green), ripple (cyan) and supra-ripple (violet) power. Blue boxes correspond to the chance-classification values, as obtained for shuffled experimental (solid boxes) and simulated (dashed boxes) data. The top and bottom of each box are the 25th and 75th percentiles of the samples, respectively; the red dots correspond to the sample median; the black lines extending below and above each box reach the sample extrema. Outliers are indicated by crosses.

Figure S7

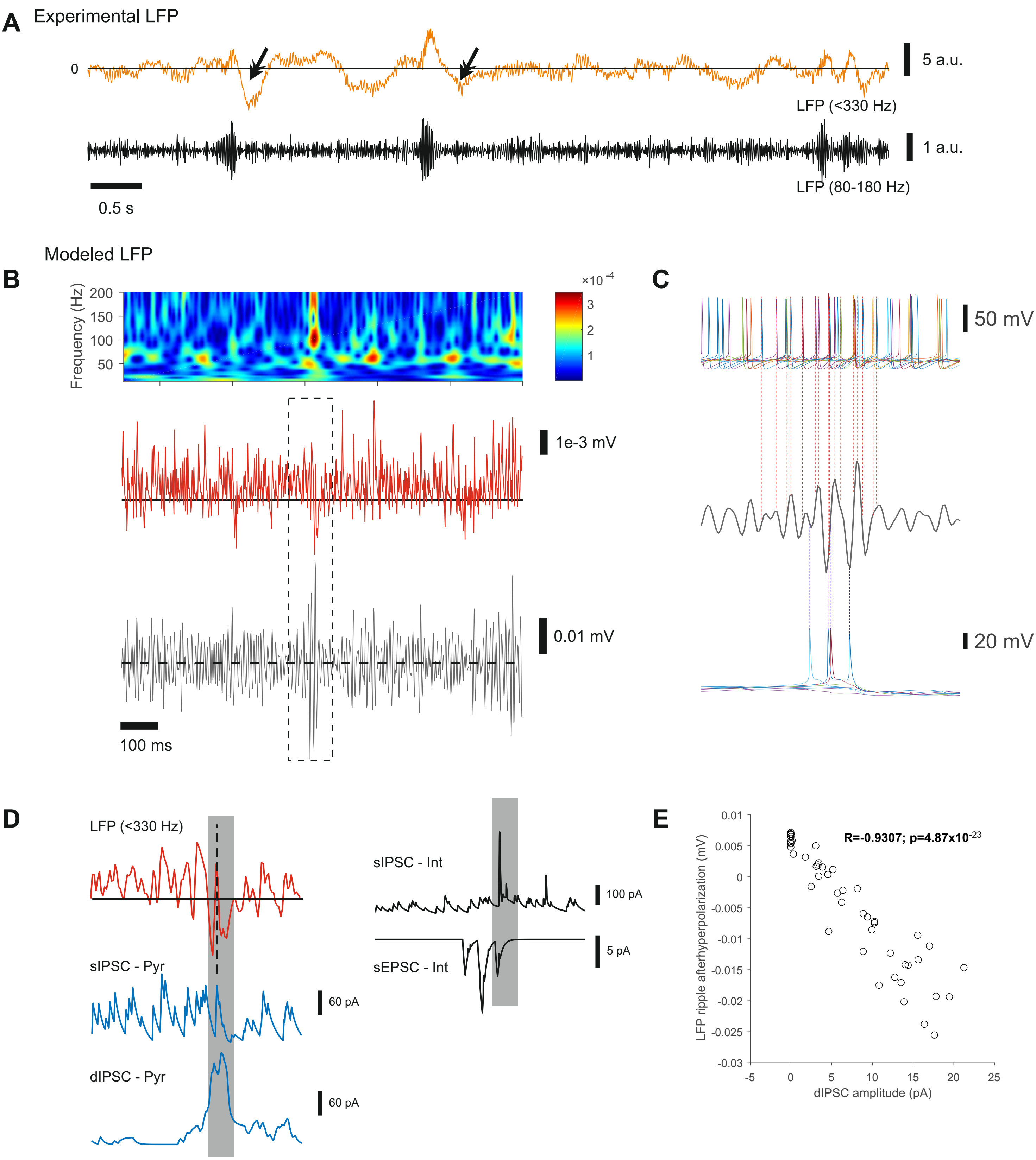
A
Experimental LFP
0
5 a.u.
LFP (<330 Hz)
1 a.u.
LFP (80-180 Hz)
0.5 s
Modeled LFP
B
Frequency (Hz)
200
150
100
50
×10 -4
3
2
1
1e-3 mV
0.01 mV
100 ms
C
50 mV
20 mV
D
LFP (<330 Hz)
sIPSC - Pyr
60 pA
dIPSC - Pyr
60 pA
sIPSC - Int
100 pA
sEPSC - Int
5 pA
E
R=-0.9307; p=4.87x10-23
LFP ripple afterhyperpolarization (mV)
0.01
0.005
0
-0.005
-0.01
-0.015
-0.02
-0.025
-0.03
-5
0
5
10
15
20
25
dIPSC amplitude (pA)

Figure S7. Dendritic inhibition underlies LFP SWR afterhyperpolarization. Related to Figure 9. (A) In vivo-recorded wide-band (<330 Hz, top) and ripple band-filtered (80-180 Hz, bottom) LFP illustrating two out of three exemplary SWR that display post-ripple hyperpolarizations (black arrows). (B) An exemplary simulated SWR (dotted line) with inhibition onto CA1 pyramidal cells' dendrites. Note the hyperpolarization (downward potential) of the LFP (red trace, only stratum pyramidale is shown). Both the spectrogram and filtered LFP traces display ripple-related signatures (top and bottom panels, respectively). (C) LFP-ripples, interneuronal (top) and pyramidal cell discharges (bottom) keep their usual relationship as illustrated by the example trace. (D) Expanded version of the LFP trace in (B) (dotted line), depicted together with its associated PSC. Note that the LFP-hyperpolarization co-occurs with the rise of dendritic IPSC (dIPSC). (E) Scatter plot illustrating that the amplitude of peri-SWR hyperpolarization correlates strongly with the maximal amplitude of the population-averaged dIPSC (N = 51 SWR episodes; 18 simulation experiments).

Supplemental Experimental Procedures

Juan F. Ramirez-Villegas, Konstantin Willeke, Nikos K. Logothetis & Michel Besserve

Selective inactivation of synaptic excitation and inhibition abolishes SWR complexes

As selective inactivation of pyramidal cells and interneurons interrupts in vivo SWR episodes (Stark *et al.*, 2014), we investigated whether selective blockade of synaptic activity within the simulated CA1 would present similar effects. In order to better understand the action of inhibitory synapses within the feedback and reciprocal inhibition of CA1, we selectively blocked the reciprocal I-I synapses (Figure S5A). The overall effect of this manipulation was an increase of inhibitory activity, until complete suppression of pyramidal-cell activity (see the suppression of synaptic currents, and the almost negligible participation of pyramidal cells in Figure S5A, right subpanels). In a similar vein, SWR activity is abolished, with a concomitant reduction of the overall LFP amplitude, to resemble less coordinated baseline-like activity. Synchronous episodes due to CA3-related depolarisations display high-frequencies, reflected by interneuron-to-pyramidal sIPSC, and likely caused by CA3 activity in absence of CA1-related synaptic coordination mechanisms (see also Main Text). Thus, inhibitory control between inhibitory cells is also critical for the emergence of SWR episodes in our model. Furthermore, it is likely that ripple-band coordination in CA1 under physiological conditions is achieved by means of both I-I and I-E sIPSC.

Next, we sought to determine whether excitatory synapses from CA3 were critical for generating SWR complexes. We addressed this question by selectively blocking dESPC. When CA3-inputs were blocked, we observed abolition of SWR-related activity, together with almost absense of coordinated bursts of activity in CA1, and LFP activity dominated by gamma oscillations (Figure S5B). However, brief high-frequency oscillations emerged when CA1 cells participated, but not by interneurons alone (Maier *et al.*, 2011; Hulse *et al.*, 2016). These episodes were, however, very short in time and displayed an overall diminished LFP amplitude (Figure S5B). These results accord with previous experimental work, where selective deactivation of CA3 leads to diminished SWR activity (Nakashiba *et al.*, 2009). In addition, our results indicate that pyramidal cell activation is required for SWR complexes to be generated, likely due to the contribution of their active currents toward the LFP of SWR, and the control exerted by inhibition over excitation.

Comparison of *in vivo* and simulated LFP dynamic components

In order to further identify each SWR-related component, we estimated the instantaneous frequency of each of them by measuring the inverse of the time between the component peaks in a [-0.1 0.1] s time window around the occurrence of each SWR event (Figure S6A). The distribution of instantaneous frequencies across oscillatory components for experimental and modeled SWRs was largely unimodal ($p>0.2$, Hartigan's dip test). These results suggest that concomitant with the occurrence of SWR episodes, there are concomitant gamma and supra-ripple oscillatory sources. Notably, our analysis of these oscillatory sources is in close correspondence with our previous study (Ramirez-Villegas *et al.*, 2015), reporting gamma oscillations occurring transiently and concomitantly with SWR episodes in macaques. Notably, as mentioned in the Main Text of this work, a similar SWR-gamma oscillatory component has been reported in previous studies in rodents (Carr *et al.*, 2012; Gillespie *et al.*, 2016).

Next, we asked whether the relation between identified gamma, supra-ripple and ripple components is systematic, in order to further check that gamma and supra-ripple components are not simply an effect of ongoing baseline activity intermingled with the occurrence of SWRs. To this end, raw components were rectified and low-pass filtered with a 4th-order Butterworth FIR filter with a cut-off frequency of 20 Hz. We found that concomitant with the expected significant power increase in SPW and ripple components during each neural event, gamma and supra-ripple components also showed transient and significant power increases above baseline activity levels (Figure S6B).

We next asked whether power profiles of oscillatory components were predictive of the occurrence of individual SWR episodes. For this purpose, we trained linear support vector machine (SVM) classifiers in order to predict the presence or absence of an SWR on the basis of its oscillatory sources. Oscillatory components were treated separately for each experimental and modelling session, wherein SPW, gamma, ripple and supra-ripple power signals were discriminated against surrogate (randomly chosen) baseline events in time windows of [-0.1 0.1] s around the detected event. Classifiers associated to experimental (and modeled) SPW, gamma, ripple and supra-ripple power performed significantly above chance ($p < 10^{-3}$ Wilcoxon's signed rank test for the comparison between ground-truth and shuffled-label classification accuracies), with 68.79 ± 5.57% (model: 57.71 ± 1.24%), 83.20 ± 3.58% (model: 69.08 ± 1.32%), 97.39 ± 1.43% (model: 96.31 ± 0.53%), and 97.74 ± 2.25% (model: 79.95 ± 1.25%) mean 10-fold cross-validation accuracy with 95% confidence interval, respectively (see Figure S6C). These results suggest that apart from SPW and ripple components, gamma and supra-ripple oscillations are two network dynamical components inherent to the SWR phenomenon.

Dendritic inhibition underlies peri-SWR hyperpolarization

In experimental recordings, in some cases SWR complexes display a after-hyperpolarization in the LFP (English *et al.* (2014); Ramirez-Villegas *et al.* (2015); see Figure S7A, LFP traces). In our work, by no modification in the model free-parameters we could attain such an effect. This result suggests that SWR after-hyperpolarization may be determined by a functional concomitant of the CA1 network, captured by LFP recordings in vivo. As our model is minimal in the number of such functional concomitants, it displays a rather limited spectrum of SWR activities. These limitations include multiple types of interneurons whose effects on the SWR-associated LFP are not well understood. For instance, bistratified cells likely play a key role in shaping some of the electrical characteristics of SWR complexes. Bistratified cells' axons present notable innervation of pyramidal cells' apical dendrites, and display firing rate increases locked to high-frequency ripples (Varga *et al.*, 2014).

We reasoned that such dendritic inhibitory component might well be at least partly responsible for the SWR after-hyperpolarization. Concordantly, the SWR subtype that displays this effect often displays higher frequency than other types of SWR episodes (Ramirez-Villegas *et al.*, 2015). To test this hypothesis with minimal modifications to the network model (i.e. without modelling the dynamics of bistratified cells), we injected IPSCs to the apical dendrites of modeled CA1 pyramidal cells, these synapses were assigned at random to 22% of the postsynaptic cells following the connections of CA3 excitatory Schaffer inputs (Klausberger & Somogyi, 2008). These dIPSC followed the amplitude and dynamics of their peri-somatic counterparts. First, we found that this increase in inhibitory drive reduced notably the participation of pyramidal cells (3 to 5 % of the population was active), however, the raw LFP of the network displayed intermittent negative deflections, in some cases associated with ripple oscillations (Figure S7B). These ripples presented similar relationship to CA1 cell discharges as that of ripples under standard conditions. Interestingly, the occurrence of this negative deflection was precisely timed to the occurrence of the injected dIPSC onto the dendrites of CA1 cells (Figure S7D), and the amplitude of the dIPSC largely correlated with the LFP SWR-afterhyperpolarization (r=0.9307, p=$4.87 * 10^{-23}$; N=51 detected SWR complexes across 18 simulation experiments; Figure S7E). These results suggest that the SWR afterhyperpolarization apparent in experimental LFP may be mediated by dendritic inhibition, in line with the suggestion that high-frequency ripples may be partly resulting from the activity of bistratified cells (Varga *et al.*, 2014). In addition, we hypothesize that bistratified cells may contribute to an enhanced ripple and supra-ripple frequency bands (see also Figure 2B), which may result in ripples with overall higher frequency.

Appendix C

Paper 3

Pontogeniculooccipital (PGO) waves reflect transient competition between brain stem and hippocampus

Juan F. Ramirez-Villegas[1,2], Yusuke Murayama[1], Henry C. Evrard[1,5], Michel Besserve[1,3] & Nikos K. Logothetis[1, 4]

[1]Department of Physiology of Cognitive Processes, Max Planck Institute for Biological Cybernetics, Spemannstrasse 38, 72076 Tübingen, Germany

[2]Graduate School of Neural & Behavioral Sciences, International Max Planck Research School, Eberhard-Karls University of Tübingen, Österbergstrasse 3, 72074 Tübingen, Germany

[3]Department of Empirical Inference, Max Planck Institute for Intelligent Systems and Max Planck ETH Center for Learning Systems, Spemannstrasse 38, 72076 Tübingen, Germany

[4]Centre for Imaging Sciences, Biomedical Imaging Institute, The University of Manchester, Manchester M13 9PT, United Kingdom

[5]Werner-Reichardt Centre for Integrative Neuroscience, Ottfried-Müller-Strasse 25, 72076 Tübingen, Germany

Abstract

Pontogeniculooccipital (PGO) waves are phasic potentials observed in electrophysiology recordings from the pons, lateral geniculate nucleus and occipital cortex of many mammals. Although they are believed to play a key role in learning and memory, how they participate in brain-wide network activities remains poorly understood. Using multi-structure intracortical recordings, we study the pontine and genicular activities associated with PGO waves and relate them to the activities of another major memory structure: the hippocampus. In line with previous evidence, analysis of ponto-geniculo field activity revealed two physiologically distinct PGO wave types: type I, having a single biphasic pattern; and type II, exhibiting multiple oscillatory cycles. Marked by antagonistic neuronal population responses, PGO wave types also related differentially to hippocampal neural events. Whereas type II PGO waves are coupled with hippocampal sigma episodes, type I PGO waves co-occur with sharp wave-ripple (SWR) complexes. Our study provides the first neurophysiological evidence for a brain state-dependent competition of phasic neuronal activities characteristic of cortico-hippocampal and ponto-geniculo-neocortical networks, likely associated with distinct memory-related functions.

Keywords: pontogeniculooccipital wave; sleep; memory; hippocampus; in vivo electrophysiology.

Introduction

Offline states –associated with periods of quiet wakefulness, slow wave sleep (SWS) and rapid-eye-movement (REM) sleep in mammalian species– play a prominent role in sensorimotor integration, dreaming, learning, and the transfer and consolidation of declarative and procedural memories. The electrophysiological correlates of these processes are particularly striking. First, during these states, tonic changes in the neuronal activity are characterized by appearance of synchronous or desynchronized activity in electroencephalographic recordings (EEG) (Datta and MacLean, 2007). Second, intracortical recordings reveal concomitant phasic patterns of activity characteristic of offline states, which often reflect short- and long-range interactions between neuronal populations (Buzsáki, 2015; Sirota and Buzsáki, 2005).

These phasic physiological episodes of sleep include bi-phasic potentials lasting approximately 100 ms –termed pontogeniculooccipital (PGO) waves– co-occurring in pontine, thalamic nuclei and occipital cortex of several mammals (Bizzi and Brooks, 1963; Brooks and Bizzi, 1963; Datta, 1997; Jouvet, 1962; McCarley et al., 1983; Morrison and Bowker, 1975; Reiner and Morrison, 1980), including human and non-human primates (Cohen and Feldman, 1968; Feldman and Cohen, 1968; McCarley et al., 1983; Vuillon-Cacciuttolo and Seri, 1978). These waves often occur in isolation (singlet PGO waves), or as groups with variable number of waves in very close temporal proximity (clustered PGO waves) (Brooks and Bizzi, 1963; Calvo and Fernandez-Guardiola, 1984; Datta et al., 1992; Morrison and Pompeiano, 1966; Steriade et al., 1990a). Singlet PGO waves have been found relatively independent of eye movement and prevalent during SWS (often termed SP-state), whereas clustered ones are typically observed coupled to ocular jerks during fully-developed episodes of paradoxical sleep (Datta et al., 1992; Steriade et al., 1990a). Correlative evidence from vestibular inactivation studies suggests that PGO waves with distinct temporal profiles may reflect the action of distinct microcircuits and possibly large-scale functional networks (Morrison and Pompeiano, 1966). While REM and SWS sleep episodes are instrumental for learning and memory, the specific role of PGO waves in these states remains largely unknown. This question arises partly due to the lack of information on the large-scale mechanisms associated with these episodes. Investigating their system-level properties may thus offer insights regarding their functional role, and ultimately, offer a better understanding of the function and neural mechanisms of REM sleep.

Contrasted phasic and tonic activities during SWS and REM sleep are also present in other brain structures. For instance, hippocampal activity exhibits phasic activities known as sharp wave-ripples (SWR). SWR are transient episodes representing massive depolarizations of the hippocampal CA1 subfield during SWS, and have been associated with declarative memory consolidation and recall (Girardeau et al., 2009; Nakashiba et al., 2009). On the other hand, hippocampal activity displays waking-like activities during REM sleep (Kemp and Kaada, 1975; Vanderwolf, 1969; Vertes, 1982).

The tone of brainstem neuromodulatory systems greatly influences the shift from predominantly external input-driven brain activity during waking, to SWS and to REM sleep. Indeed, dopamine- and acetylcholine-releasing neurons are active during REM together with almost complete aminergic demodulation (Hobson et al., 1975). Conversely, aminergic tone is highest during wakefulness and reduces –but is not absent– during SWS (Aston-Jones and Bloom, 1981; Hobson, 2010). In particular, experimental evidence suggests that serotoninergic firing during SWS is anti-correlated with REM-related activities such as PGO potentials and hippocampal theta activity (Lydic et al., 1983; Maru et al., 1979; McGinty and Harper, 1976). Thus, SWS- and REM-related hippocampal and pontine activities are likely related through large-scale network interactions. In line with this hypothesis, hippocampal SWR have been associated with episodes of metabolic neocortical activation, co-occurring with suppression of pontine, thalamic and occipital activities (Logothetis et al., 2012).

In this work, we investigate further these large-scale interactions by examining the relationship between PGO waves and hippocampal activity using electrophysiological methods. Using multi-site extracellular recordings in anaesthetized macaque monkeys (*Macaca mulatta, Macaca fascicularis*), we cluster PGO activities into two distinct subtypes: pons-thalamus-deactivating, type I PGO waves present a single biphasic pattern, and pons-thalamus-activating, type II PGO waves exhibit multiple successive biphasic patterns. Pontine- and LGN-multi unit activity (MUA) revealed antagonistic neuronal population responses suggesting these events reflect distinct circuit processes and are likely generated during two distinct brain states. In a second set of experiments, pontine and hippocampal structures were concurrently recorded. In line with our observations in pons and LGN, we found differentiated couplings of the two types of PGO waves to hippocampal activity. While type II PGO waves are coupled with hippocampal theta-like episodes, type I PGO waves are associated with hippocampal SWR complexes. Altogether, our results suggest that PGO waves with distinct LFP signatures reflect differentiated subcortico-hippocampal interactions. These results show –for the first time– physiological evidence for competition over short time scales between cortico-hippocampal and ponto-geniculo-neocortical networks. This competition is likely brain state-dependent and corresponds to differentially-activated microcircuits accomplishing distinct memory-related functions.

Results

Phasic pontine potentials. In order to study PGO waves, we recorded and analysed extracellular potentials. Laminar recording probes were positioned in the pontine region (approximately in the anatomical position of the parabrachial nucleus, PBn) and lateral geniculate nucleus (LGN) of macaque monkeys (*Macaca mulatta*) on the basis of high-resolution anatomical MRI scans (see Experimental Procedures for details). Figure 1 shows an anatomical MRI image (coronal section) with a typical electrode penetration (Figure 1A), together with a schematic representation of the recording configuration (Figure 1B). Extracellular potentials of both regions display “phasic waves”: brief episodes (ca. 100 ms) of stereotyped waves occurring in isolation or in bouts of several waves (Figure 1C). We first observed that these phasic waves may occur either in only one of the recorded areas – pons or LGN– (Figure 1C, bottom panel), or co-occur in the recording sites of both structures displaying similar time courses (Figure 1C, top panel). In the two cases, phasic waves are observed occurring synchronously over all recording channels located in the same structure, presenting similar electrical characteristics (Figure S1A-B). As a consequence, we use the LFP signal averaged across all recording sites from the same structure in order to detect and study ponto-genicular phasic events.

The general methodology to detect PGO oscillatory events relies on locating peaks in the envelope of the narrow-band-filtered LFP (5-15 Hz) exceeding a threshold proportional to the signal standard deviation (a conservative criterion of 4 SD is used). To study the occurrence and dynamics of coordinated pontine-LGN phasic activity, candidate co-occurring waves were detected across recording structures. To this end, pontine oscillatory events were initially identified as peaks in the envelope of pontine LFP, averaged across recording channels. Co-occurring phasic waves were then defined as peaks in the envelope of the LGN LFP and appearing within a time window of [-0.15, 0.15] s around the occurrence of a pontine oscillatory event (see also Experimental Procedures). These events are henceforth referred to as pontogeniculooccipital (PGO) waves, while non-co-occurring ones (detected only in pons) are referred to as P-waves.

The proportion of PGO waves in relation to the total number of detected pontine events (both P-waves and PGO waves) across experimental sessions was 12.17 ± 5.68 % (mean value with 95% confidence interval, *N*=6 experimental sessions, 2 animals), using the event detection threshold of 4 SD (see Supplemental Information for a study of the effect of the event detection threshold). We quantified the differences between PGO waves and P-waves by comparing their normalized event-triggered spectra. We found that co-occurring pons-LGN phasic waves have greater power over low frequencies (<20 Hz) ($p<10^{-7}$, two-sample permutation KS-test for the comparison of peak spectral power, Figure 1E, normalization was carried out with respect to random surrogate events). This finding likely reflects the fact that PGO waves with larger power are more reliably detected simultaneously in both structures, but it may also imply that pontine events need to recruit a larger underlying neuronal population in order to propagate toward LGN.

We then asked whether the co-occurrence of phasic potentials corresponded to neuronal field activity propagating from pons to LGN. We reasoned that this would be the case for PGO waves, as they have been reported to propagate from the pons to LGN and neocortex in cats (Bizzi and Brooks, 1963; Calvo and Fernandez-Guardiola, 1984; Datta, 1997). In order to address this question, we examined the phase relationship between LGN and pontine signals during the occurrence of PGO waves. Phase lags between LGN and pons were measured from the analytical signal of narrow-band-filtered peri-event LFP (5-15 Hz), across experimental sessions (see Figure 2A for a schema, see also Experimental Procedures). We found a consistent phase lead of pons relative to LGN across recording sites and experimental sessions ($p = 5.7_{x}10^{-59}$, $Z = 125.94$; Rayleigh test; circular mean value with 95% confidence interval 1.057±0.095 radians, Figure 2B). These results support further that our detected phasic events correspond to PGO waves as reported in classical studies (Brooks and Bizzi, 1963; Jouvet, 1962). For the reminder of the manuscript, we enforce the selectivity of our PGO wave detection procedure by restricting our analysis to detected events with phase lag within the 99% circular confidence interval of the mean pons-LGN phase relationship, corresponding to [0.9317 - 1.18026] radians.

Two physiologically distinct PGO wave subtypes in the macaque pontine/LGN LFP. As PGO waves have been reported to occur with variable temporal electrical signatures, we quantified the variability of PGO-wave subtypes present in pontine-LGN recordings of macaque monkeys. Following the methodology presented in Ramirez-Villegas et al. (2015), we used a two-step algorithm in order to jointly cluster co-occurring pontine-LGN waves. Since phasic waves occurred synchronously over all recording channels of either one structure (see Figure S1A), we used as features the peri-event (-0.3 to 0.3 around the event occurrence) time course of LFP signals averaged across the recording channels belonging to each structure in order to summarize the spatio-temporal patterns associated with each single-trial event. We used these time courses to train a growing neural gas (GNG) algorithm (Fritzke, 1995), which creates a custom number of PGO-wave templates, each approximating the trial average of a subset of peri-event PGO waves with similar time courses. The PGO wave templates were then clustered on the basis of their cosine similarity using the Normalized Cuts algorithm during the second step of the methodology (Shi and Malik, 2000). Implementation details of the algorithm can be found in (Ramirez-Villegas et al., 2015) as well as the Experimental Procedures and the Supplemental Information of the present manuscript.

We applied the algorithm to 6 experimental sessions in a session-wise fashion (2 macaque monkeys, and a total of 528 detected PGO waves), and partitioned the data into two clusters. The choice of the number of clusters was based on previous observations that associated periods of SWS- and REM-sleep with PGO waves of distinct densities (i.e. number of contiguous waves) (Chouvet and Gadea-Ciria, 1974; Datta et al., 1992; Morrison and Pompeiano, 1966). We additionally checked whether the data may be further clustered into three clusters, but this led to an additional cluster containing only few members and no additional subtype-specific differences in the analysis presented later in this work. We thus limit this study to the two-cluster case. We found that the first PGO type occurred in greater proportion than the second PGO type (p=0.01 two-sample KS-test, Figure 2C). Figure 2D depicts pons- and LGN-triggered LFP averages of the PGO-wave subtypes. Visual inspection of the time course of type I PGO waves revealed "singlet" PGO waves (PGO waves typically displaying one biphasic wave), while type II PGO waves presented a more oscillatory behaviour, displaying several oscillatory cycles. To asses this observation quantitatively, we quantified the number of half periods of single events across experimental sessions by computing the temporal derivative of the sign of PGO waves filtered below 20 Hz in a time window of [-0.3 0.3] s around the event occurrence, across recording sites. To this end, a half period was counted if its absolute peak amplitude was equal or above 70% of the largest PGO-wave peak. In addition, a criterion of less than 100 ms half-period was enforced. All individual events across experimental sessions were then pooled for population analysis. We found that type I PGO waves are predominantly biphasic, whereas type II PGO waves bear larger variability, typically displaying bouts from 3 to 6 PGO wave half-periods ($p<10^{-20}$ Wilcoxon's ranksum test for the comparison between type I and type II PGO waves; Figure 2E). We assessed the peri-event power distribution across recorded PBn channels in order to investigate whether PGO wave types presented distinct spatial profiles. For such a purpose, we computed the power of the LFP signal in the PGO-frequency band (5-20 Hz) in a peri-event time window of -0.3 to 0.3 s. This analysis revealed that all PGOs follow the same profile at the spatial resolution of our recordings (see Figure S2A, for spatial power distribution in two exemplary experimental sessions). Notably, the greatest power increase is captured by the recording contacts visually classified as PBn, in line with the high-resolution anatomical images. In addition, we provide exemplary raw traces of the two types of PGO waves in Figure S2B, from exemplary experimental sessions (monkey *cm029* and monkey *cm031*). The resulting time courses of each PGO type were in correspondence to that of several previous studies (Brooks, 1968; Jouvet, 1962; Morrison and Bowker, 1975; Nelson et al., 1983).

We next asked whether PGO-wave types differed in their power-spectral profiles. In order to address this question, we computed population complex Morlet-wavelet spectrograms thresholded according to a two-tailed permutation t-test against random, surrogate events ($p<0.05$) (Figure 2F). In line with previous studies, we found that PGO waves show significant power increases over the frequency band 0-20 Hz, displaying maximal spectral power at ca. 10 Hz, corresponding to a 100 ms period. However, analysis of the peri-event power spectral densities revealed no significant differences in power spectral density peak between type I and type II PGO waves (mean values with 95% confidence intervals 10.0319 ± 0.6821 and 9.7395 ± 0.7646, respectively; $p=0.3811$ paired KS-test).

The phase-locking analysis reported in the previous subsection of this manuscript suggests that PGO waves propagate from the pontine region towards LGN (Figure 2A, B) according to the phase shift between the two areas in the PGO-wave frequency band (5-20 Hz). However, a significant field-field relationship may also exist at other frequencies as well. In order to test whether the observed phase entrainment was specific to the PGO frequency band for both PGO types, we studied the pons-LGN

LFP relationship of PGO wave types by standard field-field coherency (FFC) for all frequencies in the range [0-200 Hz] (see also Experimental Procedures). As expected, coherograms revealed a significant increase of absolute coherency in the PGO-wave frequency band (Figure 2G), suggesting a significant entrainment between the two areas during the occurrence of PGO waves. Moreover, amongst PGO wave types, type II PGO waves presented the highest coherence magnitude values, although their difference was deemed non-significant at the population level ($p>0.05$, two-sided Wilcoxon ranksum test). The phase of coherency was also consistent with PLV analysis in both PGO types, displaying a phase lead of pontine peri-event LFP with respect to LGN peri-event LFP (Figure 2G, bottom). We next investigate whether PGO waves differ in their associated circuit activities by analysing band-limited power signals from pontine-LGN recordings.

Neural-event-triggered band-limited power (NET-BLP) signals reveal antagonistic neuronal population signatures of PGO waves. The extracellular signature of PGO waves –like other neural events in the LFP– partly relates to the peri-synaptic activities of the neuronal populations surrounding the electrode tip. PGO waves are associated with single-unit activity exhibiting a large variability (Nelson et al., 1983; Sakai and Jouvet, 1980; Steriade et al., 1990a). The combination of unit activities resulting from the functional organization of PGO-generating circuits can be observed in the multi-unit activity (MUA) band, which accounts for variations in the magnitude of extracellular spike potentials integrated over a large region surrounding the electrode. In addition, active biophysical properties of cells (e.g. active conductances), and afterpotentials associated with somatic and dendritic spikes may affect the extracellular electrical signature of certain types of episodes (Logothetis, 2008), in the MUA as well as in various LFP frequency bands (Buzsaki et al., 1988; Buzsáki, 2002). To investigate the relationship between PGO waves and distinct extracellular field potential sub-bands, we computed PGO-triggered band-limited power (BLP) signals. Raw signals (<7 kHz) were subdivided into several frequency bands on the basis of established neuronal correlates of sleep-like states (Logothetis, 2008). Band definitions were further refined based on observations from previous studies in macaque monkeys (Logothetis, 2015; Logothetis et al., 2012). Specifically, we assessed changes in delta [0.05-3 Hz], theta [3.5-8 Hz], spindle [9-15 Hz], sigma [16-29 Hz], slow and high gamma [30-55 Hz; 56-79 Hz, respectively], ripple [80-200 Hz], high-frequency oscillations [201-324 Hz], a mid-band extracellular field potential (mEFP) band [325-800 Hz] and a MUA band [800-2000 Hz].

To measure neural event-triggered BLP (NET-BLP) responses, the occurrence of each PGO wave was used as a reference (trigger) to align and average the time courses of LFP, HFO and MUA band signals (see Supplemental Materials for full methodological details). We analysed the averaged, Z-scored NET-BLP for each experimental session, across 2 animals (namely, *cm029* and *cm031*) in order to check for consistency of the results. After single-session analysis, all experiments corresponding to each session were pooled for population analysis. Expectedly, our analysis revealed significantly increased activity for all PGO wave types (in both pons and LGN) in the PGO frequency band (theta and spindle bands according to the former definition), with a significant tail expanding over sigma frequencies ($p<0.01$, one-sample permutation t-test, Bonferroni-corrected) (Figure 3A, B). Conversely, high-frequency LFP ranges such as gamma (30-79 Hz) and ripple (80-200 Hz) were not significantly modulated in most cases. Interestingly, NET-BLP signals over frequency ranges beyond LFP were markedly different across PGO-wave types. Whereas type I PGO waves relate to significant decrease of high-frequency LFP (201-324 Hz), mEFP (325-800 Hz) and MUA (801-2000 Hz) activities, type II PGO waves are associated with significant increases over such frequency bands ($p<0.01$, one-sample permutation t-test, Bonferroni-corrected; $p<0.01$, paired-samples permutation t-test for the comparison between type I and type II PGO waves, Bonferroni-corrected; see Experimental Procedures for details in the statistical test) (Figure 3C). Notably, significant modulation associated with type II PGO waves was consistent across pons and LGN for MUA and mEFP. In addition, modulations of MUA associated with type I and type II PGO waves were consistent in pons and LGN. These findings indicate differences in the underlying network dynamics associated with the occurrence of PGO waves. Specifically, these antagonistic responses may be mediated by selective activation or inactivation of distinct PGO wave-related groups of cells (Steriade et al., 1990a), where also pontine GABAergic activity may be prevalent together with increased or decreased tones of cholinergic and aminergic neurons that modulate PGO-triggering neurons (Datta, 1997; see also Torterolo et al., 2011).

Interestingly, these high frequency effects occur at time ranges beyond the duration of the observed phasic PGO activity, several seconds prior to PGO onset, and may thus partly reflect more global tonic dynamical processes (e.g., increases or decreases in cholinergic neuromodulation of pontine circuits). Next, we quantified the lag of these peri-event BLP responses by computing the time lag at which the maximal absolute power deviation from baseline was observed, taking as a reference (zero) the occurrence of the PGO wave. This statistical analysis was performed by evaluating lags in an experiment-wise manner, pooling together all experimental sessions. The result in Figure 3D confirmed that population (MUA and HFO) responses lagged by approximately 2 seconds the occurrence of PGO waves in a large number of experiments, and was significantly negative according to a sign test. Notably, these results were consistent across distinct individual experiments and experimental sessions. As additional evidence, Figure S3 displays the BLP analysis for two exemplary experimental sessions. Note the lagged population responses with respect to the onset of PGO waves are well-preserved.

In addition, we also observed a significant tail of activity lagging before the main PGO-related (9-15) Hz NET-BLP peak at event onset (Figure 3B, indicated by a black arrow). We relate this effect to evidence from previous studies where thalamic spindle activity was interrupted by stimulation-induced PGO waves (Hu et al., 1989). We explored this question by excluding the activity in a time window of [-0.5 0.5] s around the occurrence of PGO waves, and then computing the time lag at which maximal spindle activity (9-15 Hz) is observed across PGO wave subtypes. We reasoned that such analysis would provide information as to whether: first, spindle activity is present before observing PGO waves; second, spindle activity is suppressed; and third, increased MUA activity may be related to spindles, rather than phasic discharges related to PGO waves themselves. We found that, while type I PGO waves presented lags distributed around zero (p=0.5 sign test, -0.035±0.575 seconds, mean with 95% confidence interval; Figure 3E, top panel), type II PGO waves presented negative lags (p=0.004 sign test, -0.69±0.46 seconds, mean with 95% confidence interval; Figure 3E, bottom panel). These results suggest that likely the observed, delayed unit firings that occur before PGO waves may be related to interrupted spindle activity (see also confidence intervals for the lags of MUA and spindle; Figure 3D, E).

As type I and type II PGO waves have been differentially observed during distinct stages of sleep in previous studies, their field activities may be associated with neuronal subpopulations whose activity is prevalent solely during SWS or REM, respectively. These sleep regimes have a concomitant effect on the dynamics of other structures brain-wide such as hippocampus (Datta and MacLean, 2007; Vertes, 1982). Hence, we now investigate the neural correlates of PGO waves over hippocampal circuits.

PGO-wave LFP signatures reveal differentiated interactions with hippocampal neuronal ensemble activity. Some aspects of the electrical activity of the cat dorsal and ventral hippocampus have been related to occurrence of PGO phasic potentials. Phasic potentials of variable amplitude spanning the typical time scale of PGO waves are observed in the hippocampus with increased latency with respect to thalamic and pontine phasic activities. These phasic potentials may result from propagation of pontine activity (Calvo and Fernandez-Guardiola, 1984; Hobson, 1965). However, the relationship of PGO waves to hippocampal dynamics and, in particular, to hippocampal phasic events is largely unknown.

In a second set of experiments, laminar recording electrodes were positioned in the PBn and the CA1 (occasionally CA3) subfield in the anterior hippocampus of macaque monkeys on the basis of high-resolution anatomical MRI scans (see Experimental Procedures for details). Figure 4 illustrates anatomical MRI images (coronal section) with typical electrode penetration in the hippocampal CA3 and the pontine PBn (Figure 4A), together with their corresponding coronal slices in the S-L MRI-histology atlas (Figure 4B). Pontine phasic potentials with similar profiles as those observed previously in pontine/LGN recordings were also apparent in pontine/hippocampus recordings.

Hippocampal sigma, gamma and ripple episodes were also present throughout all recording sessions, displaying visual and quantitative characteristics in correspondence with our previous studies (see also Supplemental Materials and Figure S4) (Logothetis et al., 2012).

To investigate the relationship between PGO waves and hippocampal events we first detected phasic waves from pontine recordings using the approach described earlier in this manuscript (see also Experimental Procedures). Since we do not have LGN recordings in these sessions, whether the detected pontine events correspond to P-waves (not co-occurring with an LGN pair) or PGO waves cannot be directly checked. We thus develop a methodology to predict the occurrence of PGO waves solely from pontine recordings. We addressed this problem using support vector machine (SVM) classifiers.

Classifiers were trained over the first series of 6 pontine-LGN experimental sessions using the time course, spectra and MUA time course (-7 to 7 seconds around event onset) in order to discriminate between P- and PGO-waves. We first tested the prediction accuracy of the classifiers across pontine-LGN (ground-truth) experimental sessions using a leave-one-out procedure (see Figure S5A for a schema of this methodological approach). A bootstrapping procedure was used in order to balance the proportion of P- and PGO-wave event categories in each classification experiment (N=50 bootstraps). Classification accuracy was then evaluated using a 10-fold cross-validation approach in each balanced subsample (thus 500 classification assays).

We first examined the usefulness of the different features (LFP time course, LFP spectra, and MUA time course) for predicting PGO waves (see Supplemental Materials for an in-depth description). Our classification experiments revealed that peri-event time courses and spectra were the most informative features, with chance-level classification performance associated with MUA. Hence we limited our analyses to time-course and spectral features thereafter (see Figure 4C for a simplified schematic of the final methodological approach). We first used linear SVM classifiers in order to compute interpretable weights associated to each time-course and spectral feature in the classification task (see Supplemental Methods). The SVM weights show the relative contribution of each feature for solving the classification task. Figure 4E shows that weight increases in the spectra occur over the PGO frequency range (<20 Hz), but also beyond such a frequency range. Note that power increases around 20 Hz present negative values. This effect can be paired to the fact that PGO waves have more power over circa 5-20 Hz, in line with our previous analysis (Figure 1E). In addition, a low-frequency (<5 Hz) tail is associated with P-waves, as indicated by a positive weight.

While a linear classifier is interpretable, relatively low performance could be achieved with such an approach (ca. 60% cross-validation classification accuracy; see Figure S5D). Using non-linear features may improve the classification accuracy, because they can capture more complex statistical relationships in the data. Thus, after training a non-linear SVM (with a Gaussian kernel), we found that it is possible to improve the prediction performance such that it can be applied to a previously unknown experimental session dataset with an averaged classification accuracy of 70.99±0.02% (mean accuracy value with 95% confidence interval; $p<10^{-4}$ permutation test for the comparison between the session-wise averaged ground-truth performance and the session-wise empirical distribution of chance-level performance) (Figure 4D). A typical display of predicted PGO and P-wave episodes from three independent LFP traces of one exemplary experimental session are illustrated in Figure 4F. Note that both type I and type II PGO waves are identified by the SVM. All classification procedures and related experiments are described to a more detailed extent in the Supplemental Materials of this work.

We then asked whether the PGO waves identified by the classifier were related to distinct types of hippocampal LFP episodes. To this end, hippocampal events were identified as peaks in the envelope of a broad-band LFP in the range 10-180 Hz. Candidate events were clustered on the basis of their spectral signatures (see Experimental Procedures for details). Optimal event separation was obtained with 3 distinct event types in the ranges 5-20 Hz, 30-75 Hz and 80-180 Hz corresponding to sigma, gamma and SWR events, respectively (after Logothetis et al., 2012) (see population results in Figure S4). These hippocampal episodic activities have been associated with mnemonic processes. In particular, SWR complexes are believed to mediate memory transfer and consolidation (Girardeau et al., 2009; Nakashiba et al., 2009). Furthermore, hippocampal gamma rhythms are suggested to dynamically route neural information from parahippocampal structures and CA3 subfield to the CA1 subfield (Colgin et al., 2009). A SWR-related gamma component has been reported to coordinate CA3 and CA1 activities, supporting memory replay (Carr et al., 2012). While gamma and SWR have been extensively documented (for reviews see Buzsáki, 2015; Colgin and Moser, 2010), less is known about hippocampal sigma episodes in primates (Logothetis et al., 2012). These events may occur during periods of paradoxical sleep and may reflect changes in excitability of hippocampal circuits, likely mediated by brainstem activities and thalamo-neocortical circuits (Grosmark et al., 2012; Steriade et al., 1990a).

After identifying hippocampal episodes, we first noticed that episodes classified as PGO waves were correlated with the occurrence of SWR and sigma episodes. We classified the PGO waves into type I and type II as reported in previous subsections of this manuscript, and then we studied the co-occurrence of PGO waves with hippocampal events using cross-correlogram analysis (see Supplemental Methods for methodological details). Clustering of PGO waves was performed in a session-wise manner following the procedures described in the first subsection of the Supporting Information. This procedure was performed for (predicted) PGO data of 9 pons-hippocampus experimental sessions (3 macaque monkeys, namely, *cm029, cm031* and *k13*; and a total of 6544 detected phasic pontine waves, from which 1880 were classified as PGO waves). We first observed that hippocampal sigma and SWR events co-occurred with PGO waves (see Figure 5A for typical raw traces). Type I and type II PGO wave-triggered LFP averages across sessions recorded from the pontine region displayed profiles consistent with that reported earlier in this manuscript (Figure 5B). We found that hippocampal sigma events co-occurred with type II PGO waves at rates higher than that of other hippocampal episodes, while SWR showed an analogous effect with type I PGO waves (Figure 5A for exemplary raw traces). Quantitative analysis of the relationship between these events was performed by computing paired-event conditional intensities. This point-process measure quantifies conditional probability estimates based on the counts of two event types encountered in a time interval and normalised by the rate of the process of reference (occurring at zero lag) (Brillinger, 1976). We found that occurrence of type I PGO waves was significantly correlated with occurrence of SWR episodes, while type II PGO showed an analogous effect with respect to sigma events (Figure 5C). Detailed analysis of the time lag at which sigma occurred in relation to PGO waves revealed that PGO waves and sigma events occur in a synchronous manner, as indicated by a maximal correlation at zero-lag (Figure 5C, top inset). Furthermore, SWR occurred with a delay of 100 ms with respect to PGO waves (Figure 5C, bottom inset). The latter result can be paired to the fact that the time reference for SWR is established by the occurrence of the ripple oscillation, which for ‘classical’ SWR episodes 100 ms before the low-frequency SW deflection. PGO-triggered hippocampus spectra were found in close correspondence with the typical power spectral distribution of sigma and SWR (Figure 5D). In addition, we found that gamma events co-occurring with pontine waves were scarce, even at the reported SVM classification rate (Figure 5B).

Our results show that type I PGO waves are associated with SWR, while type II PGO waves relate to hp-sigma episodes. However, whether PGO waves are associated with specific effects over hippocampal neuronal populations activities is unknown. We hypothesized that PGO-to-hippocampal events coupling may have concomitant increases or decreases in population activity. Thus, in order to further study how PGO waves relate to the activity of hippocampal circuits, we investigated the effect of PGO waves over specific frequency bands of hippocampal extracellular field potential. To this end, we computed PGO wave-triggered BLP analysis. We computed averaged, Z-scored NET-BLP across 9 experimental sessions, over pooled experiments (*n*=103 experiments, 1880 detected PGO waves; 3 animals).

We found again significantly different responses in hippocampus associated with type I and type II PGO responses, as type I PGO episodes correlated with a consistent and significant increase of ripple (80-200 Hz), HFO (201-324 Hz), mEFP (325-800 Hz) and MUA (801-2000 Hz) bands in the hippocampus region (p<0.01, one-sample permutation t-test, Bonferroni-corrected; Figure 6A). Conversely, type II PGO responses were associated with significant power decrease of hippocampal ripple, HFO, mEFP and MUA (see Figure 6A for the time course grand-averages). In particular, note that the activity over high-frequency bands (ripple, mEFP and MUA) is significantly modulated before the event onset. This increase then terminates in an abrupt drop at event onset in the form of a negative deflection, contrary to SWR-associated increases over high-frequency bands. These results suggest that fundamentally different hippocampal population responses may depend upon signatures of brainstem activity. These activities probably herald a much larger chain of interactions at subcortical level (e.g., supramammillary nucleus, posterior hypothalamus and medial septum), possibly triggered by differentiated modulations of pontine circuits. Notably, hippocampal sigma and SWR episodes occur in an anti-correlated manner as suggested by the events' auto- and cross-correlations (Figure S4G). First, auto-correlations indicate that SWR complexes occur in very close temporal proximity concomitant with increases in population activity during putative neocortical (and hippocampal) up-states (see also Ji and Wilson, 2007). Second, the occurrence of sigma and SWR episodes was largely anti-correlated, suggesting that increases in sigma rate occur upon suppression of SWR episodes' rate. We thus hypothesize that SWR and hp-sigma episodes are signatures of distinct and possibly antagonistic brain states.

Since type II PGO waves are paradigmatic activities of REM sleep, their coocurrence with hp-sigma events suggests that sigma activity may in turn also be prevalent during REM sleep in non-human primate, instead of theta activity observed in rodent (see also Karashima et al., 2004). These REM related episodes probably involve changes in the overall level of excitation of hippocampal neuronal ensembles reflected by cell discharge decreases, contrary to periods of waking and SWS in the hippocampus (Grosmark et al., 2012; Montgomery et al., 2008). The above PGO-triggered BLP analysis results confirm a decrease in MUA band activity at type II PGO event onset, following a moderate and slow increase of activity (Figure 6A). We now try to address these hypotheses by investigating the relationship between field activity and unit discharges.

As both SWS- and REM-like field activities are correlated with single- and multi-unit discharges in CA1, we asked whether ripples and hp-sigma activities presented analogous discharge relationships (Montgomery et al., 2008; Sullivan et al., 2014). Using the hippocampal multiunit spiking activity, we computed peri-event time histograms (25-ms bins) for each event type across experimental sessions. Our analysis was limited to the electrode tip with largest averaged ripple- and sigma-band LFP power in stratum pyramidale in a time window of [-0.2 0.2] s around event occurrence. Our analysis revealed a high diversity of peri-event discharges. In agreement with our BLP analysis, at a coarse level (25-ms bins histograms), sigma episodes displayed diminished multi-unit activity with respect to baseline activity with a latency of ~100 ms before the event onset (event centre). Following event occurrence, only a moderate but sharp discharge increase could be noticed (Figure 6B, right panel), possibly reflecting a rebound of neural activity following inhibition. Furthermore, as previously reported in many studies, ripples were related to increased probability of multi-unit discharges, with a rapid (~100 ms) above-baseline increase of spike counts at event onset (Figure 6B, left panel).

Precise peri-event time histogram analysis (1-ms bins) was further performed in order to investigate the phase relationship of peri-event LFP to the firing of participating units during sigma and SWR episodes. For this analysis, raw LFP signals were bandpass-filtered in the hp-sigma (5-20 Hz) and ripple range (80-180 Hz). The location of the largest oscillation trough was set as event onset. Trough-triggered peri-event time histograms showed that unit discharges occur preferentially at the ripple troughs (Figure 6B, left inset), in line with previous studies in macaques and rats (Buzsaki et al., 1992; Ramirez-Villegas et al., 2015). Conversely, during hp-sigma events, unit discharges occur at the rising phase of the oscillation (Figure 6B, right inset). This observation is in striking correspondence with previous studies in rats, recorded during periods of REM sleep (Montgomery et al., 2008; Sullivan et al., 2014). Our findings agree with the notion that firing rate deceleration dominates the hippocampus during REM-associated theta activities (Grosmark et al., 2012; Montgomery et al., 2008). However, in the activity changes reported in this work, oscillatory REM-like activity (here hypothesized to be associated with hp-sigma events) occurs in the form of (transient) neural events separated by desynchronized activity as it has been reported in cats, humans and other monkey studies during awake behaviour (Bennett, 1970; Ekstrom et al., 2005; Jutras et al., 2013; Leonard et al., 2015).

Finally, if the detected locking between PGO episodes and hippocampal ones corresponds to propagating pontine neuronal activity, significant locking would exist between pontine multi-unit spiking activity and hippocampus field activity during PGO waves. In order to investigate this question, peri-event time histogram analysis (2-ms bins) was performed between the bandpass-filtered hippocampal peri-event LFP (5-20 Hz, corresponding to both sharp-wave and hp-sigma ranges) and the firing of pontine units during PGO episodes. We first observed that pontine discharges occurred rhythmically, following the time course of sigma episodes. Furthermore, pontine discharge probability was synchronized to the falling phase of hp-sigma episodes (Figure 6C, right subpanel), establishing a phase lead of approximately 2 radians (~30 ms) with respect to hp-sigma-related hippocampal discharges. Conversely, PGO type I-related multiunit discharges probability increased close to the trough of the SW (Figure 6C, left subpanel), giving rise to a phase lead of approximately 1.2 radians (~20 ms) with respect to sharp wave-related hippocampal discharges. Our findings thus suggest that PGO waves propagate to hippocampus likely through poly-synaptic mechanisms and do not appear correlated to hp-sigma or SWR episodes only as a product of slow mechanisms associated with global neuromodulation, corresponding to distinct putative sleep stages.

Our findings suggest that hippocampal LFP event signatures –likely emerging during distinct brain states and characterized by differentiated pontine field activity– are probably associated with the activity of distinct brain stem neuronal populations (see also Torterolo et al., 2011), and may be implicated in mnemonic processes such as memory transfer and consolidation.

Discussion

In the present study we identified two distinct types of PGO waves on the basis of their electrical LFP signatures, displaying quantitative and qualitative electrophysiological differences over micro- and mesoscopic scales. These two LFP patterns are in close correspondence with findings of classical studies (Bowker, 1985; Datta et al., 1992; Hobson, 1965; Morrison and Pompeiano, 1966). These studies had identified potential functional differences amongst distinct types of PGO episodes. Specifically, whereas PGO waves occurring in isolation were observed to a greater extent during SWS and the transition period between SWS and REM sleep, clustered PGO waves –episodes displaying series of consecutive LFP deflections– were found in fully-developed episodes of REM sleep. The physiological nature of these event types –to the best of our knowledge– had remained unexplored. Adopting the approach originally introduced in our previous work (Ramirez-Villegas et al., 2015), we clustered peri-event PGO-wave spatio-temporal series into two distinct event subtypes, examine their temporal and spectral properties, and finally relate their dynamics with activities over thalamic and limbic structures of the brain (i.e. LGN and hippocampus, respectively).

Our results demonstrate that these two types of PGO activities establish differentiated relationships with downstream forebrain targets. These relationships, together with the notable opposite neuronal population responses associated with PGO-wave subtypes are a strong suggestion of distinct pontine and brain-wide neuronal mechanisms that may be instrumental for mnemonic processes such as memory retrieval and consolidation during natural sleep.

Two physiologically distinct PGO-wave LFP signatures

PGO wave subtypes identified in this work –in correspondence with early studies– differ on the basis of their temporal waveforms. We found PGO waves with a single or up to two contiguous oscillations (type I PGO waves), and PGO waves with multiple (or temporally clustered) contiguous oscillations (type II PGO waves). The observed signatures, while similar in their LFP frequency properties, have different relationships with their associated MUA, are thus likely mediated by distinct neuronal mechanisms that may reflect competing physiological processes during offline states. Indeed, distinct types of PGO waves may relate to the activation of distinct pontine neuronal subgroups. For instance, Steriade et al. (1990a) studied six categories of PGO-related cells in the parabrachial and laterodorsal tegmental cholinergic nuclei with direct thalamic projections. These categories were related in a differentiated manner to pontine and thalamic components of PGO waves, with single or bursts of spikes occurring from 20 to 150 ms prior to these episodes. Notably, cell types presented both phasic and tonic activity modes characterized by the occurrence of spikes during, before, and after the occurrence of PGO waves. These cell groups are responsible not only for transfer of PGO-related potentials upstream, but also for inducing and maintaining episodes of synchronized and desynchronized sleep (Steriade et al., 1990b).

In line with this evidence, we found that type II PGO waves were associated with increased MUA. These activities, however, were relatively slow and presented delays in the order of approximately two seconds before the event onset in both pontine and LGN regions. These delays were further confirmed by clustering techniques applied to the peri-PGO wave MUA traces, and visual examination of unit discharges. We hypothesize that the observed variations in the MUA probably correspond –to a great extent– to neuromodulatory activity reflecting global brain-state transitions or activation of tonic cholinergic elements, rather than being contributed by phasic discharges at the time of occurrence of a PGO wave, such as that of PGO burst cells. We speculate that discharges related to type II PGO waves may be at least partly contributed by parabrachial cholinergic tonic cells. Experimental evidence suggests that parabrachial cholinergic tonic cells (Steriade et al., 1990a) are larger than other cell types (Kang and Kitai, 1990). Moreover, large cells have been found to receive more synaptic drive in a previous structural study of the cat's pedunculopontine nucleus, having higher bouton coverage ratios than small cells (Moriizumi et al., 1989). Notably, these cells are directly implicated in both triggering and maintaining episodes of paradoxical sleep (Steriade et al., 1990b). Thus, it would be reasonable to postulate that our observations reflect slow neuronal activities specifically associated with the occurrence of PGO wave subtypes. In line with this statement, our results suggest that disruption SWS-related activity such as thalamic spindles occurs before type II PGO waves are generated (Hu et al., 1989).

Notably, we discovered that opposite neuronal population signatures in pons and LGN were associated with distinct PGO wave episodes. This variability may be explained by the influence of neuronal subpopulations selectively active during either one type of PGO wave. In this regard, using immunohistochemical techniques, Torterolo et al. (2011) observed a group of cells located in the caudolateral parabrachial region selectively active during SWS. This cell cluster was neither cholinergic, nor (catechol-) aminergic, but circa 50% GABAergic in nature. Notably, the number of SWS-immunoreactive parabrachial cells in their study was positively correlated with the time spent in SWS by the animals. Whether these activities are associated with particular pontine event types remained unknown in their study. Interestingly, our data shows that type I PGO waves are related to significant decrease of MUA. This decrease of activity starts before PGO activity is observed, suggesting that it may be partly an effect of aminergic modulation of pontine circuits, with consequent suppression of cholinergic elements. Whether indeed type I PGO waves –likely suppressed during REM sleep– are partly mediated by GABAergic cell activity in both pons and LGN during SWS remains to be addressed in future investigations. However, the slow reduction in MUA was often accompanied by a rapid (phasic) increase at the time of PGO wave occurrence, suggesting that although the circuit may be suppressed, glutamatergic neurotransmission may be present during the generation and propagation of these potentials (Datta, 1997; see also Torterolo et al., 2011).

PGO-wave LFP signatures relate to differentiated interactions with hippocampal neuronal ensembles.

Part of the present investigation was dedicated to study the relationship between PGO and hippocampal activities. The activity of the hippocampus has been related to offline memory consolidation. It is believed that distinct regulatory processes and phasic (event-related) activities such as SWR complexes and PGO waves, apparent during the expression of both non-REM and REM sleep, partly mediate such processes. One of the key findings of this work is that PGO wave subtypes not only present opposite neuronal population responses as evidenced by increases or decreases of ponto-thalamic MUA, but also they are associated with changes in the hippocampal electrical activity. On the basis of previous studies (Buzsaki et al., 1992; Logothetis et al., 2012; Skaggs et al., 2007; Sullivan et al., 2011), we identified hippocampal sigma, gamma and SWR episodes, as they are key paradigmatic markers of hippocampal off-line activity. Strikingly, we found that type I PGO waves were associated with SWR complexes, whereas type II PGO waves were linked to hippocampal sigma episodes. In both cases, the events followed similar LFP time courses, suggesting large-scale network mechanisms involving pontine nuclei, LGN and hippocampal circuits.

PGO phasic potentials have been related to episodes in the electrical activity of basolateral amygdala, anterior and posterior cingulate gyrus, dorsal hippocampus, anterior ventral thalamic nucleus, and sensory motor cortex in the cat brain (Calvo and Fernandez-Guardiola, 1984; Hobson, 1965). Calvo & Fernandez-Guardiola (1984) observed potentials of variable amplitude spanning the typical time scale of PGO waves in the lateral geniculate body, concomitantly with partner episodes in the aforementioned limbic structures. These PGO-related potentials were increasing in latency with respect to the leading pontine wave, with hippocampus-related potentials occurring with an approximate delay of 35 ms. In line with these observations, we found that type II PGO waves lead hippocampal sigma events for approximately 30 ms, taking an PGO wave center-frequency of 10 Hz (as demonstrated by detailed spectral analysis). These observations are in line with the fact that type II PGO waves are coupled with eye movement-related potentials (Morrison and Pompeiano, 1966), which was the population of PGO episodes analysed in the work of Calvo & Fernandez-Guardiola (1984).

Conversely, the underlying nature of type I PGO activity remains unknown. However, evidence from lesion and pharmacological studies has related PGO potentials to at least two differentiated inputs impinging upon thalamic nuclei during sleep. One of these inputs is thought to be extravestibular –

probably originated in reticular nuclei– and responsible for the modulatory effects upon LGN and possibly hippocampus associated with type I PGO waves. Vestibular nuclei, in turn, influence the activity of LGN neurons during the occurrence of bursts of REM that are related to type II PGO activity. Indeed, inactivation of vestibular nuclei abolishes bursts of REM and type II PGO wave activity, while facilitating type I PGO wave activity with consequent reduction of desynchronized sleep periods (Morrison and Pompeiano, 1966). Conversely, pharmacological manipulations upon PGO-generating circuits via carbachol enhance the activity of cholinergic and PGO burst cells. This evidence indicates that REM and associated PGO (type II) activity are specifically mediated by endogenous release of acetylcholine (Datta et al., 1992, 1998). Altogether, in line with our results, these findings suggest that PGO waves of distinct types, while having a common origin, may have distinct physiological nature, propagating across distinct pathways in a sleep state-dependent manner.

In all likelihood, the transient coupling between hippocampus and pontine-LGN assembly activities over PGO frequencies suggests that PGO waves are ubiquitous over distinct brain domains, and may establish signatures for selective communication between brainstem, thalamic, limbic and neocortical structures. The functional purpose of these signatures, however, remains elusive from the current data, and opens a number of additional questions. First, are hippocampal sigma-episodes present during different brain states as compared to most SWR complexes? Our data and analyses provide only indirect evidence to this question, since hippocampal ripples and sigma events occur in an anti-correlated manner. This result demonstrates that SWR and sigma episodes at least occur over distinct time scales. Furthermore, beyond the inherent limitations of anaesthesia (see also last subsection of the Discussion), our observations of hippocampal activity and time scales of appearance of sigma and SWR may support the idea of two global states: an SWS-like state characterized by oscillatory unit activity spanning the occurrence of multiple putative neocortical and hippocampal up- and down-state transitions (Ji and Wilson, 2007); and a REM-like state, characterized by more desynchronized hippocampal unit and LFP activity (Moroni et al., 2007; Tamura et al., 2013), where sigma (theta-like) episodes are prevalent (Logothetis et al., 2012). These hypotheses accord with vast experimental evidence relating type I PGO wave activity with periods of synchronized sleep, and type II PGO wave activity with fully developed episodes of paradoxical sleep (Bowker, 1985; Datta et al., 1992; Hobson, 1965; Morrison and Pompeiano, 1966; Steriade et al., 1990b).

The hypothesis that antagonistic neural events relate to distinct information routing pathways or signatures of brain-wide communication during offline states was supported by the concurrent electrophysiology-fMRI study of Logothetis et al. (2012). In particular, hippocampal SWR episodes were associated with down-regulation of large portions of subcortex, including both pontine and thalamic nuclei. Additional metabolic down-regulation was detected in occipital V1, despite the overall increase of activity of other primary and associative neocortical areas. Yet, the authors speculated on the possibility of a selective suppression of the REM-sleep-related ponto-geniculo-occipital pathway during SWR episodes occurring during SWS. Our results support this hypothesis, we suggest that this suppression during SWR and type I PGO waves might be caused by a suppression of brainstem cholinergic elements. The activation of these elements, in turn, probably reflects type II PGO waves in a REM sleep-like state, characterized by concomitant lower hippocampal LFP amplitude. As discussed earlier, this hypothesis is in line with the fact that pontine cholinergic neurons are associated with disruption of SWS-related thalamo-cortical oscillations and disinhibition from RT GABAergic neurons of thalamocortical neurons related to periods of synchronized sleep.

Limitations of this study.

One of the key limitations of this study is the use of opioid anaesthesia in order to induce sleep-like states in macaque monkeys. While discussion about the effects of anaesthesia on potential mechanisms related to cognition is perfectly justified, we argue that our anaesthesia protocol had no influence whatsoever in neither in spontaneous, nor in sensory-evoked neuronal activity. This fact has been particularly demonstrated in our previous research (Logothetis et al., 2012; Ramirez-Villegas et al., 2015) in which neuronal activities associated with hippocampal circuits (in particular, those associated with SWS), and brain-wide metabolic regulations remained virtually unaffected by the anaesthetics. In a similar line, experimental evidence suggests that opioid anaesthesia (remifentanil) does not affect acetylcholine release in the pontine region of cats (Mortazavi et al., 1999). In consequence, our findings establish a link between PGO-related potentials in sleep-like conditions and potentials observed during multiple stages of natural, drug-free sleep. However, beyond the results reported in this work, we were unable to track LFP signatures corresponding to different “true” sleep stages. Although anaesthesia levels remain stable throughout the recording sessions as evident in the multi-structure electrical activity (see also Ramirez-Villegas et al., 2015), we had no access to ground-truth markers from naturalistic SWS or REM episodes, in order to classify distinct putative sleep stages in the current anaesthetized model.

Experimental Procedures

Surgical procedures and electrophysiology recordings

fMRI and electrophysiological data were collected from three healthy macaque monkeys (*Macaca fascicularis*: two females; *Macaca mulatta*: one female; 4-6 kg). All experimental and surgical procedures were approved by the local authorities (Regierungspräsidium, Tübingen, Germany) and were in full compliance with the guidelines of the European Community (EUVD 86/609/EEC) for the care and use of laboratory animals. Details of the surgical procedures and experimental preparation can be found elsewhere (Logothetis et al., 2012). In specific, two custom-made recording chambers were implanted directly on to the skull of each animal under general anesthesia (balanced anesthesia consisting of isoflurane 1.3% and remifentanil 0.2-0.5 µg/kg/min iv). The angles of the chamber were designed to minimize the penetration of blood vessels in deep structures, by combining individual skull surface, brain and blood vessels extracted from structural MRI and MR angiography volumes.

The experiments were conducted under general anesthesia maintained with remifentanil (1-3 µg/kg/min iv) in combination with a fast-acting paralytic (mivacurium chloride, 5-7 mg/kg/hr iv). The physiological state of the animal was monitored continuously and maintained tightly in normal limits. Acidosis was prevented by the administration of lactated Ringer's solution with 2.5% glucose, infused at 10 ml/kg/hr.

Concurrent electrophysiological and functional MRI (fMRI) recordings were made following our previous work (Logothetis et al., 2012). We made measurements in a vertical 4.7 T scanner with a 40 cm diameter bore (BioSpec 47/40v, Bruker BioSpin, Ettlingen, Germany). A customized quadrature volume radiofrequency coil was used for imaging of deep brain structures. Typically, 22 axial slices were acquired, covering the entire brain. BOLD activity from these slices was acquired at a temporal resolution of 2 s with two-shot gradient-echo EPI images (repetition time = 1000 ms, echo time = (20) ms, bandwidth = (150) kHz, flip angle = (60) degrees, FOV = 96 x 96 mm, 2 mm slice thickness). T2-weighted RARE images with the same FOV were obtained using a matrix of 256x256, rare factor of 8, effective TE of 60 ms, TR of 8500 ms, BW 38 kHz, and 2-4 averages. The anatomical images were later morphed to match with EPI images, and then the morphed images were used to draw regions of interest (ROIs). In order to avoid different image intensities in functional scans, each voxel in the scan was normalized by dividing by the mean value of all voxels above an intensity threshold and multiplied by a user value of 1000.

Custom-made multichannel electrodes (10 contacting sites spaced by 150-250 µm, after Logothetis et al., 2012) were placed in or close to the parabrachial nucleus (PBn; occasionally in the reticular pontine nuclei, PnO), in the hippocampus (CA1 or CA3 subfields) and/or in the lateral geniculate nucleus (LGN), on the basis of high-resolution anatomical MRI scans. A total of 6 experimental sessions were paired pons-LGN recordings (animals *cm029* and *cm031*), while 9 experimental sessions were pons-hippocampus ones (animals cm029, cm031 and k13). A detailed description of the recording and procedures for compensating MRI-gradient interference can be found elsewhere (Logothetis et al. 2012).

Processing and analysis of neural data

Analyses of electrophysiology and fMRI data were performed using MATLAB (The MathWorks). Signal denoising and frequency band isolation procedures have been described in detail in a previous study (Logothetis et al., 2012). In the following, we describe the main signal processing and analysis performed on the denoised broad-band LFP signals (0.05 Hz – 7 kHz).

For PGO event detection, we examined changes of power in the band-pass filtered, averaged LFP signal (5-15 Hz) of recording electrodes that targeted the pontine region (including the peribrachial nucleus) and the lateral geniculate nucleus (LGN), respectively. Recordings of the two structures were analyzed jointly. To this end, the filtered signals were rectified, low-pass filtered at 20 Hz, and then z-score normalized. Initially, pontine waves were detected as epochs during which the resulting signal exceeded a 4 SD threshold. These events were considered candidate PGO waves. Since PGO waves are phasic potentials that must occur synchronously in pons, LGN and several other brain domains (Calvo and Fernandez-Guardiola, 1984), only significant power increases that occurred in both structures within a time window of [-0.15 0.15] s taking the pontine region as a reference were selected for further analysis.

Clustering of PGO waves/MUA time series. PGO waves may occur in isolation or in very close temporal proximity (clustered PGO waves), displaying between 3 and 6 consecutive LFP deflections (Morrison & Pompeiano, 1966; Datta et al., 1992). In order to prevent multiple detections, detected events within 300 ms were considered a single event. Upon event selection (phasic waves propagating from pons to LGN), perievent PGO waves were clustered according to their temporal electrical signatures using a two-stage methodology reported in a previous study of our laboratory (Ramirez-Villegas et al., 2015). Briefly, in the first stage, spatio-temporal PGO waves (of a selected LGN and pons site) were aligned and then grouped into 100 to 200 representative signals using a growing neural gas (GNG) algorithm (Fritzke, 1995). The GNG generates noise-reduced signal templates corresponding to the averaged time course of PGO waves that have similar time courses. In the second stage, the representative signals were clustered based on their pair-wise cosine similarity using the normalized cuts algorithm, a clustering technique that creates partitions on the data by maximizing the ratio of summed intra-cluster similarity to summed inter-cluster similarity (Shi and Malik, 2000). Each PGO-wave dataset was partitioned on the basis of clustering quality analysis (after Ramirez-Villegas et al., 2015) and also based on findings of classical studies (Datta et al., 1992; Morrison and Pompeiano, 1966). For the two previous cases, PGO waves were then sorted according to their MUA-responses, and then averaged across experimental sessions.

Detection of hippocampal events. Following a methodology presented in Logothetis et al. (2012), we examined changes of power in the broad-band signal (10 – 180 Hz). The broad-band signal was rectified, low-pass filtered at 20 Hz and then normalized. Candidate events were detected as epochs during which the signal exceeded a 3.5 SD threshold. Since initially increases in power may result from oscillations occurring in different frequency bands, we clustered the spectra using a Non-

Negative Matrix Factorization (NNMF) algorithm, an unsupervised technique that creates data decompositions for a user-defined number of groups or clusters. In correspondence with our previous studies, stable representation of the data was achieved by a partition in three clusters, corresponding to increases over different frequency bands, namely sigma (8-22 Hz), gamma (25-75 Hz) and ripple (80-180 Hz). These three event types were taken for further analysis without further pre-processing.

Phase relationship between LGN and pontine region. Phase relationships between recording sites were retrieved by computing the angle of the Hilbert-transformed LGN/pontine PGO wave-band-filtered (5-20 Hz) signal pairs for single experimental sessions, in the range $\left[-\pi,\pi\right]$. The phase-locking value (PLV) was subsequently computed as: $\Gamma_{nm} = \frac{1}{N}\sum_{t=1}^{N}\left[\exp\left(i\,\Delta\varphi_{nm}^{t}\right)\right]$, where N is the number of time samples, and $\Delta\varphi_{nm}^{t} = \varphi_{n}^{t} - \varphi_{m}^{t}$ accounts for the difference between the phase estimates of the signal corresponding to the recording site n and m, respectively. Circular averages were computed across paired LGN-pontine recording channels. Histograms and event grand-averages were computed from the resulting single PLV for each PGO wave.

Spectral analysis and field-field coherence (FFC). Spectral analysis was conducted using Morlet-wavelet spectrograms. The spectrograms were Z-scored with respect to spectrograms obtained from the same number of events with randomized inter-event intervals.

FFC was computed for all pairs of recording sites located in the LGN and pontine region, across all PGO-wave broad-band signal events using a tapering window duration of 200 ms with an increment of 10 ms, using the Chronux toolbox available at http://chronux.org. This process outputs a complex-valued matrix F x n x m x M, where F is the number of frequencies in the broad-band (usually 0-200 Hz), n is the number of time windows, m is the total number of LGN-pontine recording pairs and M is the total number of PGO waves. Complex-numbered coefficients of this matrix account for the entrainment between the LFP recorded in one spatial location and the LFP recorded at a second spatial location, at particular frequency and time points. Taking LGN recordings as a reference, FFC was applied to pair-wise recording LFP channels across pontine region and LGN. Coherency maps were then averaged across all couples, resulting in a three-dimensional matrix F x n x M. FFCs with the same cluster label were averaged, resulting in two F x n matrices. The resulting matrices were then analysed in magnitude (absolute value in the range [0, 1]) and phase (in the range $\left[-\pi,\pi\right]$). Finally, quantification of phase lags (and phase histograms) was done as an event-wise phase circular average below 20 Hz in a time window of 400 ms around the occurrence of a detected (or SVM-predicted) PGO episode.

Point-process conditional intensity. In order to compute the conditional intensities related to the occurrence of events, we consider the time stamps of PGO and hippocampal events stationary point processes. Then, we compute histogram-type estimates of the auto- and cross-correlation functions of the (bivariate) point processes corresponding to paired event types. Specifically, suppose that the process $\{N_1(t), N_2(t)\}$ is given by the events that occur in the interval $(0, T]$. For the times of events of type $S = \{\tau_1, \tau_2, ..., \tau_n\}$ and the times of events of type $K = \{t_1, t_2, ..., t_m\}$, the conditional probability estimates are based on the counts of events *S* and *K* that belong to the following set:

$$W_{SK}\left(u\right) = \left\{\left(j,k\right) \middle| u - \beta < s_j - t_k < u + \beta\right\} \quad \forall\, s_j \neq t_k, \qquad (1)$$

$$J_{SK}\left(u\right) = \sum_{j,k} \begin{cases} 1 & (j,k) \in W_{SK}(u) \\ 0 & otherwise \end{cases}, \qquad (2)$$

Hence, J_{SK} are the counts of number of events of type *S* within a cell of size 2β (i.e. the histogram bin size, with *u* being the center of the bin). From this count variable, we get the following probability estimate:

$$p_{SK}\left(u\right) = {J_{SK}(u)}\big/{\left[2\beta N_K(T)\right]}, \qquad (3)$$

To correct for border effects, the following modified estimate is proposed (Brillinger, 1976):

$$p_{SK}'\left(u\right) = p_{SK}\left(u\right) + {|u|\, N_S(T)}\big/{T^2}, \qquad (4)$$

A detailed account on the statistical testing procedure is reported in Supplemental Information, Section A of this manuscript.

Band-limited power (BLP) signals. MRI-denoised, raw broad-band (<7 kHz) multi-site signals were decomposed into various frequency ranges. Band separation and BLP signal calculations were performed following a two-step methodology. First, raw signals were filtered into a low- and a high-frequency range (<500 Hz, LFR; >100 Hz, HFR) by low- and high-pass 4th-order Butterworth finite impulse response (FIR) filtering, respectively. Second, BLP signals were extracted from LFP using a Kaiser-window filter with a transition band of 1 Hz, a stop-band attenuation of -60 dB and a pass-band ripple of 0.01 dB. MUA signals were derived using 4th-order Butterworth FIR filters. For all frequency bands, resulting signals were rectified, low-pass filtered at 4 Hz, and resampled at 660 Hz. Each BLP signal was tested for significance using a two-tailed permutation t-test (Blair and Karniski, 1993), the outcome of this test was then Bonferroni-corrected across all frequency bands.

Frequency bands in this study were determined from EEG studies and were refined on the basis of recent observations in intracortical recordings in macaques (Elul, 1972; Logothetis, 2008; Logothetis et al., 2012). Specifically, we assessed changes in delta [0.05-3 Hz], theta [3.5-8 Hz], spindle [9-15 Hz], sigma [16-29 Hz], slow and high gamma [30-55 Hz; 56-79 Hz, respectively], ripple [80-200 Hz], high-frequency oscillations [201-324 Hz]. Finally, high frequencies were subdivided into a mid-band extracellular field potential (mEFP) band [325-800 Hz] and a MUA band [801-2000 Hz].

References

Aston-Jones, G., and Bloom, F.E. (1981). Activity of norepinephrine-containing locus coeruleus neurons in behaving rats anticipates fluctuations in the sleep-waking cycle. J. Neurosci. *1*, 876–886.

Bennett, T.L. (1970). Hippocampal EEG correlates of behavior. Electroencephalogr. Clin. Neurophysiol. *28*, 17–23.

Bizzi, E., and Brooks, D.C. (1963). Pontine reticular formation: relation to lateral geniculate nucleus during deep sleep. Science *141*, 270–272.

Blair, R.C., and Karniski, W. (1993). An alternative method for significance testing of waveform difference potentials. Psychophysiology *30*, 518–524.

Bowker, R.M. (1985). Variability in the characteristics of pontogeniculooccipital spikes during paradoxical sleep. Exp. Neurol. *87*, 212–224.

Brillinger, D.R. (1976). Estimation of the second-order intensities of a bivariate stationary point process. J. R. Stat. Soc. Ser. B Methodol. 60–66.

Brooks, D.C. (1968). Waves associated with eye movement in the awake and sleeping cat. Electroencephalogr. Clin. Neurophysiol. *24*, 532–541.

Brooks, D.C., and Bizzi, E. (1963). Brain stem electrical activity during deep sleep. Arch. Ital. Biol. *101*, 648–665.

Buzsáki, G. (2002). Theta oscillations in the hippocampus. Neuron *33*, 325–340.

Buzsáki, G. (2015). Hippocampal sharp wave-ripple: A cognitive biomarker for episodic memory and planning: Hippocampal sharp wave-ripple. Hippocampus *25*, 1073–1188.

Buzsaki, G., Horvath, Z., Urioste, R., Hetke, J., and Wise, K. (1992). High-frequency network oscillation in the hippocampus. Science *256*, 1025–1027.

Buzsaki, G.Y., Bickford, R.G., Ponomareff, G., Thal, L.J., Mandel, R., and Gage, F.H. (1988). Nucleus basalis and thalamic control of neocortical activity in the freely moving rat. J. Neurosci. *8*, 4007–4026.

Calvo, J.M., and Fernandez-Guardiola, A. (1984). Phasic activity of the basolateral amygdala, cingulate gyrus, and hippocampus during REM sleep in the cat. Sleep *7*, 202–210.

Carr, M.F., Karlsson, M.P., and Frank, L.M. (2012). Transient Slow Gamma Synchrony Underlies Hippocampal Memory Replay. Neuron *75*, 700–713.

Chouvet, G., and Gadea-Ciria, M. (1974). Analyse sequentielle de l'activite PGO chez le chat. Electroencephalogr. Clin. Neurophysiol. *36*, 597–607.

Cohen, B., and Feldman, M. (1968). Relationship of electrical activity in pontine reticular formation and lateral geniculate body to rapid eye movements. J. Neurophysiol. *31*, 806–817.

Colgin, L.L., and Moser, E.I. (2010). Gamma Oscillations in the Hippocampus. Physiology *25*, 319–329.

Colgin, L.L., Denninger, T., Fyhn, M., Hafting, T., Bonnevie, T., Jensen, O., Moser, M.-B., and Moser, E.I. (2009). Frequency of gamma oscillations routes flow of information in the hippocampus. Nature *462*, 353–357.

Datta, S. (1997). Cellular Basis of Pontine Ponto-geniculo-occipital Wave Generation and Modulation. Cell. Mol. Neurobiol. *17*, 341–365.

Datta, S., and MacLean, R.R. (2007). Neurobiological mechanisms for the regulation of mammalian sleep–wake behavior: Reinterpretation of historical evidence and inclusion of contemporary cellular and molecular evidence. Neurosci. Biobehav. Rev. *31*, 775–824.

Datta, S., Calvo, J.M., Quattrochi, J.J., and Hobson, J.A. (1992). Cholinergic microstimulation of the peribrachial nucleus in the cat. I. Immediate and prolonged increases in ponto-geniculo-occipital waves. Arch. Ital. Biol. *130*, 263–284.

Datta, S., Siwek, D.F., Patterson, E.H., and Cipolloni, P.B. (1998). Localization of pontine PGO wave generation sites and their anatomical projections in the rat. Synapse *30*, 409–423.

Ekstrom, A.D., Caplan, J.B., Ho, E., Shattuck, K., Fried, I., and Kahana, M.J. (2005). Human hippocampal theta activity during virtual navigation. Hippocampus *15*, 881–889.

Elul, R. (1972). The Genesis of the Eeg. In International Review of Neurobiology, Carl C. Pfeiffer and John R. Smythies, ed. (Academic Press), pp. 227–272.

Feldman, M., and Cohen, B. (1968). Electrical activity in the lateral geniculate body of the alert monkey associated with eye movements. J. Neurophysiol. *31*, 455–466.

Fritzke, B. (1995). A growing neural gas network learns topologies. Adv. Neural Inf. Process. Syst. *7*, 625–632.

Girardeau, G., Benchenane, K., Wiener, S.I., Buzsaki, G., and Zugaro, M.B. (2009). Selective suppression of hippocampal ripples impairs spatial memory. Nat Neurosci *12*, 1222–1223.

Grosmark, A.D., Mizuseki, K., Pastalkova, E., Diba, K., and Buzsáki, G. (2012). REM Sleep Reorganizes Hippocampal Excitability. Neuron *75*, 1001–1007.

Hobson, J.A. (1965). The effects of chronic brain-stem lesions on cortical and muscular activity during sleep and waking in the cat. Electroencephalogr. Clin. Neurophysiol. *19*, 41–62.

Hobson, J.A. (2010). REM sleep and dreaming: towards a theory of protoconsciousness. Nat. Rev. Neurosci.

Hobson, J., McCarley, R., and Wyzinski, P. (1975). Sleep cycle oscillation: reciprocal discharge by two brainstem neuronal groups. Science *189*, 55–58.

Hu, B., Steriade, M., and Descheˆnes, M. (1989). The cellular mechanism of thalamic ponto-geniculo-occipital waves. Neuroscience *31*, 25–35.

Ji, D., and Wilson, M.A. (2007). Coordinated memory replay in the visual cortex and hippocampus during sleep. Nat. Neurosci. *10*, 100–107.

Jouvet, M. (1962). Recherches sur les structures nerveuses et les mecanismes responsables des differentes phases du sommeil physiologique. Arch. Ital. Biol. *100*, 125–206.

Jutras, M.J., Fries, P., and Buffalo, E.A. (2013). Oscillatory activity in the monkey hippocampus during visual exploration and memory formation. Proc. Natl. Acad. Sci. *110*, 13144–13149.

Kang, Y., and Kitai, S.T. (1990). Electrophysiological properties of pedunculopontine neurons and their postsynaptic responses following stimulation of substantia nigra reticulata. Brain Res. *535*, 79–95.

Karashima, A., Nakao, M., Honda, K., Iwasaki, N., Katayama, N., and Yamamoto, M. (2004). Theta wave amplitude and frequency are differentially correlated with pontine waves and rapid eye movements during REM sleep in rats. Neurosci. Res. *50*, 283–289.

Kemp, I.R., and Kaada, B.R. (1975). The relation of hippocampal theta activity to arousal, attentive behaviour and somato-motor movements in unrestrained cats. Brain Res. *95*, 323–342.

Leonard, T.K., Mikkila, J.M., Eskandar, E.N., Gerrard, J.L., Kaping, D., Patel, S.R., Womelsdorf, T., and Hoffman, K.L. (2015). Sharp Wave Ripples during Visual Exploration in the Primate Hippocampus. J. Neurosci. *35*, 14771–14782.

Logothetis, N.K. (2008). What we can do and what we cannot do with fMRI. Nature *453*, 869–878.

Logothetis, N.K. (2015). Neural-Event-Triggered fMRI of large-scale neural networks. Curr. Opin. Neurobiol. *31*, 214–222.

Logothetis, N.K., Eschenko, O., Murayama, Y., Augath, M., Steudel, T., Evrard, H.C., Besserve, M., and Oeltermann, A. (2012). Hippocampal–cortical interaction during periods of subcortical silence. Nature *491*, 547–553.

Lydic, R., McCarley, R.W., and Hobson, J.A. (1983). The time-course of dorsal raphe discharge, PGO waves, and muscle tone averaged across multiple sleep cycles. Brain Res. *274*, 365–370.

Maru, E., Takahashi, L.K., and Iwahara, S. (1979). Effects of median raphe nucleus lesions on hippocampal EEG in the freely moving rat. Brain Res. *163*, 223–234.

McCarley, R.W., Winkelman, J.W., and Duffy, F.H. (1983). Human cerebral potentials associated with REM sleep rapid eye movements: links to PGO waves and waking potentials. Brain Res. *274*, 359–364.

McGinty, D.J., and Harper, R.M. (1976). Dorsal raphe neurons: depression of firing during sleep in cats. Brain Res. *101*, 569–575.

Montgomery, S.M., Sirota, A., and Buzsaki, G. (2008). Theta and Gamma Coordination of Hippocampal Networks during Waking and Rapid Eye Movement Sleep. J. Neurosci. *28*, 6731–6741.

Moriizumi, T., Nakamura, Y., Tokuno, H., Kudo, M., and Kitao, Y. (1989). Synaptic organization of the pedunculopontine tegmental nucleus of the cat. Brain Res. *478*, 315–325.

Moroni, F., Nobili, L., Curcio, G., De Carli, F., Fratello, F., Marzano, C., De Gennaro, L., Ferrillo, F., Cossu, M., Francione, S., et al. (2007). Sleep in the Human Hippocampus: A Stereo-EEG Study. PLoS ONE *2*, e867.

Morrison, A.R., and Bowker, R.M. (1975). The biological significance of PGO spikes in the sleeping cat. Acta Neurobiol Exp *35*, 821–840.

Morrison, A.R., and Pompeiano, O. (1966). Vestibular influences during sleep. Functional relations between vestibular nuclei and lateral geniculate nucleus during desynchronized sleep. Arch. Ital. Biol. *104*, 425–458.

Mortazavi, S., MD, Thompson, J., BS, Baghdoyan, H.A., PhD, and Lydic, R., PhD (1999). Fentanyl and Morphine, but not Remifentanil, Inhibit Acetylcholine Release in Pontine Regions Modulating Arousal. Anesthesiology *90*, 1070–1077.

Nakashiba, T., Buhl, D.L., McHugh, T.J., and Tonegawa, S. (2009). Hippocampal CA3 output is crucial for ripple-associated reactivation and consolidation of memory. Neuron *62*, 781–787.

Nelson, J.P., McCarley, R.W., and Hobson, J.A. (1983). REM sleep burst neurons, PGO waves, and eye movement information. J. Neurophysiol. *50*, 784–797.

Ramirez-Villegas, J.F., Logothetis, N.K., and Besserve, M. (2015). Diversity of sharp-wave–ripple LFP signatures reveals differentiated brain-wide dynamical events. Proc. Natl. Acad. Sci. *112*, E6379–E6387.

Reiner, P.B., and Morrison, A.R. (1980). Pontine-geniculate-occipital spikes in the albino rat: Evidence for the presence of the pontine component as revealed by cerebellar lesions. Exp. Neurol. *69*, 61–73.

Sakai, K., and Jouvet, M. (1980). Brain stem PGO-on cells projecting directly to the cat dorsal lateral geniculate nucleus. Brain Res. *194*, 500–505.

Shi, J., and Malik, J. (2000). Normalized cuts and image segmentation. Pattern Anal. Mach. Intell. IEEE Trans. On *22*, 888–905.

Sirota, A., and Buzsáki, G. (2005). Interaction between neocortical and hippocampal networks via slow oscillations. Thalamus Relat. Syst. *3*, 245–259.

Skaggs, W.E., McNaughton, B.L., Permenter, M., Archibeque, M., Vogt, J., Amaral, D.G., and Barnes, C.A. (2007). EEG sharp waves and sparse ensemble unit activity in the macaque hippocampus. J. Neurophysiol. *98*, 898–910.

Steriade, M., Pare, D., Datta, S., Oakson, G., and Dossi, R.C. (1990a). Different cellular types in mesopontine cholinergic nuclei related to ponto-geniculo-occipital waves. J. Neurosci. *10*, 2560–2579.

Steriade, M., Datta, S., Pare, D., Oakson, G., and Dossi, R.C. (1990b). Neuronal activities in brain-stem cholinergic nuclei related to tonic activation processes in thalamocortical systems. J. Neurosci. *10*, 2541–2559.

Sullivan, D., Csicsvari, J., Mizuseki, K., Montgomery, S., Diba, K., and Buzsaki, G. (2011). Relationships between hippocampal sharp waves, ripples, and fast gamma oscillation: influence of dentate and entorhinal cortical activity. J. Neurosci. *31*, 8605–8616.

Sullivan, D., Mizuseki, K., Sorgi, A., and Buzsaki, G. (2014). Comparison of Sleep Spindles and Theta Oscillations in the Hippocampus. J. Neurosci. *34*, 662–674.

Tamura, R., Nishida, H., Eifuku, S., Fushiki, H., Watanabe, Y., and Uchiyama, K. (2013). Sleep-Stage Correlates of Hippocampal Electroencephalogram in Primates. PLoS ONE *8*, e82994.

Torterolo, P., Sampogna, S., and Chase, M.H. (2011). A restricted parabrachial pontine region is active during non-rapid eye movement sleep. Neuroscience *190*, 184–193.

Vanderwolf, C.H. (1969). Hippocampal electrical activity and voluntary movement in the rat. Electroencephalogr. Clin. Neurophysiol. *26*, 407–418.

Vertes, R.P. (1982). Brain stem generation of the hippocampal EEG. Prog. Neurobiol. *19*, 159–186.

Vuillon-Cacciuttolo, G., and Seri, B. (1978). Effets de la section des nerfs optiques chez le babouin sur l’activite a type de pointes genouillees et corticales au cours des divers etats de vigilance. Electroencephalogr. Clin. Neurophysiol. *44*, 754–768.

Figure Legends

Figure 1. Electrode position, pontine-LGN recordings and co-occurrence of phasic waves in pons and LGN of the macaque monkey. (A) T2-weighted (RARE) MRI scan showing the electrode position a coronal (left and right panels, fragment) and sagittal (middle panel) slice of monkey *cm031*. (B) MRI images were superimposed on the Saleem-Logothetis (S-L) MRI-histology atlas of the Rhesus Monkey brain. The approximate location of the recording electrodes is indicated by a red cross for pons and by a red arrow for LGN. Typically the electrode targeted the pons in or around the parabrachial nucleus (PBn). (C) Raw multi-site averaged LFP traces (0.5-325 Hz). Labels indicate the area targeted by the electrode: 'LGN' for lateral geniculate nucleus, 'PO' for pontine region. Phasic potentials in either pons or LGN may occur in isolation (bottom panel, red dots), or co-occur in the two areas (top panel, green dot and dashed line). (D) Number of co-occurring pontine-LGN phasic waves over total detected pontine waves across experimental sessions. (E) Averaged, z-scored multi-taper spectra illustrating the power spectral distribution of co-occurring and non-co-occurring pontine phasic waves. Related to Figure S1.

Figure 2. Pontine-LGN phase relationship and classification of PGO waves across 6 experimental sessions. (A) Schematic diagram illustrating the phase-locking calculation between the recorded structures (pons and LGN). An exemplary time-resolved PLV map is provided to show that phasic potentials propagate from pons toward LGN, thus corresponding to PGO waves (bottom panel, negative LGN-pons phase-shift). (B) Empirical distribution of pontine-LGN phase lags during PGO waves. The average phase corresponds to a time lag of ca. 16 ms. (C) Box plots illustrating the statistics of the number of PGO waves over total detected pontine waves across experimental sessions, and two identified types of PGO waves. On each box, the top and bottom are the 25th and 75th percentiles of the samples, respectively; the red dot in the middle of each box is the sample median; the dashed lines are drawn from the ends of the interquartile ranges (25th and 75th percentiles) to the extreme points. (D) Grand averages of PGO-wave LFP signatures across pontine (top panel) and LGN (bottom panel) peri-event field potentials (recording tips of either one area were first averaged for each experimental session). The centre of each PGO wave is marked by dashed lines. Shaded areas indicate standard error of the mean (SEM). (E) Proportion of half-period statistics of individual type I and type II PGO waves across experimental sessions. The two population statistics differ significantly ($p<10^{-20}$) according to a Wilcoxon's ranksum test. (F) Complex Morlet-wavelet spectrograms in correspondence with each PGO wave subtype and recorded area (pons top row; LGN bottom row as in D). Averages are first computed across all pons/LGN recording sites. Thresholding was applied according to a permutation statistical test (see Main Text). (G) Averaged PGO-triggered LGN-pons absolute (top row) and phase (bottom row) coherograms corresponding to each PGO wave subtype. Absolute and

phase were computed across all pontine-LGN recording electrode pairs. Phase-maps thresholding was applied according to a permutation statistical test (see Main Text). Related to Figure S2.

Figure 3. PGO-wave-triggered band-limited power (BLP) extracellular field potentials. (A) Type I PGO wave-triggered BLP signals grand averages in and beyond the LFP frequency range: delta [0.05-3 Hz], theta [3.5-8 Hz], spindle [9-15 Hz], sigma [16-29 Hz], slow and high gamma [30-55 Hz; 56-79 Hz, respectively], ripple [80-200 Hz] and high-frequency oscillations [201-324 Hz], mEFP [325-800 Hz] and MUA [801-2000 Hz]. BLP signals were z-scored and averaged across all pontine/LGN domains. Asterisks indicate significant deviation ($p<0.01$) from zero according to a one-sample permutation t-test. Responses in the panels were thresholded at a level $p<0.1$ only for illustration purposes. (B) Type II PGO-wave triggered BLP signals grand averages in the same frequency ranges as in panel A. (C) Time courses of BLP modulations in LGN (left subpanels) and pons (right subpanels) over spindle [9-15 Hz] and MUA [801-2000 Hz] frequency ranges, across PGO-wave subtypes. (D) Pontine (left subpanels) and LGN (right subpanels) PGO-related time delay to maximal response over distinct BLP domains, illustrating that mEFP- and MUA-band power signals (325-800 Hz and 801-2000 Hz, respectively) present significantly delayed maximal responses. As expected, PGO-related bands present maximal responses around zero-lag (event occurrence). Colours indicate PGO-wave subtypes as indicated in Figure 2. Asterisks indicate a significant deviation from zero according to a sign test. (E) LGN spindle-related time delay to maximal response. Vertical (black) bars indicate the period excluded from the maximal response lag-analysis. The results illustrate that while type II PGO waves are related to significant spindle activity occurring several seconds before the onset of the PGO event, type I PGO waves are associated with no spindle activity whatsoever. Note the striking correspondence between the delay of type II-related spindle activity and the delay of type II maximal MUA activity in LGN (panel E). Related to Figure S3.

Figure 4. Pontine-hippocampus recordings and prediction of PGO waves by SVM classifier. (A) T2-weighted (RARE) MRI scan showing the electrode position a coronal (left and right panels, fragment) and sagittal (middle panel) slice of monkey *cm029*. (B) MRI images were superimposed on the Saleem-Logothetis (S-L) MRI-histology atlas of the Rhesus Monkey brain. The approximate location of the recording electrodes is indicated by a red cross for pons and by a red arrow for hippocampus. Typically the electrode targeted the pons in or around the parabrachial nucleus (PBn), whilst the electrode in hippocampus targeted the CA3 or CA1 subfields at the level of both *stratum pyramidale* and *stratum radiatum*. (C) Simplified schematic of the methodological approach to predict PGO waves, solely from pontine peri-event LFP (candidate P-waves). A detailed illustration of the methodology can be found in Figure S5A. (D) Statistics of the leave-one-out procedure across experimental sessions show that it is possible to train a non-linear SVM to be applied to a previously unknown experimental session with an averaged accuracy of ca. 70%. On each box, the top and

bottom are the 25th and 75th percentiles of the samples, respectively; the red dot in the middle of each box is the sample median; the lines extending from below and above are drawn from the ends of the interquartile ranges to the extreme points; red crosses in the diagrams are the outliers of the samples (E) Linear SVM-feature weights computed for spectro-temporal features. Distribution of large SVM-coefficients show that low LFP frequencies (<50 Hz) are the most relevant for solving the classification task, as it is apparent both in the spectral (top panel) and time course (bottom panel) features. Note that the averaged power spectral density of the temporal weights indicates that PGO frequencies are dominant. (F) SVM-predicted PGO waves (indicated by a violet dot) and P-waves (indicated by a red dot), superimposed on spatially-averaged pontine (black trace) and LGN (red trace) LFP signal (< 325 Hz). Related to Figure S5.

Figure 5. Type I PGO waves are associated with SWR complexes, whereas type II PGO waves are related to sigma episodes. (A) Broad-band (< 325 Hz) LFP traces extracted from one exemplary experimental session. The traces illustrate co-occurring pontine-hippocampus episodes that can either be oscillatory (type II PGO waves) or biphasic in nature (type I PGO waves). Event-wise coupling between the two areas is visually traceable from raw data. (B) Grand averages of PGO-wave subtypes as retrieved from cluster analysis of the events. The shapes of the grand averages type I and type II PGO waves are in correspondence with those found in the first series of pontine-LGN experimental sessions. (C) Point-process conditional intensities (cross-correlograms) computed between the occurrences of PGO waves and hippocampal sigma, gamma and ripple events. The event of reference is the first for each the couple. Cross-correlograms were computed from pooled experiments across pons-LGN experimental sessions, at a resolution of 10 ms bins. Asterisks indicate a significant relationship (p<0.01, Bonferroni-corrected) at the time of the occurrence of PGO waves, according to a permutation test. The plots illustrate that the occurrence of type I PGO waves is significantly correlated with occurrence of SWR episodes with a (ripple-related) averaged delay of ~100 ms, whereas type II PGO waves show an equivalent effect with respect to sigma events at zero-lag. (D) PGO-wave-triggered averaged spectra over hippocampus recording tips. The spectra show increases over ripple (80-180 Hz) and sigma (5-20 Hz) frequency ranges, related to type I and type II PGO waves, respectively. Related to Figure S4-S6.

Figure 6. PGO wave-triggered hippocampus responses and spike-field relationship. (A) PGO-wave triggered BLP signals grand averages in and beyond the LFP frequency range over the hippocampus region. Coloured asterisks indicate significant deviation (p<0.01) from zero on the basis of a one-sample permutation t-test (red for type I and blue for type II PGO waves, as in Figure 2). Coloured dashed lines indicate significance for lags different to zero. (B) Peri-event time histogram analysis of hippocampal multiunit discharges (25-ms bins) with respect to hippocampal SWR (left subpanel) and sigma events (right subpanel). Insets show the trough-triggered hp-sigma (5-20 Hz) and ripple (80-180

Hz) peri-event time histograms (1-ms bins) responses (rate below baseline levels is subtracted). Statistics are made across all detected events and experimental sessions. Note the increased discharge probability at the early rising phase of sigma, the late rising phase of the sharp-wave, and at the ripple-trough. (C) Trough-triggered hp-sigma and sharp-wave (5-20 Hz) peri-event time histograms (1-ms bins) of pontine multiunit discharges (right and left subpanels, respectively), showing that discharge probability increases at the falling phase of sigma, and close to the trough of the sharp-wave, respectively. The inset (left subpanel) shows that hippocampal cells discharges (only those related to type I PGO waves) occur at the late rising phase of the sharp-wave. Related to Figure S4 and Figure S6.

Supplemental Figure Legends

Figure S1. Exemplary P-waves, LGN-waves and PGO waves from pontine-LGN recordings in macaques. (A) Raw LFP traces (0-100 Hz) display stereotypical waves (solid lines), occurring with high synchrony across recording tips targeting LGN and pontine region. (B) Raw LFP traces (0-100 Hz) display waves co-occurring in LGN and pontine region, thus corresponding to PGO waves (dashed lines).

Figure S2. Laminar power distribution and PGO wave type raw traces. (A) Laminar power profiles of PGO waves type I and type II in a [-0.3 0.3] s peri-event time window, illustrating that PGO wave subtypes have similar power distributions across recording channels. Note that electrode contacts labelled as PBn (close or in PBn) usually capture more power, than those labelled 'PO' (pons). On each box, the top and bottom are the 25th and 75th percentiles of the samples, respectively; the dot in the middle of each box is the sample median; the dashed lines are drawn from the ends of the interquartile ranges (25th and 75th percentiles) to the extreme points. Crosses are outliers. (B) Type I and type II PGO waves (red and blue dots, respectively) in pons (black) and LGN (blue) raw exemplary traces. Note the differences in field signatures, as explained in the Main Text of the present manuscript.

Figure S3. PGO-wave-triggered band-limited power (BLP) extracellular field potentials for two exemplary experimental sessions. Individual sessions are shown in panels A and B. Type I (left subpanels) and type II (right subpanels) PGO wave-triggered BLP signals grand averages across distinct frequency bands: delta [0.05-3 Hz], theta [3.5-8 Hz], spindle [9-15 Hz], sigma [16-29 Hz], slow and high gamma [30-55 Hz; 56-79 Hz, respectively], ripple [80-200 Hz] and high-frequency oscillations [201-324 Hz], mEFP [325-800 Hz] and MUA [801-2000 Hz]. BLP signals were z-scored and averaged across all pontine/LGN domains. Responses were thresholded at a level $p<0.1$ according to a permutation t-test only for illustration purposes. The asterisks indicate the bands where $p<0.05$. Note that statistical significance is harder to reach, due to the limited number of experiments per individual session.

Figure S4. Hippocampal event features in pontine-hippocampus records of macaque monkeys. (A) Sigma- (left panel), gamma- (middle panel) and ripple-triggered (right panel) complex Morlet-wavelet power spectrograms. (B) Averaged zero-lag spectral profiles in correspondence with each hippocampal event type. Shaded areas indicate SEM. (C) Hippocampal event auto-correlograms illustrating that unlike sigma and gamma events, ripple events tend to occur in very close temporal proximity. (D) Bivariate distribution of full-width at half-maximum (FWHM) versus frequency peak (after Logothetis et al., 2012) (left panel). FWHM (middle panel) and frequency peak (right panel) box plots are shown separately. Colours indicate the hippocampal event type shown in B. On each box, the top and bottom are the 25th and 75th percentiles of the samples, respectively; the middle line of each box is the sample median; the dashed lines extending below and above each box are drawn to the extreme points; black crosses in the diagrams are the outliers of the samples. (E) Sigma- (top), gamma- (middle) and SWR-triggered (bottom) BLP signals grand averages in and beyond the LFP frequency range: delta [0.05-3 Hz], theta [3.5-8 Hz], spindle [9-15 Hz], sigma [16-29 Hz], slow and high gamma [30-55 Hz; 56-79 Hz, respectively], ripple [80-200 Hz] and high-frequency oscillations [201-324 Hz], mEFP [325-800 Hz] and MUA [801-2000 Hz]. BLP signals were z-scored and averaged across all recording tips. Asterisks indicate significant deviation ($p<0.01$) from zero according to a one-sample permutation t-test. All responses were thresholded at a statistical significance level $p<0.05$ and Bonferroni-corrected. (F) Time course grand averages of BLP modulations in hippocampus over low-frequencies [3.5-8 Hz] (sharp waves, sigma events), gamma [56-79 Hz], ripple [80-200 Hz] and MUA [801-2000 Hz]. Note the prevalent negative modulation over high-frequency domains associated with sigma events, as opposed by a consistent increase of activity associated with ripple events. (G) Point-process conditional intensities (cross-correlograms) accounting for the relationship between the occurrences of sigma, gamma and SWR episodes. Conditional intensities were computed from pooled experiments across pons-hippocampus experimental sessions, at a resolution of 50 ms bins. Red asterisks indicate a significant relationship ($p<0.01$, Bonferroni-corrected) at the time of the occurrence of sigma (top), gamma (middle) and SWR (bottom) events, according to a permutation test. The reference event for computing the intensity is indicated by the first event of each pair in the upper-right box.

Figure S5. SVM classifier for the prediction of PGO waves. (A) Diagram of the methodological approach. A leave-one-out procedure is implemented in order to predict the occurrence of PGO waves from pontine recordings features. Five experimental sessions are used for training the SVM and the remaining one is used for testing its prediction accuracy. The classifier is tested using a k-fold cross-validation approach. (B) Number of PGO waves detected by chance over the total number of detected pontine phasic waves, as a function of the event detection thresholds. As the sensitivity of the detection raises, putative false detections become scarcer, eventually reaching zero percent. (C) Event-triggered averages of power (top panels) and broad-band LFP (bottom panels) for P- and PGO-waves (left and right columns, respectively). (D) Performance of linear and non-linear SVM classifiers for distinct sets of features in a 10-fold cross validation approach (spectra, event time course, MUA and spectra plus time), illustrating that spectro-temporal features reach the largest prediction accuracy. Note that the non-linear (Gaussian-kernel) SVM outperforms the linear one. (E) Statistics of the leave-one-out procedure across experimental sessions, show that the classifier trained (and tested) on each PGO-wave subtype does not make the performance significantly different (right panel).

Figure S6. Co-occurrence of pontine and hippocampal neural events and SVM-based approach for the prediction PGO waves in pons-hippocampus experimental sessions. (A) Exemplary LFP traces of pontine and hippocampal activities. Pontine episodes (PGO waves) can co-occur with SWR (diamonds, top row) or hp-sigma (circles, bottom row) traces, displaying similar time courses. Arrows indicate the occurrence of the ripple oscillation in a LFP trace filtered in the range (80 – 180 Hz). (B) Statistics of the testing procedure across pons-LGN experimental sessions show that co-occurring pons-hippocampus events may be PGO waves, reaching very similar performance (~65%) as compared to the classification assays reported in Figure S5 and Figure 4. (C) Class-prediction label consistency illustrates a ca. 71% labelling consistency between the SVM trained from pons-LGN data and the SVM trained using pons-hippocampus data (magenta box plots). Consistency across cross-validations for each classifier (red and blue, respectively) reaches ca. 90%. (D) Spectral profiles of SVM-predicted PGO waves and co-occurring P-waves with hippocampus events. Strong correlation between the spectra of each category is visually apparent. Labelling consistency between SVM-predicted PGO waves and co-occurring P-waves with hippocampus events reaches ca. 83% in this example.

Figure 1

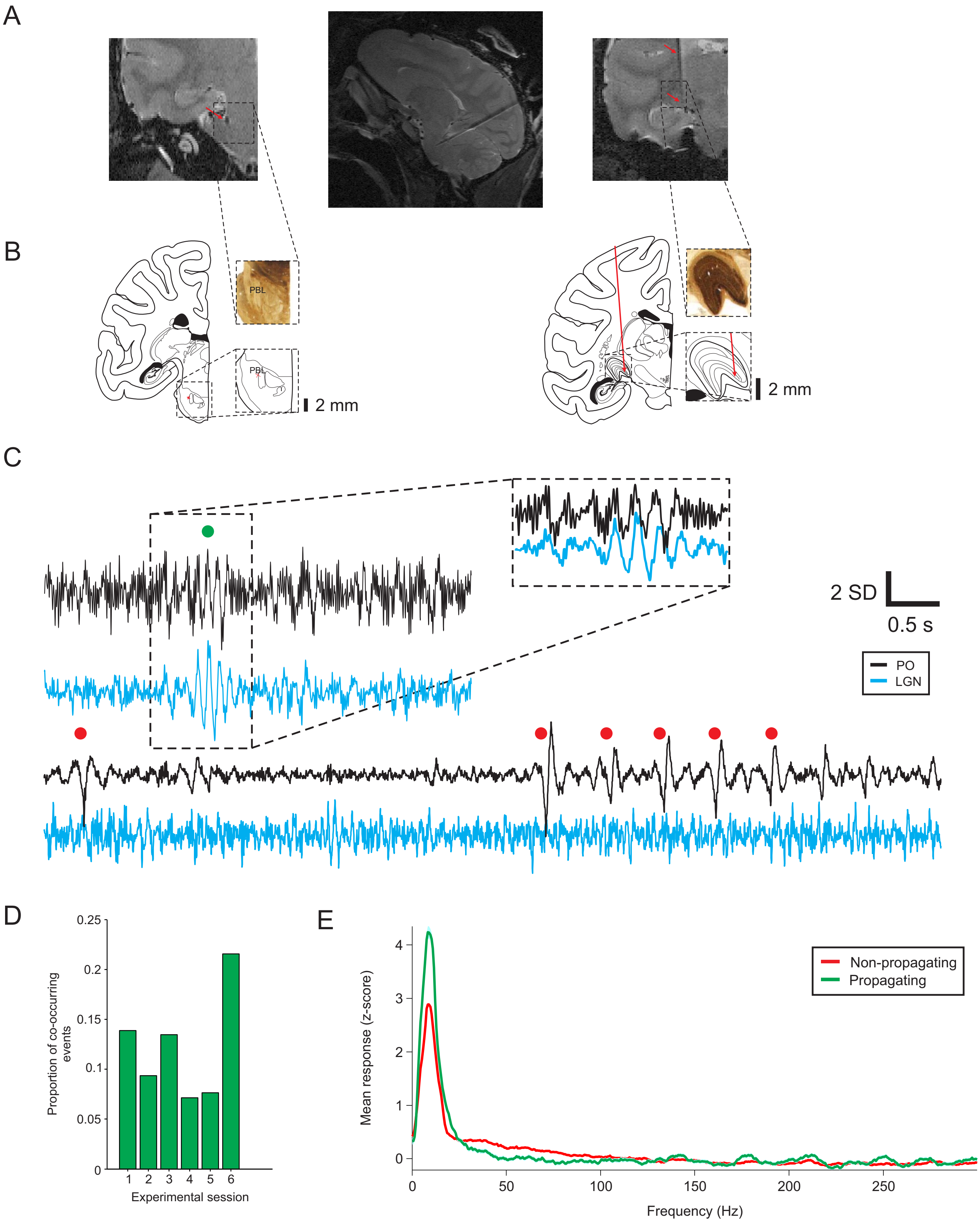
A
B
PBL
PBL
2 mm
2 mm
C
2 SD
0.5 s
PO
LGN
D
Proportion of co-occurring events
0.25
0.2
0.15
0.1
0.05
0
1
2
3
4
5
6
Experimental session
E
Mean response (z-score)
4
3
2
1
0
Non-propagating
Propagating
0
50
100
150
200
250
Frequency (Hz)

Figure 2

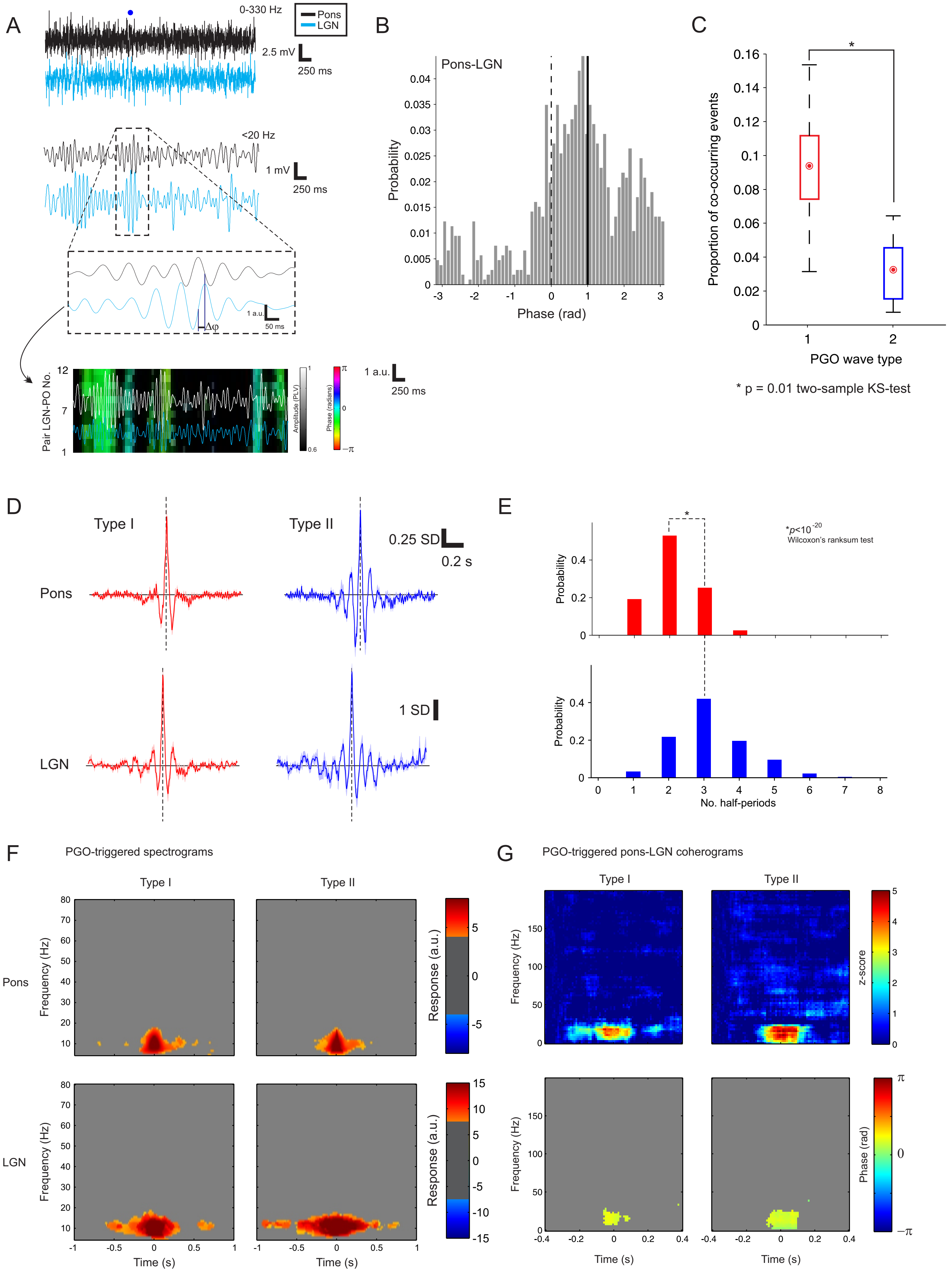
A
0-330 Hz
Pons
LGN
2.5 mV
250 ms
<20 Hz
1 mV
250 ms
1 a.u.
50 ms
Δφ
Pair LGN-PO No.
12
7
1
Amplitude (PLV)
1
0.6
Phase (radians)
π
0
−π
1 a.u.
250 ms
B
Pons-LGN
Probability
0.04
0.035
0.03
0.025
0.02
0.015
0.01
0.005
0
-3
-2
-1
0
1
2
3
Phase (rad)
C
*
Proportion of co-occurring events
0.16
0.14
0.12
0.1
0.08
0.06
0.04
0.02
0
1
2
PGO wave type
* p = 0.01 two-sample KS-test
D
Type I
Type II
0.25 SD
0.2 s
Pons
1 SD
LGN
E
*
*p<10-20
Wilcoxon's ranksum test
Probability
0.4
0.2
0
Probability
0.4
0.2
0
0
1
2
3
4
5
6
7
8
No. half-periods
F
PGO-triggered spectrograms
Type I
Type II
Pons
Frequency (Hz)
80
70
60
50
40
30
20
10
Response (a.u.)
5
0
-5
LGN
Frequency (Hz)
Response (a.u.)
15
10
5
0
-5
-10
-15
-1
-0.5
0
0.5
1
Time (s)
G
PGO-triggered pons-LGN coherograms
Type I
Type II
Frequency (Hz)
150
100
50
0
z-score
5
4
3
2
1
0
Frequency (Hz)
Phase (rad)
π
0
−π
-0.4
-0.2
0
0.2
0.4
Time (s)

Figure 3

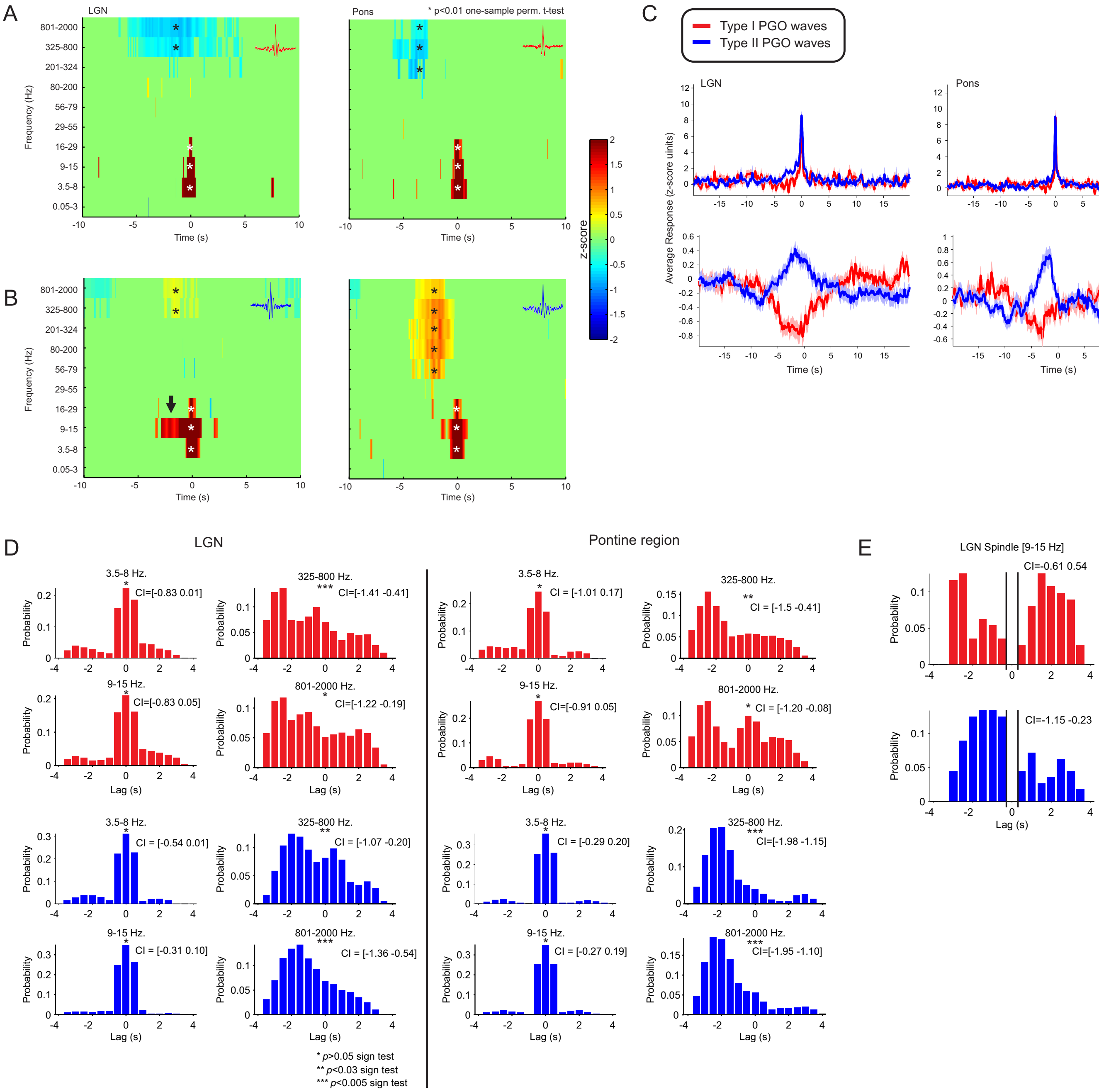
A
LGN
Pons
* p<0.01 one-sample perm. t-test
801-2000
325-800
201-324
80-200
56-79
29-55
16-29
9-15
3.5-8
0.05-3
Frequency (Hz)
Time (s)
-10
-5
0
5
10
z-score
2
1.5
1
0.5
0
-0.5
-1
-1.5
-2
B
C
Type I PGO waves
Type II PGO waves
LGN
Pons
9-15 Hz
800-2000 Hz
Average Response (z-score units)
Time (s)
D
LGN
Pontine region
3.5-8 Hz.
CI=[-0.83 0.01]
325-800 Hz.
CI=[-1.41 -0.41]
9-15 Hz.
CI=[-0.83 0.05]
801-2000 Hz.
CI=[-1.22 -0.19]
CI = [-1.01 0.17]
CI = [-1.5 -0.41]
CI=[-0.91 0.05]
CI = [-1.20 -0.08]
CI = [-0.54 0.01]
CI = [-1.07 -0.20]
CI = [-0.29 0.20]
CI=[-1.98 -1.15]
CI = [-0.31 0.10]
CI = [-1.36 -0.54]
CI = [-0.27 0.19]
CI=[-1.95 -1.10]
Probability
Lag (s)
* p>0.05 sign test
** p<0.03 sign test
*** p<0.005 sign test
E
LGN Spindle [9-15 Hz]
CI=-0.61 0.54
CI=-1.15 -0.23
Probability
Lag (s)

Figure 4

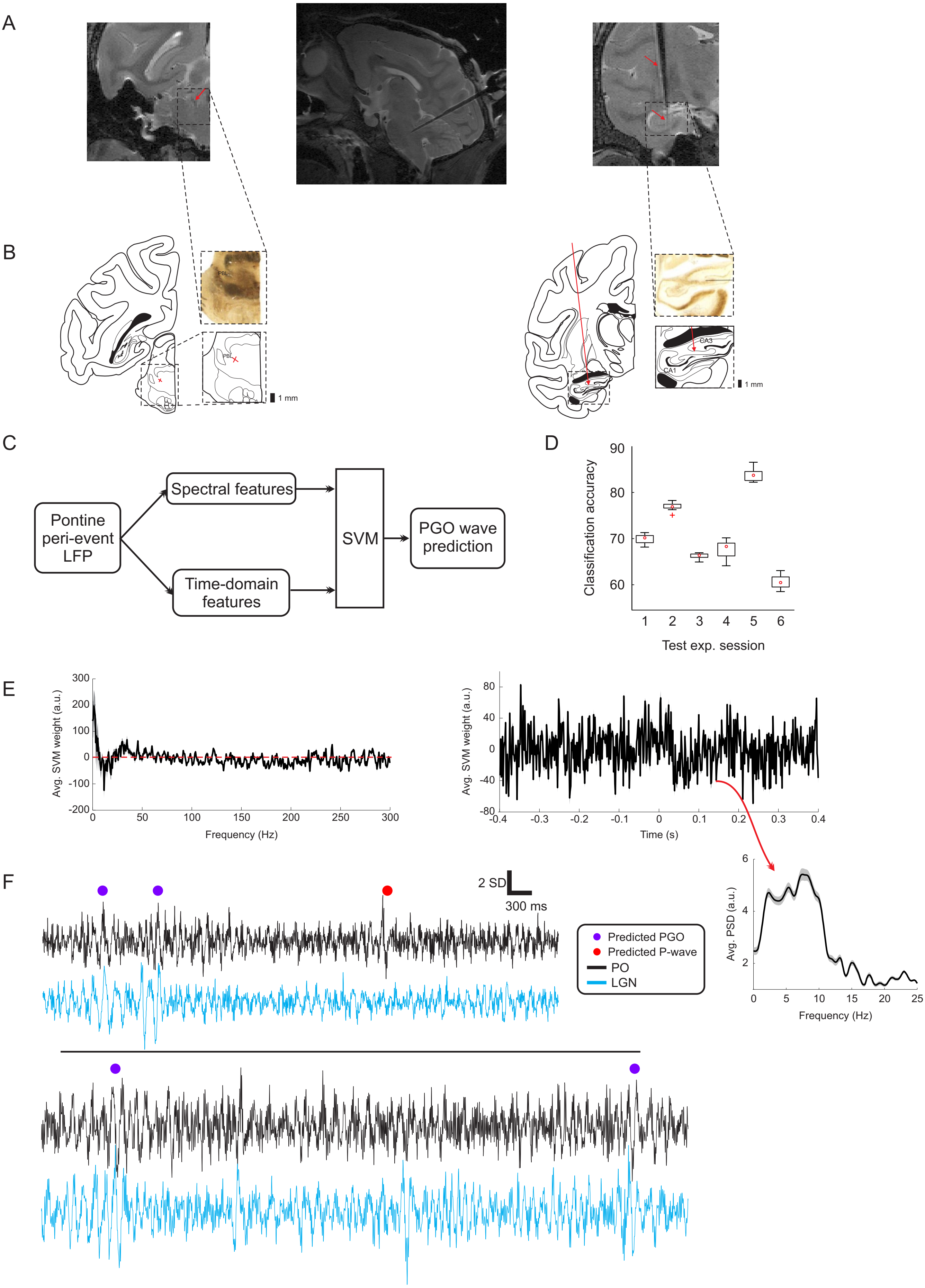
A
B
PBL
PBL
1 mm
CA3
CA1
1 mm
C
Pontine peri-event LFP
Spectral features
Time-domain features
SVM
PGO wave prediction
D
Classification accuracy
90
80
70
60
1
2
3
4
5
6
Test exp. session
E
Avg. SVM weight (a.u.)
300
200
100
0
-100
-200
0
50
100
150
200
250
300
Frequency (Hz)
Avg. SVM weight (a.u.)
80
40
0
-40
-80
-0.4
-0.3
-0.2
-0.1
0
0.1
0.2
0.3
0.4
Time (s)
Avg. PSD (a.u.)
6
4
2
0
5
10
15
20
25
Frequency (Hz)
F
2 SD
300 ms
● Predicted PGO
● Predicted P-wave
PO
LGN

Figure 5

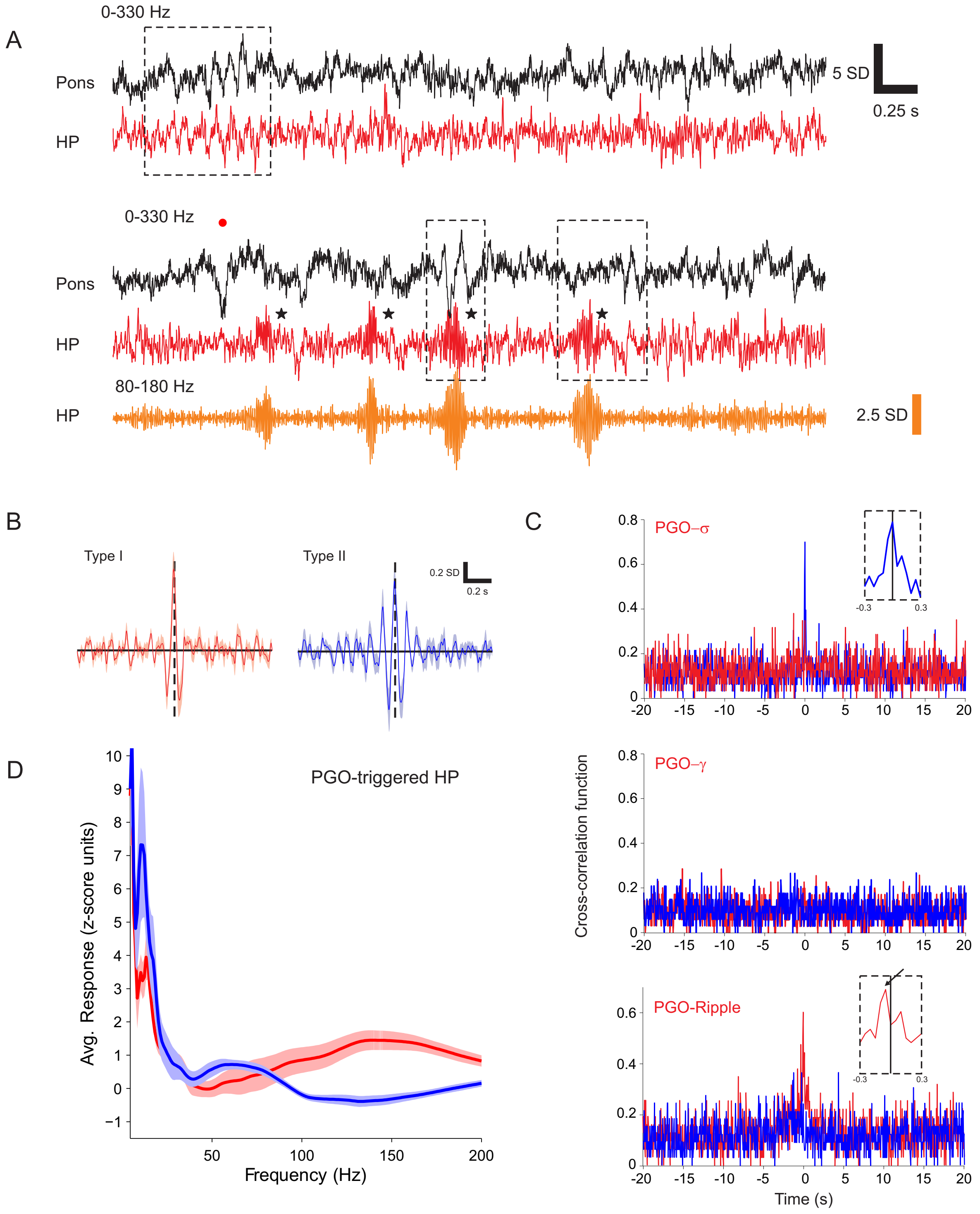
A
0-330 Hz
Pons
HP
5 SD
0.25 s
0-330 Hz
Pons
HP
80-180 Hz
HP
2.5 SD
B
Type I
Type II
0.2 SD
0.2 s
C
PGO–σ
-0.3
0.3
PGO–γ
PGO-Ripple
-0.3
0.3
Cross-correlation function
Time (s)
0
0.2
0.4
0.6
0.8
-20
-15
-10
-5
0
5
10
15
20
D
PGO-triggered HP
Avg. Response (z-score units)
Frequency (Hz)
10
9
8
7
6
5
4
3
2
1
0
−1
50
100
150
200

Figure 6

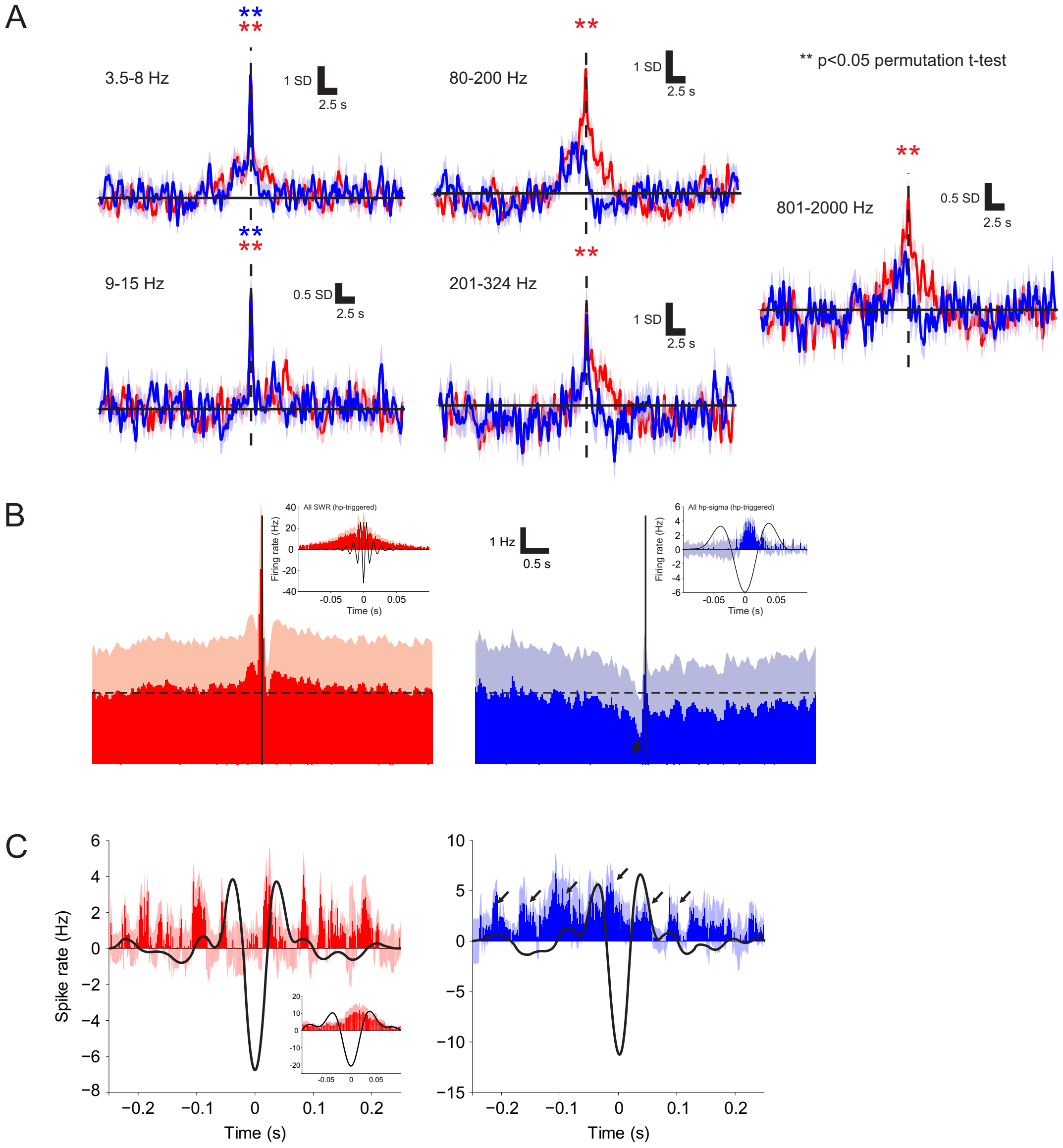
A
3.5-8 Hz
1 SD
2.5 s
80-200 Hz
1 SD
2.5 s
** p<0.05 permutation t-test
**
**
9-15 Hz
0.5 SD
2.5 s
201-324 Hz
1 SD
2.5 s
801-2000 Hz
0.5 SD
2.5 s
B
All SWR (hp-triggered)
Firing rate (Hz)
40
20
0
-20
-40
-0.05
0
0.05
Time (s)
1 Hz
0.5 s
All hp-sigma (hp-triggered)
Firing rate (Hz)
6
4
2
0
-2
-4
-6
-0.05
0
0.05
Time (s)
C
Spike rate (Hz)
6
4
2
0
−2
−4
−6
−8
−0.2
−0.1
0
0.1
0.2
Time (s)
20
10
0
-10
-20
-0.05
0
0.05
10
5
0
−5
−10
−15
−0.2
−0.1
0
0.1
0.2
Time (s)

Figure S1

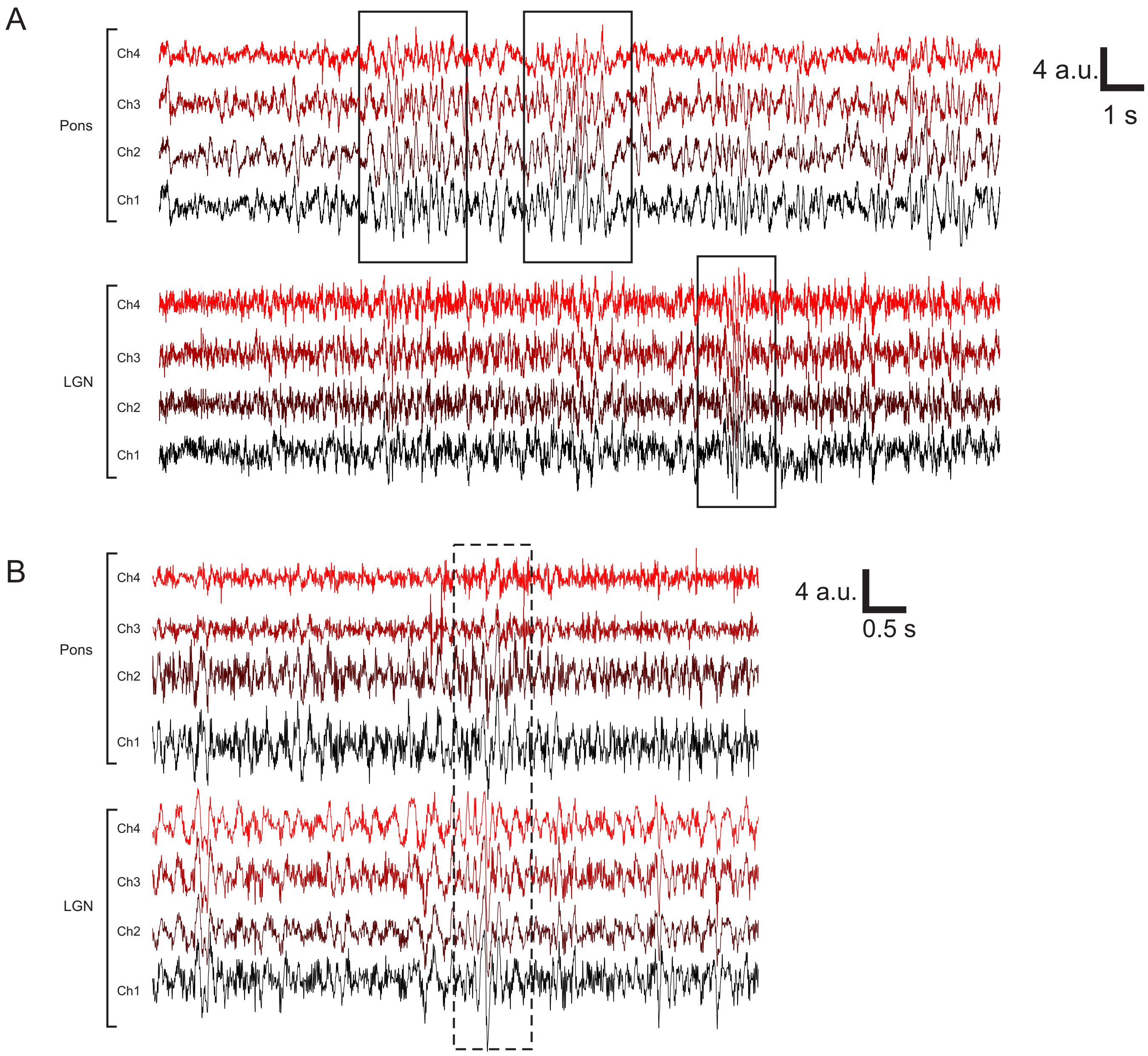
A
Pons
Ch4
Ch3
Ch2
Ch1
LGN
Ch4
Ch3
Ch2
Ch1
4 a.u.
1 s
B
Pons
Ch4
Ch3
Ch2
Ch1
LGN
Ch4
Ch3
Ch2
Ch1
4 a.u.
0.5 s

Figure S2

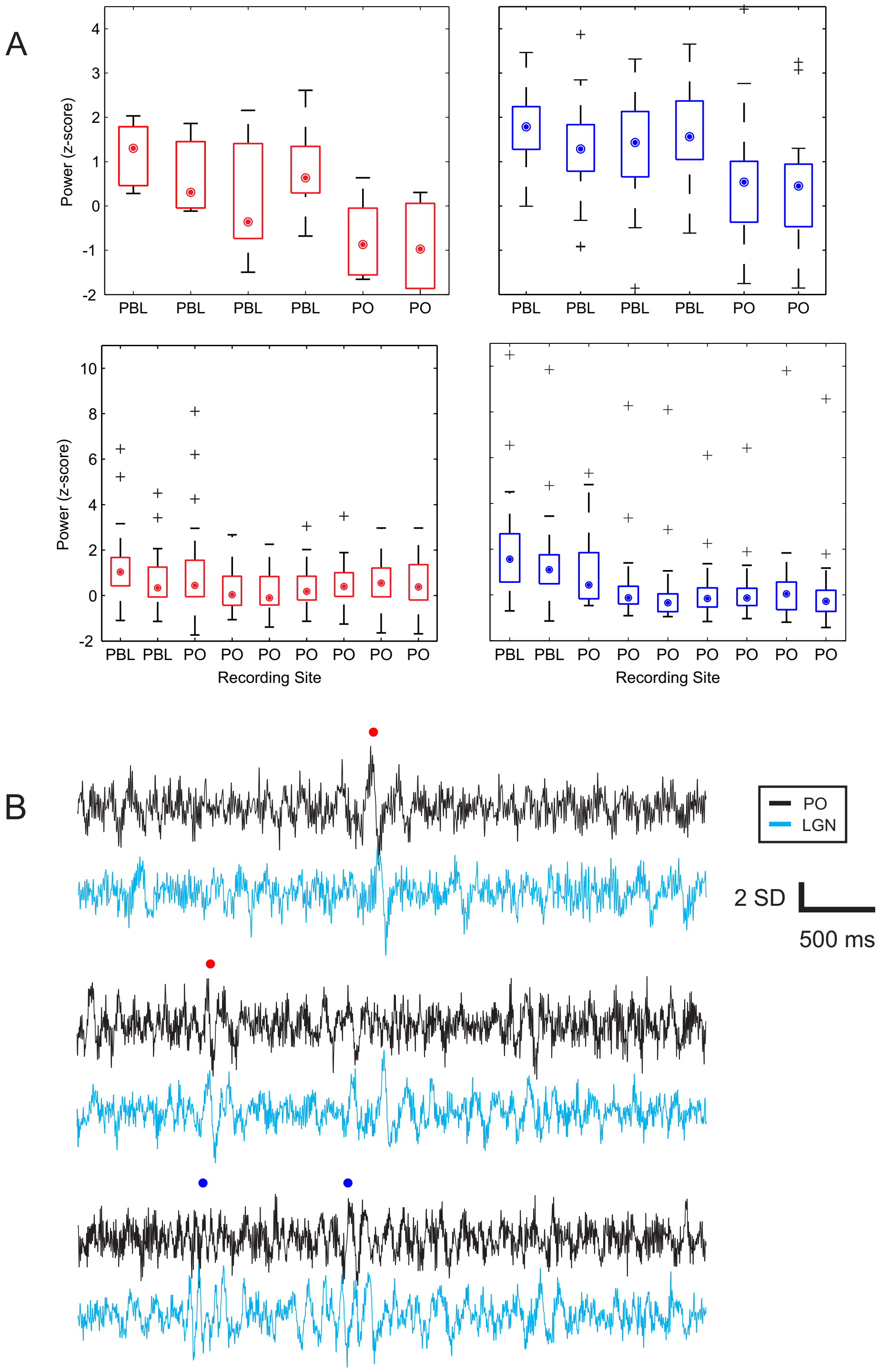
A
Power (z-score)
4
3
2
1
0
-1
-2
PBL
PBL
PBL
PBL
PO
PO
PBL
PBL
PBL
PBL
PO
PO
Power (z-score)
10
8
6
4
2
0
-2
PBL
PBL
PO
PO
PO
PO
PO
PO
PO
Recording Site
PBL
PBL
PO
PO
PO
PO
PO
PO
PO
Recording Site
B
PO
LGN
2 SD
500 ms

Figure S3

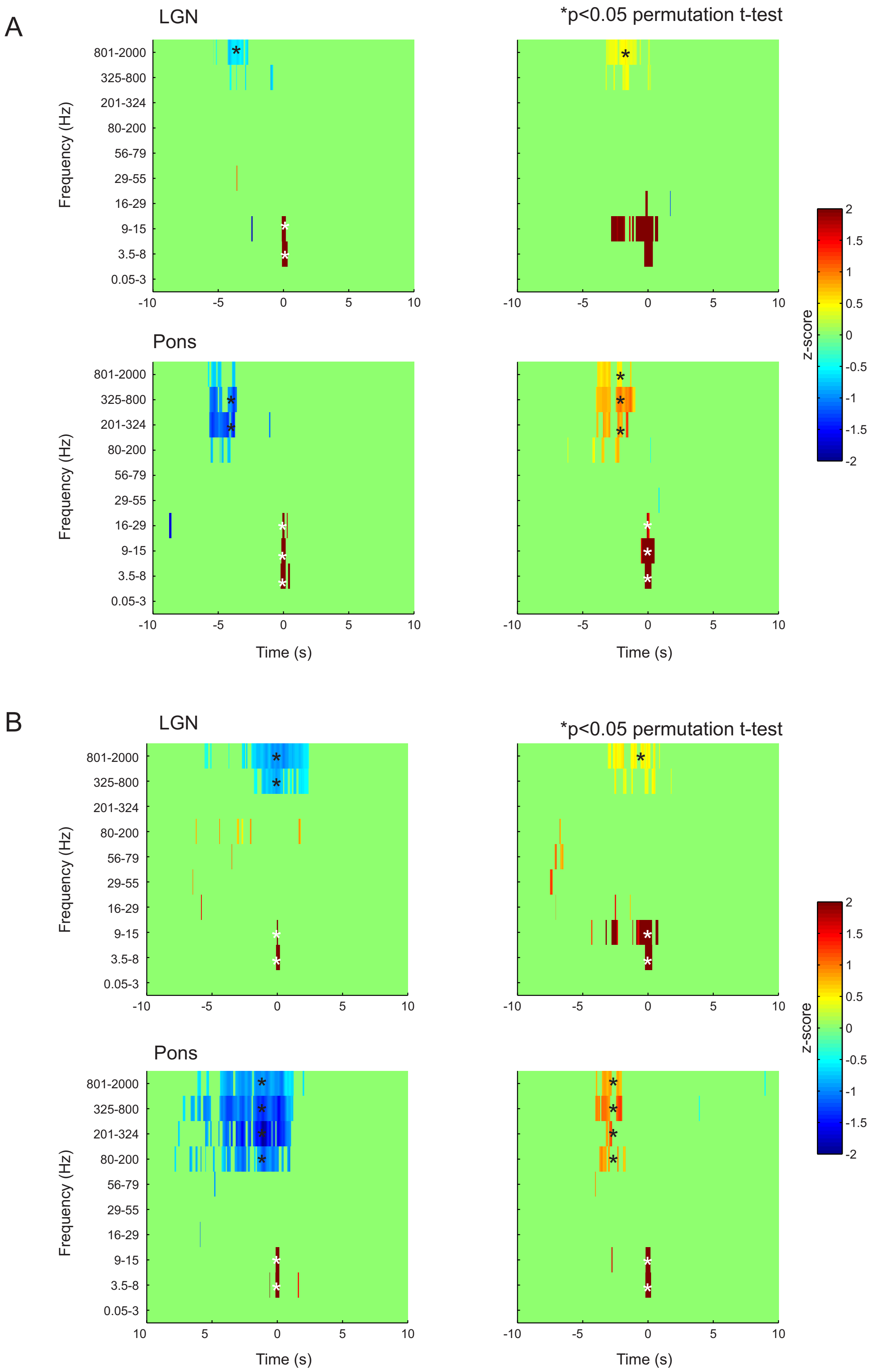
A
LGN
*p<0.05 permutation t-test
801-2000
325-800
201-324
80-200
56-79
29-55
16-29
9-15
3.5-8
0.05-3
Frequency (Hz)
-10
-5
0
5
10
Pons
Time (s)
z-score
2
1.5
1
0.5
0
-0.5
-1
-1.5
-2
B
LGN
*p<0.05 permutation t-test
Pons
10
5
0
5
10
Time (s)
z-score

Figure S4

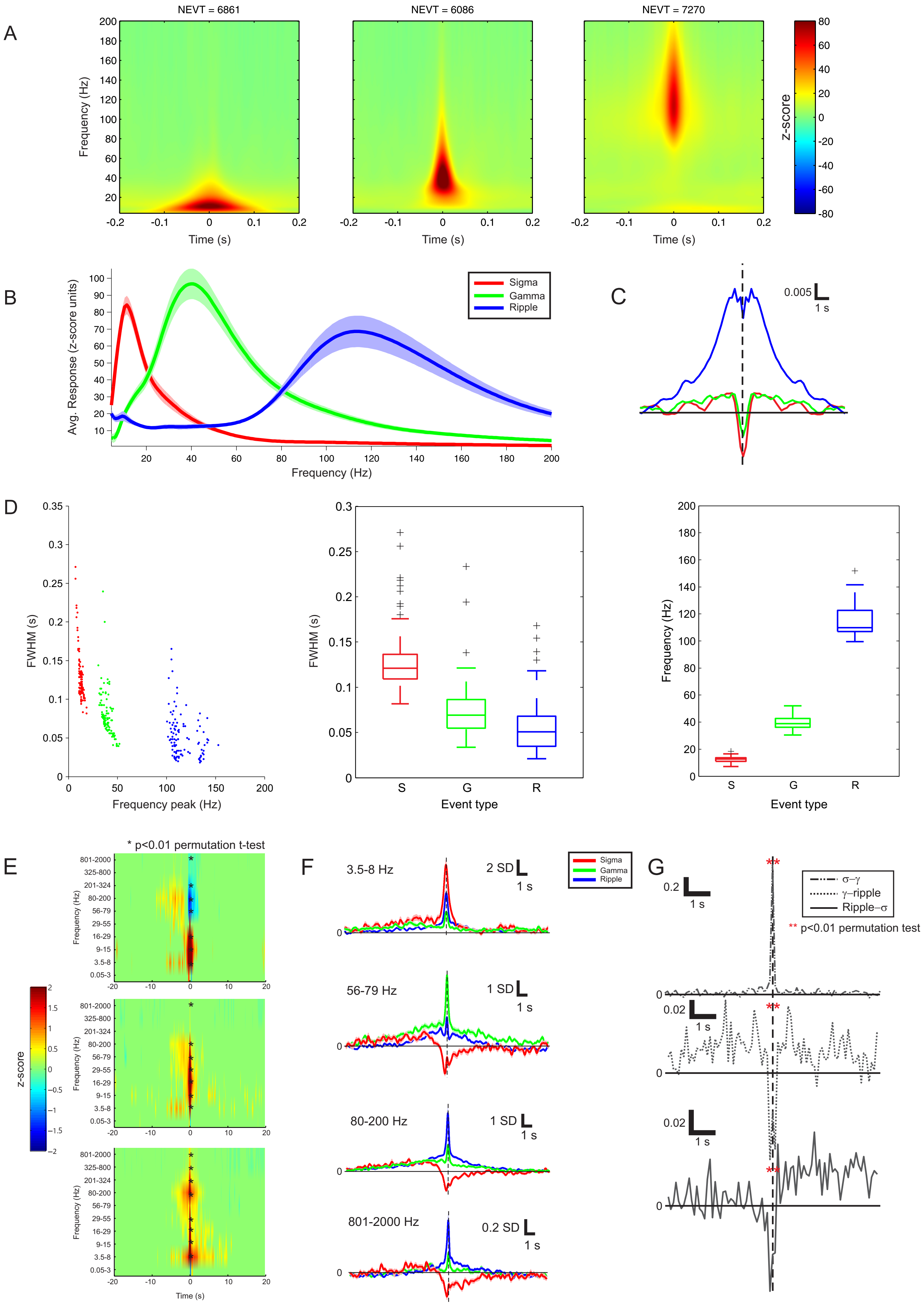
A
NEVT = 6861
NEVT = 6086
NEVT = 7270
Frequency (Hz)
200
180
160
140
120
100
80
60
40
20
-0.2
-0.1
0
0.1
0.2
Time (s)
z-score
80
60
40
20
0
-20
-40
-60
-80
B
Avg. Response (z-score units)
Frequency (Hz)
Sigma
Gamma
Ripple
C
0.005
1 s
D
FWHM (s)
Frequency peak (Hz)
Event type
S
G
R
Frequency (Hz)
E
* p<0.01 permutation t-test
801-2000
325-800
201-324
80-200
56-79
29-55
16-29
9-15
3.5-8
0.05-3
Frequency (Hz)
Time (s)
z-score
F
3.5-8 Hz
2 SD
56-79 Hz
1 SD
80-200 Hz
1 SD
801-2000 Hz
0.2 SD
1 s
Sigma
Gamma
Ripple
G
0.2
0.02
0.02
1 s
σ−γ
γ−ripple
Ripple−σ
** p<0.01 permutation test

Figure S5

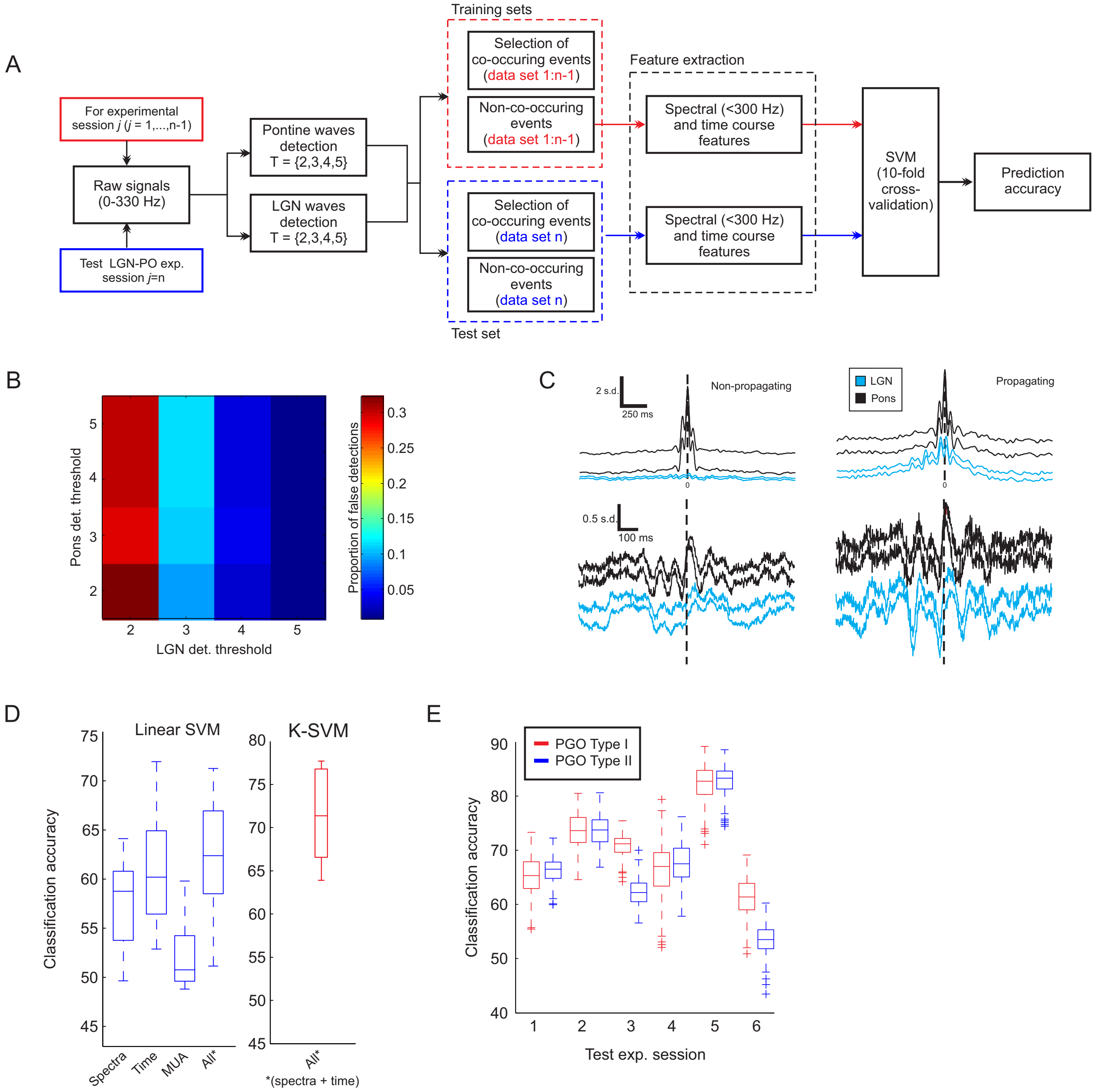
A
For experimental session j (j = 1,...,n-1)
Raw signals (0-330 Hz)
Test LGN-PO exp. session j=n
Pontine waves detection T = {2,3,4,5}
LGN waves detection T = {2,3,4,5}
Training sets
Selection of co-occuring events (data set 1:n-1)
Non-co-occuring events (data set 1:n-1)
Selection of co-occuring events (data set n)
Non-co-occuring events (data set n)
Test set
Feature extraction
Spectral (<300 Hz) and time course features
Spectral (<300 Hz) and time course features
SVM (10-fold cross-validation)
Prediction accuracy
B
Pons det. threshold
5
4
3
2
2
3
4
5
LGN det. threshold
Proportion of false detections
0.3
0.25
0.2
0.15
0.1
0.05
C
2 s.d.
250 ms
Non-propagating
LGN
Pons
Propagating
0
0
0.5 s.d.
100 ms
D
Linear SVM
K-SVM
Classification accuracy
75
70
65
60
55
50
45
80
75
70
65
60
55
50
45
Spectra
Time
MUA
All*
All*
*(spectra + time)
E
PGO Type I
PGO Type II
Classification accuracy
90
80
70
60
50
40
1
2
3
4
5
6
Test exp. session

Figure S6

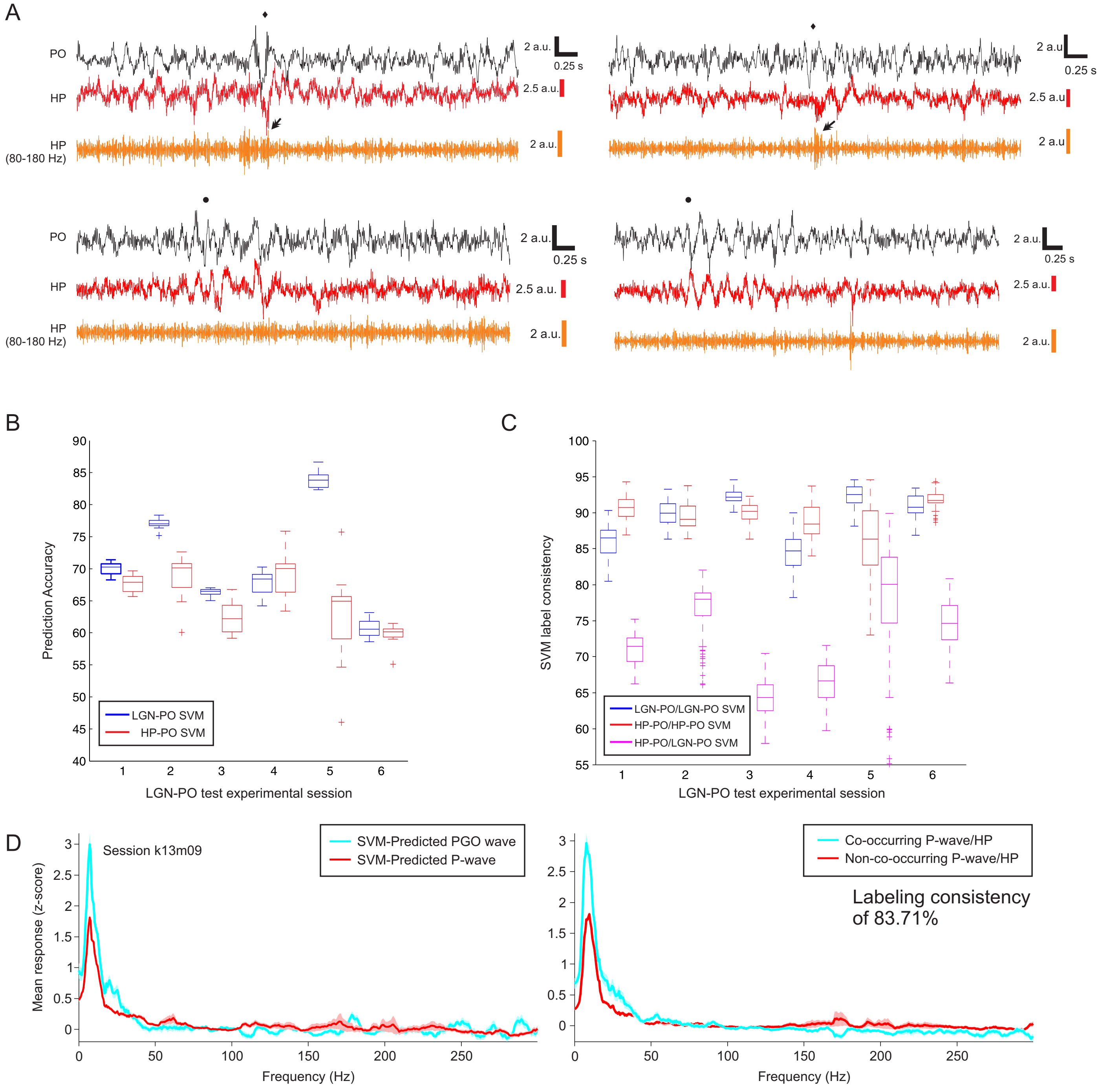
A
PO
HP
HP
(80-180 Hz)
2 a.u.
0.25 s
2.5 a.u.
2 a.u.
B
Prediction Accuracy
LGN-PO SVM
HP-PO SVM
LGN-PO test experimental session
C
SVM label consistency
LGN-PO/LGN-PO SVM
HP-PO/HP-PO SVM
HP-PO/LGN-PO SVM
LGN-PO test experimental session
D
Session k13m09
SVM-Predicted PGO wave
SVM-Predicted P-wave
Mean response (z-score)
Frequency (Hz)
Co-occurring P-wave/HP
Non-co-occurring P-wave/HP
Labeling consistency
of 83.71%
Frequency (Hz)

Supporting Information

Juan F. Ramirez-Villegas, Yusuke Murayama, Henry C. Evrard, Michel Besserve & Nikos K. Logothetis

SI Section A: Conditioning of neural data

Clustering of PGO-wave LFP spatio-temporal series. Cluster analysis was applied to each experimental session separately. Spatially-averaged peri-event PGO-wave signal time courses were used for clustering. Thus, we clustered two concomitant LFP traces simultaneously: one corresponding to LGN and one corresponding to pons. For the first stage of the clustering approach, the spatio-temporal PGO wave series were grouped in a maximum of 80 representative signals using a growing neural gas (GNG) algorithm (Fritzke, 1995) (after Ramirez-Villegas et al., 2015). Since representative signals are easier to cluster due to average-based noise reduction, these representatives were clustered based on their pairwise cosine similarity matrix using the normalized cuts algorithm (Shi and Malik, 2000). PGO waves were sorted and then averaged across all sessions. This procedure was performed for PGO data of 6 pontine-LGN experimental sessions in the first part of the study (2 macaque monkeys, and a total of 528). In the second part of this study, the same procedure was performed for predicted PGO waves of 9 pons-hippocampus experimental sessions (3 macaque monkeys, 1880 predicted PGO waves). For group analysis, PGO waves were first sorted in a session-wise manner according to their triggered MUA-response. This procedure was supported by visual assessment of the LFP- and MUA averaged event-triggered responses.

Spectral features of PGO waves and hippocampal events. Spectral analysis of PGO waves and hippocampal events was performed using Morlet-wavelet spectrograms. All spectrograms were Z-scored with respect to spectrograms computed using the same number of events with randomized inter-event intervals (i.e. random, baseline events). Sigma, gamma, ripple and PGO frequency peaks of individual events were extracted using this spectral technique. In addition, a measure of event time duration was computed for hippocampal events (after Logothetis et al., 2012). This measure was computed as the full-width at half-maximum (FWHM) of the LFP response at the time of event occurrence. Data from distinct experimental sessions then was pooled and statistics on population data were displayed and reported.

Prediction of PGO waves exclusively from pontine LFP traces via support vector machine (SVM). Non-linear SVM were used in order to predict the occurrence of PGO waves using solely features extracted from pontine recordings, across experimental sessions. This problem arises due to the need of discriminating PGO waves from P-waves in multi-structure recordings without a recording electrode placed in LGN. The classification experiments performed in this work were divided into three stages as follows:

1) Prior to data classification, we first devised a procedure for determining the sensitivity of the PGO-event detection threshold. P-waves were detected using thresholds in the range [2-5] SD. As a candidate P-wave was detected, partner waves were detected in LGN in the same range of thresholds. With this procedure, we build a matrix displaying the proportion of detected putative PGO waves (co-occurring waves across pontine-LGN structures) over the total detected P-waves. In parallel, we ask: what is the proportion of putative PGO waves that could be detected by chance? To this end, we select peri-event time windows at random matching the rate of the detected "ground-truth" P-waves. We then defined a putative false detection as an above-threshold episode detected over a randomly selected time window of 300 ms. In this step, we seek to determine whether the same or a similar amount of PGO waves could be detected at random at a given event detection threshold. Thus, we build a second matrix displaying the proportion of detected events by chance over the total "ground-truth" P-waves.

2) Classifiers were learnt over the first series of 6 pontine-LGN experimental sessions and initially using the time course, spectra and MUA of propagating and non-propagating pontine-LGN waves. Features were extracted as follows: time courses were averaged across pontine recording sites, aligned and arranged as peri-event time windows of ±0.4 s around the occurrence of the event. Peri-event z-scored multi-taper spectra were computed in this time window and then averaged across pontine recording sites, thus accounting for spectral features. Finally, a time window of ±10 s was taken as MUA-band [800-2000] Hz features. The procedure for computing the MUA is described in the previous subsection of the present Supplemental Information.

We first tested the prediction accuracy of the classifiers across pontine-LGN (ground-truth) experimental sessions using a leave-one-out procedure (training using 5 experimental sessions, 1 experimental session for testing) (see Figure S4A for a schema of this methodological approach). Extensive classification experiments were performed initially to determine whether linear or non-linear (Gaussian kernel) SVM were appropriate for predicting PGO waves, subject to the event detection threshold of 4 SD. A bootstrapping procedure was used in order to balance the proportion of co-occurring and non-co-occurring event categories in each classification experiment (*N*=50 bootstraps). Classification experiments were then performed using a 10-fold cross-validation approach in each balanced subsample.

All reported statistics are based on these 500 per-session classification assays. Statistics across sessions were only used in order to compare linear vs. non-linear SVM prediction accuracy.

Performance of the non-linear SVM was proven significantly above the linear one. MUA features were discarded due to chance-level performance. On the basis of these results, both linear and non-linear SVMs were learnt using solely temporo-spectral features. Linear SVMs were instrumental for computing the weights associated with each feature in the classification task. SVM-related weights associated with spatio-temporal features –i.e. the most discriminative information extracted from candidate PGO waves– were computed as follows:

Let $\mathbf{x}^{(s)}$ be a matrix with N_s support vectors and M time samples, $\left\{\alpha_i\right\}_{i=1}^{N_s}$ be the Lagrange multipliers associated to the N support vectors and $\left\{\mathbf{x}_j, d_j\right\}_{j=1}^{L}$ be the training sample, where $d_j \in \left\{-1,1\right\}$ is the desired label class (e.g., 1 for PGO wave; -1 for P-wave) assigned to the j^{th} M-dimensional data point $\mathbf{x}_j$. Here, the M -dimensional data points are long feature vectors comprising concatenated time courses and spectra each candidate PGO wave. Since the support vectors are the most difficult data points to classify, we may compute a weight w for each feature in order to know how discriminative it is for the classification task. Note that the more far away from the decision boundary (which is closest to the support vectors), the more discriminative a given data point is (which varies linearly with the weight):

$$v_j = \mathbf{w}^T \mathbf{x}_j + b, \qquad (1)$$

where $w = \sum_{i=1}^{N_s} \alpha_i d_i \mathbf{x}_i^{(s)}$ and $b = 1 - \mathbf{w}_0^T \mathbf{x}^{(s)}$ for $d^{(s)} = 1$.

Note that we do not make any assumption on whether the patters are separable or not. Further, we compute the weights during the cross validation procedure and report the statistics across-sessions as specified in each plot.

Finally, it is important to test whether the classification accuracy obtained using the final non-linear classifier was statistically significant for each experimental session. This question was addressed using non-parametric statistical methods. A permutation test was performed by randomly shuffling the observations across classes (PGO waves vs. P-waves) and running the SVM prediction using this shuffled data. We built an estimation of the null (H0) distribution of classification accuracy values from a total of 500 randomizations, per experimental session. We then obtained a probability value (*p*-value) for the ground-truth (non-shuffled) classification accuracy accounting for the final statistical significance. This *p*-value thus corresponds to the proportion of classification assays that may have surpassed the theoretical chance level (50%), by chance (Combrisson and Jerbi, 2015).

3) Upon observing that predicted PGO waves and hippocampal events tend to co-occur at fine timescales, we asked whether pontine phasic waves co-occurring with hippocampal events were indeed PGO waves. We tested this hypothesis by learning a second non-linear SVM classifier, but instead of training on pons-LGN experimental sessions, we trained them using pons-hippocampus sessions ($N = 9$ experimental sessions). The classifiers were learnt using the same set of temporo-spectral features considered before, extracted solely from pontine LFP traces. Classifiers were tested using the six pons-LGN "ground-truth" data sets for the prediction of true PGO waves in an experimental session-wise manner. Cross-validation procedures were performed as detailed in the previous section. Statistics across sessions were computed using the total of 500 classification assays. Then a grand average was computed together with its 95% confidence interval and significance level.

As our results suggest that co-occurring pontine-hippocampus events may be PGO waves, the overall classification performance may arise from a combination of misclassified events in addition to some true PGO waves. In order to rule out this possibility, SVM prediction consistency was measured on each testing subset using the following equation:

$$Q^{\mu} = 1 - \frac{1}{N}\sum_{i=1}^{N} F\left(x_i^{\mu} - y_i^{\mu}\right), \qquad (2)$$

where x_i^{μ} and y_i^{μ} are the *i*-th predicted labels of the μ-th cross-validation, N is the total number of signals in the test set, and $F(x)$ is described by the following function:

$$F(x) = \begin{cases} 0 & x = 0 \\ 1 & otherwise \end{cases}, \qquad (3)$$

Thus, when the sets cluster labels $X^{\mu} = \left\{x_1^{\mu}, x_2^{\mu}, \ldots, x_N^{\mu}\right\}$ and $Y^{\mu} = \left\{y_1^{\mu}, y_2^{\mu}, \ldots, y_N^{\mu}\right\}$ are identical the consistency takes value 1 (or 100% consistency).

In a similar vein, we examined the spectral profiles of predicted PGO waves and co-occurring pontine-hippocampus events, together their pair-wise Spearman correlation coefficient. A level of $p<0.05$ was considered a significant correlation.

Unsupervised cluster analysis of SVM-predicted PGO waves. In order to cluster SVM-predicted PGO waves, we used the two-stage clustering technique described previously and cross-correlation analyses.

Clustering was performed in a session-wise manner following the procedures described in the first subsection of the Supporting Information. Analogous to the first analyses, PGO wave time series were grouped in a maximum of 80 representative signals using the GNG algorithm, which were then clustered on the basis of their pairwise cosine similarity matrix using the normalized cuts algorithm. It is worth noting that here we used only pontine waves for clustering, since LGN was not recorded. This procedure was performed for PGO data of 9 pontine-hippocampus experimental sessions (3 macaque monkeys).

Cross-correlation analysis was carried out by computing the conditional intensities related to the occurrence of PGO events as determined by the clustering technique (namely, type I and type II LFP activities), as explained in the Main Text of this manuscript. Sigma-, gamma- and ripple-pontine wave pairs were assessed statistically by comparing against random surrogate point-processes of the same rate, up to several permutations ($N = 500$ permutations). A two-tailed test under this null distribution was then performed in order to compute the significance of the correlation at a given lag.

SI Section B: Supporting results on hippocampal events and prediction of PGO waves

Differentiated extracellular field potential signatures of hippocampal neuronal-ensemble events. Hippocampal ensemble episodes may be coupled to PGO waves, as suggested a previous study (Calvo and Fernandez-Guardiola, 1984). A detailed characterization of hippocampal events may provide clues not only about the activity of hippocampal neuronal ensembles, but also will deepen our understanding of the relationship between pontine and hippocampal activities during sleep-like states. To this end, we first identified candidate hippocampal events using the process described in Logothetis et al. (2012). Hippocampal sigma (8-22 Hz; $N\sigma = 6861$ events), gamma (25-75 Hz; $N\gamma = 6086$ events) and ripple (80-180 Hz; $N\rho = 7270$ events) episodes were consistently identified across 9 experimental sessions, recorded from 3 different animals (Figure S4A-F).

We scrutinized the relationship between hippocampal events and distinct sub-bands at and beyond the local field activity. Raw hippocampal extracellular signals (<7 kHz) were subdivided into several frequency bands following the rationale of the previous subsection of the present study. The occurrence of each hippocampal event was used as a reference to align and average the time courses over LFP, HFO, mEFP and MUA domains. We computed averaged, Z-scored NET-BLP for each experimental session, across 3 animals (namely, *cm029*, *cm031* and *k13*). Then, the experiments of 9 experimental sessions were pooled for population statistical analysis (n=103 experiments).

In correspondence with each event type, we found significantly increased activity related to hippocampal events over frequency bands corresponding to sigma (8-22 Hz), gamma (25-75 Hz) and SWR events (<20 Hz and 80-180 Hz) (Figure S4E, F; see also Figure S3A-C). Sigma and SWR events also presented significant tails conflating with gamma frequencies (p<0.01, one-sample permutation t-test, Bonferroni-corrected). Furthermore, Figure S4E displays significant power deviations, albeit antagonistic over high-frequency LFP ranges, mEFP and MUA at the time of occurrence of hippocampal sigma and SWR events. While hippocampal sigma episodes are associated with significant suppression of ripple (80-200 Hz), HFO (201-324 Hz), mEFP (325-800 Hz) and MUA (801-2000 Hz) bands (p<0.01, one-sample permutation t-test, Bonferroni-corrected), hippocampal SWR episodes showed the opposite effect, as they were characterized by a consistent and significant power increase over these frequency domains (p<0.01, one-sample permutation t-test, Bonferroni-corrected). We also observed that increases and decreases of power started 2 seconds before the occurrence of each event. These results indicate that hippocampal SWR and sigma episodes are associated with distinct microcircuit dynamics.

We reasoned that opposite population responses spanning over a time scale of seconds may indicate that the occurrences of sigma and SWR events are (anti-)correlated, thus possibly occurring preferentially over distinct time frames. In order to address this question, we computed cross-correlograms taking as point-processes the occurrence of sigma, gamma and SPW-R events. Statistical significance was assessed against randomized point-processes with the same rate as each individual event type in an experiment-wise manner, up to several permutations. Sigma-SWR point-process conditional intensities displayed a significant drop around the occurrence of the events (p<0.01 permutation test, Bonferroni-corrected; Figure S4G, bottom panel). Furthermore, on average, this correlation drop started approximately one second before the onset of SPW-R episodes (taking this event type as reference in the correlation). We also found event-specific effects in relation to gamma events, which were significantly correlated with sigma episodes, while also significantly anti-correlated with the occurrence of SWR episodes (p<0.01

permutation test, Bonferroni-corrected; Figure S4G, middle and top panels). These results suggest that sigma and SWR episodes appear over distinct time scales.

Prediction of PGO waves via SVM. Before attempting to classify the PGO data, our first analysis revealed that the rate of chance-level detections decreased as we augmented the detection sensitivity (Figure S5B). Based on this procedure, we selected a threshold of 4 SD, accounting for false detections as high as 5%. While the selection of the event detection thresholds is highly arbitrary and depends on empirical criteria (Patel et al., 2013; Sullivan et al., 2011), 4 SD is a stringent threshold. It is likely that the final set of analysed PGO waves in this work is a lower bound of the ground-truth events that occur across the recorded structures.

After determining an optimal event detection threshold, classification experiments revealed that peri-event time courses and spectra were the most informative features. On the basis a linear SVM, PGO wave time courses and spectra reported an averaged classification accuracy of circa 60%, with chance-level classification performance associated with MUA. Thus, we limited our analyses to time-course and spectral features. We next found that non-linear SVM classifiers performed significantly better than linear ones, associated with an averaged performance of up to ~70% (p=0.01 paired-samples t-test, Figure S5D, right subpanel). However, as mentioned in main text, we used linear SVM classifiers in order to compute the weight associated to each time-course and spectral feature in the classification task. Finally, the finding that it is possible to train a non-linear SVM classifier such that it can be applied to previously unknown data (see Main Text, Results section) led us to speculate that the performance could be driven by a specific PGO wave subtype. We reasoned that higher performance could be achieved by training (and testing) the classifier with PGO traces of the same subtype. Nonetheless, we found that non-linear SVM trained on each PGO-wave subtype did not produce significantly different classification performance (Figure S5E; p>0.05 paired-samples t-test for the comparison between type I and type II PGO waves, non-corrected).

During subsequent stages, we asked whether co-occurring events in pons and hippocampus field activities were PGO waves (see Figure S6A for exemplary traces). As additional evidence, after learning a non-linear SVM classifier on 6 pons-LGN experimental sessions, we applied the trained classifier to pons-hippocampus experimental sessions in order to identify which ones amongst the candidate detected phasic potentials correspond to true PGO waves in ground-truth pons-LGN experimental sessions. We found that co-occurrence of pontine-LGN phasic potentials (PGO waves) could be predicted from pontine-wave features computed from co-occurring pontine-hippocampus events, reaching an average of 65.13±0.014% (mean value ± 95% confidence interval) cross-validation prediction accuracy (Figure S6B).

In addition, we performed a labeling consistency analysis, and examined the spectral profiles of predicted PGO waves and co-occurring pontine-hippocampus events. This procedure revealed that event class labels (propagating and non-propagating pontine waves) were largely consistent for pons-LGN and pons-hippocampus sessions (mean value with 95% confidence interval 71.78±0.005%; Figure S6C). Moreover, the averaged spectral profiles of co-occurring pontine-hippocampal events were highly correlated with the spectral profiles of the SVM-predicted PGO waves (Spearman correlation coefficient $\rho=0.9646$ and $\rho=0.9564$, $p<10^{-50}$; see Figure S6D for an exemplary experimental session).

In addition, we found that labeling consistency was higher when comparing the leave-one-out classification assays for a given SVM classifier than across the two distinct SVM classifiers (89.32±0.004% for LGN-pons, and 89.52±0.004% for hippocampus-pons sessions; Figure S6D). On the basis of the previous results, we determined that circa 10% of the non-consistently classified PGO events are due to variations induced by the cross-validation procedure. Conversely, the additional 15% of non-consistently labelled candidate PGO waves in pontine-hippocampal sessions may be attributable to the event detection protocol, since hippocampal episodes are detected from relatively broad-band signals (10-180 Hz), while pontine-LGN events are detected from narrow-band signals (5-15 Hz).

References

Blair, R.C., and Karniski, W. (1993). An alternative method for significance testing of waveform difference potentials. Psychophysiology *30*, 518–524.

Calvo, J.M., and Fernandez-Guardiola, A. (1984). Phasic activity of the basolateral amygdala, cingulate gyrus, and hippocampus during REM sleep in the cat. Sleep *7*, 202–210.

Combrisson, E., and Jerbi, K. (2015). Exceeding chance level by chance: The caveat of theoretical chance levels in brain signal classification and statistical assessment of decoding accuracy. J. Neurosci. Methods *250*, 126–136.

Fritzke, B. (1995). A growing neural gas network learns topologies. Adv. Neural Inf. Process. Syst. *7*, 625–632.

Logothetis, N.K., Eschenko, O., Murayama, Y., Augath, M., Steudel, T., Evrard, H.C., Besserve, M., and Oeltermann, A. (2012). Hippocampal–cortical interaction during periods of subcortical silence. Nature *491*, 547–553.

Patel, J., Schomburg, E.W., Berenyi, A., Fujisawa, S., and Buzsaki, G. (2013). Local Generation and Propagation of Ripples along the Septotemporal Axis of the Hippocampus. J. Neurosci. *33*, 17029–17041.

Shi, J., and Malik, J. (2000). Normalized cuts and image segmentation. Pattern Anal. Mach. Intell. IEEE Trans. On *22*, 888–905.

Sullivan, D., Csicsvari, J., Mizuseki, K., Montgomery, S., Diba, K., and Buzsaki, G. (2011). Relationships between hippocampal sharp waves, ripples, and fast gamma oscillation: influence of dentate and entorhinal cortical activity. J. Neurosci. *31*, 8605–8616.